

中国石油大学 (北京)

2023 年申报硕士研究生指导教师评审材料目录

[illegible]

报告编号：2023-1935

论文收录引用 检索证明报告



中华人民共和国教育部科技查新站（SH01）



论文作者： 龚露

委托单位： 中国石油大学（北京）

论文发表年限： 2019-2023 年

检索数据库：

SCI-EXPANDED	2001- present	网络版
--------------	---------------	-----

检索结果：（作者提供文章）

1) SCI-E 收录：有 8 篇被收录

（详细结果见附件）

特此证明！

检索报告人：

王稳姬



（盖章）

2023 年 11 月 23 日



附件:

一、SCI-E 收录情况

第 1 条, 共 8 条

标题: Fabricating Tunable Superhydrophobic Surfaces Enabled by Surface-Initiated Emulsion Polymerization in Water

作者: Gong, L (Gong, Lu); Yang, WS (Yang, Wenshuai); Sun, YX (Sun, Yongxiang); Zhou, CL (Zhou, Chengliang); Wu, FY (Wu, Feiyi); Zeng, HB (Zeng, Hongbo)

来源出版物: ADVANCED FUNCTIONAL MATERIALS 卷: 33 期: 18 DOI: 10.1002/adfm.202214947 提前访问日期: FEB 2023 出版年: MAY 2023

Web of Science 核心合集中的 "被引频次": 6

被引频次合计: 6

入藏号: WOS:000922451000001

文献类型: Article

地址: [Gong, Lu; Yang, Wenshuai; Sun, Yongxiang; Zhou, Chengliang; Wu, Feiyi; Zeng, Hongbo] Univ Alberta, Dept Chem & Mat Engr, Edmonton, AB T6G 1H9, Canada.

[Zhou, Chengliang] Hunan Univ, Coll Chem & Chem Engr, Changsha 410082, Hunan, Peoples R China.

[Zhou, Chengliang] Hunan Univ, Adv Catalyt Engr Res Ctr, Minist Educ, Changsha 410082, Hunan, Peoples R China.

通讯作者地址: Zeng, HB (通讯作者), Univ Alberta, Dept Chem & Mat Engr, Edmonton, AB T6G 1H9, Canada.

电子邮件地址: hongbo.zeng@ualberta.ca

ISSN: 1616-301X

eISSN: 1616-3028

2022 年期刊的影响因子: 19

2022 年期刊的中科院分区 (升级版): 大类 材料科学 1 TOP

第 2 条, 共 8 条

标题: Unraveling the hydrophobic interaction mechanisms of hydrocarbon and fluorinated surfaces

作者: Gong, L (Gong, Lu); Wu, FY (Wu, Feiyi); Yang, WS (Yang, Wenshuai); Huang, CR (Huang, Charley); Li, WH (Li, Wenhui); Wang, XG (Wang, Xiaogang); Wang, JM (Wang, Jianmei); Tang, T (Tang, Tian); Zeng, HB (Zeng, Hongbo)

来源出版物: JOURNAL OF COLLOID AND INTERFACE SCIENCE 卷: 635 页: 273-283 DOI: 10.1016/j.jcis.2022.12.084 提前访问日期: DEC 2022 出版年: APR 2023

Web of Science 核心合集中的 "被引频次": 3

被引频次合计: 3

入藏号: WOS:000916109100001

文献类型: Article

地址: [Gong, Lu; Wu, Feiyi; Yang, Wenshuai; Huang, Charley; Li, Wenhui; Zeng, Hongbo] Univ Alberta, Dept Chem & Mat Engr, Edmonton, AB T6G 1H9, Canada.

[Wang, Xiaogang; Wang, Jianmei] Taiyuan Univ Sci & Technol, Heavy Machinery Engr Res Ctr, Educ Minist, Taiyuan 030024, Peoples R China.

[Tang, Tian] Univ Alberta, Dept Mech Engr, Edmonton, AB T6G 1H9, Canada.

通讯作者地址: Zeng, HB (通讯作者), Univ Alberta, Dept Chem & Mat Engr, Edmonton, AB T6G 1H9, Canada.



电子邮件地址: hongbo.zeng@ualberta.ca

ISSN: 0021-9797

eISSN: 1095-7103

2022 年期刊的影响因子: 9.9

2022 年期刊的中科院分区 (升级版): 大类 化学 1 TOP

第 3 条, 共 8 条

标题: Ion-specific effect on self-cleaning performances of polyelectrolyte-functionalized membranes and the underlying nanomechanical mechanism

作者: Gong, L (Gong, Lu); Zhang, JW (Zhang, Jiawen); Wang, WD (Wang, Wenda); Xiang, L (Xiang, Li); Pan, MF (Pan, Mingfei); Yang, WS (Yang, Wenshuai); Han, LB (Han, Linbo); Wang, JM (Wang, Jianmei); Yan, B (Yan, Bin); Zeng, HB (Zeng, Hongbo)

来源出版物: JOURNAL OF MEMBRANE SCIENCE 卷: 634 文献号: 119408 DOI: 10.1016/j.memsci.2021.119408 提前访问日期: MAY 2021 出版年: SEP 15 2021

Web of Science 核心合集中的 "被引频次": 4

被引频次合计: 5

入藏号: WOS:000660297600001

文献类型: Article

地址: [Gong, Lu; Zhang, Jiawen; Wang, Wenda; Xiang, Li; Pan, Mingfei; Yang, Wenshuai; Han, Linbo; Yan, Bin; Zeng, Hongbo] Univ Alberta, Dept Chem & Mat Engr, Edmonton, AB T6G 1H9, Canada.

[Han, Linbo] Shenzhen Technol Univ, Coll Hlth Sci & Environm Engr, Shenzhen 518118, Peoples R China.

[Han, Linbo] Taiyuan Univ Sci & Technol, Heavy Machinery Engr Res Ctr, Educ Minist, Taiyuan 518118, Peoples R China.

[Wang, Jianmei] Taiyuan Univ Sci & Technol, Heavy Machinery Engr Res Ctr, Educ Minist, Taiyuan 030024, Peoples R China.

[Yan, Bin] Sichuan Univ, Coll Biomass Sci & Engr, Natl Engr Lab Clean Technol Leather Manufacture, Chengdu 610065, Peoples R China.

通讯作者地址: Yan, B; Zeng, HB (通讯作者), Univ Alberta, Dept Chem & Mat Engr, Edmonton, AB T6G 1H9, Canada.

电子邮件地址: yanbinscu@126.com; hongbo.zeng@ualberta.ca

ISSN: 0376-7388

eISSN: 1873-3123

2022 年期刊的影响因子: 9.5

2022 年期刊的中科院分区 (升级版): 大类 工程技术 1 TOP

第 4 条, 共 8 条

标题: Characterizing foulants on slotted liner and probing the surface interaction mechanisms in organic media with implication for an antifouling strategy in oil production

作者: Gong, L (Gong, Lu); Wang, JY (Wang, Jingyi); Xiang, L (Xiang, Li); Huang, J (Huang, Jun); Fattahpour, V (Fattahpour, Vahidoddin); Roostaei, M (Roostaei, Morteza); Mamoudi, M (Mamoudi, Mahdi); Fermaniuk, B (Fermaniuk, Brent); Luo, JL (Luo, Jing-Li); Zeng, HB (Zeng, Hongbo)

来源出版物: FUEL 卷: 290 文献号: 120008 DOI: 10.1016/j.fuel.2020.120008 出版年: APR 15 2021

Web of Science 核心合集中的 "被引频次": 7

被引频次合计: 7



入藏号: WOS:000618094000007

文献类型: Article

地址: [Gong, Lu; Wang, Jingyi; Xiang, Li; Huang, Jun; Luo, Jing-Li; Zeng, Hongbo] Univ Alberta, Dept Chem & Mat Engr, Edmonton, AB T6G 1H9, Canada.

[Fattahpour, Vahidoddin; Roostaei, Morteza; Mamoudi, Mahdi; Fermaniuk, Brent] RGL Reservoir Management Inc, 3735 6908 42th St, Leduc, AB T9E 0R8, Canada.

通讯作者地址: Zeng, HB (通讯作者), Univ Alberta, Dept Chem & Mat Engr, Edmonton, AB T6G 1H9, Canada.

电子邮件地址: hongbo.zeng@ualberta.ca

ISSN: 0016-2361

eISSN: 1873-7153

2022 年期刊的影响因子: 7.4

2022 年期刊的中科院分区 (升级版): 大类 工程技术 1 TOP

第 5 条, 共 8 条

标题: Surface Interactions between Water-in-Oil Emulsions with Asphaltenes and Electroless Nickel-Phosphorus Coating

作者: Gong, L (Gong, Lu); Zhang, L (Zhang, Ling); Xiang, L (Xiang, Li); Zhang, JW (Zhang, Jiawen); Fattahpour, V (Fattahpour, Vahidoddin); Mamoudi, M (Mamoudi, Mahdi); Roostaei, M (Roostaei, Morteza); Fermaniuk, B (Fermaniuk, Brent); Luo, JL (Luo, Jing-Li); Zeng, HB (Zeng, Hongbo)

来源出版物: LANGMUIR 卷: 36 期: 4 页: 897-905 DOI: 10.1021/acs.langmuir.9b03498 出版年: FEB 4 2020

Web of Science 核心合集中的 "被引频次": 12

被引频次合计: 13

入藏号: WOS:000511509900009

文献类型: Article

地址: [Gong, Lu; Zhang, Ling; Xiang, Li; Zhang, Jiawen; Luo, Jing-Li; Zeng, Hongbo] Univ Alberta, Dept Chem & Mat Engr, Edmonton, AB T6G 1H9, Canada.

[Fattahpour, Vahidoddin; Mamoudi, Mahdi; Roostaei, Morteza; Fermaniuk, Brent] RGL Reservoir Management Inc, Calgary, AB T2P 2W1, Canada.

通讯作者地址: Zeng, HB (通讯作者), Univ Alberta, Dept Chem & Mat Engr, Edmonton, AB T6G 1H9, Canada.

电子邮件地址: hongbo.zeng@ualberta.ca

ISSN: 0743-7463

2022 年期刊的影响因子: 3.9

2022 年期刊的中科院分区 (升级版): 大类 化学 2 TOP

第 6 条, 共 8 条

标题: Fundamentals and Advances in the Adhesion of Polymer Surfaces and Thin Films

作者: Gong, L (Gong, Lu); Xiang, L (Xiang, Li); Zhang, JW (Zhang, Jiawen); Chen, JS (Chen, Jingsi); Zeng, HB (Zeng, Hongbo)

来源出版物: LANGMUIR 卷: 35 期: 48 特刊: SI 页: 15914-15936 DOI: 10.1021/acs.langmuir.9b02123 出版年: DEC 3 2019

Web of Science 核心合集中的 "被引频次": 51

被引频次合计: 52

入藏号: WOS:000500838500052



文献类型: Article

地址: [Gong, Lu; Xiang, Li; Zhang, Jiawen; Chen, Jingsi; Zeng, Hongbo] Univ Alberta, Dept Chem & Mat Engr, Edmonton, AB T6G 1H9, Canada.

通讯作者地址: Zeng, HB (通讯作者), Univ Alberta, Dept Chem & Mat Engr, Edmonton, AB T6G 1H9, Canada.

电子邮件地址: hongbo.zeng@ualberta.ca

ISSN: 0743-7463

2022 年期刊的影响因子: 3.9

2022 年期刊的中科院分区 (升级版): 大类 化学 2 TOP

第 7 条, 共 8 条

标题: Fouling mechanisms of asphaltenes and fine solids on bare and electroless nickel-phosphorus coated carbon steel

作者: Gong, L (Gong, Lu); Wang, JY (Wang, Jingyi); Zhang, L (Zhang, Ling); Fattahpour, V (Fattahpour, Vahidoddin); Mamoudi, M (Mamoudi, Mahdi); Roostaei, M (Roostaei, Morteza); Fermaniuk, B (Fermaniuk, Brent); Luo, JL (Luo, Jing-Li); Zeng, HB (Zeng, Hongbo)

来源出版物: FUEL 卷: 252 页: 188-199 DOI: 10.1016/j.fuel.2019.04.113 出版年: SEP 15 2019

Web of Science 核心合集中的 "被引频次": 11

被引频次合计: 12

入藏号: WOS:000470113800019

文献类型: Article

地址: [Gong, Lu; Wang, Jingyi; Zhang, Ling; Luo, Jing-Li; Zeng, Hongbo] Univ Alberta, Dept Chem & Mat Engr, Edmonton, AB T6G 1H9, Canada.

[Fattahpour, Vahidoddin; Mamoudi, Mahdi; Roostaei, Morteza; Fermaniuk, Brent] RGL Reservoir Management Inc, 3735 8th St, Nisku, AB T9E 8J8, Canada.

通讯作者地址: Zeng, HB (通讯作者), Univ Alberta, Dept Chem & Mat Engr, Edmonton, AB T6G 1H9, Canada.

电子邮件地址: hongbo.zeng@ualberta.ca

ISSN: 0016-2361

eISSN: 1873-7153

2022 年期刊的影响因子: 7.4

2022 年期刊的中科院分区 (升级版): 大类 工程技术 1 TOP

第 8 条, 共 8 条

标题: Interaction Mechanisms of Zwitterions with Opposite Dipoles in Aqueous Solutions

作者: Gong, L (Gong, Lu); Xiang, L (Xiang, Li); Zhang, JW (Zhang, Jiawen); Han, LB (Han, Linbo); Wang, JY (Wang, Jingyi); Wang, XG (Wang, Xiaogang); Liu, JF (Liu, Jifang); Yan, B (Yan, Bin); Zeng, HB (Zeng, Hongbo)

来源出版物: LANGMUIR 卷: 35 期: 7 页: 2842-2853 DOI: 10.1021/acs.langmuir.8b04091 出版年: FEB 19 2019

Web of Science 核心合集中的 "被引频次": 11

被引频次合计: 11

入藏号: WOS:000459642300041

文献类型: Article

地址: [Gong, Lu; Xiang, Li; Zhang, Jiawen; Han, Linbo; Wang, Jingyi; Liu, Jifang; Yan, Bin; Zeng, Hongbo] Univ Alberta, Dept Chem & Mat Engr, Edmonton, AB T6G 1H9, Canada.



[Han, Linbo] Shenzhen Technol Univ, Coll Hlth Sci & Environm Engn, Shenzhen 518118, Peoples R China.

[Wang, Xiaogang] Taiyuan Univ Sci & Technol, Heavy Machinery Engn Res Ctr, Coll Mat Sci & Engn, Educ Minist, Taiyuan 030024, Shanxi, Peoples R China.

[Liu, Jifang] Guangzhou Med Univ, Affiliated Hosp 5, Guangzhou 510700, Guangdong, Peoples R China.

[Yan, Bin] Sichuan Univ, Coll Light Ind Text & Food Engn, Chengdu 610065, Sichuan, Peoples R China.

通讯作者地址: Yan, B; Zeng, HB (通讯作者), Univ Alberta, Dept Chem & Mat Engn, Edmonton, AB T6G 1H9, Canada.

Yan, B (通讯作者), Sichuan Univ, Coll Light Ind Text & Food Engn, Chengdu 610065, Sichuan, Peoples R China.

电子邮件地址: yanbinscu@126.com; hongbo.zeng@ualberta.ca

ISSN: 0743-7463

2022 年期刊的影响因子: 3.9

2022 年期刊的中科院分区 (升级版): 大类 化学 2 TOP

(End)

经委托人确认签字:



Fabricating Tunable Superhydrophobic Surfaces Enabled by Surface-Initiated Emulsion Polymerization in Water

Lu Gong, Wenshuai Yang, Yongxiang Sun, Chengliang Zhou, Feiyi Wu, and Hongbo Zeng*

Fabricating controllable superhydrophobic surfaces remains challenging in various fields ranging from chemical industries to biomedical engineering. Conventional methods commonly require volatile organic solvents and the assistance of special surface deposition and modification equipment, which are detrimental to environment and limit their applications in micro-devices. Herein, an equipment-free method is reported to directly transform fluorinated monomer micro-droplets into hydrophobic polymer particles on flat substrate surfaces in water, simultaneously depositing hydrophobic coatings with tunable surface structures. The as-prepared surfaces show superior superhydrophobicity and great stability in extreme conditions (e.g., varying acidity, basicity, and heating conditions), and excellent anti-fouling property. Meanwhile, surface hydrophobicity can be manipulated by adjusting emulsion droplet number density and reaction time. Hence, superhydrophobic surfaces with tunable hydrophobicity gradients have been successfully fabricated in one pot. This study provides an equipment-free method to facilely fabricate controllable superhydrophobic surfaces, with great potential in the development of smart superhydrophobic materials in various engineering and industrial applications.

intensively investigated due to their excellent properties, such as anti-sticking,^[2] anti-fouling,^[3] anti-icing,^[4] bubble/drop manipulation,^[5] self-cleaning^[6] and anti-corrosion.^[7] Even though great efforts have been made to fabricate numerous superhydrophobic surfaces for decades, surface modification techniques fulfilling versatile fabrication conditions and variable application conditions are still in high demand.

Conventional methods to prepare superhydrophobic surfaces always consist of two steps: covering the surface with hydrophobic materials and constructing surface microstructure.^[8] The former step could be achieved using self-assembly and self-organization of hydrophobic particles, such as the chemical deposition,^[9] layer-by-layer deposition,^[10] colloidal assembly,^[11] phase separation,^[12] and electrospinning.^[13] The surface structure would be fabricated via lithographic and template-based techniques,^[14] etching processes,^[15] and plasma treatment.^[16] However, these

methods are usually complex and require the assistance of special advanced equipment, such as nanoimprinter, etching machine, electrospinning apparatus, and so on. In confined situations of fine chemical engineering, such as the inner surface of a thin tube and the tiny substrate with irregular surface morphology, the operation conditions of equipment are very limited, and robust surface superhydrophobicity is difficult to be fabricated. Besides, volatile organic solvents, which are commonly used to dissolve hydrophobic materials, are detrimental to environment and human health. Meanwhile, the controllable superhydrophobic surface with designed hydrophobicity gradient becomes more and more important in directional bubble/drop manipulation, microfluidics, microbiology, and smart robots,^[17] which is complex and difficult to be prepared using conventional methods. Therefore, an equipment-free and universal fabrication technique to fabricate controllable superhydrophobic surfaces in water should be developed.

In aqueous solutions, insoluble hydrophobic materials prefer to aggregate due to the strong hydrophobic interactions,^[18] thus preventing the uniform distribution of hydrophobic materials. Nevertheless, liquid hydrophobic materials can be easily dispersed in water and distributed evenly on a substrate surface in the form of emulsions.^[19] However, liquid hydrophobic materials cannot stably stay on a substrate surface and achieve superior superhydrophobicity.^[20] Many hydrophobic polymer monomers are liquid, but corresponding polymers are solid.

1. Introduction

Superhydrophobic surfaces, which show high water contact angle (WCA) and low contact angle hysteresis in air,^[1] have been

L. Gong, W. Yang, Y. Sun, C. Zhou, F. Wu, H. Zeng
Department of Chemical & Materials Engineering
University of Alberta
Edmonton, Alberta T6G 1H9, Canada
E-mail: hongbo.zeng@ualberta.ca

C. Zhou
College of Chemistry and Chemical Engineering
Hunan University
Changsha, Hunan 410082, P. R. China

C. Zhou
Advanced Catalytic Engineering Research Center of the Ministry of Education
Hunan University
Changsha, Hunan 410082, P. R. China

 The ORCID identification number(s) for the author(s) of this article can be found under <https://doi.org/10.1002/adfm.202214947>.

© 2023 The Authors. Advanced Functional Materials published by Wiley-VCH GmbH. This is an open access article under the terms of the Creative Commons Attribution-NonCommercial License, which permits use, distribution and reproduction in any medium, provided the original work is properly cited and is not used for commercial purposes.

DOI: 10.1002/adfm.202214947

If heterogeneous polymerization process could be initiated on a substrate surface, monomer droplets would be transformed into solid polymer particles and grafted onto substrate surface, which thereby may achieve surface superhydrophobicity directly without any assistance of surface deposition and modification equipment.

In this work, we, for the first time, report a new method to initiate polymerization processes of fluorinated monomer droplets on substrate surfaces to generate hydrophobic particles in aqueous solutions without any special advanced equipment. This method can simultaneously deposit hydrophobic materials on flat substrate surfaces and create surface structure, hence fabricating superhydrophobic surfaces. As-prepared surface exhibited a very high WCA of $\approx 167.7^\circ$ and low WCA hysteresis of $\approx 0.7^\circ$, as well as excellent water drop behaviors, including sliding, rolling, and bouncing. Great surface stability in extreme conditions including varying acidity, basicity, high-temperature conditions, and organic solvents was explored. Besides, anti-fouling properties were tested via the adhesion with different foulants (e.g., sodium dodecyl sulfate (SDS), cetyltrimethylammonium bromide (CTAB), dopamine hydrochloride (DOPA), Bovine Serum Albumin (BSA), and humic acid (HA)). Scanning Electron Microscopy (SEM) and Energy Dispersive X-Ray Spectroscopy (EDS) results showed evenly scattered fluorinated polymer particles on the surface, which could be manipulated by reaction time and density of emulsion droplets. Hence, polymerization mechanism and building process on substrate surfaces were proposed. Meanwhile, a superhydrophobic surface with tunable hydrophobicity gradient was successfully prepared by creating density difference of bulk monomer droplets. In this work, we have developed the surface-initiated emulsion polymerization method to fabricate facile and tunable superhydrophobic surfaces in water, which not only simultaneously alters surface wettability and creates surface structure, but also gets rid of the limitation of organic solvents and special equipment.

2. Results and Discussion

2.1. Characterization of Superhydrophobic Surface

Figure 1A shows schematic image of preparing superhydrophobic surfaces via the method combining surface-initiated radical polymerization and emulsion polymerization. Namely, fluorinated monomer was first dispersed in water to form stable emulsion system. Then, monomer droplets would gradually diffuse to contact substrate surface with initiators, where polymerization processes could occur. **Figure 1B** shows the optical images of silicon substrate before (left) and after (right) polymerization process. Obviously, before polymerization, silicon substrate with initiators was quite clean, whereas there was a layer of grey film on the substrate surface after polymerization, suggesting that hydrophobic monomer could be transformed into solid particles and grafted on substrate surface via polymerization reaction. The water contact angle (WCA) in air was $169.7^\circ \pm 1.3^\circ$ as shown in **Figure 1C**, and the contact angle hysteresis measured from the difference between advancing and receding contact angle was $0.7^\circ \pm 0.3^\circ$ as in **Figure 1D**. Such extremely large WCA and ultralow contact angle hysteresis in air demonstrated the excellent surface superhydrophobicity. When immersing a superhydrophobic surface in water (**Figure 1E**), the underwater area turned out to be much more reflective than that in air, indicating that a layer of air could be trapped on the surface due to the excellent superhydrophobicity.

The surface morphology of prepared superhydrophobic surface was characterized by SEM images as shown in **Figure 2A**, which exhibited that substrate surface was covered by numerous assembled particles. Enlarged SEM image in **Figure 2B** elucidated that these particles were relatively small in size of several hundred nanometers, which then aggregated and stacked into micron-sized particles on surface. On the other hand, silicon substrate with initiators was quite flat with only several small nanoaggregates (**Figure S1A**, Supporting Information). The

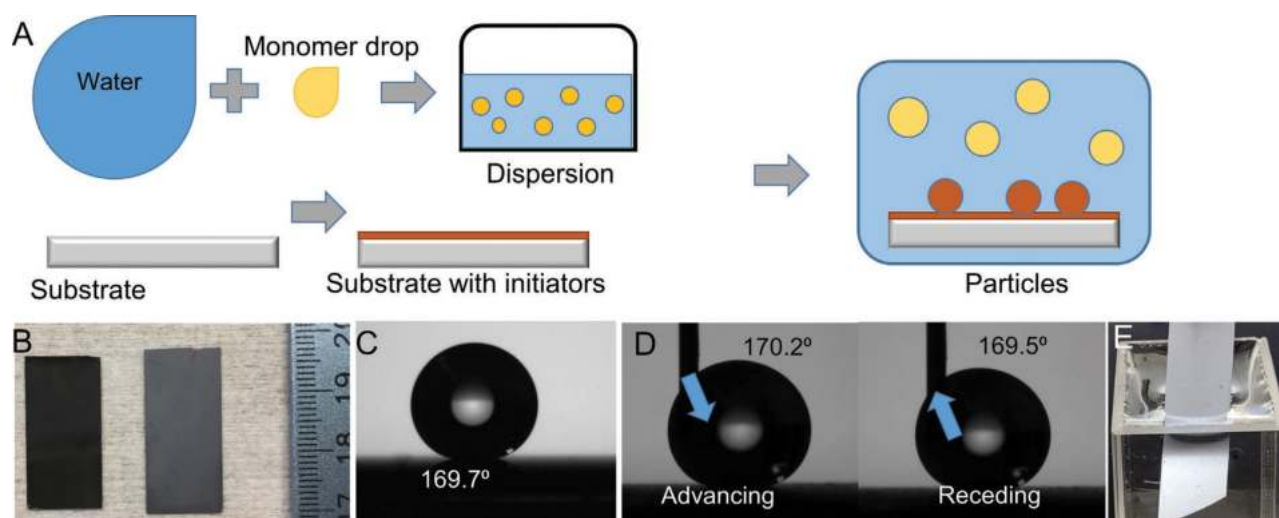


Figure 1. A) Schematic for preparing superhydrophobic surfaces in this work. B) Optical images of silicon substrate with initiators (left) and as-prepared substrate after polymerization (right). C) WCA image on substrate surface. D) Advancing (left) and receding (right) WCA images on substrate surface. The blue arrows show pump-in and pump-out flowing of water via a needle. E) Optical image of the superhydrophobic surface immersed in water.

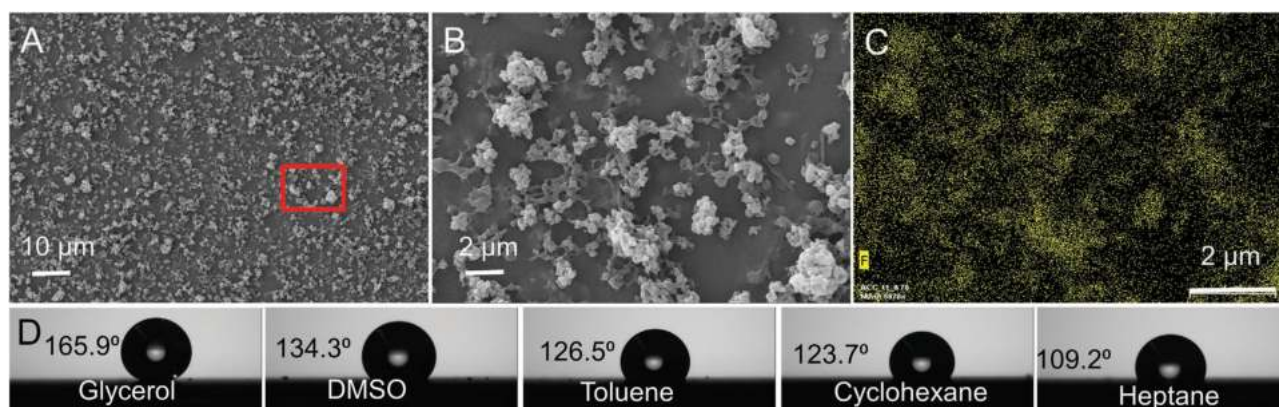


Figure 2. SEM image A), enlarged SEM image B), and corresponding EDS image of fluorine (F) element of superhydrophobic surface. D) Contact angles of polar and apolar organic solvents on superhydrophobic surface, including glycerol, DMSO, toluene, cyclohexane, and heptane.

root-mean-squared surface roughness (R_q) was measured to be 0.52 nm and the WCA was only $\approx 76.3^\circ$ in air (Figure S1B, Supporting Information). Hence, generated hydrophobic particles and confined air among them can make the Cassie–Baxter state and render the surface with excellent superhydrophobicity.^[21] Figure 2C shows the surface distribution of fluorine (F) element on superhydrophobic surface. The bright yellow area in this figure indicates the high concentration of F, which matches the scattered particles in Figure 2B. This result demonstrated that the particles could come from fluorinated monomer droplets. Besides, XPS results in Figure S2 (Supporting Information) show $-\text{CH}_2-$ peak at 283.5 eV, $-\text{CF}_2-$ peak at 289.6 eV, and $-\text{CF}_3$ peak at 291.8 eV, attesting to the presence of fluorinated polymer on the surface.

To ensure that polymer particles were generated via surface-initiated emulsion polymerization instead of bulk polymerization before depositing on substrate surface, a clean silicon substrate without initiators was placed in monomer–water emulsion (including catalyst Cu(I)Br and copper ligand) for 12 h. Obtained substrate was characterized by AFM surface imaging as in Figure S3 (Supporting Information). The surface was still quite smooth with a surface roughness (R_q) of 0.82 nm and WCA in air of 80.9° . This result demonstrated that no polymerization process occurred in bulk. Therefore, prepared superhydrophobic surface was fabricated via the surface-initiated emulsion polymerization process of hydrophobic monomer droplets. Figure 2D shows the contact angle with organic liquids, which is 165.9° for glycerol, 134.3° for dimethyl sulfoxide (DMSO), 126.5° for toluene, 123.7° for cyclohexane, and 109.2° for heptane, respectively. These large oil contact angles were due to the very low surface energy of fluorinated materials.^[22] Hence, prepared substrate surface is both superhydrophobic and oleophobic in air.

2.2. Stability and Water Drop Behaviors of Superhydrophobic Surface

The stability of as-prepared superhydrophobic surface was examined by WCA measurement after the superhydrophobic surface was treated in extreme conditions including a broad pH

range from 0 to 14, high salinity of 3 M NaCl, and high temperature of 120°C in air for 2 h. Measured results are shown in Figure 3A. It should be noted that even though the superhydrophobic surface was treated under these extreme conditions, WCAs were still larger than 165° , and contact angle hysteresis was less than 1° , which indicated that the superhydrophobic surface owned excellent stability.

Figure 3B shows a water drop standing on the superhydrophobic surface while the surface was smoothly dragged in lateral directions (Movie S1, Supporting Information). It was noted that the contact angle change of $\approx 0.8^\circ$ was quite small as water drop was sliding on surface, indicating ultralow friction between water drop and superhydrophobic surface. Since measured contact angle hysteresis in Figure 1C was $0.7^\circ \pm 0.3^\circ$, a water drop could easily roll down on superhydrophobic surface at an inclination angle as small as 1° (Figure 3C; Movie S1, Supporting Information). Besides, when a water drop fell from a height of 5 cm to impact the superhydrophobic surface (Figure 3D; Movie S1, Supporting Information), this water drop became a pancake shape, and then bounced back as one drop to the height of ≈ 1 cm. During impacting process, most dynamic energy of a water drop could be dissipated in drop shape change, and very little energy was consumed in the contact area change between water and substrate due to the extremely weak adhesion.^[23] The outstanding water drop sliding, rolling, and bouncing behaviors not only showed the excellent surface superhydrophobicity, but also demonstrated the good surface uniformity on a macroscopic scale.

Figure 3E,G show the WCA of $174.5^\circ \pm 0.8^\circ$ and $172.1^\circ \pm 0.7^\circ$ on superhydrophobic surface in toluene and heptane, respectively. These very high contact angles were attributed to the excellent surface hydrophobicity (or low surface energy) and the buoyance force in organic media. Figure 3F,H show water drop rolling on superhydrophobic surface at a small inclination angle of 2° in toluene and heptane, respectively (Movie S2, Supporting Information). The moving velocity was measured to be 3.5 mm s^{-1} in toluene and 8.0 mm s^{-1} in heptane, respectively. Faster moving velocity in heptane was due to the lower viscosity of heptane than that of toluene.^[24] Hence, prepared substrate exhibited the excellent surface superhydrophobicity in both air and organic media.

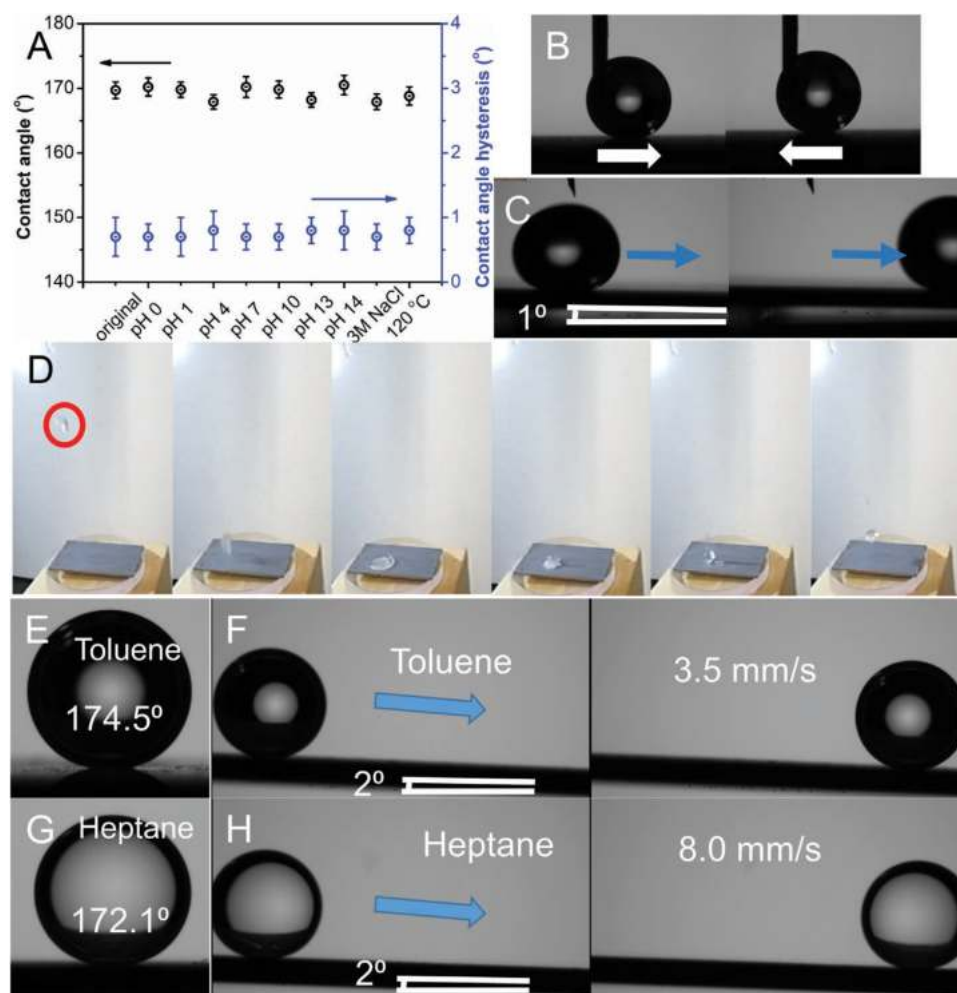


Figure 3. A) WCA and contact angle hysteresis on superhydrophobic surface before and after treated in extreme conditions, including a broad pH range (0, 1, 4, 7, 10, 13, and 14), high salinity (3 M NaCl solution), and high temperature (120 °C) in air for 2 h. B) Superhydrophobic surface was dragged laterally to move right and left with a water drop standing on it. C) A water drop was rolling down on superhydrophobic surface at a small inclination angle of 1°. D) A water drop was impacting the superhydrophobic surface from a height of 5 cm and bouncing back. WCA in E) toluene or G) heptane on superhydrophobic surface. Water drop was rolling on superhydrophobic surface in F) toluene or H) heptane.

2.3. Antifouling Performances of Superhydrophobic Surface

The antifouling performance of superhydrophobic surface has been conducted using water drop washing method. A layer of kaolin powder was gently pressed on superhydrophobic surface, followed by being flipped over to remove unstable powder. This fouled surface was then placed in a disk to form an incline, as in Figure 4A and Movie S3 (Supporting Information). Water was continuously dropped from the upper side and smoothly rolled down due to surface superhydrophobicity. During this process, kaolin foulants were carried by rolling water drops to disk, and the surface became clean again. This result suggested the excellent self-cleaning property of superhydrophobic surface, which was attributed to the stronger adhesion of water with the foulant (e.g., kaolin powder) than that with superhydrophobic surface.^[25]

Besides, the antifouling property was explored via measuring surface interactions between superhydrophobic surface and water drops (50 mM PBS buffer, pH 7.4) dissolved

with surfactants (SDS or CTAB) or common bio-foulants (DOPA, BSA, or HA), as in Figure 4B. Measured force profiles are shown in Figure 4C, and normalized adhesion results are shown in Figure 4D. It was noted that even though great loading force ($\approx 0.3 \text{ N m}^{-1}$) was applied to press water drops to substrate surface, measured adhesion during detachment was so weak, suggesting that the foulants could be easily removed from substrate surface. This could be due to the excellent superhydrophobicity and low surface energy. Adding surfactants or bio-foulants in water drop slightly enhanced the drop-surface adhesion (Figure 4D), which may be the presence of van der Waals (VDW) interaction and hydrophobic attraction of surfactants or bio-foulants with superhydrophobic surface.

2.4. Polymerization Mechanism of Superhydrophobic Surface

As shown in Figure 2A, fabricated superhydrophobic surface was covered by numerous nano-sized fluorinated polymer

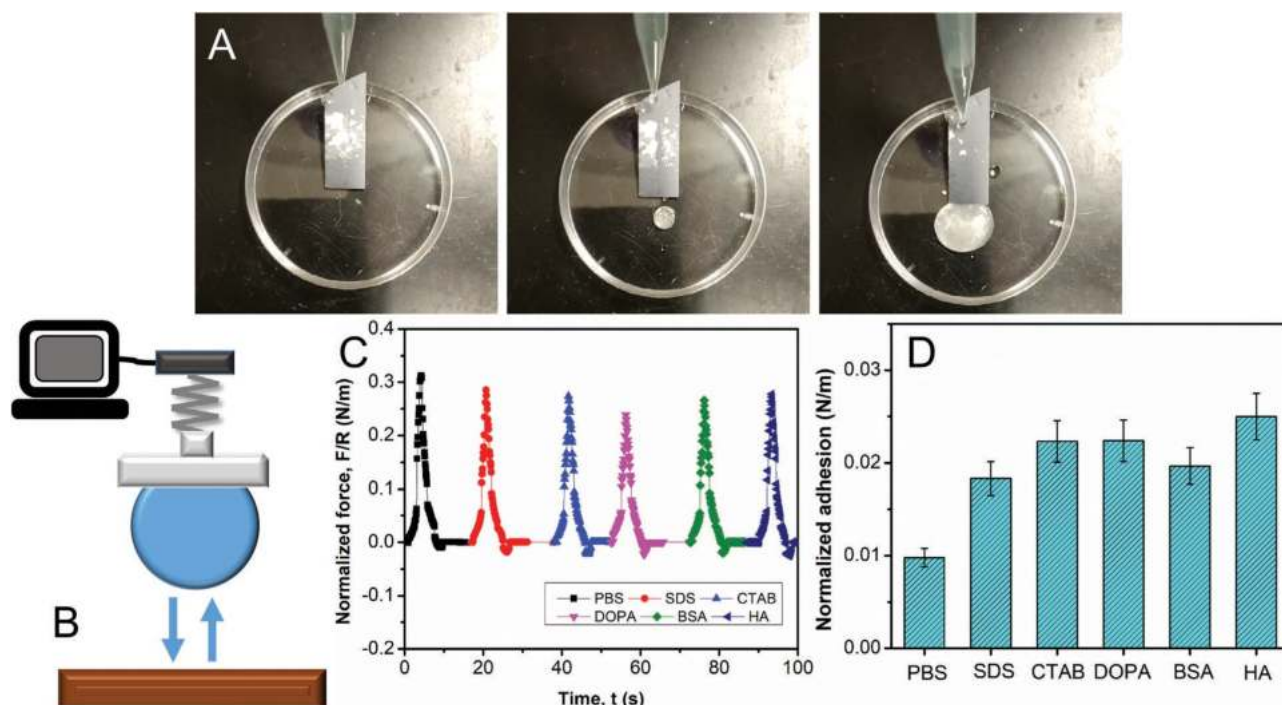


Figure 4. A) Antifouling performance of superhydrophobic surface. B) Illustration image for force measurement set-up. Measured force profiles C) and normalized adhesion D) between superhydrophobic surface and water drops (PBS buffer) with SDS, CTAB, DOPA, BSA, and HA.

particles, which could be the result of surface-initiated emulsion polymerization of fluorinated monomer droplets on substrate surface in water. To understand polymerization mechanism and building process, emulsion systems with both high (2.5 vol.%) and low (0.1 vol.%) monomer content for different reaction times have been exploited. Obtained substrates were characterized by SEM images and WCA measurements as shown in Figure 5.

Figure 5A–C shows the SEM images of silicon substrate surfaces in polymerization systems with high content (2.5 vol.%) for 2, 4, and 8 h, respectively. Surprisingly, there were some polymer particles scattering on the surface after polymerization process for a short time of 2 h. It was noted that the most polymer particles were in single form, while only a small part of them aggregated to form relatively large particles. After polymerization for 4 h, more polymer particles were assembled

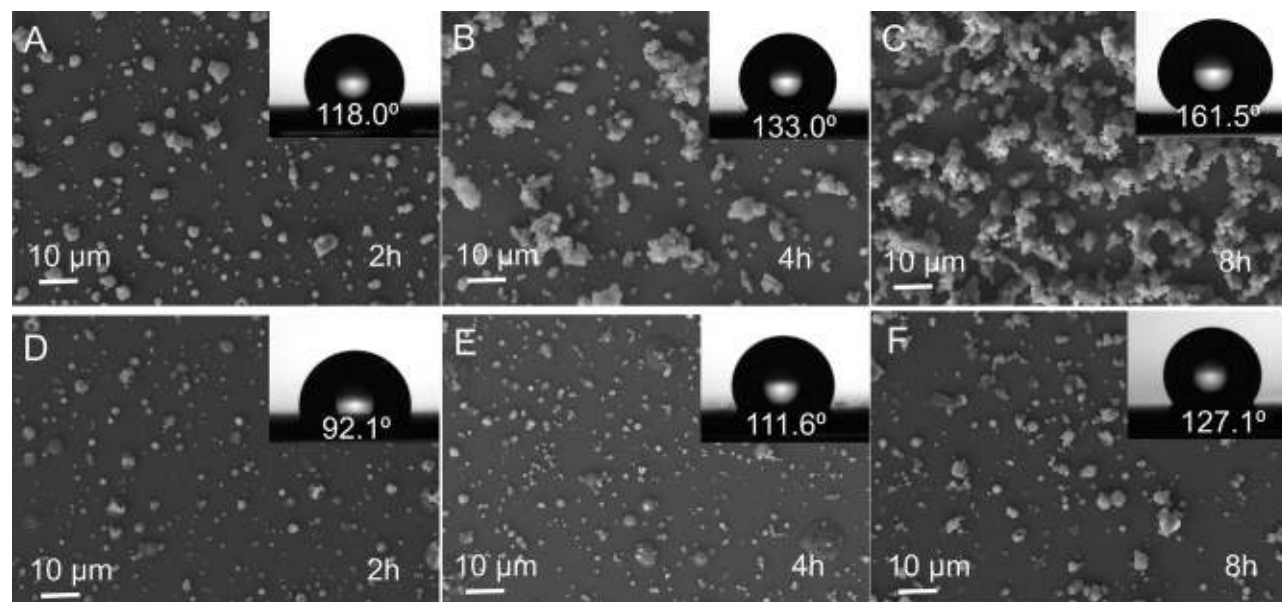


Figure 5. SEM images and WCA in air (inset) of silicon substrates in the polymerization systems with A–C) high (2.5 vol. %) and D–F) low (0.1 vol. %) monomer content for 2, 4, and 8 h, respectively.

on substrate surface and the number of large polymer particle aggregates increased distinctly. After 8 h, most surface area was covered by polymer particles, and almost all the polymer particles were in aggregation form and stacked into large polymer particles with a size of several microns. The WCA in air on these substrates also increased from $118.0^\circ \pm 1.7^\circ$ for 2 h, to $133.0^\circ \pm 1.4^\circ$ for 4 h, and $161.5^\circ \pm 1.1^\circ$ for 8 h, respectively, suggesting the significantly enhanced surface hydrophobicity. Figure 5D–F shows the SEM images after polymerization in 0.1 vol.% for 2, 4, and 8 h, respectively. Similarly, polymer particles were observed for even 2 h. As reaction time increased, more and more polymer particles were assembled on substrate surface. However, most particles were still single. Only very limited polymer particle aggregates were observed after polymerization for 8 h. The WCA in air also increased from $92.1^\circ \pm 0.8^\circ$ for 2 h, to $111.6^\circ \pm 1.2^\circ$ for 4 h, and $127.1^\circ \pm 0.9^\circ$ for 8 h, respectively, suggesting the slightly enhanced surface hydrophobicity. Compared with high monomer content cases, the density of polymer particles on substrate surface was distinctly decreased, and the size of polymer particle aggregates

was much smaller. Obtained substrates in low monomer content were hydrophobic but not superhydrophobic. The size distribution of monomer droplets in water after supersonication for 30 min (Figure S4, Supporting Information) proved that more and larger droplets could be generated when monomer content was higher (e.g., 2.5%), which further led to the higher possibility of monomer droplets attached onto silicon substrate with initiators. Hence, more polymer particles could be generated and aggregated. It should also be noted that enough surface density and micron-sized aggregates of polymer particles were required to achieve excellent surface superhydrophobicity.

The supersonication effect has also been included to investigate polymerization mechanism. Figure 6A shows the SEM image of obtained substrate surface after polymerization with 2.5 vol.% monomer for 8 h when applied supersonication time was only 10 min. There were many particles grafted on substrate surface, but they did not aggregate into large particles during polymerization process. The size of single particles was also relatively larger than that for 30 min supersonication (Figure 5C). Measured WCA in air was only $100.9^\circ \pm 1.0^\circ$,

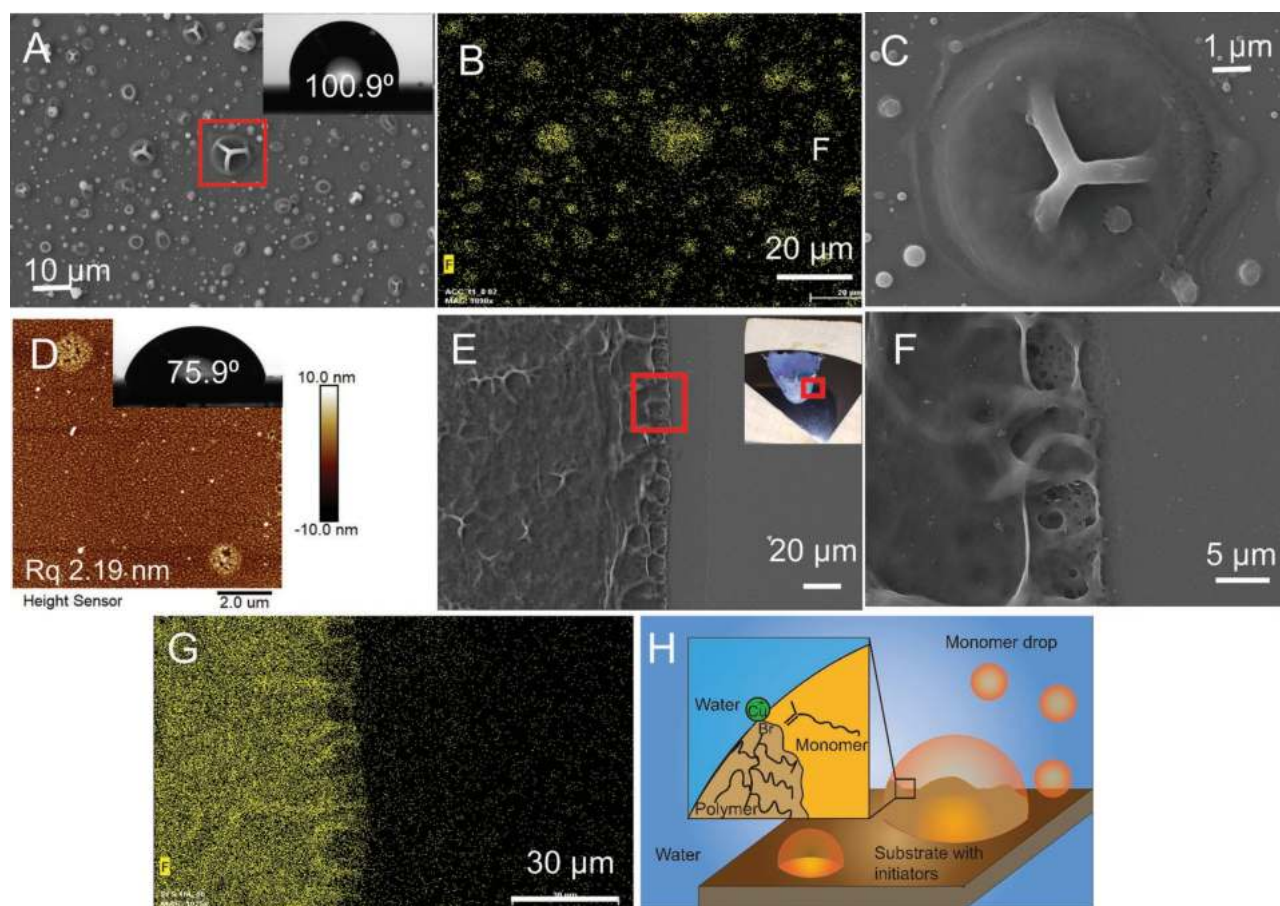


Figure 6. A) SEM image of silicon substrate after polymerization for 8 h when the applied supersonication time was only 10 min. The inset image shows WCA in air. B) Corresponding EDS elemental image for fluorine. C) Enlarged SEM image for the area highlighted by the red rectangular box. D) AFM topography image of silicon substrate after polymerization for 8 h when no supersonication was applied. E) SEM image of polymer drop boundary on silicon substrate after polymerization for 8 h when only one drop of 150 μL monomer was carefully placed on the silicon substrate surface and no supersonication was applied. The inset is the optical image of obtained substrate surface after cleaning and drying. F) Enlarged SEM image of boundary area of polymer and silicon substrate surface. G) Corresponding EDS image of fluorine element. H) Schematic illustration for polymerization process at monomer-water interface.

suggesting that this substrate was hydrophobic but not superhydrophobic. The EDS element distribution image in Figure 6B shows that particles were still composed of fluorinated polymer. Surprisingly, some strange-shaped polymer particles were observed on substrate surface. These particles were relatively large, exhibiting three short ridges connecting with one of their ends, stretching out in the angle of $\approx 120^\circ$, and standing on a round pancake base. Element distribution image in Figure 6B confirmed that the main element of three ridge-shaped particles was fluorine, suggesting that they were also the product of polymerization. The size of some monomer droplets might be so large after the shot-time supersonication (i.e., 10 min) (Figure S4, Supporting Information). Hence, the center part of large monomer droplets could not be consumed in the polymerization process due to the absence of catalyst and ligand, thus remaining liquid form. This part of liquid monomer would be drained out after polymerization, leaving the hollow polymer shell collapsed to form three-ridged shape. Based on this result, it could be speculated that polymerization process would only occur at monomer-water interface and could continue when one monomer droplet is attached onto a polymer particle.

To support this speculation, polymerization process was first initiated with no supersonication and no direct contact of monomer drop with silicon substrate. AFM surface image of obtained substrate in Figure 6D shows that surface was flat with lots of small nano-sized particles and several larger particles, compared with the AFM surface image of silicon substrate with initiators (Figure S1, Supporting Information). Small particles could be the polymerization product of a trace amount of dissolved fluorinated monomers in water.^[26] Large particles could be due to the coalescence of dissolved monomers. WCA on the surface was only $75.9^\circ \pm 0.7^\circ$. Subsequently, only one drop of 150 μL monomer was carefully placed on silicon substrate with initiators for polymerization of 8 h, and no supersonication was applied. Obtained substrate is shown in the inset image of Figure 6E. It should be noted that monomer liquid was found when cleaning the substrate after polymerization process. This interesting surface with a drop-breaking shape was caused by surface cleaning and drying procedure. SEM image on the contact line of polymer and substrate is shown in Figure 6E,F. The left area was polymer while the right area was silicon substrate, which was then confirmed by EDS element distribution result in Figure 6G. At boundary area, polymer layer was observed to graft onto silicon substrate surface through numerous polymer strands, thus leaving some pores at the contact line. This structure also suggests that polymerization process could be initiated from the contact line of monomer and substrate, and propagate at monomer-water interface with the assistance of catalyst (i.e., Cu(I)) and ligand, as shown in Figure 6H. In summary, when a substrate surface with initiators was immersed in monomer-water emulsion, monomer droplets would diffuse and attach onto substrate surface due to hydrophobic interaction. Subsequently, polymerization process started at the contact line, which turned liquid monomer into solid polymer strands. Small monomer droplets on substrate surface could be easily transformed into polymer particles, whereas large monomer droplets would mostly have polymerization reactions at monomer-water interface, which could generate a polymer shell. Polymerization process could continue at the interface of

another monomer droplet once it contacted a reacting droplet, which thereby would generate large particle aggregates. These results have demonstrated that dispersing monomer liquid into sub-micron-sized droplets could play an important role in fabrication process of superhydrophobic surfaces. It should be noted that this surface-initiated emulsion polymerization would be expected to occur on any substrate surface with initiators (including both flat and non-flat surfaces), which could be achieved via the substrate-independent deposition of polydopamine.^[27]

2.5. Emulsion Polymerization for Controllable Superhydrophobic Surface

According to the Boltzmann distribution theories, micro-sized droplets in a stable emulsion system would have a density difference under external energy field, such as gravity.^[28] Namely, higher droplet density could exist at bottom of an emulsion, whilst less droplets at top. Hence, it is feasible to fabricate a surface with controllable hydrophobicity gradient via adjusting monomer drop density in gravity field. A monomer-water emulsion system was prepared via sonication for 30 min and injected into a glass with the diameter of 2 cm and the height of 10 cm (Figure 7A). After standing for 24 h, this emulsion system became stable and the droplet density difference was formed under the gravity field. Then, a silicon substrate with initiators was placed vertically in the vial. After polymerization time of 8 h, the substrate was cleaned with water and dried in vacuum.

Figure 7B shows the WCAs on prepared substrate. Five water drops (5 μL) were separately placed on different spots of the substrate and measured WCAs exhibited a distinct decreasing trend from left to right. The left side of substrate, which was placed at bottom of emulsion system, owned the great superhydrophobicity with WCA of 164.7° , whereas the right side placed at top only showed the WCA of 117.7° . This WCA change indicated the successful fabrication of superhydrophobic surface with controlled hydrophobicity gradient. The SEM images of the left and right area of this substrate (Figure 7C) also revealed the distinct difference in surface structure and particle density, which led to surface hydrophobicity gradient. Figure 7D shows the underwater bubble behaviors on this substrate. Air bubbles were continuously injected at less hydrophobic side in water, and found to move on the surface from left side to right side (Movie S4, Supporting Information), which finally detached due to the buoyance. This indicated that this hydrophobicity-gradient surface would have potential applications in directional bubble/drop manipulation.

3. Conclusion

In this research, for the first time, superhydrophobic surfaces have been fabricated in water via a simple method combining surface-initiated radical polymerization and emulsion polymerization without any assistance of special surface deposition and modification equipment. Water contact angle measurement results showed that the as-prepared surfaces possessed superior superhydrophobicity and excellent stability in extreme

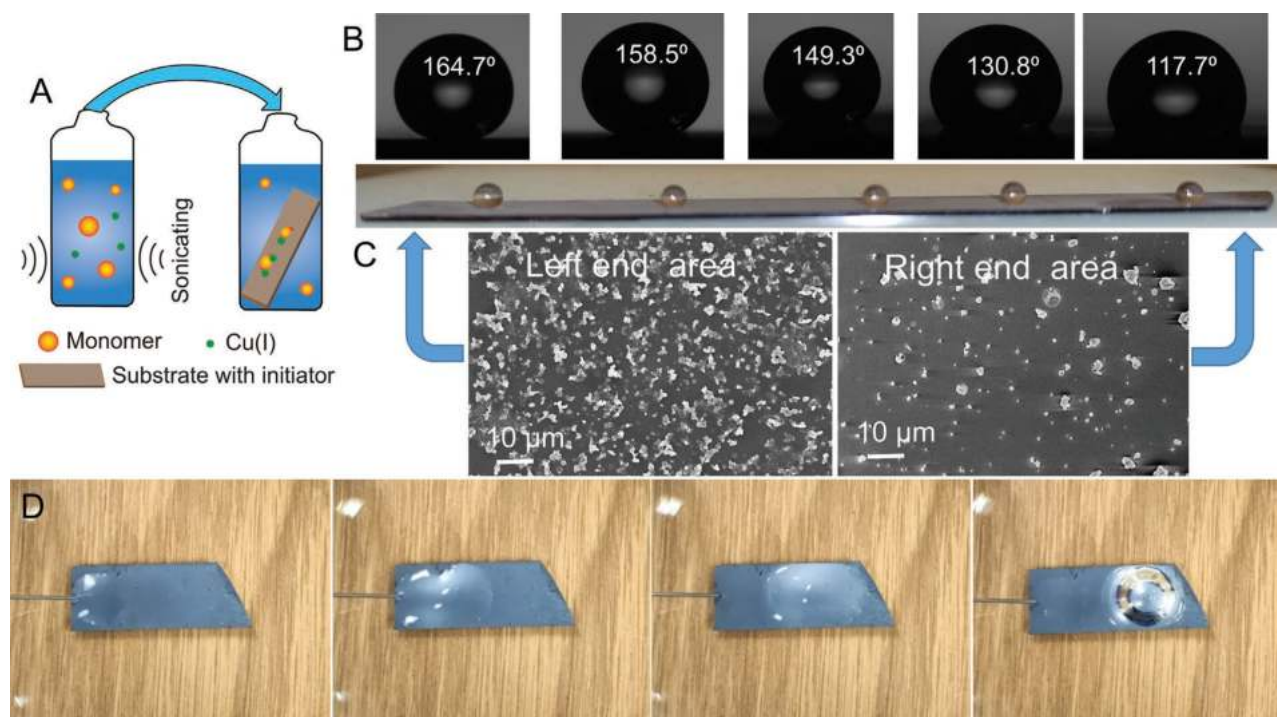


Figure 7. A) Schematic illustration of the emulsion polymerization system for preparing superhydrophobic surface with controlled hydrophobicity gradient. B) WCA images and optical images of superhydrophobic surfaces with controlled hydrophobicity gradient. C) SEM images of the left and right end regions of the superhydrophobic surface with hydrophobicity gradient. D) Directional transportation of air bubbles on superhydrophobic surface with controlled hydrophobicity gradient.

conditions, including varying acidity, basicity, high-temperature conditions, and organic media. Besides, various water drop behaviors, such as sliding, rolling, and bouncing, were observed when they interacted with the as-prepared surfaces. Meanwhile, water-washing processes and surface force measurement results exhibited that these surfaces also had excellent antifouling properties against solids, surfactants, and bio-foulants. SEM and EDS results elucidated that during fabrication process, fluorinated monomer micro-droplets gradually attached onto substrate surface with initiators, and polymerization reaction turned liquid monomer droplets into solid particles, thus achieving great surface superhydrophobicity. Based on this polymerization process and the number density difference of monomer droplets in gravity field, superhydrophobic surface with tunable hydrophobicity gradient was successfully fabricated and showed potential applications in underwater bubble/drop transportation. This work has developed a simple and equipment-free method to fabricate controllable superhydrophobic surfaces in water, which not only paves the way for development of advanced and environment-friendly surface modification techniques but also expands the applications of superhydrophobic surfaces in micro-devices (e.g., micro-fluidics and micro-robots).

4. Experimental Section

Materials: The hydrophobic monomer of 3,3,4,4,5,5,6,6,7,7,8,8,9,9,10,10,10 heptafluorodecyl methacrylate (HFMA) was purchased from

Sigma Aldrich, Canada. The silicon wafer was purchased from NanoFAB, University of Alberta, and used as the substrate. Sulfuric acid (H_2SO_4 , 95%, Sigma-Aldrich, Canada) and hydrogen peroxide solution (H_2O_2 , 30%, Sigma-Aldrich, Canada) was used to clean the silicon substrates. The copper (I) bromide (CuBr), (3-aminopropyl) triethoxysilane (APTES), 2-bromo-2-methylpropionyl bromide (BiBB), triethylamine (TEA), and 2,2'-bipyridyl (bpy) were purchased from the Sigma Aldrich, Canada, and used in the surface fabrication. All the aqueous solutions were prepared using Milli-Q water with a resistivity of $18.2 \text{ M}\Omega\cdot\text{cm}$ (BARNSTEAD Smart2Pure, Thermo Scientific, Canada). Ethanol ($\text{CH}_3\text{CH}_2\text{OH}$, Sigma-Aldrich, Canada), dichloromethane (DCM, CH_2Cl_2 , Sigma-Aldrich, Canada), toluene (C_7H_8 , Sigma-Aldrich, Canada), and heptane (C_7H_{16} , Sigma-Aldrich, Canada) were used as received. The hydrochloric acid, KOH, CaCl_2 , and K_2CO_3 were purchased from Sigma Aldrich, Canada, and used as received.

Preparation of Silicon Substrates with Initiators: The preparation process of the silicon substrates with initiators is shown in Figure S5 (Supporting Information). Silicon substrates (1 × 1 cm) were cut using the diamond knife and washed using Milli-Q water and ethanol, followed by drying in pure nitrogen. Piranha solution was prepared by carefully mixing hydrogen peroxide solution in sulfuric acid with volume ratio of 3:7. Silicon substrates were carefully immersed in Piranha solution, and temperature was maintained at 80 °C for at least 2 h. Cleaned silicon substrates were immersed in APTES-in-ethanol solution (0.5 vol.%) for 30 min to own amino groups on surface, followed by being washed with ethanol and dried in pure nitrogen. Subsequently, the APTES-modified substrates were immersed in 6 mL DCM solution with 0.37 mol BiBB and 0.42 mol TEA for 30 min. The substrates were rinsed with ethanol and DI water, and dried in pure nitrogen. Then, silicon substrates with initiators were prepared. Figure S1A (Supporting Information) shows the AFM surface images of the as-prepared silicon substrate with initiators, which was quite flat with only several small aggregates on the surface. The root-mean-squared surface roughness (R_q) was measured to be

0.52 nm. Figure S1B (Supporting Information) shows the WCA of 76.3° in air. These results demonstrated the successful preparation of the substrate surfaces with initiators.

Emulsion Polymerization for Superhydrophobic Surfaces: Superhydrophobic surfaces were prepared using the method combining the surface-initiated radical polymerization and the emulsion polymerization.^[29] Fluorinated monomer HFMA was injected into 20 mL deoxygenated water at volume ratio of 2% in a glass vial. Then, 0.08 g Cu(I)Br and 0.16 g bpy were added. The mixture was treated by supersonic for 30 min to prepare the emulsion. Subsequently, silicon substrate with initiators was placed in the vial to initiate the polymerization on the substrate surface. This glass vial was sealed and left under ambient conditions for 12 h. Finally, obtained substrate was washed with water and ethanol, and dried in vacuum for 4 h.

Superhydrophobic Surface Characterization: The surface morphology and the elemental distribution of the as-prepared superhydrophobic substrate were characterized by the Scanning Electron Microscopy (SEM) with Energy Dispersive X-ray Spectroscopy (EDS) (Zeiss Sigma 300 VP-FESEM, Germany), and the X-ray photoelectron spectrometer (XPS).

The water contact angle (WCA) in air was measured using the goniometer (Ramé-hart Instrument Company, USA). A water drop (5 μ L) was carefully placed on the superhydrophobic substrate, and the angle value was measured by the software from the image. The advancing or receding WCA was measured when water was pumped in or out at the rate of 1 μ L s⁻¹ via a needle, respectively. The contact angle hysteresis was determined by the difference between advancing and receding WCA values.

Antifouling Performance: The anti-fouling performances on superhydrophobic substrates were conducted with the solid foulants of kaolin powders (Sigma-Aldrich, Canada). First, solid foulants were forcibly pressed on as-prepared substrate surface. This surface was then flipped over to remove unstable solids, followed by being placed in a disk to form an inclination. One milliliter of water was dropped using a pipet on the substrate to let water drops roll down the substrate. This process was recorded using a camera.

The antifouling performances on superhydrophobic substrate were examined by measuring the adhesion between substrate and water drop (50 mm PBS buffer, pH 7.4) with 2 mg mL⁻¹ of different surfactants or biomaterials, including sodium dodecyl sulfate (SDS, Sigma-Aldrich, Canada), cetyltrimethylammonium bromide (CTAB, Sigma-Aldrich, Canada), dopamine hydrochloride (DOPA, Sigma-Aldrich, Canada), Bovine Serum Albumin (BSA, Sigma-Aldrich, Canada), and humic acid (HA, Sigma-Aldrich, Canada), using the Force Tensiometer (Sigma 700, Attension, Biolin Scientific, UK). The measuring process is shown in Figure S6A (Supporting Information). A custom-made ring (diameter \approx 4 mm) with 30 μ L water drop was hung on the force sensor of the machine, and the as-prepared substrate was placed on the sample plate. To measure the interaction force, the substrate was lifted by the sample plate to approach the water drop at the velocity of 20 mm s⁻¹, till the radical deformation of the water drop reached 1 mm. Then, the substrate was withdrawn to the original place. The force profile was obtained from the software. Figure S6B (Supporting Information) shows the measured force profile between water drop (50 mm PBS buffer) and the as-prepared substrate. A very weak adhesion of 0.00886 mN was measured, indicating the excellent surface hydrophobicity.

Statistical Analysis: The averaged contact angle values and standard deviation was calculated from at least 5 measurements on 2 independently prepared substrates. The averaged normalized adhesion was from at least 5 measurements.

Supporting Information

Supporting Information is available from the Wiley Online Library or from the author.

Acknowledgements

This work was supported by the Natural Sciences and Engineering Research Council of Canada (NSERC), the Canada Foundation for Innovation (CFI), and the Canada Research Chairs Program (H.Z.).

Conflict of Interest

The authors declare no conflict of interest.

Data Availability Statement

The data that support the findings of this study are available from the corresponding author upon reasonable request.

Keywords

fluorinated monomer droplets, superhydrophobic surfaces, surface-initiated emulsion polymerization, tunable hydrophobicity

Received: December 23, 2022

Revised: January 18, 2023

Published online: February 2, 2023

- [1] H. Rathgen, F. Mugele, *Faraday Discuss.* **2010**, 146, 49.
- [2] a) D. Choi, J. Yoo, S. M. Park, D. S. Kim, *Appl. Surf. Sci.* **2017**, 393, 449; b) C. C. Liang, C. H. Lin, T. C. Cheng, J. Shieh, H. H. Lin, *Adv. Mater. Interfaces* **2015**, 2, 1500030.
- [3] a) X. Yin, S. Yu, K. Wang, R. Cheng, Z. Lv, *Chem. Eng. J.* **2020**, 394, 124925; b) Z. Wang, Y. Tang, B. Li, *J. Membr. Sci.* **2017**, 540, 401.
- [4] a) Y. Wang, J. Xue, Q. Wang, Q. Chen, J. Ding, *ACS Appl. Mater. Interfaces* **2013**, 5, 3370; b) L. Wang, Q. Gong, S. Zhan, L. Jiang, Y. Zheng, *Adv. Mater.* **2016**, 28, 7729.
- [5] a) D. Gao, J. Cao, Z. Guo, *Chem. Commun.* **2019**, 55, 3394; b) H. Wang, Z. Zhang, J. Zheng, J. Zhao, Y. Liang, X. Li, L. Ren, *Chem. Eng. J.* **2021**, 417, 127944.
- [6] a) K. M. Wisdom, J. A. Watson, X. Qu, F. Liu, G. S. Watson, C.-H. Chen, *Proc. Natl. Acad. Sci. USA* **2013**, 110, 7992; b) H. Li, S. Yu, *Appl. Surf. Sci.* **2017**, 420, 336.
- [7] a) D. Sebastian, C.-W. Yao, I. Lian, *Coatings* **2018**, 8, 162; b) S. Xu, Q. Wang, N. Wang, X. Zheng, *J. Mater. Sci.* **2019**, 54, 13006.
- [8] a) X.-M. Li, D. Reinholdt, M. Crego-Calama, *Chem. Soc. Rev.* **2007**, 36, 1350; b) C.-H. Xue, S.-T. Jia, J. Zhang, J.-Z. Ma, *Sci. Technol. Adv. Mater.* **2010**; c) K. Manoharan, S. Bhattacharya, *J. Micromanuf.* **2019**, 2, 59; d) S. G. Moghadam, H. Parsimehr, A. Ehsani, *Adv. Colloid Interface Sci.* **2021**, 290, 102397.
- [9] a) S. Rezaei, I. Manoucheri, R. Moradian, B. Pourabbas, *Chem. Eng. J.* **2014**, 252, 11; b) L. Huang, S. P. Lau, H. Yang, E. Leong, S. F. Yu, S. Praver, *J. Phys. Chem. B* **2005**, 109, 7746.
- [10] a) N. Zhao, F. Shi, Z. Wang, X. Zhang, *Langmuir* **2005**, 21, 4713; b) T. Ogawa, B. Ding, Y. Sone, S. Shiratori, *Nanotechnology* **2007**, 18, 165607.
- [11] a) G. Zhang, D. Wang, Z.-Z. Gu, H. Möhwald, *Langmuir* **2005**, 21, 9143; b) J. Li, J. Fu, Y. Cong, Y. Wu, L. Xue, Y. Han, *Appl. Surf. Sci.* **2006**, 252, 2229.
- [12] a) N. Zhao, Q. Xie, L. Weng, S. Wang, X. Zhang, J. Xu, *Macromolecules* **2005**, 38, 8996; b) S. Kato, A. Sato, *J. Mater. Chem.* **2012**, 22, 8613.

- [13] a) X. Wang, B. Ding, J. Yu, M. Wang, *Nano Today* **2011**, 6, 510; b) V. A. Ganesh, A. S. Nair, H. K. Raut, T. T. Y. Tan, C. He, S. Ramakrishna, J. Xu, *J. Mater. Chem.* **2012**, 22, 18479.
- [14] a) J. Victor, D. Facchini, U. Erb, *J. Mater. Sci.* **2012**, 47, 3690; b) Y. Chen, H. Wang, Q. Yao, B. Fan, C. Wang, Y. Xiong, C. Jin, Q. Sun, *J. Mater. Sci.* **2017**, 52, 7428.
- [15] a) M. Ruan, W. Li, B. Wang, Q. Luo, F. Ma, Z. Yu, *Appl. Surf. Sci.* **2012**, 258, 7031; b) H. Jie, Q. Xu, L. Wei, Y. Min, *Corros. Sci.* **2016**, 102, 251.
- [16] a) R. Jafari, S. Asadollahi, M. Farzaneh, *Plasma Chem. Plasma Process.* **2013**, 33, 177; b) J. Ryu, K. Kim, J. Park, B. G. Hwang, Y. Ko, H. Kim, J. Han, E. Seo, Y. Park, S. J. Lee, *Sci. Rep.* **2017**, 7, 1981.
- [17] a) O. I. Vinogradova, A. L. Dubov, *Mendeleev Commun.* **2012**, 22, 229; b) E. Ueda, P. A. Levkin, *Adv. Mater.* **2013**, 25, 1234; c) C. Yang, Q. Zeng, J. Huang, Z. Guo, *Adv. Colloid Interface Sci.* **2022**, 306, 102724; d) W. Li, Y. Zhan, A. Amirfazli, A. R. Siddiqui, S. Yu, *Prog. Org. Coat.* **2022**, 168, 106877; e) X. Wang, L. Dai, N. Jiao, S. Tung, L. Liu, *Chem. Eng. J.* **2021**, 422, 129394.
- [18] T. M. Raschke, J. Tsai, M. Levitt, *Proc. Natl. Acad. Sci. USA* **2001**, 98, 5965.
- [19] a) C. Chern, *Prog. Polym. Sci.* **2006**, 31, 443; b) J. Ugelstad, F. Hansen, *Rubber Chem. Technol.* **1976**, 49, 536.
- [20] a) M. Cao, D. Guo, C. Yu, K. Li, M. Liu, L. Jiang, *ACS Appl. Mater. Interfaces* **2016**, 8, 3615; b) R. Stoddard, K. Nithyanandam, R. Pitchumani, *J. Colloid Interface Sci.* **2022**, 608, 662.
- [21] a) D. Murakami, H. Jinnai, A. Takahara, *Langmuir* **2014**, 30, 2061; b) J.-H. Hao, Z.-J. Wang, *J. Dispersion Sci. Technol.* **2016**, 37, 1208.
- [22] a) H. Peng, *Polym. Rev.* **2019**, 59, 739; b) W. Wu, Q. Zhu, F. Qing, C. C. Han, *Langmuir* **2009**, 25, 17.
- [23] a) B.-B. Wang, Y.-P. Zhao, T. Yu, *J. Adhes. Sci. Technol.* **2011**, 25, 93; b) D. J. Lee, H. M. Kim, Y. S. Song, J. R. Youn, *ACS Nano* **2012**, 6, 7656; c) A. M. Moqaddam, S. S. Chikatamarla, I. V. Karlin, *J. Fluid Mech.* **2017**, 824, 866.
- [24] A. H. S. Dehaghani, M. H. Badizad, *Petroleum* **2016**, 2, 415.
- [25] a) F. Geyer, M. D'Acunzi, A. Sharifi-Aghili, A. Saal, N. Gao, A. Kaltbeitzel, T.-F. Slood, R. Berger, H.-J. Butt, D. Vollmer, *Sci. Adv.* **2020**, 6, eaaw9727; b) B. Bhushan, Y. C. Jung, K. Koch, *Langmuir* **2009**, 25, 3240; c) W. Zheng, J. Huang, X. Zang, X. Xu, W. Cai, Z. Lin, Y. Lai, *Adv. Mater.* **2022**, 34, 2204581.
- [26] a) D. K. Nordstrom, E. A. Jenne, *Geochim. Cosmochim. Acta* **1977**, 41, 175; b) P. LoNostro, S.-M. Choi, C.-Y. Ku, S.-H. Chen, *J. Phys. Chem. B* **1999**, 103, 5347.
- [27] a) W. O. Yah, H. Xu, H. Soejima, W. Ma, Y. Lvov, A. Takahara, *J. Am. Chem. Soc.* **2012**, 134, 12134; b) R. Yang, J. Xu, G. Ozaydin-Ince, S. Y. Wong, K. K. Gleason, *Chem. Mater.* **2011**, 23, 1263; c) N. D. Brault, C. Gao, H. Xue, M. Piliarik, J. Homola, S. Jiang, Q. Yu, *Biosens. Bioelectron.* **2010**, 25, 2276; d) L. Han, L. Gong, J. Chen, J. Zhang, L. Xiang, L. Zhang, Q. Wang, B. Yan, H. Zeng, *ACS Appl. Mater. Interfaces* **2018**, 10, 2166.
- [28] a) A. Sanfeld, A. Steinchen, *Adv. Colloid Interface Sci.* **2008**, 140, 1; b) S. Aghion, O. Ahlén, C. Amsler, A. Ariga, T. Ariga, A. Belov, G. Bonomi, P. Bräunig, J. Bremer, R. Brusa, *J. Instrum.* **2013**, 8, P08013.
- [29] a) K. He, H. Duan, G. Y. Chen, X. Liu, W. Yang, D. Wang, *ACS Nano* **2015**, 9, 9188; b) K. Matyjaszewski, *Macromolecules* **2012**, 45, 4015; c) Q. Wang, S. Fu, T. Yu, *Prog. Polym. Sci.* **1994**, 19, 703.



Ion-specific effect on self-cleaning performances of polyelectrolyte-functionalized membranes and the underlying nanomechanical mechanism

Lu Gong^a, Jiawen Zhang^a, Wenda Wang^a, Li Xiang^a, Mingfei Pan^a, Wenshuai Yang^a,
Linbo Han^{a,b}, Jianmei Wang^c, Bin Yan^{a,d,**}, Hongbo Zeng^{a,*}

^a Department of Chemical & Materials Engineering, University of Alberta, Edmonton, Alberta, T6G 1H9, Canada

^b College of Health Science and Environmental Engineering, Shenzhen Technology University, Shenzhen, 518118, China

^c Heavy Machinery Engineering Research Center of Education Ministry, Taiyuan University of Science and Technology, Taiyuan, 030024, China

^d National Engineering Laboratory for Clean Technology of Leather Manufacture, College of Biomass Science and Engineering, Sichuan University, Chengdu, 610065, China

ARTICLE INFO

Keywords:

Antifouling property
Ion-specific effect
Polyelectrolyte surfaces
Wetting behavior
Surface interactions

ABSTRACT

In chemical and environmental engineering processes, polyelectrolyte surfaces have been widely used and exploited for their antifouling and self-cleaning properties. Ions widely exist in these processes; however, the influence of ions has been conventionally over-simplified. Herein, we have investigated the ion-specific effect on the wetting behaviors on polyelectrolyte surfaces as well as the self-cleaning performance of polyelectrolyte-functionalized membranes. The underlying nanomechanical mechanisms were characterized by direct force measurements between water droplets and various polyelectrolyte surfaces in oil (i.e., toluene). Interestingly, the aqueous anions can significantly modulate the surface interactions through aligning or disordering interfacial water molecules, which subsequently facilitate or inhibit the water wetting behaviors on polyelectrolyte surfaces, respectively. The ion-specific effect of different anions coincides with the well-known Hofmeister series. In contrast, cations show negligible effect. The polyelectrolyte-functionalized membranes show excellent antifouling and self-cleaning performances to oil in KAc and KCl solutions, but relatively poor performance in KSCN solution, agreeing well with the force measurements. This work provides new insights into the ion-specific interaction mechanism between water and polyelectrolyte surfaces, with useful implications for the efficient use of the antifouling and self-cleaning properties of polyelectrolyte-based materials in various chemical and environmental engineering applications (e.g., membrane filtration, oil/water separation).

1. Introduction

Polyelectrolytes are ubiquitously found in nature and in biological systems with negatively and/or positively charged group in molecules, such as proteins, DNA and enzymes [1–6]. The superior water wettability and hydration of polyelectrolyte materials endows their surfaces with excellent properties due to the strong electrostatic attraction between the polyelectrolytes and nearby water molecules, such as underwater oil repellence, and lubrication [7–10]. In biological systems, the firmly bound water molecules have been demonstrated to play a vital role in the structure and function of various proteins [11–13]. In

chemical, biomedical and environmental engineering processes, the polyelectrolyte-based materials have been widely used and exploited for their well-known antifouling and self-cleaning properties, which is also contributed by their strong interaction with water [14–19]. For example, during the membrane filtration processes in waste water treatment and water/oil separation, polyelectrolyte coatings can render the membranes with strong hydration layer, leading to high water flux and excellent antifouling and self-cleaning properties [20–26]. Hence, the membrane service time can be sufficiently prolonged and the maintenance cost will be greatly reduced. Over the past two decades, filtration membranes have been applied in increasingly harsh and

* Corresponding author.

** Corresponding author. Department of Chemical & Materials Engineering, University of Alberta, Edmonton, Alberta, T6G 1H9, Canada.

E-mail addresses: yanbinscu@126.com (B. Yan), hongbo.zeng@ualberta.ca (H. Zeng).

<https://doi.org/10.1016/j.memsci.2021.119408>

Received 27 February 2021; Received in revised form 26 April 2021; Accepted 30 April 2021

Available online 7 May 2021

0376-7388/© 2021 Elsevier B.V. All rights reserved.

complex working conditions, such as complex water chemistries (e.g., salinity, pH, and ion species). Maintaining the superior hydration state and antifouling/self-cleaning properties of the polyelectrolyte surfaces under various conditions ensures the excellent performance of polyelectrolyte-coated membranes in related chemical and environmental engineering applications.

In previous studies, it was found that the hydrophobic oil can readily spread on the polyelectrolyte surface in air due to the high surface energy and the re-orientation of the polyelectrolyte molecules [27–29]. When the oil-fouled polyelectrolyte surface was immersed in water, the strong interaction between water molecules and the polyelectrolyte molecules across oil could lead to the depletion of the confined oil film and finally achieve the detachment of the oil in water, thus contributing to its excellent antifouling and self-cleaning properties [29]. It should be noted that the interaction forces involving water can be significantly influenced by the water chemistries (e.g., salinity, pH, and ion species) [30–32]. Varying the salinity and pH of the aqueous solutions has been demonstrated to affect the hydration behavior and antifouling performance of polyelectrolyte surfaces [33–36]. In the applications of polyelectrolyte surfaces, the influence of aqueous ion species, which are practically inevitable, has been conventionally over-simplified [30]. Previous studies have demonstrated that the different ions can adsorb onto polyelectrolyte surface and competitively interact with the charges of the polyelectrolytes, thus significantly affecting the molecular conformation and related performances of polyelectrolytes in aqueous solutions [27,37–43]. However, the interaction mechanisms of water with polyelectrolyte surface across surrounding medium (e.g., hydrophobic oil), especially under ion-specific effect, still remain unrevealed [30,44]. Thereby, investigating the underlying nanomechanical interactions between water and polyelectrolyte surfaces across oil with different aqueous ion species is of both fundamental and practical importance to reveal the physical mechanisms of ion-specific effect on surface wetting behavior, and to maintain the efficient antifouling and self-cleaning performances of polyelectrolyte materials in practical applications, such as membrane filtration.

In this work, the influence of the ion species on the antifouling and spontaneous oil cleaning performances of polyelectrolyte surfaces has been investigated. The nanomechanics between water and polyelectrolyte surfaces in oil under the ion-specific effect have been systematically and quantitatively investigated using the drop probe atomic force microscope (AFM) technique, which reveal the underlying interaction mechanisms of the ion-specific effect. Furthermore, the antifouling properties of polyelectrolyte-coated membranes have been tested to examine the influence of the ion-specific effect in practical applications of polyelectrolyte materials. Our Results improve the fundamental understandings on surface wetting behavior, fouling and antifouling phenomena, and self-cleaning processes of polyelectrolyte surfaces, and facilitate the development of polyelectrolyte materials for various engineering applications such as membrane filtration and oil/water separation.

2. Methods

Preparation of polyelectrolyte surfaces. The silicon substrates were carefully cut using a diamond knife into proper size. After washed with DI water and ethanol and dried with pure nitrogen, these silicon substrates were cleaned by the Piranha solution ($\text{H}_2\text{SO}_4:\text{H}_2\text{O}_2 = 7:3$ (v:v)) in 80 °C for at least 2 h to remove possible organic contaminants on the surfaces. Then, the substrates were rinsed with a large amount of distilled (DI) water and ethanol, and dried with pure nitrogen, and immediately immersed in 0.5 vol% (3-aminopropyl) triethoxysilane (APTES)-in-ethanol solution for 30 min, followed by being carefully rinsed with anhydrous ethanol and dried with pure nitrogen. The APTES-treated substrates were immersed in 10 mL dichloromethane (DCM) solution with 0.37 mol 2-bromo-2-methylpropionyl bromide (BiBB) and 0.42 mol triethylamine (TEA) for 30 min. Finally, these

substrates were washed with ethanol and DI water, and dried with pure nitrogen. The substrates with initiators were prepared for next experiments.

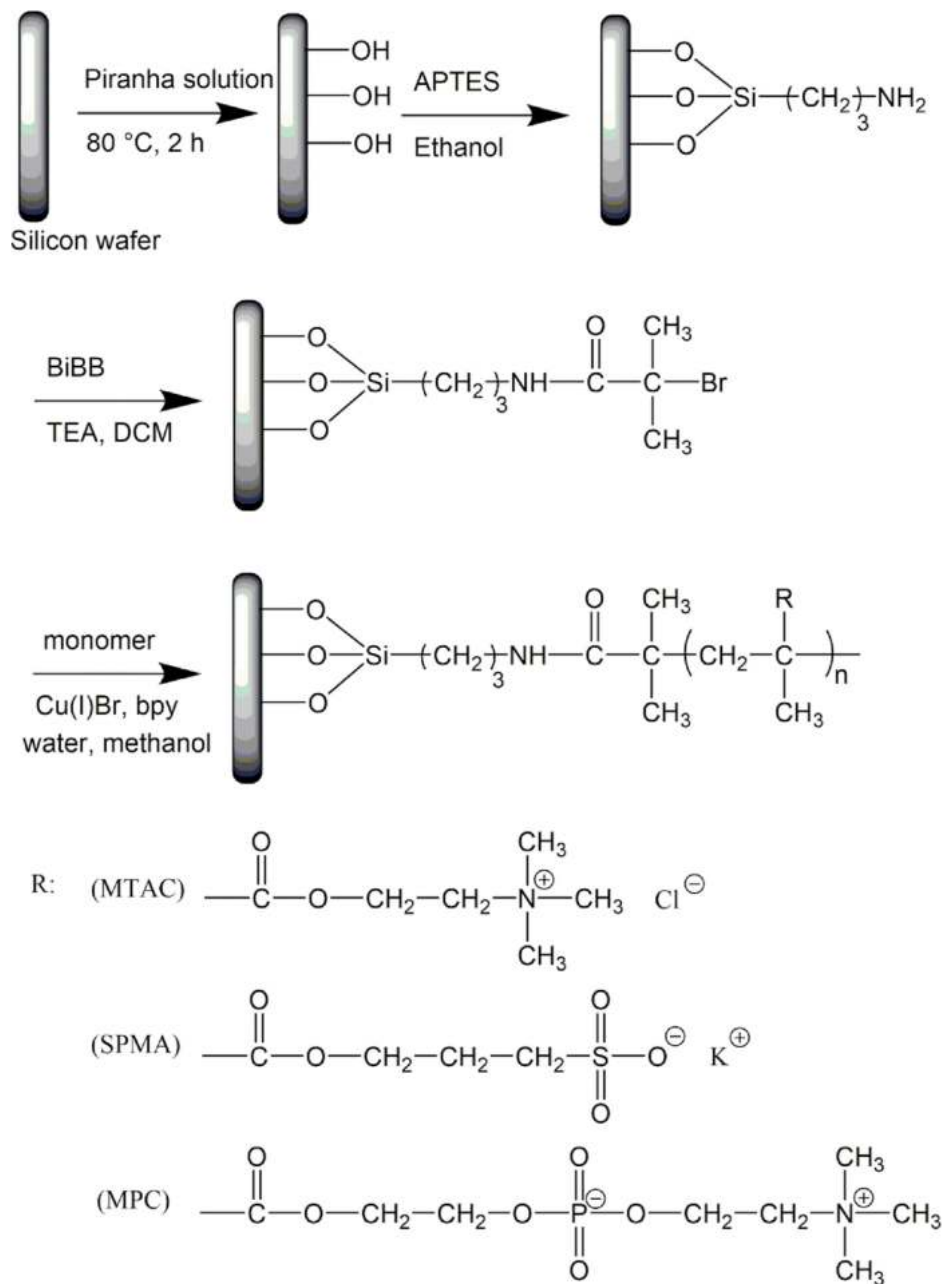
The polyelectrolyte brush surfaces were prepared using the surface initiated atom transfer radical polymerization (SI-ATRP) on the silicon substrates with initiators. The schematic of SI-ATRP process is shown in Scheme 1. The substrates with surface initiator were placed in a 25 mL vial with flat bottom, and the air in vial was purged with argon. The polymerization solution was prepared using 10 mL water-methanol solvent (v:v = 2:1) and 1–2 g monomers in another sealed vial. This solution was stirred at the speed of 300 rpm using a magnetic bar and the pure argon was injected in the solution in the form of bubbles for 30 min to remove the dissolved oxygen. Then, 0.08 g CuBr and 0.16 g 2,2'-bipyridyl (bpy) were added carefully and the argon was continuously injected for another 30 min. After that, the solution was pumped into the 25 mL vial with substrates through a connecting pipe to start the polymerization. The whole vial was sealed and kept in room temperature for 18 h. The substrates were washed with DI water and ethanol for several times to remove the unreacted materials and dried with pure nitrogen. These substrates were immersed in 3 M NaCl solution for at least 48 h to remove the copper ions on polymer surfaces.

Force measurements using drop probe AFM technique. The interaction forces between the water drop with different salts and polyelectrolyte surfaces in toluene were directly measured using the drop probe AFM technique. A MFP-3D-Bio AFM system (Asylum Research, Santa Barbara, CA) was exploited in this work. The detailed experimental process was reported elsewhere [29,45–47].

In a typical force measurement using the drop probe AFM technique, the water drops were carefully generated using a custom-made glass pipet in the fluid cell filled with toluene. The glass substrate of the fluid cell was firstly hydrophobized using the octadecyl (trichloro) silane OTS (5 mM in ethanol) to render a water contact angle (WCA) of $\sim 90^\circ$ in air, which therefore facilitated the immobilization of water drops on the glass substrate in toluene and the following pick-up process by the AFM cantilever. After stabilized for 10 min, the custom-made AFM rectangular tipless silicon cantilever (size $400\ \mu\text{m} \times 70\ \mu\text{m} \times 2\ \mu\text{m}$) was introduced into the toluene and carefully lowered down to pick up one water drop. Thus, the water drop probe was prepared via anchoring the water drop on the AFM cantilever.

For the force measurement between the water drop and polyelectrolyte surface, the as-prepared water drop probe was moved and positioned just above the polyelectrolyte surface, which was placed near the immobilized water drops before the AFM cantilever was immersed in toluene. Voltage was applied on the piezo actuator through the AFM software to control the deformation of the piezo. The water drop probe was driven by the piezo actuator to approach the polyelectrolyte surface from a large separation till water drop jumped off from the cantilever to the substrate due to strong attraction. The AFM cantilever acted as a force spring, and the surface interactions between water drop and substrate surface caused the cantilever deflection. After a selected force measurement was completed, the cantilever was lifted up to the original position. The moving velocity of the cantilever was set to be $1\ \mu\text{m/s}$. Meanwhile, the laser beam, reflected from the tip of the backside of the AFM cantilever, was pointing on a photo detector. Thus, the cantilever deflection was detected and recorded. The spring constant of the cantilever was calibrated using the Hutter-Bechhoefer method [48]. Therefore, the interaction force between the water drop and polyelectrolyte surface in toluene was measured and obtained from the AFM software as the function of piezo displacement and time. It should be noted that the piezo displacement ΔX in this work is the relative moving distance of the cantilever driven by the piezo, which is different from the separation distance between the water drop and polyelectrolyte surface and from the cantilever deflection.

Theoretical analysis of measured force profiles. To theoretically describe the measured force profiles, the model combining the Reynolds lubrication equation and augmented Young-Laplace equation was



Scheme 1. The process of the SI-ATRP and the chemical structures of polyelectrolyte brush surfaces.

applied here [49–52]. During the AFM force measurement, the relative motion between the drop and the substrate (in axisymmetric geometry) could generate hydrodynamic interaction, arising from the flow of the continuous phase (i.e., toluene) confined between the water drop and the polyelectrolyte substrate. Since the separation distance (typically several micrometers or less) is small compared to the size of the drop and the typical moving velocity was also slow (e.g., 1 $\mu\text{m/s}$), and the Reynold number is low, the flow of the confined fluid is mainly in the radial direction and hydrodynamic pressure only varies in the radial direction as well. Previous studies have shown that such hydrodynamic drainage processes can be described by the Reynolds lubrication theory, where deformable drops are involved, as shown in Equation (1) [50,52–54].

$$\frac{\partial h}{\partial t} = \frac{1}{12\mu r} \frac{\partial}{\partial r} \left(r h^3 \frac{\partial p}{\partial r} \right) \quad (1)$$

where, h is the thickness of the confined oil film, t is the time, μ is the

viscosity of toluene, r is the radial coordinate, and p is the excess hydrodynamic pressure. Moreover, the water drop would deform upon the external pressure including the hydrodynamic pressure and disjoining pressure, which could be described using the augmented Young-Laplace pressure, as shown in Equation (2) [52].

$$\frac{\sigma}{r} \frac{\partial}{\partial r} \left(r \frac{\partial h}{\partial r} \right) = \frac{2\sigma}{R} - \Pi - p \quad (2)$$

where, σ is the interfacial tension of the water-toluene interface, R is the radius of the water drop and Π is the disjoining pressure. In literatures, the variation of the interfacial tension of water/oil or water/air interface due to the presence of the inorganic salts is quite small ($< \pm 1.5 \text{ mN/m}$), even though the salt concentration exceeds 1 M [55–59]. In this work, the interaction forces between water drop and polyelectrolyte surface are measured in the organic hydrophobic oil (i.e., toluene), where the electric double layer (EDL) cannot be created. Thus, according to the

classic Derjaguin-Landau-Verwey-Overbeek (DLVO) theory, only van der Waals (VDW) force, which was majorly contributed by the dipole-dipole interaction between water drop and polyelectrolyte surface in this work, contributed to the obtained force profiles. The VDW force Π_{vdw} can be calculated in following Equation (3) [30].

$$\Pi_{vdw} = -\frac{A_H}{6\pi h^3} \quad (3)$$

where, A_H is the Hamaker constant between water and polyelectrolyte surface across toluene. The total interaction force F was calculated by integrating the hydrodynamic pressure and disjoining pressure over the contact area, as shown in Equation (4).

$$F = 2\pi \int_0^\infty (p + \Pi) \cdot r dr \quad (4)$$

Preparation of the polyelectrolyte-coated membrane and the water flux tests. The polyelectrolyte-coated (i.e., poly [2-(methacryloyloxy) ethyltrimethylammonium chloride] (PMTAC)) membrane was prepared based on commercial hydrophilic polyvinylidene fluoride (PVDF) membrane (diameter ~ 47 mm, mean pore size ~ 0.22 μm) by following a reported method [60,61]. Firstly, the PVDF membranes were treated by the UV ozone for 30 min to active the surface. Then, the membranes were immersed in 10 mL DCM solution with 0.37 mol BiBB and 0.42 mol TEA for 30 min to obtain the initiators. Finally, the polyelectrolyte PMTAC brushes were coated on the membrane surfaces via the aforementioned SI-ATRP polymerization method. The polyelectrolyte-coated membranes were cleaned by ethanol and DI water, dried in pure nitrogen, and immersed in 3 M NaCl solution for at least 48 h before used in experiments. These polyelectrolyte-coated membranes were characterized using field-emission scanning electron microscope (SEM) (Zeiss Sigma 300 VP-FESEM, Germany) coupled with energy-dispersive X-ray spectroscopy (EDS) at an electron acceleration voltage of 10.2 keV and Fourier transform infrared (FTIR) spectroscopy (Thermo Scientific Nicolet, iS50 FTIR) to ensure the successful functionalization on PVDF membranes.

The antifouling property of the PMTAC-coated membranes was evaluated by water flux tests. Briefly, the prepared membrane was firstly fouled by dropping 50 μL toluene on the surface, followed by immersion in pure water or saline solutions (i.e., 100 mM KAc, KCl or KSCN) for 20 min to clean the toluene. Subsequently, the pure water permeability of the PMTAC membrane was measured using a dead-end filtration setup under a constant pressure (70 kPa). The effective filtration area was a round shape with the diameter of ~ 36 mm. The water flux J was determined as follows,

$$J = \frac{V}{t \cdot S \cdot \Delta P} \quad (5)$$

where V is the volume of the filtrated water, t is the filtration time, S is the effective filtration area, and ΔP is the pressure difference during filtration. For the filtration test of the water-toluene mixture (i.e., emulsions), the water-toluene emulsions (70 mL water or aqueous solution and 30 mL toluene) were firstly prepared using a homogenizer at the speed of 8000 rpm for 5 min, and then separated using the same filtration setup. The water flux was measured using the same method, and the oil removal efficiency η was calculated using the following equation.

$$\eta = 1 - \frac{m_f}{m_o} \quad (6)$$

where, m_f and m_o are the mass of the toluene in the solutions after and before the filtration process, respectively. The mass of toluene in the solution after the filtration process was determined using the total organic carbon (TOC) technique.

3. Results and discussion

Characterizations of the polyelectrolytes surfaces. The polyelectrolyte surfaces are prepared using the surface-initiated atom transfer radical polymerization (SI-ATRP) on silicon substrates (Scheme 1). In Fig. S1, the silicon surface is quite flat and smooth with a very small root-mean-squared (RMS) surface roughness of 0.11 nm, whereas the initiator surface has some small particles with the size of tens of nanometers, which could be due to the aggregation of APTES. The RMS surface roughness of the initiator surface is slightly increased to 0.17 nm. Fig. 1a-1c show the AFM surface images of the prepared cationic poly [2-(methacryloyloxy) ethyltrimethylammonium chloride] (PMTAC) surface, anionic poly [3-sulfopropyl methacrylate potassium] (PSPMA) surface, and zwitterionic poly [2-(methacryloyloxy) ethyl phosphorylcholine] (PMPC) surface, respectively. It is noted that the polyelectrolyte surfaces become much rougher than silicon surface and initiator surface with plenty of fiber-like strands on the surfaces, indicating the successful polymerization processes on silicon surfaces. The RMS surface roughness of PMTAC, PSPMA, and PMPC surfaces is 0.37 nm, 0.48 nm, and 0.89 nm, respectively. Fig. 1d-1f shows the water contact angles (WCAs) on PMTAC, PSPMA, and PMPC surfaces in air, respectively. It is noted that the WCAs in air are very small because of the polyelectrolytes' well-known hydrophilicity and wettability for water. Fig. 1g-1i shows the oil (i.e., toluene) contact angles (OCAs) on PMTAC, PSPMA, and PMPC surfaces in air, respectively, which are also quite small. When the hydrophobic oil contacts the polyelectrolyte surface in air, the polyelectrolyte molecules would alter their orientation, burying their charged groups inside and exposing the hydrophobic carbon backbone to the oil [8,28,29,62,63]. Therefore, the hydrophilic polyelectrolyte surface could turn to be hydrophobic and wetted by oil in air.

Bulk wetting performances of polyelectrolyte surfaces. The spontaneous oil cleaning performances of the polyelectrolyte (e.g., PMTAC) surface have been conducted. The silicon oil (~ 15 μL) was firstly dropped on the PMTAC substrates. When a silicon oil-wetted PMTAC surface is gently immersed in water (Fig. 1a & Video S1), the silicon oil drop, which firstly spreads on PMTAC surface in air, turns back into a spherical drop and finally detaches from the surface in 1.9 s after immersing in water. When immersed in 100 mM KAc solution, the oil drop immediately detaches (Fig. 1b & Video S2). In KCl solution, the oil drop also detaches after 2.8 s (Fig. 1c & Video S3). Surprisingly, in KSCN solution, the oil drop stably stays on PMTAC surface without detachment even for more than 5 min (Fig. 1d & Video S4). Therefore, the addition of KAc can promote the detachment behavior of oil drop on PMTAC surface in water, while the KSCN can effectively inhibit such behavior, and the KCl shows the influence between these two cases. During the oil detachment process, the oil-PMTAC interface is spontaneously replaced by the water-PMTAC interface due to the strong attraction between water and polyelectrolytes [29], which obviously could be modulated by the dissolved ion species.

Supplementary video related to this article can be found at <https://doi.org/10.1016/j.memsci.2021.119408>.

Surface interactions between water drops and PMTAC surfaces in oil. The surface interaction forces between water droplets and PMTAC surfaces in oil (i.e., toluene) are quantitatively investigated using the drop probe AFM technique (Fig. 3), and the measured force profiles are shown in Fig. 4.

In Fig. 4a, the black force curve shows a sudden "jump-in" behavior (indicated by the red arrow) when pure water droplet (0 mM) approaches the PMTAC surface in toluene. It was observed from the microscope that the water droplet jumped off from the AFM cantilever and quickly spread on PMTAC surface (Fig. S2a & S2b). In organic solvent (i.e., toluene), the only effective surface interaction is the van der Waals (VDW) interaction, which consists of the dispersion interaction and dipole-dependent induction and orientation interactions [30]. In this case, the dipole-dependent interactions between polar water molecules

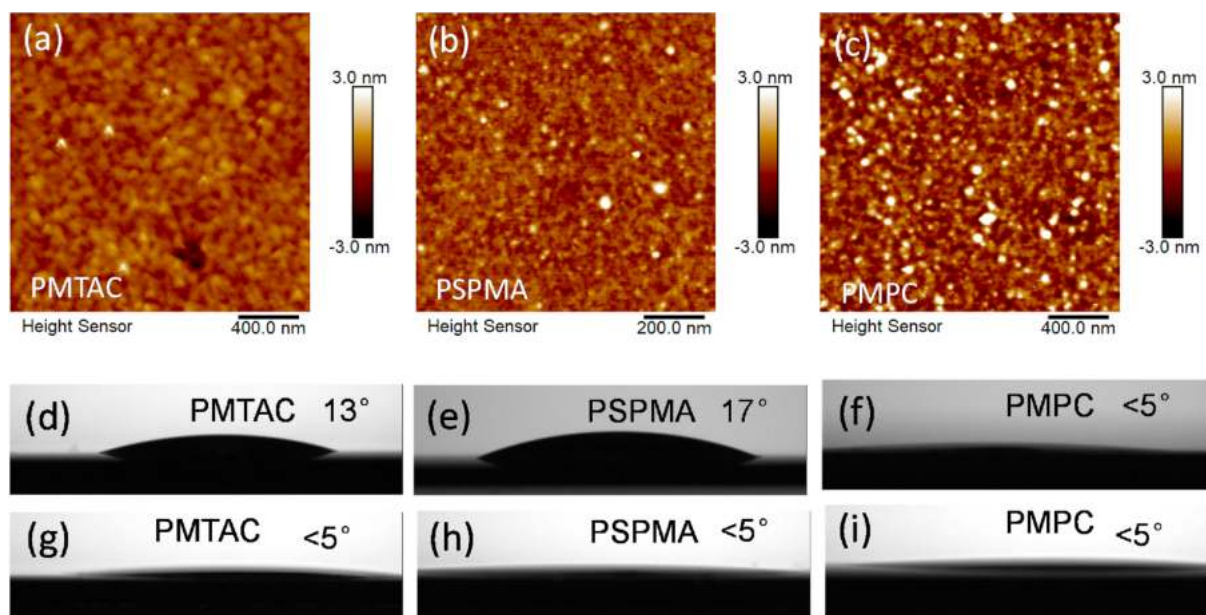


Fig. 1. The (a–c) AFM surface images, (d–f) water contact angles and (g–i) oil (i.e., toluene) contact angles of cationic PMTAC surface, anionic PSPMA surface, and zwitterionic PMPC surface.

and large dipoles of polyelectrolytes (positive and negative charges) are the main contribution and much stronger than the normal VDW interaction between two small molecules (e.g., water molecules) [29,64–66]. Hence, the Hamaker constant theoretically estimated from the “jump-in” behavior of the force curve is 4.5×10^{-19} J, close to the reported value [29]. Likewise, the “jump-in” behavior has also been observed with 10 mM KAc in water. However, as KAc concentration increases to 100 and 1000 mM, the strong attraction with the range of ~ 300 nm is detected before attachment. The calculated Hamaker constant increases from 5.5×10^{-19} J for 10 mM, to 13×10^{-19} J for 100 mM, and 15×10^{-19} J for 1000 mM, respectively. Meanwhile, the calculated confined oil film thickness before attachment behavior (Fig. 4d) also increases from 31 nm for pure water case, to 39 nm for 10 mM, 67 nm for 100 mM, and 71 nm for 1000 mM KAc, respectively. Therefore, the addition of KAc in water can significantly enhance the attraction between water and PMTAC surface in toluene, promoting the water attachment behavior. For the KCl cases in Fig. 4b, even though the concentration in water increases from 0 to 1000 mM, the measured force curves remain almost unchanged as well as the calculated Hamaker constant and confined oil film thickness (Fig. 4e), suggesting the negligible influence of KCl. In Fig. 4c, the force curve with 10 mM KSCN in water is close to that of pure water. However, when KSCN concentration exceeds 100 mM, a small repulsive force of ~ 0.5 nN has been measured before attachment behavior, suggesting that the addition of KSCN in water can remarkably weaken the attraction between water and PMTAC surface in toluene and inhibit the water attachment behavior. This repulsion originates from the hydrodynamic repulsion due to the movement of water droplets. The Hamaker constant decreases from 4.5×10^{-19} J for 10 mM, to 0.8×10^{-19} J for 100 mM, and 0.7×10^{-19} J for 1000 mM KSCN cases, respectively. The calculated confined oil film thickness before “jump-in” behavior (Fig. 4f) also reduces to 32 nm for 10 mM, 20 nm for 100 mM, and 12 nm for 1000 mM KSCN cases, respectively. It should be noted that all the force curves measured between the water drop and the substrate surface in this work are mainly contributed by the attractive VDW interaction and the repulsive hydrodynamic interaction. Since the sizes of the water drops (radius ~ 70 μ m) were close and the force measurements were conducted in the same liquid medium (i.e., toluene), the repulsive hydrodynamic force would be similar. For the KAc case (Fig. 4a), the force curves became more and more attractive before the jump-in behavior with increasing the KAc concentration, thus

suggesting the dipole-dipole attraction was strengthened. The hydrodynamic repulsion was overwhelmed by the strong dipole-dipole attraction. For the KSCN case (Fig. 4c), the force curves changed from attractive to repulsive before the jump-in behavior when the KSCN concentration increased, indicating the dipole-dipole interaction was weakened. Hence, the hydrodynamic repulsion became dominant. The force measurement Results demonstrate the enhancing influence of KAc, almost negligible influence of KCl, and weakening influence of KSCN at high concentration (e.g., 100 mM) in the dipole-dependent interactions between water and PMTAC surface in toluene, which agree with the observations in Fig. 2.

Surface interactions between water drops and PSPMA or PMPC surfaces in oil. The surface interactions between water droplets and anionic PSPMA surface or zwitterionic PMPC surface in toluene have also been investigated and the measured force profiles are shown in Fig. 5a & 5b, respectively. Similarly, compared with the force curves of pure water drop, the presence of 100 mM KAc in water can significantly enhance the attractive interaction between water and polyelectrolyte surface in oil. While the presence of 100 mM KSCN in water can remarkably weaken the attraction, and the addition of KCl shows minimum influence on the interaction between water and polyelectrolyte surface. This result demonstrates the universal ion-specific effect on polyelectrolyte surfaces of various charge properties.

Effect of surfactants on the surface interactions. The surface interactions between water droplets with 100 mM KAc, KCl, or KSCN and PMTAC surface in toluene have been measured when 0.35 mM surfactants such as sodium dodecyl sulfate (SDS) are present in water. The result is shown in Fig. 6. Interestingly, all the force curves, even though different ions have been dissolved in water, still exhibit to be similar with that of pure water, showing that the ion-specific effect has been eliminated. This result suggests that the rearrangement of ions and water molecules due to the interfacially adsorbed SDS molecules and their negatively charged sulfonic groups could significantly suppress the ion-specific effect [67–69]. Therefore, the ions at/near the water-oil interface are critical to the surface interactions between water and polyelectrolyte surfaces.

Surface interactions in the presence of different anions and cations. The surface interactions between water droplets with 100 mM salts of different anions or cations and PMTAC surface in toluene have been investigated and shown in Fig. 7.

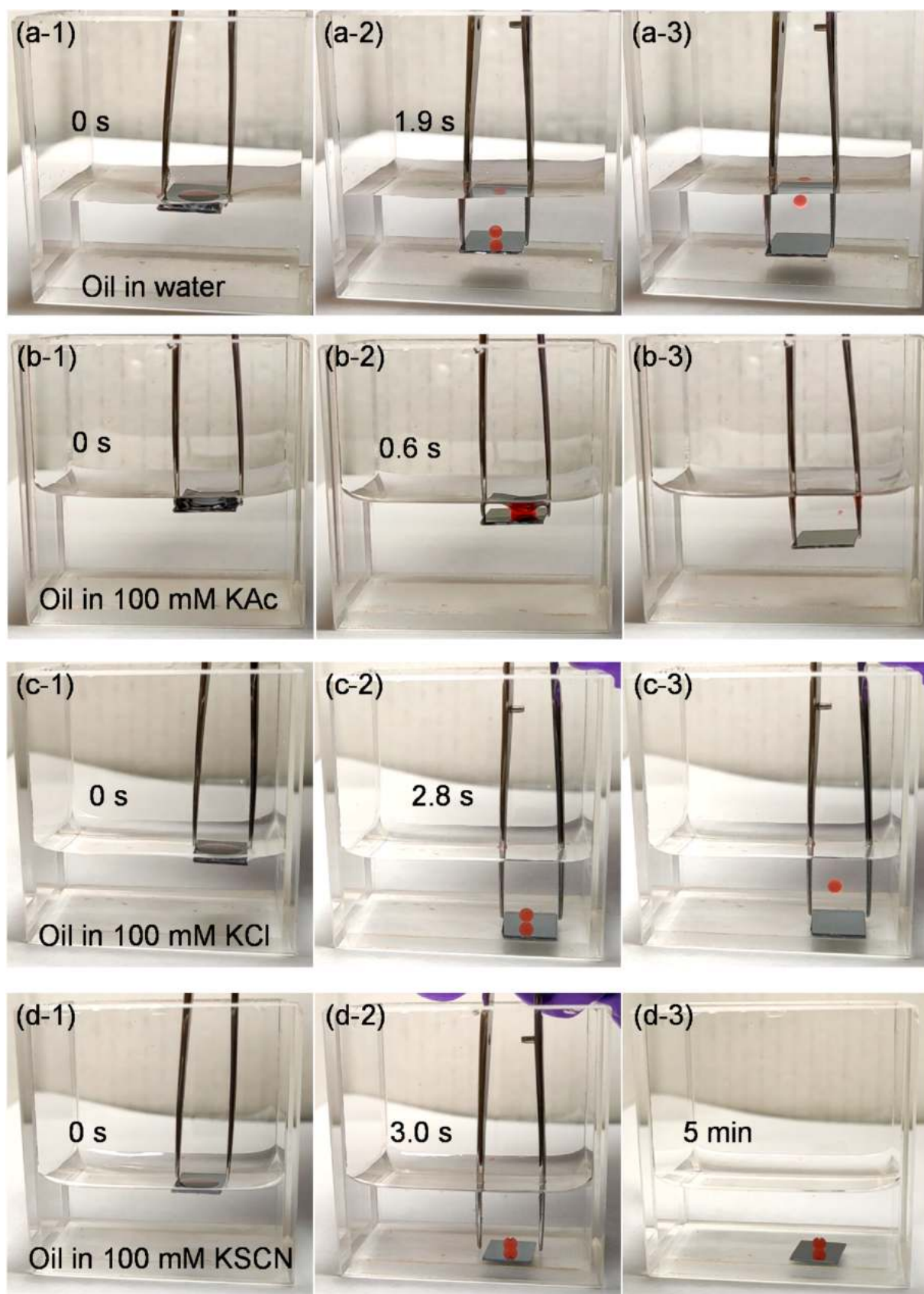


Fig. 2. The PMTAC surfaces, pre-wetted by silicon oil (colored by Red Oil), are immersed in (a) water, (b) 100 mM KAc, (c) KCl, and (d) KSCN solutions. The volume of the silicon oil drop is $\sim 15 \mu\text{L}$. (For interpretation of the references to color in this figure legend, the reader is referred to the Web version of this article.)

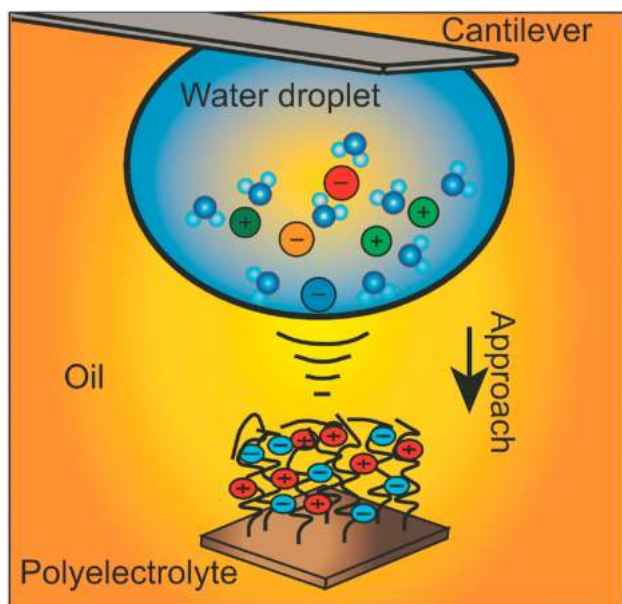


Fig. 3. Illustration of force measurements using the drop probe AFM technique between water droplets and polyelectrolyte surfaces in oil.

Fig. 7a and b shows the force curves between water droplets with 100 mM salts of different monovalent or divalent anions and PMTAC surface in toluene, respectively, including K_2HPO_4 , K_2SO_4 , K_2CO_3 , KAc,

KH_2PO_4 , KF, KCl, KBr, KI, and KSCN. Following this sequence, the force curves gradually turn from the strong long-ranged attraction before water attachment (e.g., HPO_4^{2-} , SO_4^{2-} , CO_3^{2-} , Ac^- or H_2PO_4^-), to the sudden “jump-in” behavior with no obvious attraction (e.g., F^- and Cl^-), and to the repulsion before attachment (e.g., Br^- , I^- and SCN^-), attesting to the significant ion-specific effect. This order as $\text{HPO}_4^{2-} \approx \text{SO}_4^{2-} \approx \text{CO}_3^{2-} > \text{Ac}^- > \text{H}_2\text{PO}_4^- > \text{F}^- > \text{Cl}^- > \text{Br}^- > \text{I}^- > \text{SCN}^-$ also coincides with the famous Hofmeister series [70–72]. Fig. 7c shows the measured force Results between water drop with different cations and PMTAC surface in toluene, including BaCl_2 , CaCl_2 , MgCl_2 , NH_4Cl , CsCl, KCl, NaCl, and LiCl. All the force curves are similar with that of pure water drop in Fig. 4, indicating that the influence of different cations in the surface interactions between water and polyelectrolyte is minimum.

Mechanisms of the ion-specific effect on the surface interactions between water and polyelectrolyte surfaces. In Fig. 7a, the force curves of KF and KCl are similar with the sudden attachment behavior, and in Fig. 7b, the force curves of K_2SO_4 , K_2CO_3 and KAc are also similar with the strong attraction before the attachment behavior. The F^- , CO_3^{2-} and Ac^- are the weak acid ions, while Cl^- and SO_4^{2-} are the extremely strong acid ions. Therefore, the hydrogen or hydroxide ions produced by the protonation of weak acid ions have negligible influence on the surface interactions between water drop and polyelectrolyte surface. Previous molecular dynamics simulation and experimental results have shown that the hydrated anions and cations could be repelled from the water/air or water/oil interface by image charge effect to possess different surface propensities with respect to their bulk concentration [55,65,73,74]. Following Hofmeister series, the anions gradually become less hydrated [75,76]. Generally, the strongly hydrated anions (e.g., HPO_4^{2-} , SO_4^{2-} , CO_3^{2-} , or H_2PO_4^-) due to large charge density and/or

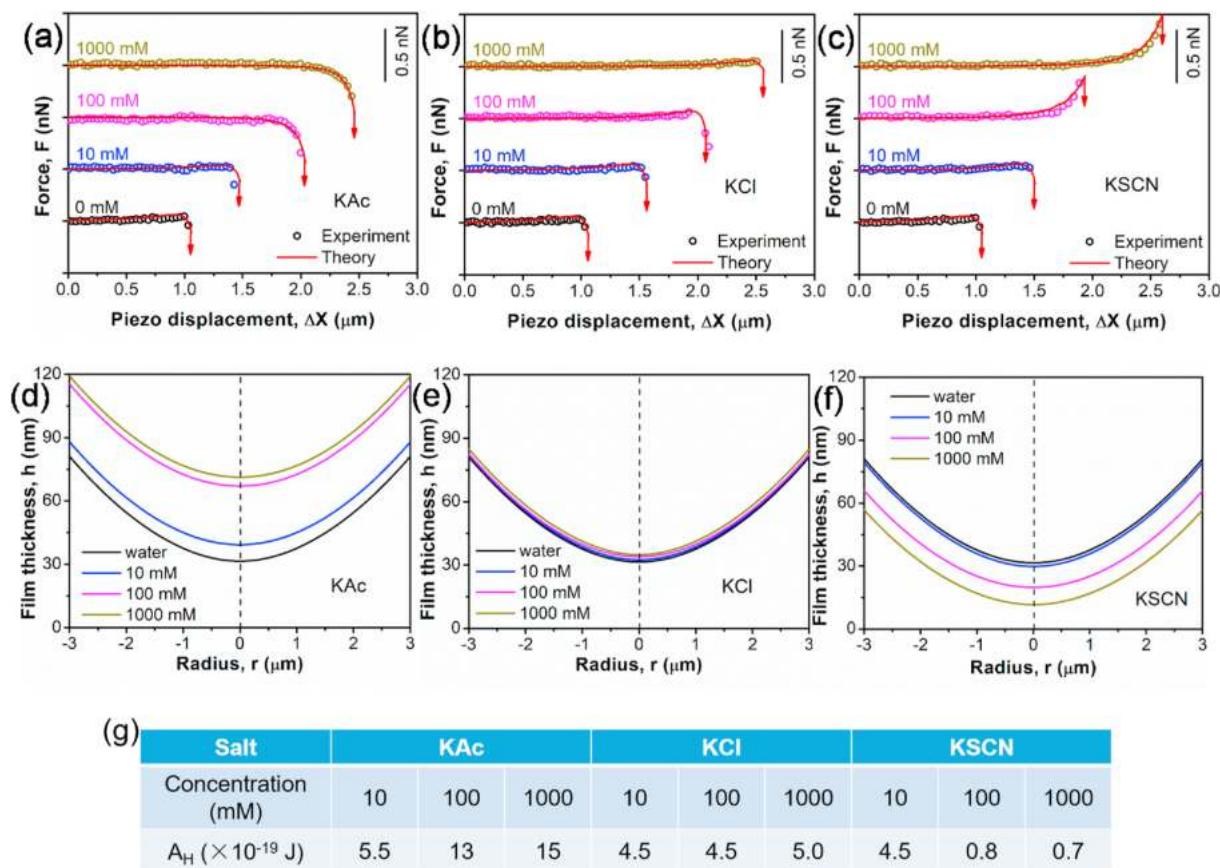


Fig. 4. The measured force curves between water droplets with (a) KAc, (b) KCl and (c) KSCN at the concentration of 0, 10, 100, and 1000 mM and PMTAC surface in toluene. Hollow circle symbols are experimental data, and red solid lines are theoretical calculation Results. (d–f) The corresponding confined oil film thickness between water droplet and PMTAC surface in toluene. (g) The Hamaker constants from theoretical analysis. (For interpretation of the references to color in this figure legend, the reader is referred to the Web version of this article.)

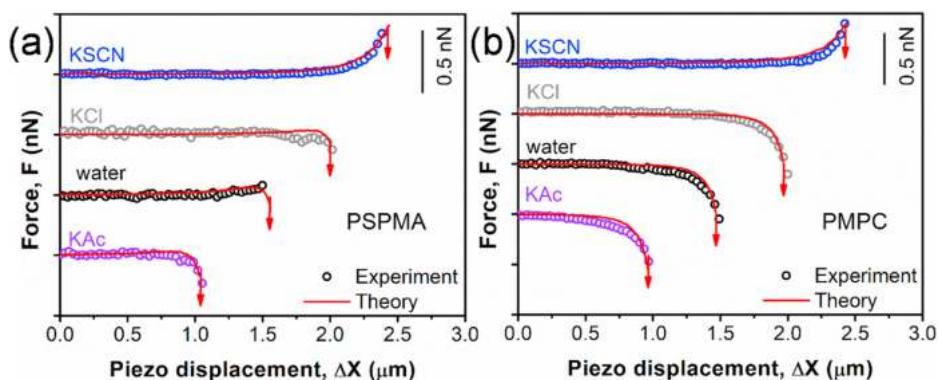


Fig. 5. Measured interaction force profiles between water droplets (with 100 mM KAc, KCl, or KSCN) and (a) anionic PSPMA surface or (b) zwitterionic PMPC surface in toluene. Hollow circle symbols are experimental data, and red solid lines are theoretical calculation Results. (For interpretation of the references to color in this figure legend, the reader is referred to the Web version of this article.)

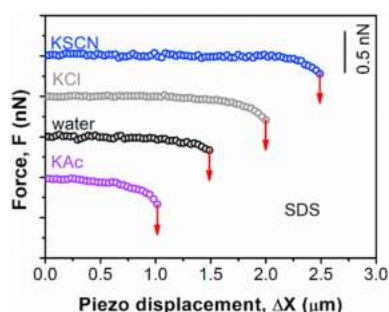


Fig. 6. Measured force curves between water (with KAc, KCl, or KSCN) and PMTAC surface when 0.35 mM SDS is added in water.

dispersion interaction, known as kosmotropes, are found to be repelled further away from the interface than the cations (e.g., K^+), leaving the cations relatively closer to the interface [55,66,74,77]. As a result, the orientation of the interfacial water molecules, which preferentially point their hydrogen atoms to oil at pristine water/oil interface [65,73,74], could be enhanced by the electric field of cations, which in turn strengthens the dipole-dependent attraction between water and polyelectrolyte surface across oil. Nevertheless, Ac^- ions are exceptional and have great surface enrichment because of the hydrophobic methyl group [78,79]. The interactions (e.g., electrostatic interaction and hydrogen bond) between water and highly oriented Ac^- anions can also align interfacial water molecules and lead to the strong attraction. Besides, the small nonpolarizable anions (e.g., F^- and Cl^-) have been discovered to have the similar surface propensities with K^+ cations [73,74]. Hence, the

influence of the electric field generated by cations could be minimized by that of anions. However, the large polarizable anions (e.g., Br^- , I^- and SCN^-), also known as chaotropes, are weakly-hydrated and able to get close or even adsorbed to the interface [64,80–82]. They can disrupt the hydrogen bonding network, lower the number density of water molecules, and disorder the interfacial water orientation [75,76,83], thus weakening the dipole-dependent interactions. Moreover, the common cations are strongly hydrated and their surface propensities could be in a narrow variation range, which are comparable with that of Cl^- anions [59,73]. Therefore, the influence of different cations is neglected.

Attachment test of water drops on polyelectrolyte surfaces in nonpolar oil. The ion-specific effect can also be observed when water droplets fall on PMTAC surface in nonpolar organic solvent (i.e., cyclohexane). The pure water droplet will spontaneously spread on the surface in ~ 0.13 s after contacting (Fig. 8a & Video S5). However, the immediate attachment of KAc droplet at the moment of contacting (Fig. 8b & Video S6) shows the enhancing influence of Ac^- . The KCl droplet (Fig. 8c & Video S7) stays on the surface for ~ 0.20 s, which is close with pure water droplet case. The KSCN droplet stays on PMTAC surface for ~ 0.73 s before attachment (Fig. 8d & Video S8), exhibiting the weakening role of SCN^- . This observation agrees with the above observations and force measurement results in polar oil (i.e., toluene).

Supplementary video related to this article can be found at .

Characterization of polyelectrolyte-coated membranes and antifouling tests. The polyelectrolyte PMTAC-coated membranes were prepared based on the commercial PVDF membranes via the aforementioned SI-ATRP polymerization. Fig. 9a shows the images of water droplets on the pristine PVDF membrane, initiator-coated membrane and PMTAC-coated membrane. Obviously, the water drop can be partially spread on and readily attached to the pristine membrane, but

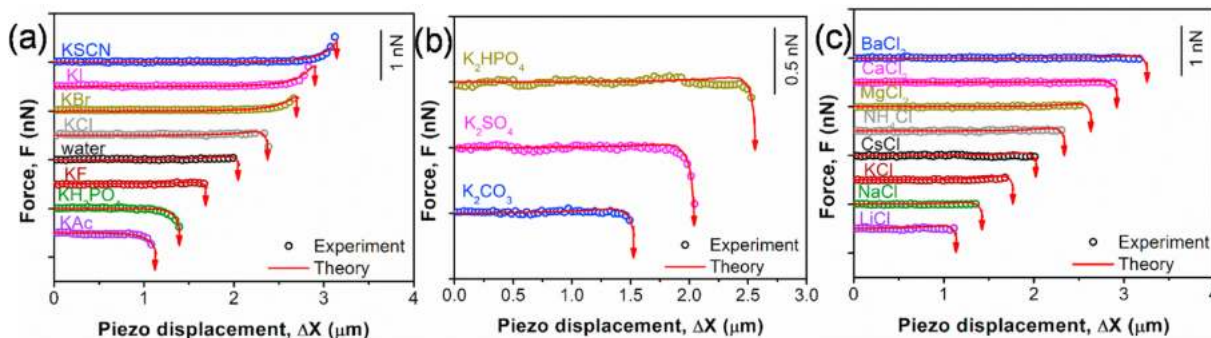


Fig. 7. Measured force curves between water with different (a) monovalent anions, (b) divalent anions, or (c) cations and PMTAC surfaces in toluene. The salt concentration is 100 mM. Hollow circle symbols are experimental data, and red solid lines are theoretical calculation Results. (For interpretation of the references to color in this figure legend, the reader is referred to the Web version of this article.)

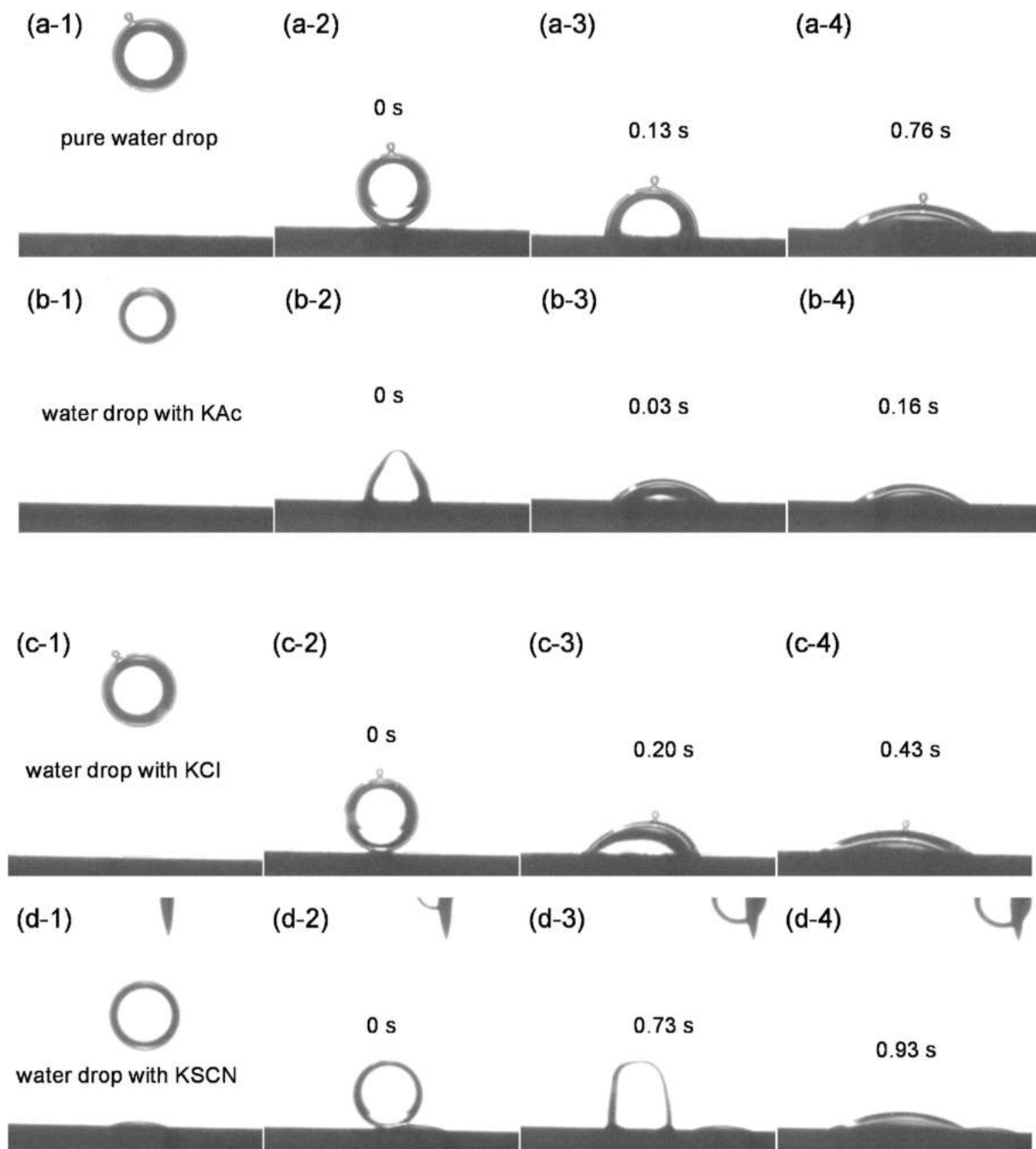


Fig. 8. Images of (a) pure water droplet or water droplet with 100 mM (b) KAc, (c) KCl and (d) KSCN falling on PMTAC surface in cyclohexane.

stably stand on the initiator-coated membrane surface due to the surface hydrophobicity and morphology of the functionalized membrane. After the surface polymerization, the water drop can instantly wet the PMTAC membrane, indicating the successful deposition of polyelectrolytes on the membrane surface and their excellent hydrophilicity. Fig. 9b–c show the SEM images of the pristine membrane and PMTAC-coated membrane, which exhibit similar porous structures for both membranes. The coated polyelectrolytes on the membrane surface did not damage the porous structure. Fig. 9d–e show the EDS element mapping images and the surface weight percentages of C, F and N elements for the pristine membrane and PMTAC-coated membrane. The C and F elements were originated from the PVDF membrane materials. The N element could majorly come from the quaternary ammonium group of the MTAC. The weight percentages of C, F and N are 52.7%, 44.3%, and 1.1% for pristine membrane, and 62.5%, 33.3%, and 3.2% for PMTAC-coated

membrane, respectively. It is noted that the increment of C element on PMTAC-coated membrane was mainly caused by the carbon backbone of MTAC, while the increment of N element came from the quaternary ammonium groups of MTAC. The decrease of F element could be due to the absence of fluorine in MTAC and the replacement of fluorine atoms from the PVDF chains when grafting the polymerization initiators. Fig. 9f shows the FTIR spectrum of PMTAC-coated membrane. The strong peaks detected at 1731.59 cm^{-1} and 1180.04 cm^{-1} were due to the ester groups of the MTAC segments [84,85]. All these Results demonstrated the successful deposition of PMTAC coating on the membrane surface.

Fig. 9g shows the water permeation flux of the prepared PMTAC membrane in the antifouling tests. The water flux of the as-prepared PMTAC-coated membrane reached $3367.95\text{ L}/(\text{m}^2\cdot\text{h}\cdot\text{bar})$, which was due to the excellent hydrophilicity of the coated polyelectrolyte PMTAC.

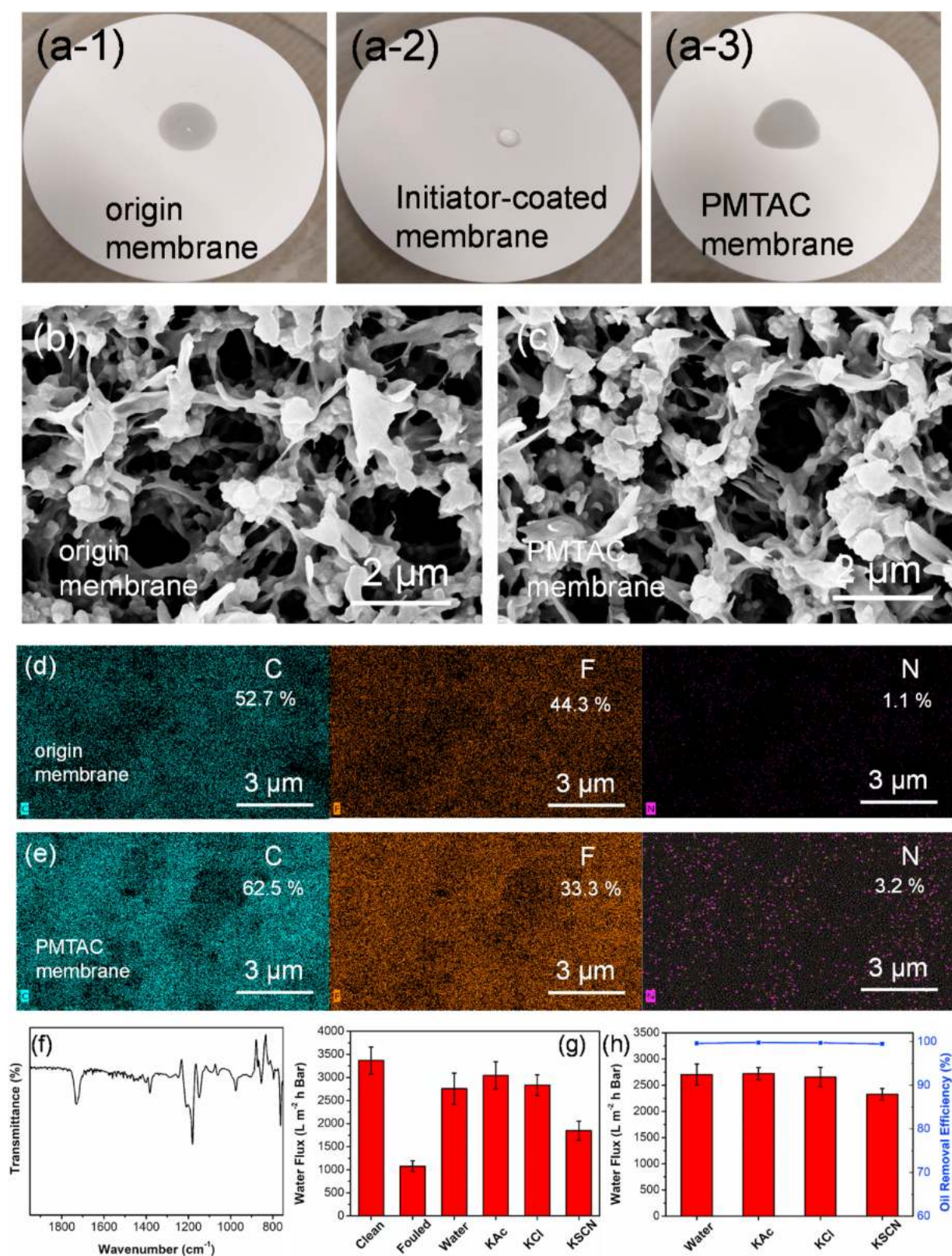


Fig. 9. (a) Image of water drops on pristine PVDF membrane, initiator-coated membrane, and PMTAC-coated membrane. (b–c) The SEM images of the pristine membrane and PMTAC-coated membrane. (d–e) The EDS elemental mapping images and the surface weight percentages of C, F and N elements for (d) pristine membrane and (e) PMTAC-coated membrane, respectively. (f) The FTIR spectrum of PMTAC membrane. (g) Water flux of the as-prepared clean PMTAC membrane, toluene-fouled membrane, the membrane after immersion in pure water, 100 mM KAc, KCl and KSCN solutions. (h) Water flux and oil removal efficiency of the PMTAC membrane in separating the water-toluene mixture with pure water, 100 mM KAc, KCl and KSCN solutions.

However, when fouled by toluene, the water flux of the membrane was significantly reduced to 1077.17 L/(m²•h•bar), caused by the attachment of toluene on the membrane surface. After immersed in pure water, 100 mM KAc, KCl or KSCN solution for 20 min, the water flux of the membrane was recovered to 81.8%, 90.3%, 84.1%, and 54.9% of the water flux of the clean membrane, respectively, exhibiting the antifouling property of the polyelectrolyte PMTAC surfaces. It is also noted that the best antifouling and self-cleaning performance of the treated PMTAC-coated membrane was observed for the case of KAc solution, which was due to the enhanced attraction between water and polyelectrolyte surfaces in toluene. The KCl solution showed similar influence on the membrane performance with the pure water. However, the PMTAC-coated membrane showed weakened antifouling and self-cleaning performances after cleaned in KSCN solution, which was caused by the repulsion detected in AFM force measurements between water (KSCN solution) and PMTAC surface in toluene before surface attachment. The similar trend of the ion-specific effect was also observed in the filtration results of the water-toluene mixtures/emulsions (volume ratio 7:3) prepared using pure water, 100 mM KAc, KCl or KSCN (Fig. 9h). The KAc and KCl cases showed the similar water flux as the pure water case, while there was an obvious reduction of the water flux for KSCN case, which was due to the weakened self-cleaning property of PMTAC in KSCN solution. For comparison, divalent ions (e.g., 100 mM CaCl₂, MgCl₂ or K₂SO₄) were also used to prepare the water-toluene emulsions, and the water flux results were close to the pure water case (Fig. S4), which was due to the negligible influence of Ca²⁺ and Mg²⁺ cations and the enhancing influence of SO₄²⁻ anions in the surface interaction between water and PMTAC surface (Fig. 7). Therefore, the antifouling and self-cleaning property of the polyelectrolyte-coated membrane can be affected by the ion species in the aqueous media. Such results well agree with the AFM force measurements.

4. Conclusions

In this work, the effect of the aqueous ion species on the surface wetting behavior and self-cleaning performances of polyelectrolyte surfaces has been investigated, and the underlying interaction mechanisms between water and various polyelectrolyte surfaces across oil medium under ion-specific effect have been quantitatively characterized via direct surface force measurements. It was discovered that dissolved ion species in water could significantly affect the spontaneous oil cleaning performances of the polyelectrolyte surfaces as well as the surface interfaces between water and polyelectrolytes across oil film. The force measurement results revealed that the HPO₄²⁻, SO₄²⁻, CO₃²⁻, Ac⁻, and H₂PO₄⁻ anions can enhance the dipole-dipole attraction between water droplets and polyelectrolyte surface in toluene by enhancing or aligning the interfacial water orientation, hence promoting the water attachment on the polyelectrolyte surfaces. The F⁻ and Cl⁻ anions may have the similar surface propensity with cations (i.e., K⁺) and thus show minimum influence on the interfacial water orientation. In contrast, the Br⁻, I⁻, and SCN⁻ anions can get close or even adsorbed onto interface, break the interfacial hydrogen network, and disorder interfacial water molecules, which thereby weaken the dipole-dipole attraction. The specific-ion effect of the different anions follows the order as HPO₄²⁻ ≈ SO₄²⁻ ≈ CO₃²⁻ > Ac⁻ > H₂PO₄⁻ > F⁻ > Cl⁻ > Br⁻ > I⁻ > SCN⁻, which coincides with the well-known Hofmeister series. Meanwhile, the cations show negligible influence. Similar ion-specific effect has been observed in nonpolar oil medium (i.e., cyclohexane). On the basis of the water flux test results, the antifouling and self-cleaning properties of the as-prepared polyelectrolyte-coated membranes was also found to be excellent in KAc and KCl solutions and pure water, but poor in KSCN solution, which was in consistent with the force measurements. This work has revealed the nanomechanical mechanism of ion-specific effect on the water wetting behaviors and surface functionalities (e.g., antifouling and self-cleaning) of polyelectrolyte surfaces, with useful implications on the efficient applications of

polyelectrolyte-based materials in diverse engineering processes (e.g., membrane filtration, oil/water separation).

Author contributions

Lu Gong: Conceptualization, Methodology, Investigation, Data Analysis, Writing -Original Draft, Writing - Review & Editing.

Jiawen Zhang: Methodology, Data Analysis, Writing - Review & Editing.

Wenda Wang: Methodology, Writing - Review & Editing.

Li Xiang: Methodology, Writing - Review & Editing.

Mingfei Pan: Methodology, Writing - Review & Editing.

Wenshuai Yang: Methodology, Writing - Review & Editing.

Linbo Han: Writing - Review & Editing.

Jianmei Wang: Writing - Review & Editing.

Bin Yan: Conceptualization, Methodology, Resources, Supervision, Writing - Review & Editing.

Hongbo Zeng: Conceptualization, Methodology, Resources, Supervision, Project Administration, Funding Acquisition, Writing - Review & Editing.

Declaration of competing interest

The authors declare that they have no known competing financial interests or personal relationships that could have appeared to influence the work reported in this paper.

Acknowledgements

This work was supported by the Natural Sciences and Engineering Research Council of Canada (NSERC), the Canada Foundation for Innovation (CFI), and the Canada Research Chairs Program (H. Zeng).

Appendix A. Supplementary data

Supplementary data and videos to this article can be found online at <https://doi.org/10.1016/j.memsci.2021.119408>.

References

- [1] M. Kobayashi, Y. Terayama, M. Kikuchi, A. Takahara, Chain dimensions and surface characterization of superhydrophilic polymer brushes with zwitterion side groups, *Soft Matter* 9 (2013) 5138–5148.
- [2] S. Jiang, Z. Cao, Ultralow-fouling, functionalizable, and hydrolyzable zwitterionic materials and their derivatives for biological applications, *Adv. Mater.* 22 (2010) 920–932.
- [3] M. Balz, H.A. Therese, J. Li, J.S. Gutmann, M. Kappl, L. Nasdala, W. Hofmeister, H. J. Butt, W. Tremel, Crystallization of vaterite nanowires by the cooperative interaction of tailor-made nucleation surfaces and polyelectrolytes, *Adv. Funct. Mater.* 15 (2005) 683–688.
- [4] J. Yu, J. Mao, G. Yuan, S. Satija, Z. Jiang, W. Chen, M. Tirrell, Structure of polyelectrolyte brushes in the presence of multivalent counterions, *Macromolecules* 49 (2016) 5609–5617.
- [5] F. Stauffer, B. Peter, H. Alem, D. Funschilling, N. Dumas, C. Serra, T. Roques-Carmes, Polyelectrolytes layer-by-layer surface modification of PDMS microchips for the production of simple O/W and double W/O/W emulsions: from global to localized treatment, *Chemical Engineering and Processing-Process Intensification* (2019) 107685.
- [6] E. te Brinke, D.M. Reurink, I. Achterhuis, J. de Groot, W.M. de Vos, Asymmetric polyelectrolyte multilayer membranes with ultrathin separation layers for highly efficient micropollutant removal, *Applied Materials Today* (2019) 100471.
- [7] R.R. Costa, J.F. Mano, Polyelectrolyte multilayered assemblies in biomedical technologies, *Chem. Soc. Rev.* 43 (2014) 3453–3479.
- [8] K. He, H. Duan, G.Y. Chen, X. Liu, W. Yang, D. Wang, Cleaning of oil fouling with water enabled by zwitterionic polyelectrolyte coatings: overcoming the imperative challenge of oil-water separation membranes, *ACS Nano* 9 (2015) 9188–9198.
- [9] J.M. Silva, R.L. Reis, J.F. Mano, Biomimetic extracellular environment based on natural origin polyelectrolyte multilayers, *Small* 12 (2016) 4308–4342.
- [10] W. Zhang, Q. Zhao, J. Yuan, Porous polyelectrolytes: the interplay of charge and pores for new functionalities, *Angew. Chem. Int. Ed.* 57 (2018) 6754–6773.
- [11] G. Némethy, H.A. Scheraga, Structure of water and hydrophobic bonding in proteins. II. Model for the thermodynamic properties of aqueous solutions of hydrocarbons, *J. Chem. Phys.* 36 (1962) 3401–3417.

- [12] M.M. Teeter, Water-protein interactions: theory and experiment, *Annu. Rev. Biophys. Biophys. Chem.* 20 (1991) 577–600.
- [13] M. Chaplin, Do we underestimate the importance of water in cell biology? *Nat. Rev. Mol. Cell Biol.* 7 (2006) 861.
- [14] S. Zarroug, S.B. Mahmoud, A.H. Hamzaoui, W. Essafi, Study of the interaction between methylene blue dye and quenched polyelectrolyte with tunable hydrophobicity in aqueous media, *Journal of Environmental Chemical Engineering* 7 (2019) 103312.
- [15] M. Caldera-Villalobos, A.-A. Peláez-Cid, M.-A. Martins-Alho, A.-M. Herrera-González, Removal of textile dyes in wastewater using polyelectrolytes containing tetrazole groups, *Kor. J. Chem. Eng.* 35 (2018) 2394–2402.
- [16] A. Lourenço, J. Arnold, J.A. Gamelas, O.J. Cayre, M.G. Rasteiro, Anionic polyelectrolytes synthesized in an aromatic-free-oils process for application as flocculants in dairy-industry-effluent treatment, *Ind. Eng. Chem. Res.* 57 (2018) 16884–16896.
- [17] V.S. Meka, M.K. Sing, M.R. Pichika, S.R. Nali, V.R. Kolapalli, P. Kesharwani, A comprehensive review on polyelectrolyte complexes, *Drug Discov. Today* 22 (2017) 1697–1706.
- [18] N. Cai, H. Zeng, J. Fu, V. Chan, M. Chen, H. Li, F. Yu, Synergistic effect of graphene oxide-silver nanofillers on engineering performances of polyelectrolyte complex nanofiber membranes, *J. Appl. Polym. Sci.* 135 (2018) 46238.
- [19] I.C. Iakovides, A.G. Pantziaros, D.P. Zagklis, C.A. Paraskeva, Effect of electrolytes/polyelectrolytes on the removal of solids and organics from olive mill wastewater, *J. Appl. Chem. Biotechnol.* 91 (2016) 204–211.
- [20] X. Zhao, R. Zhang, Y. Liu, M. He, Y. Su, C. Gao, Z. Jiang, Antifouling membrane surface construction: chemistry plays a critical role, *J. Membr. Sci.* 551 (2018) 145–171.
- [21] T.V. Plisko, A.V. Bilyukevich, K.S. Burts, S.S. Ermakov, A.V. Penkova, A. I. Kuzminova, M.E. Dmitrenko, T.A. Hliavitskaya, M. Ulbricht, One-step preparation of antifouling polysulfone ultrafiltration membranes via modification by a cationic polyelectrolyte based on polyacrylamide, *Polymers* 12 (2020) 1017.
- [22] Y. Ma, J. Dai, L. Wu, G. Fang, Z. Guo, Enhanced anti-ultraviolet, anti-fouling and anti-bacterial polyelectrolyte membrane of polystyrene grafted with trimethyl quaternary ammonium salt modified lignin, *Polymer* 114 (2017) 113–121.
- [23] Y.-L. Ji, Q.-F. An, Y.-S. Guo, W.-S. Hung, K.-R. Lee, C.-J. Gao, Bio-inspired fabrication of high perm-selectivity and anti-fouling membranes based on zwitterionic polyelectrolyte nanoparticles, *J. Mater. Chem.* 4 (2016) 4224–4231.
- [24] M.R. Moradi, A. Pihlajamäki, M. Hesampour, J. Ahlgren, M. Mänttari, End-of-life RO membranes recycling: reuse as NF membranes by polyelectrolyte layer-by-layer deposition, *J. Membr. Sci.* 584 (2019) 300–308.
- [25] D. Menne, C. Üzümlü, A. Koppelman, J.E. Wong, C. van Foeken, F. Borre, L. Dähne, T. Laakso, A. Pihlajamäki, M. Wessling, Regenerable polymer/ceramic hybrid nanofiltration membrane based on polyelectrolyte assembly by layer-by-layer technique, *J. Membr. Sci.* 520 (2016) 924–932.
- [26] J. Irigoyen, N. Politakos, R. Murray, S.E. Moya, Design and fabrication of regenerable polyelectrolyte multilayers for applications in foulant removal, *Macromol. Chem. Phys.* 215 (2014) 1543–1550.
- [27] X. Liu, C. Leng, L. Yu, K. He, L.J. Brown, Z. Chen, J. Cho, D. Wang, Ion-specific oil repellency of polyelectrolyte multilayers in water: molecular insights into the hydrophilicity of charged surfaces, *Angew. Chem. Int. Ed.* 54 (2015) 4851–4856.
- [28] S. Gao, J. Sun, P. Liu, F. Zhang, W. Zhang, S. Yuan, J. Li, J. Jin, A robust polyionized hydrogel with an unprecedented underwater anti-crude-oil-adhesion property, *Adv. Mater.* 28 (2016) 5307–5314.
- [29] C. Shi, B. Yan, L. Xie, L. Zhang, J. Wang, A. Takahara, H. Zeng, Long-range hydrophilic attraction between water and polyelectrolyte surfaces in oil, *Angew. Chem. Int. Ed.* 55 (2016) 15017–15021.
- [30] J.N. Israelachvili, *Intermolecular and Surface Forces*, Academic press, 2011.
- [31] D.H. Everett, *Basic Principles of Colloid Science*, Royal society of chemistry, 2007.
- [32] M.A. Henderson, The interaction of water with solid surfaces: fundamental aspects revisited, *Surf. Sci. Rep.* 46 (2002) 1–308.
- [33] R.E. Holmlin, X. Chen, R.G. Chapman, S. Takayama, G.M. Whitesides, Zwitterionic SAMs that resist nonspecific adsorption of protein from aqueous buffer, *Langmuir* 17 (2001) 2841–2850.
- [34] M. Hadidi, A.L. Zydney, Fouling behavior of zwitterionic membranes: impact of electrostatic and hydrophobic interactions, *J. Membr. Sci.* 452 (2014) 97–103.
- [35] E. Ostuni, R.G. Chapman, M.N. Liang, G. Meluleni, G. Pier, D.E. Ingber, G. M. Whitesides, Self-assembled monolayers that resist the adsorption of proteins and the adhesion of bacterial and mammalian cells, *Langmuir* 17 (2001) 6336–6343.
- [36] T. Goda, M. Tabata, M. Sanjoh, M. Uchimura, Y. Iwasaki, Y. Miyahara, Thiolated 2-methacryloyloxyethyl phosphorylcholine for an antifouling biosensor platform, *Chem. Commun.* 49 (2013) 8683–8685.
- [37] X. Xu, D. Mastropietro, M. Ruths, M. Tirrell, J. Yu, Ion-specific effects of divalent ions on the structure of polyelectrolyte brushes, *Langmuir* 35 (2019) 15564–15572.
- [38] Z. Liu, Z. He, J. Lv, Y. Jin, S. Wu, G. Liu, F. Zhou, J. Wang, Ion-specific ice propagation behavior on polyelectrolyte brush surfaces, *RSC Adv.* 7 (2017) 840–844.
- [39] D. Kovačević, S. Van der Burgh, A. De Keizer, M. Cohen Stuart, Specific ionic effects on weak polyelectrolyte multilayer formation, *J. Phys. Chem. B* 107 (2003) 7998–8002.
- [40] B. Kim, I.H. Jung, M. Kang, H.-K. Shim, H.Y. Woo, Cationic conjugated polyelectrolytes-triggered conformational change of molecular beacon aptamer for highly sensitive and selective potassium ion detection, *J. Am. Chem. Soc.* 134 (2012) 3133–3138.
- [41] B.A. Humphreys, E.C. Johnson, E.J. Wanless, G.B. Webber, Poly (N-isopropylacrylamide) response to salt concentration and anion identity: a brush-on-brush study, *Langmuir* 35 (2019) 10818–10830.
- [42] E.C. Johnson, L.J. Gresham, S.W. Prescott, A. Nelson, E.J. Wanless, G.B. Webber, The direction of influence of specific ion effects on a pH and temperature responsive copolymer brush is dependent on polymer charge, *Polymer* 214 (2021) 123287.
- [43] H. Robertson, E.C. Johnson, L.J. Gresham, S.W. Prescott, A. Nelson, E.J. Wanless, G. B. Webber, Competitive specific ion effects in mixed salt solutions on a thermoresponsive polymer brush, *J. Colloid Interface Sci.* 586 (2021) 292–304.
- [44] P. Ghosh, *Colloid and Interface Science*, PHI Learning Pvt. Ltd., 2009.
- [45] L. Gong, X. Qiu, L. Zhang, J. Huang, W. Hu, L. Xiang, D. Zhu, R. Sabbagh, M. Mahmoudi, V. Fattahpour, Probing the interaction mechanism between oil-in-water emulsions and electroless nickel-phosphorus coating with implications for antifouling in oil production, *Energy Fuels* 33 (2018) 3764–3765.
- [46] C. Shi, L. Zhang, L. Xie, X. Lu, Q. Liu, J. He, C.A. Mantilla, F.G. Van den Berg, H. Zeng, Surface interaction of water-in-oil emulsion droplets with interfacially active asphaltenes, *Langmuir* 33 (2017) 1265–1274.
- [47] L. Gong, L. Zhang, L. Xiang, J. Zhang, V. Fattahpour, M. Mamoudi, M. Roostaei, B. Fermaniuk, J.-L. Luo, H. Zeng, Surface interactions between water-in-oil emulsions with asphaltenes and electroless nickel-phosphorus coating, *Langmuir* 36 (2020) 897–905.
- [48] J.L. Hutter, J. Bechhoefer, Calibration of atomic-force microscope tips, *Rev. Sci. Instrum.* 64 (1993) 1868–1873.
- [49] D.Y. Chan, E. Klaseboer, R. Manica, Dynamic deformations and forces in soft matter, *Soft Matter* 5 (2009) 2858–2861.
- [50] D.Y. Chan, E. Klaseboer, R. Manica, Film drainage and coalescence between deformable drops and bubbles, *Soft Matter* 7 (2011) 2235–2264.
- [51] C. Shi, D.Y. Chan, Q. Liu, H. Zeng, Probing the hydrophobic interaction between air bubbles and partially hydrophobic surfaces using atomic force microscopy, *J. Phys. Chem. C* 118 (2014) 25000–25008.
- [52] D.Y. Chan, E. Klaseboer, R. Manica, Theory of non-equilibrium force measurements involving deformable drops and bubbles, *Adv. Colloid Interface Sci.* 165 (2011) 70–90.
- [53] C.K. Batchelor, G. Batchelor, *An Introduction to Fluid Dynamics*, Cambridge university press, 2000.
- [54] L.G. Leal, *Advanced Transport Phenomena: Fluid Mechanics and Convective Transport Processes*, Cambridge University Press, 2007.
- [55] P. Jungwirth, D.J. Tobias, Specific ion effects at the air/water interface, *Chem. Rev.* 106 (2006) 1259–1281.
- [56] M. Boström, W. Kunz, B.W. Ninham, Hofmeister effects in surface tension of aqueous electrolyte solution, *Langmuir* 21 (2005) 2619–2623.
- [57] L.M. Pegram, M.T. Record, Hofmeister salt effects on surface tension arise from partitioning of anions and cations between bulk water and the air–water interface, *J. Phys. Chem. B* 111 (2007) 5411–5417.
- [58] R.I. Slavchov, J.K. Novev, Surface tension of concentrated electrolyte solutions, *J. Colloid Interface Sci.* 387 (2012) 234–243.
- [59] Y. Marcus, Individual ionic surface tension increments in aqueous solutions, *Langmuir* 29 (2013) 2881–2888.
- [60] Y. Chang, C.-Y. Ko, Y.-J. Shih, D. Quémener, A. Deratani, T.-C. Wei, D.-M. Wang, J.-Y. Lai, Surface grafting control of PEGylated poly (vinylidene fluoride) antifouling membrane via surface-initiated radical graft copolymerization, *J. Membr. Sci.* 345 (2009) 160–169.
- [61] Y. Han, S. Song, Y. Lu, D. Zhu, A method to modify PVDF microfiltration membrane via ATRP with low-temperature plasma pretreatment, *Appl. Surf. Sci.* 379 (2016) 474–479.
- [62] M. Kobayashi, Y. Terayama, H. Yamaguchi, M. Terada, D. Murakami, K. Ishihara, A. Takahara, Wettability and antifouling behavior on the surfaces of superhydrophilic polymer brushes, *Langmuir* 28 (2012) 7212–7222.
- [63] M. Wang, Z. Zhang, Y. Wang, X. Zhao, M. Yang, X. Men, Durable superwetting materials through layer-by-layer assembly: Multiple separations towards water/oil mixtures, water-in-oil and oil-in-water emulsions, *Colloid. Surface. Physicochem. Eng. Aspect.* 571 (2019) 142–150.
- [64] N. Ji, V. Ostroverkhov, C. Tian, Y. Shen, Characterization of vibrational resonances of water-vapor interfaces by phase-sensitive sum-frequency spectroscopy, *Phys. Rev. Lett.* 100 (2008), 096102.
- [65] C.L. McFearn, D.K. Beaman, F.G. Moore, G.L. Richmond, From franklin to today: toward a molecular level understanding of bonding and adsorption at the Oil–water interface, *J. Phys. Chem. C* 113 (2009) 1171–1188.
- [66] S. Gopalakrishnan, P. Jungwirth, D.J. Tobias, H.C. Allen, Air–liquid interfaces of aqueous solutions containing ammonium and sulfate: spectroscopic and molecular dynamics studies, *J. Phys. Chem. B* 109 (2005) 8861–8872.
- [67] S.J. Rehfeld, Adsorption of sodium dodecyl sulfate at various hydrocarbon-water interfaces, *J. Phys. Chem.* 71 (1967) 738–745.
- [68] K. Motomura, M. Aratono, N. Matubayasi, R. Matuura, Thermodynamic studies on adsorption at interfaces: III. Sodium dodecyl sulfate at water/hexane interface, *J. Colloid Interface Sci.* 67 (1978) 247–254.
- [69] T.D. Gurbkov, D.T. Dimitrova, K.G. Marinova, C. Bilke-Crause, C. Gerber, I. B. Ivanov, Ionic surfactants on fluid interfaces: determination of the adsorption; role of the salt and the type of the hydrophobic phase, *Colloid. Surface. Physicochem. Eng. Aspect.* 261 (2005) 29–38.
- [70] M. Cacace, E. Landau, J. Ramsden, The Hofmeister series: salt and solvent effects on interfacial phenomena, *Q. Rev. Biophys.* 30 (1997) 241–277.
- [71] J. Lyklema, Simple hofmeister series, *Chem. Phys. Lett.* 467 (2009) 217–222.

- [72] K.P. Gregory, G.B. Webber, E.J. Wanless, A.J. Page, Lewis strength determines specific-ion effects in aqueous and nonaqueous solvents, *J. Phys. Chem.* 123 (2019) 6420–6429.
- [73] C. Tian, S.J. Byrnes, H.-L. Han, Y.R. Shen, Surface propensities of atmospherically relevant ions in salt solutions revealed by phase-sensitive sum frequency vibrational spectroscopy, *J. Phys. Chem. Lett.* 2 (2011) 1946–1949.
- [74] W. Hua, A.M. Jubb, H.C. Allen, Electric field reversal of Na_2SO_4 , $(\text{NH}_4)_2\text{SO}_4$, and Na_2CO_3 relative to CaCl_2 and NaCl at the air/aqueous interface revealed by heterodyne detected phase-sensitive sum frequency, *J. Phys. Chem. Lett.* 2 (2011) 2515–2520.
- [75] V. Mazzini, G. Liu, V.S. Craig, Probing the Hofmeister series beyond water: specific-ion effects in non-aqueous solvents, *J. Chem. Phys.* 148 (2018) 222805.
- [76] M.C. Gurau, S.-M. Lim, E.T. Castellana, F. Albertorio, S. Kataoka, P.S. Cremer, On the mechanism of the Hofmeister effect, *J. Am. Chem. Soc.* 126 (2004) 10522–10523.
- [77] P. Mason, J. Cruickshank, G. Neilson, P. Buchanan, Neutron scattering studies on the hydration of phosphate ions in aqueous solutions of K_3PO_4 , K_2HPO_4 and KH_2PO_4 , *Phys. Chem. Chem. Phys.* 5 (2003) 4686–4690.
- [78] B. Minofar, R. Vácha, A. Wahab, S. Mahiuddin, W. Kunz, P. Jungwirth, Propensity for the air/water interface and ion pairing in magnesium acetate vs magnesium nitrate solutions: molecular dynamics simulations and surface tension measurements, *J. Phys. Chem. B* 110 (2006) 15939–15944.
- [79] B. Minofar, P. Jungwirth, M.R. Das, W. Kunz, S. Mahiuddin, Propensity of formate, acetate, benzoate, and phenolate for the aqueous solution/vapor interface: surface tension measurements and molecular dynamics simulations, *J. Phys. Chem. C* 111 (2007) 8242–8247.
- [80] P. Jungwirth, D.J. Tobias, Molecular structure of salt solutions: a new view of the interface with implications for heterogeneous atmospheric chemistry, *J. Phys. Chem. B* 105 (2001) 10468–10472.
- [81] T. Ishiyama, A. Morita, Molecular dynamics study of Gas– liquid aqueous sodium halide interfaces. I. Flexible and polarizable molecular modeling and interfacial properties, *J. Phys. Chem. C* 111 (2007) 721–737.
- [82] R.M. Onorato, D.E. Otten, R.J. Saykally, Adsorption of thiocyanate ions to the dodecanol/water interface characterized by UV second harmonic generation, *Proc. Natl. Acad. Sci. Unit. States Am.* 106 (2009) 15176–15180.
- [83] P. Mason, G. Neilson, C. Dempsey, A. Barnes, J. Cruickshank, The hydration structure of guanidinium and thiocyanate ions: implications for protein stability in aqueous solution, *Proc. Natl. Acad. Sci. Unit. States Am.* 100 (2003) 4557–4561.
- [84] Y. Yang, C. Nie, Y. Deng, C. Cheng, C. He, L. Ma, C. Zhao, Improved antifouling and antimicrobial efficiency of ultrafiltration membranes with functional carbon nanotubes, *RSC Adv.* 6 (2016) 88265–88276.
- [85] E. Rizzarelli, T. Theophanides, *Chemistry and Properties of Biomolecular Systems*, Springer Science & Business Media, 1991.



Contents lists available at ScienceDirect

Journal of Colloid and Interface Science

journal homepage: www.elsevier.com/locate/jcis

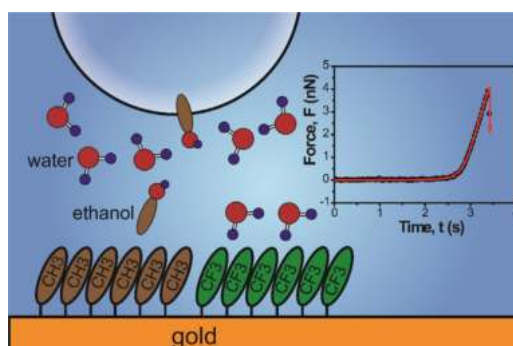
Unraveling the hydrophobic interaction mechanisms of hydrocarbon and fluorinated surfaces

Lu Gong^a, Feiyi Wu^a, Wenshuai Yang^a, Charley Huang^a, Wenhui Li^a, Xiaogang Wang^b, Jianmei Wang^b, Tian Tang^c, Hongbo Zeng^{a,*}^a Department of Chemical & Materials Engineering, University of Alberta, Edmonton, Alberta T6G 1H9, Canada^b Heavy Machinery Engineering Research Center of Education Ministry, Taiyuan University of Science and Technology, Taiyuan 030024, China^c Department of Mechanical Engineering, University of Alberta, Edmonton, Alberta T6G 1H9, Canada

HIGHLIGHTS

- Hydrophobic interaction mechanisms of hydrocarbon and fluorinated surfaces has been investigated.
- Fluorinated surface shows different hydrophobic interaction behaviors with hydrocarbon surface.
- Hydrophobic interactions can be modulated by the ethanol content in water.
- Ethanol exhibits greater influence in hydrophobic interactions of hydrocarbon surface than fluorinated surface.

GRAPHICAL ABSTRACT



ARTICLE INFO

Article history:

Received 18 October 2022

Revised 15 December 2022

Accepted 18 December 2022

Available online 20 December 2022

Keywords:

Hydrocarbon surface

Fluorinated surface

Hydrophobic mechanisms

Hydrogen bonds

Ordered water layer

ABSTRACT

Hypothesis: Numerous hydrocarbon and fluorine-based hydrophobic surfaces have been widely applied in various engineering and bioengineering fields. It is hypothesized that the hydrophobic interactions of hydrocarbon and fluorinated surfaces in aqueous media would show some differences.

Experiments: The hydrophobic interactions of hydrocarbon and fluorinated surfaces with air bubbles in aqueous solutions have been systematically and quantitatively measured using a bubble probe atomic force microscopy (AFM) technique. Ethanol was introduced to water for modulating the solution polarity. The experimental force profiles were analyzed using a theoretical model combining the Reynolds lubrication theory and augmented Young-Laplace equation by including disjoining pressure arisen from the Derjaguin-Landau-Verwey-Overbeek (DLVO) and non-DLVO interactions (i.e., hydrophobic interactions).

Findings: The experiment results show that the hydrophobic interactions were firstly weakened and then strengthened by increasing ethanol content in the aqueous media, mainly due to the variation in interfacial hydrogen bonding network. The fluorinated surface exhibited less sensitivity to ethanol than hydrocarbon surface, which is attributed to the presence of ordered interfacial water layer. Our work reveals the different hydrophobic effects of hydrocarbon and fluorinated surfaces, with useful implications on modulating the interfacial interactions of relevant materials in various engineering and bioengineering applications.

© 2022 Elsevier Inc. All rights reserved.

* Corresponding author at: Department of Chemical and Materials Engineering, University of Alberta, Canada.

E-mail address: hongbo.zeng@ualberta.ca (H. Zeng).

1. Introduction

Hydrophobic (HB) interactions between hydrophobic surfaces in aqueous solution play a vital role in the applications of hydrophobic materials ranging from engineering to biomedical applications, such as mineral flotation [1,2], water/oil separation [3,4], gas transportation [5], protein folding [6], cell manipulation [7], and drug delivery [8]. So far, numerous different hydrophobic materials have been designed and synthesized to satisfy various and complicated working conditions. They can primarily be chemically categorized into two groups: hydrocarbon materials and fluorinated materials [9]. Although both hydrocarbon and fluorinated materials have exhibited the excellent ability to endow a surface with great hydrophobicity, their different chemical compositions and properties should lead to some diversities in hydrophobic interaction behaviors during applications.

The intrinsic mechanisms of hydrophobic interactions have been under investigations for decades. Typically, in aqueous solutions, hydrocarbon surfaces (or air bubbles) would repel neighboring water molecules due to their inability to form hydrogen bonds, which subsequently could restrict the arrangement of interfacial water molecules and create a depletion (or vapor) layer [10–12]. Thermodynamically, this system prefers to minimize total surface energy and exposed interfacial area. Hence, a strong attraction between hydrophobic surfaces in aqueous solution has been found to drive the surfaces to contact with each other, which is generally referred to as “hydrophobic interaction”. However, for fluorinated surfaces, C–F bond has a larger dipole moment than C–H bond [9,13,14]. Thus, fluorinated surfaces are expected to form attractive interactions (e.g., dipole–dipole interactions) with neighboring polar water molecules and exhibit surface hydrophilicity, which undoubtedly is inconsistent with the well-known hydrophobicity of fluorinated surfaces [15,16]. Recently, molecular dynamics simulations have speculated that a layer of highly ordered water molecules may exist on many solid surfaces, such as metal and diamond surfaces, which normally could be hydrophilic but become hydrophobic under special conditions (e.g., high temperature) [17–21]. It is believed that the hydrogen bonds among ordered water molecules are confined inside and no hydrogen bond can be formed with bulk water molecules. Hence, this ordered water layer acts as a “hydrophobic coating”. Very recent experiment results by sum frequency generation vibrational spectroscopy (SFG-VS) have suggested the presence of such water layer on a polytetrafluoroethylene (PTFE) surface [22]. Therefore, fluorinated surfaces may have different hydrophobic interaction mechanism when compared to hydrocarbon surfaces, which should be further explored.

Previous reported work has demonstrated that the hydrophobic interaction or depletion layer of a common hydrophobic surface (e.g., hydrocarbon surface) could be significantly modulated by adjusting the stability of hydrogen bond network and interfacial molecular mobility, such as altering surface hydrophobicity, controlling surface phase status (e.g., liquid status or solid status), and adding chaotropic salts in water [23–28]. However, direct experimental study on the presence or absence of depletion layer is very limited. Decreasing aqueous solution polarities, such as adding ethanol, could improve liquid wettability on hydrophobic surfaces, which could significantly compress the depletion layer. Hydrophobic interactions have been measured to be tremendously weakened in pure ethanol or ethanol-in-water solutions with a high concentration [29–32]. However, many simulation and experimental results have shown that diluted ethanol (molar fraction less than 0.1 ~ 0.2) could gradually sabotage hydration shells of hydrophobic solutes (e.g., alkanes and hydrophobic polymers) in water, whereas concentrated ethanol stabilizes them [33–36]. This

interesting phenomenon suggests that ethanol may have variable influence in solvent–solute interactions, whose underlying mechanisms have not been elucidated yet. Therefore, systematic investigations on hydrophobic interaction behaviors and mechanisms of hydrocarbon and fluorinated surfaces in aqueous solutions with different polarities are of fundamental and practical importance.

Herein, the hydrophobic interaction behaviors and mechanisms of hydrocarbon and fluorinated surfaces have been quantitatively investigated using the bubble probe atomic force microscopy (AFM) technique in aqueous solutions. Ethanol at different concentrations (molar fraction less than 0.1) was introduced to modulate solution polarity. 1-decanethiol and 1H, 1H, 2H, 2H-perfluorodecanethiol have been employed to prepare hydrocarbon (donated as CH₃) and fluorinated (donated as CF₃) surfaces, respectively. This linear alkane and its fluorinated derivative were used as model hydrophobic systems due to their simple chemical structure and inability to form other specific interactions (e.g., cation- π and anion- π interactions). Ultra-smooth gold surfaces with root-mean-squared (RMS) roughness less than 0.3 nm were used to minimize the effect of surface morphology. The experimental force profiles were analyzed using a theoretical model combining the Reynolds lubrication theory and augmented Young-Laplace equation by including disjoining pressure arisen from the Derjaguin-Landau-Verwey-Overbeek (DLVO) and non-DLVO interactions (i.e., hydrophobic interactions). Obtained results reveal the different hydrophobic interaction mechanisms of hydrocarbon and fluorinated surfaces in aqueous solutions with different polarities, which provide useful guidance in material selections and applications of hydrophobic surfaces.

2. Materials and methodology

2.1. Materials

1-decanethiol (99 %, Sigma-Aldrich, Canada) and 1H, 1H, 2H, 2H-perfluorodecanethiol (97 %, Sigma-Aldrich, Canada) were used as received to prepare the hydrophobic hydrocarbon and fluorinated surfaces, respectively. Anhydrous ethanol (≥ 99.5 %, Sigma-Aldrich, Canada) was used as the solvent. Silicon wafers purchased from NanoFAB, University of Alberta, were used as the substrates. Aqueous solutions were prepared using Milli-Q water with a resistivity of 18.2 M Ω ·cm (BARNSTEAD Smart2Pure, Thermo Scientific, Canada). Sodium chloride (NaCl, ≥ 99 %) was purchased from Aldrich Sigma, Canada, and used as the electrolytes. The prepared ethanol in 1 M NaCl aqueous solutions with different molar fractions were degassed via sonication treatment under vacuum before experiments.

2.2. Preparation of ultrasmooth hydrocarbon and fluorinated surfaces

Ultrasmooth gold surfaces were prepared on silicon substrates using the template-stripping method [37,38]. Firstly, a gold layer was deposited onto freshly cleaved molecularly smooth mica surfaces via electron beam evaporation (EBE) technique with a thickness larger than 100 nm. This gold layer was directly glued onto a UV-cleaned silicon substrate using epoxy glue with the mica surface exposed. Then, mica pieces were carefully peeled off from one side in ethanol, leaving the gold layer strongly bonded to the supporting substrate. Subsequently, the prepared gold surfaces were immediately immersed in 50 mM 1-decanethiol or 1H, 1H, 2H, 2H-perfluorodecanethiol-in-ethanol solution for 2 h. The self-assembled monolayer (SAM) hydrocarbon or fluorinated surfaces were thoroughly washed with a large amount of ethanol and dried with nitrogen. The successful surface modification was confirmed by AFM surface imaging and water contact angle (WCA) measure-

ments. The thickness of the hydrocarbon and fluorinated surfaces was measured using spectroscopic ellipsometer (Sopra GESP-5, France).

2.3. Surface interaction measurements between air bubbles and the hydrophobic substrate in aqueous solutions.

Surface interactions between air bubbles and hydrocarbon or fluorinated substrates in 1 M NaCl solutions were directly measured by the AFM bubble probe technique using a MFP-3D-Bio AFM (Asylum Research, Santa Barbara, USA). The detailed experiment setup was previously reported in literature [24,25,39]. Experiments were conducted at room temperature (23 ± 1 °C). Prior to force measurements, the rectangular AFM tipless cantilever ($400 \mu\text{m} \times 70 \mu\text{m} \times 2 \mu\text{m}$) with a circular gold patch (diameter $\sim 65 \mu\text{m}$) at the end was firstly hydrophobized in ethanol solution with 20 mM 1-undecanethiol for ~ 24 h in order to pick up air bubbles in the following experiments. The cantilever's spring constant was calibrated to be ~ 0.45 N/m using the Hutter-Bechhoefer method [40]. The glass substrate of AFM fluid cell was immersed in ethanol solution with 50 mM trichloro(octadecyl)silane (OTS, $\geq 90\%$, Sigma-Aldrich, Canada) in order to have proper hydrophobicity for the immobilization of air bubbles in water. The schematic illustration of AFM force measurement is shown in Fig. 1A. The AFM fluid cell was firstly filled with a desired aqueous solution, and air bubbles with radii of $60\text{--}70 \mu\text{m}$ were generated on the slightly hydrophobized glass substrate using a customized sharp glass pipet. The as-prepared hydrophobic hydrocarbon or fluorinated surface was carefully placed in the fluid cell near air bubbles. Then, hydrophobized AFM tipless cantilever was driven to slowly approach one applicable air bubble and pick it up to make the bubble probe, as shown in Fig. 1B. Subsequently, this bubble probe was moved above the hydrophobic substrate, and driven to approach the substrate at a velocity of 200 nm/s until contact or upon reaching a preset loading force. During movement, the deflection of AFM tipless cantilever was monitored by a laser beam reflected at the backside of the cantilever to a quartered photo detector. Hence, the interaction force between air bubble and substrate with respect to time was obtained from the AFM software. For each case, two independently prepared substrates were used for multiple measurements. In this work, air bubbles were discovered to detach from the AFM tipless cantilever and spread on hydrophobic substrates when they were brought to the substrate during approaching process, as shown in Fig. 1C. Typically, the bubble probe AFM force measurement for one approach-

separation cycle can be completed within a few minutes; thus, the influence of ethanol evaporation and bubble size change can be neglected (Fig. 1C & D).

2.4. Theoretical analysis of measured force profiles

The measured force profiles were analyzed using a theoretical model combining Reynolds lubrication theory and augmented Young-Laplace equation [41,42]. When an air bubble was driven to approach a substrate, the aqueous solution film confined between bubble and substrate was drained out of contact area due to the applied pressure. The drainage behaviors of the confined aqueous film was described by Reynolds lubrication theory, as shown in Equation (1) [41,42].

$$\frac{\partial h}{\partial t} = \frac{1}{12\mu r} \frac{\partial}{\partial r} \left(r h^3 \frac{\partial p}{\partial r} \right) \quad (1)$$

In this equation, h is the thickness of the confined aqueous film, t is the time, μ is the aqueous solution viscosity, r is the radial coordinate, and p is the excess hydrodynamic pressure. Air bubbles are soft materials, which could deform to respond to external pressures. In this work, the deformation behavior of the air bubble during force measurements was described by augmented Young-Laplace equation (Equation (2)) [41,42],

$$\frac{\sigma}{r} \frac{\partial}{\partial r} \left(r \frac{\partial h}{\partial r} \right) = \frac{2\sigma}{R} - \Pi - p \quad (2)$$

where, σ is the surface tension of the aqueous solution, R is the radius of the air bubble, and Π is the disjoining pressure. The surface tensions of 1 M NaCl aqueous solutions with different ethanol contents were directly measured using the pendant drop shape method with a goniometer (Ramé-hart Instrument Company, USA) [43]. Measured results were shown in Figure S1, which were consistent with reported values [44]. DLVO interactions (i.e., van der Waals (VDW) interaction and electric double layer (EDL) interaction) and non-DLVO interaction (i.e., hydrophobic (HB) interaction) were applied to describe the surface interactions between air bubbles and hydrophobic surfaces (i.e., hydrocarbon and fluorinated surfaces) in aqueous solutions [45]. A very high salinity of 1 M NaCl was applied in aqueous solutions, which could significantly compress the electric double layer (Debye length ~ 0.32 nm) and result in negligible EDL interaction [45]. Hence, VDW pressure Π_{VDW} and HB pressure Π_{HB} were the major contributors to disjoining pressure Π . The thickness of hydrocarbon and fluorinated SAMs was so thin (less than 2 nm) that its influence on the VDW

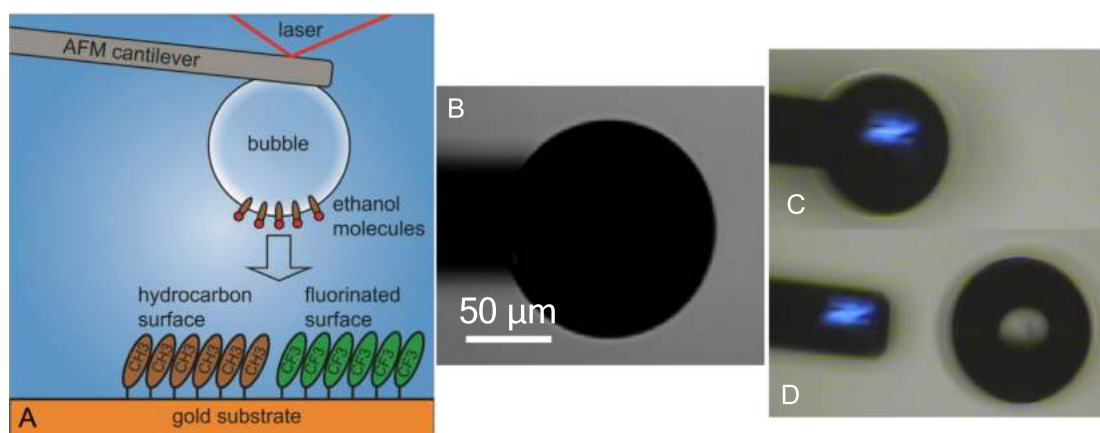


Fig. 1. (A) Schematic illustration of AFM force measurement between an air bubble and hydrophobic substrate (i.e., hydrocarbon or fluorinated surface) in aqueous solutions. (B) Optical images of an air bubble anchored on rectangular AFM tipless cantilever. (C-D) An air bubble detached from AFM cantilever and attached onto a substrate surface when approaching the substrate in aqueous solutions.

interaction could be ignored [24]. Since ethanol concentration in 1 M NaCl aqueous solution was very low (molar fraction less than 0.1), the effect was also negligible, which was demonstrated by the interaction forces between two air bubbles (Figure S2). Thereby, the Hamaker constant of this air/water/gold system was adopted in theoretical analysis based on the Lifshitz theory [24,45]. In thermodynamics, the free energy of HB interactions per unit area could be derived from surface energy change of an air bubble attaching onto hydrophobic surface, which has been discovered to decay exponentially with surface separation [25,46,47]. Hence, the VDW interaction and HB interaction could be calculated using Equation (3) and (4), respectively.

$$\Pi_{VDW} = -\frac{A_H}{6\pi(h+T)^3} \quad (3)$$

$$\Pi_{HB} = -\frac{C}{D_0} \exp\left(-\frac{h}{D_0}\right) = -\frac{\sigma(1-\cos\theta)}{D_0} \exp\left(-\frac{h}{D_0}\right) \quad (4)$$

Here, A_H is the Hamaker constant between air and gold in water, T is the thickness of the hydrocarbon and fluorinated SAMs, θ is the water contact angle in air, C is the pre-exponential factor of HB interaction determined by the surface energy change incorporated with Young-Laplace pressure ($C = \sigma(1 - \cos\theta)$), and D_0 is the characteristic decay length. The decay length is commonly used to characterize the influence strength of HB interaction. The overall interaction force between air bubble and hydrophobic substrate in aqueous solution was then calculated by integrating hydrodynamic pressure p and disjoining pressure Π , as shown in Equation (5) [41,42].

$$F(t) = 2\pi \int_0^\infty [p + \Pi] \cdot r dr \quad (5)$$

3. Results and discussion

3.1. Characterization of hydrophobic hydrocarbon and fluorinated surfaces

The as-prepared hydrocarbon and fluorinated SAM surfaces were characterized by AFM surface imaging and water contact angle (WCA) measurements. Fig. 2A–C show AFM surface images of a bare gold surface, hydrocarbon (donated as CH3) surface, and fluorinated (donated as CF3) surface in 1 M NaCl solution,

respectively. It is noted that all the surfaces are ultrasmooth with root-mean-squared (RMS) surface roughness less than 0.3 nm. Meanwhile, there is no nano-bubble detected on surfaces. Therefore, the effects of surface morphologies and nano-bubbles could be neglected in following surface force analysis [48]. Fig. 2D–F show water contact angles (WCA) in air of bare gold surface, CH3 surface and CF3 surface, respectively. The bare gold surface has an extremely low WCA of less than 5° due to its high surface energy [49,50]. After surface modification using hydrophobic thiols, CH3 and CF3 surfaces exhibit the WCA of 100°±1° and 102°±1°, respectively, which suggests the successful grafting of hydrocarbon and fluorocarbon thiols on gold surfaces [51,52]. The thickness of CH3 and CF3 SAMs was determined by spectroscopic ellipsometer to be 1.2 ± 0.2 nm and 1.3 ± 0.2 nm, respectively. The similar thickness was attributed to the same carbon number of hydrocarbon thiol and fluorocarbon thiol, which could minimize the influence of film thickness and surface nanoscale structure. Besides, the contact angles of 1 M NaCl aqueous solutions with different ethanol molar fractions (denoted as X) were also measured on both CH3 and CF3 surfaces in air. In Fig. 3 and Figure S3, the solution contact angle on CH3 surface monotonically decreases from 100°±1° for no ethanol to 54°±1° for ethanol molar fraction of 0.1, indicating that adding ethanol in aqueous solutions could facilitate wetting behaviors on hydrophobic hydrocarbon surface [53,54]. It should be noted that the addition of ethanol in aqueous solutions could lead to the significant reduction of liquid surface energy (Figure S1), as ethanol molecules prefer to stay at water/air interface [55,56]. Hence, the decreasing WCA is expected [57]. The similar decreasing contact angle with the increasing ethanol content was also observed on CF3 surface. Besides, it should be noted that for the same ethanol concentration, the contact angle on CF3 surface was larger than that on CH3 surface as the consequence of relatively lower surface energy of fluorinated surface [58,59]. This may also imply that fluorinated surface owns stronger hydrophobicity than hydrocarbon surface.

3.2. Interaction forces between bubbles and hydrocarbon surface in 1 M NaCl solutions

The interaction forces between air bubbles and CH3 surface in 1 M NaCl solutions with different ethanol molar fractions were directly measured using bubble probe AFM technique. Obtained force results are shown in Fig. 4 and analyzed using theoretical model.

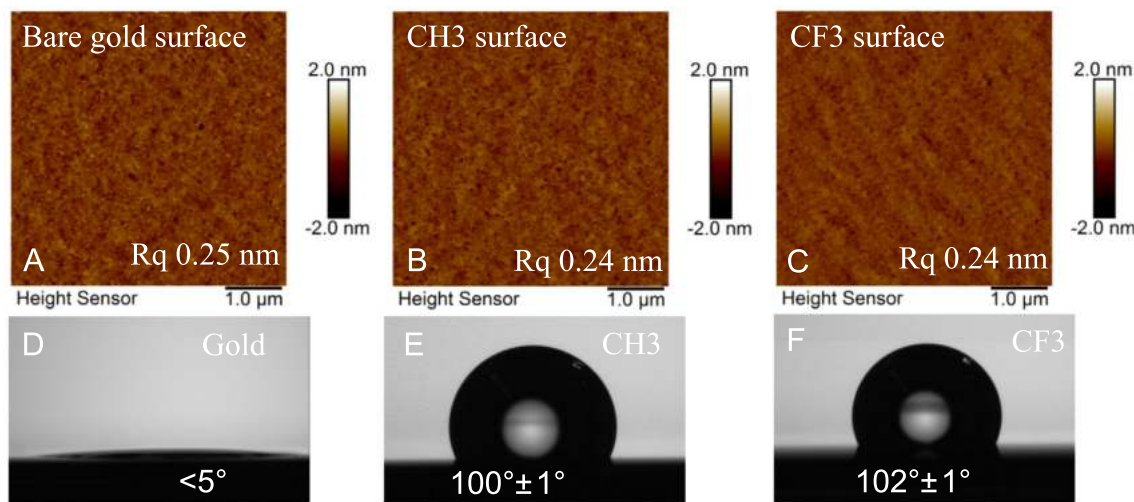


Fig. 2. AFM surface images in 1 M NaCl solution and water contact angles (WCA) in air of (A, D) bare gold surface, (B, E) hydrocarbon (CH3) surface, and (C, F) fluorinated (CF3) surface. At least five independent contact angle measurements have been conducted in each case.

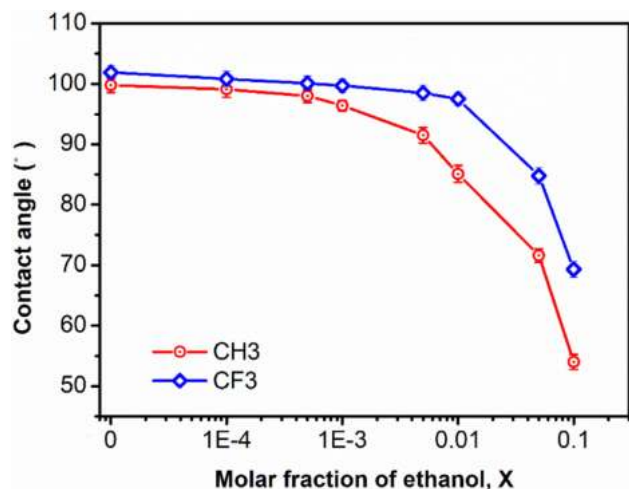


Fig. 3. Contact angles of 1 M NaCl aqueous solutions with different ethanol molar fractions (X) on hydrocarbon (CH3) and fluorinated (CF3) surfaces in air. At least five independent contact angle measurements have been conducted in each case.

Fig. 4A shows the measured surface force between the bubble and CH3 surface in 1 M NaCl solution. As the air bubble was driven to approach CH3 surface, a maximum repulsion of ~ 4.1 nN was detected at the moment when the bubble immediately detached from AFM cantilever and attached onto the substrate surface (as shown in Fig. 1C and D). In such high salinity (e.g., 1 M NaCl), the electric double layer is significantly compressed (Debye length ~ 0.32 nm) to the point where the EDL interaction could be ignored [45]. Meanwhile, the VDW interaction becomes repulsive due to the negative Hamaker constant of the air/water/gold system [45,50]. Therefore, this sudden attachment behavior is attributed to the strong hydrophobic attraction between bubble and CH3 surface [48]. In theoretical analysis, the HB interaction decay length D_0 was determined to be 1.59 ± 0.02 nm. This is consistent with values reported in literature [48,60]. The confined aqueous film thickness profile before attachment, the contributed surface interactions, and the disjoining pressure involving VDW interaction and HB interaction have been reconstructed in Figure S4 based on theoretical results, which demonstrate that the HB attraction plays dominant role in bubble attachment onto CH3 surface. Fig. 4B shows measured force profiles between air bubble and CH3 surface in 1 M NaCl solution with ethanol molar fraction $X = 0.0001$. Similar force profile with a sudden attachment behavior was observed, however the maximum repulsion became larger (~ 5.2 nN) than that without ethanol (Fig. 4A). Since the ethanol concentration is so low, the VDW repulsion would be regarded as unaltered (see Supporting Information section 2). Hence, this increased maximum repulsion before bubble attachment is mainly attributed to weakened hydrophobic attraction between air bubble and CH3 surface. In theoretical analysis, the HB interaction decay length D_0 is fitted to be 1.54 ± 0.02 nm, which is smaller than that without ethanol. Hence, adding ethanol in aqueous solution at such diluted concentration could still result in a weakened HB interaction. As ethanol molar fraction increases to 0.0005 and 0.001 (Fig. 4C and D), the maximum repulsion before bubble attachment increased to ~ 6.5 nN and ~ 10.3 nN, respectively. Analogously, the HB interaction strength was gradually reduced as ethanol molar fraction increased. Fitted HB interaction decay length D_0 is also decreased to 1.36 ± 0.02 nm for $X = 0.0005$ and 1.24 ± 0.02 nm for $X = 0.001$. This result demonstrates that adding ethanol in aqueous solutions could gradually inhibit hydrophobic interactions between bubbles and CH3 surface [61].

When ethanol molar fraction increases to 0.005 (Fig. 4E), the maximum repulsion no longer increases, but decreases (~ 9.2 nN) compared with that at ethanol molar fraction of 0.001 in Fig. 4D, suggesting that HB interaction between bubbles and CH3 surface is strengthened. As ethanol molar fraction increases to 0.01 and 0.05 (Fig. 4F and G), the maximum repulsion becomes further decreased to ~ 7.4 nN and ~ 6.9 nN, respectively, indicating that HB interaction was strengthened with the increasing ethanol content. Fitted HB interaction decay length D_0 is gradually increased to 1.34 ± 0.02 nm for $X = 0.005$, 1.48 ± 0.02 nm for $X = 0.05$, and 1.57 ± 0.02 nm for $X = 0.05$, respectively. As ethanol molar fraction increases to 0.1 (Fig. 4H), the maximum repulsion before attachment behavior rises to ~ 19 nN, indicating that the HB interaction is weakened again. However, fitted HB interaction decay length D_0 is 1.55 ± 0.02 nm, which is only slightly smaller than that with ethanol molar fraction of 0.05. Such significant weakening in force profiles could be the consequence of the great decrease of liquid surface energy and contact angle at high ethanol molar concentration ~ 0.1 (Fig. 3A and Figure S1), which lead to vigorous reduction in the pre-exponential factor of HB interaction (i.e., C in Equation (4)).

The HB interactions between bubbles and CH3 surface in 1 M NaCl solutions with increasing ethanol content have been reconstructed based on theoretical analysis in Fig. S5A and B. It is noted that HB interaction gradually becomes weakened when ethanol molar fraction increases from 0 to 0.001, but then turns to be strengthened as X continuously increases from 0.001 to 0.05. The HB interaction becomes slightly weakened again as X increased to 0.1. This interesting varying behavior of HB interaction with ethanol content seems contradictory with the monotonic decreasing of WCAs on CH3 surface (Fig. 3A) and surface energy (Figure S1). It should be noted that the HB interaction between bubbles and hydrophobic surface in aqueous solutions is not only related to the free energy change of bubble attachment (i.e., surface energies), but also affected by the stability of interfacial hydrogen bond network and molecular mobility [23–28]. Hence, this varying phenomenon also implies that ethanol at different concentrations may play variable roles in interfacial hydrogen bond network and/or molecular mobility.

3.3. Interaction forces between bubbles and fluorinated surface in 1 M NaCl solutions

Surface interactions between air bubbles and fluorinated (CF3) surfaces in 1 M NaCl solutions with ethanol molar fraction increasing from 0 to 0.1 have been quantified and theoretical analyzed in Fig. 5.

In Fig. 5A, measured interaction force between the bubble and CF3 surface in 1 M NaCl solution exhibits the maximum repulsion of ~ 3.0 nN before attachment behavior, which is weaker than that for CH3 surface (Fig. 4A). Since different SAMs have negligible influence in VDW interaction, this weaker repulsion could indicate a stronger HB interaction with CF3 surface than that with CH3 surface. Fitted HB interaction decay length D_0 for CF3 surface is 1.71 ± 0.02 nm, which is greater than that of CH3 surface. The greater hydrophobicity of fluorocarbons over hydrocarbons has been explained by relatively larger excluded volume per fluorocarbon molecule in water, which thereby leads to a higher surface free energy penalty as surrounded by water molecules [62]. Namely, fluorocarbons are relatively “fatter” than hydrocarbons in water. Fig. 5B–H show measured surface interactions between bubbles and CF3 surface in 1 M NaCl solutions with ethanol molar fraction of 0.0001, 0.0005, 0.001, 0.005, 0.01, 0.05 and 0.1, respectively. The maximum repulsion gradually increases from ~ 4.0 nN to ~ 48 nN as ethanol content increases. However, fitted decay length D_0 is discovered to firstly decrease from 1.68 ± 0.02 nm for ethanol

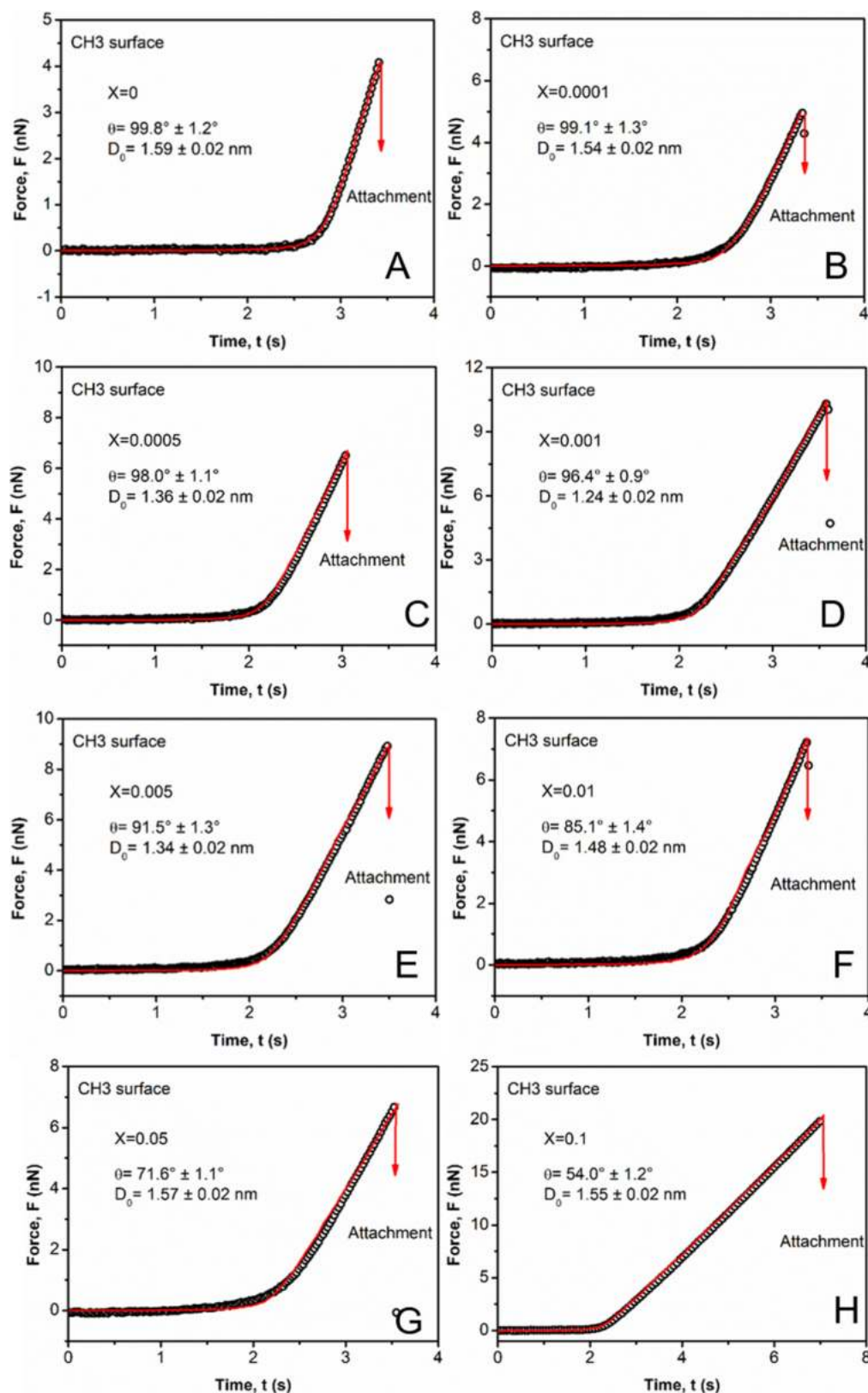


Fig. 4. Measured surface interactions between bubbles and hydrocarbon (CH₃) surface in 1 M NaCl solutions with ethanol molar fraction of (A) 0, (B) 0.0001, (C) 0.0005, (D) 0.001, (E) 0.005, (F) 0.01, (G) 0.05, and (H) 0.1, respectively. The black circles are experiment data and the red lines are theoretical results. The arrows indicates the attachment of bubbles onto the substrates. (For interpretation of the references to colour in this figure legend, the reader is referred to the web version of this article.)

molar fraction of 0.0001 to 1.26 ± 0.02 nm for ethanol molar fraction of 0.01, but then increase to 1.37 ± 0.02 nm for ethanol molar fraction of 0.05, and to 1.50 ± 0.02 nm for ethanol molar fraction of

0.1, respectively. Namely, the HB interaction between the bubble and CF₃ surface becomes weakened firstly and then turns to be strengthened with increasing ethanol content, which is similar to

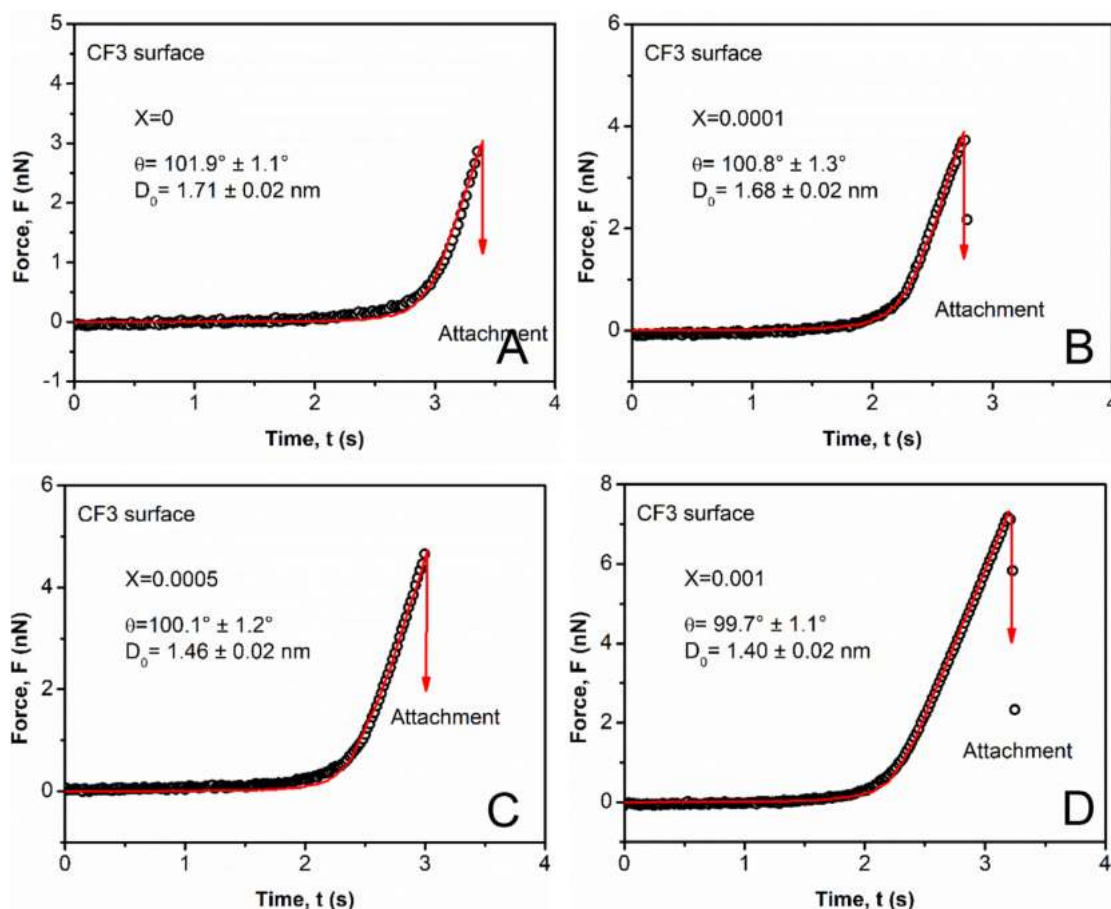


Fig. 5. Measured surface interactions between bubbles and fluorinated (CF3) surface in 1 M NaCl solutions with ethanol molar fraction of (A) 0, (B) 0.0001, (C) 0.0005, (D) 0.001, (E) 0.005, (F) 0.01, (G) 0.05, and (H) 0.1, respectively.

the tendency of CH3 surface. For surface interactions with ethanol molar fraction of 0.05 and 0.1 (Fig. 5G and H), the strengthened maximum repulsion should suggest the weakened HB interactions, but the larger decay length D_0 indicates the strengthened HB interactions. This discrepancy can also be attributed to the vigorously decreased liquid surface energy and contact angle on CF3 surface with the presence of ethanol ($X = 0.05$ and 0.1) (Fig. 3B and Figure S1), which subsequently lower free energy change of bubble attachment behavior on CF3 surface (i.e., the pre-exponential factor C of HB interaction in Equation (4)).

HB interactions between bubbles and CF3 surface in 1 M NaCl solution with different ethanol content have also been reconstructed in Fig. S5C and D. It is noted that the HB interaction is gradually weakening when ethanol molar fraction increases from 0 to 0.01, and then becoming strengthened as the fraction continues to increase to 0.1. This varying tendency of the HB interactions with the increasing ethanol concentration is similar with that of CH3 surface.

3.4. Hydrophobic interaction mechanisms on hydrocarbon and fluorinated surfaces

Fig. 6 summarizes measured liquid contact angles in air and fitted HB decay length D_0 of CH3 and CF3 surfaces as ethanol molar fraction increases from 0 to 0.1. Liquid contact angles on both CH3 and CF3 surfaces decrease monotonously with the increasing ethanol content. This result agrees with practical observation that ethanol could promote the wetting phenomena on hydrophobic

surfaces. Besides, CF3 surface owns larger liquid contact angle than CH3 surface, which is attributed to its relatively lower surface energy. Conventionally, hydrophobic substrate surface with larger water contact angle in air is expected to have stronger hydrophobic attraction [45]. However, a recent work has revealed that hydrophobic surfaces with similar water contact angles in air could show different hydrophobic interactions with air bubbles in aqueous solutions, which could be attributed to interfacial water molecules' mobility in the vicinity of hydrophobic surfaces [24]. The HB decay length D_0 of both CH3 and CF3 surfaces shows decreasing tendency with the addition of ethanol at very low concentration, but then turning into increasing trend as ethanol concentration continuously increases, suggesting that addition of ethanol in aqueous solutions could firstly weaken HB interaction, but then strengthen it. This interesting varying behavior could be explained by the presence of ethanol affecting the hydrogen bonding network of water molecules [63–65]. Previous experiment and simulation results have demonstrated that water molecules at water-hydrophobic surface (or air) interface would sacrifice some hydrogen bonds to minimize contact area during wetting process, hence creating some free polar hydroxyl (OH) groups at the interface (Fig. 7A) [66–69]. These free dangling OH groups prefer to point towards hydrophobic surface (or air), thereby generating the strong dipole–dipole attraction between two hydrophobic surface, namely hydrophobic interaction [27,70–73]. There are two kinds of water molecules at interface: water molecules with a free dangling OH group, and water molecules having hydrogen bonds with other molecules. Ethanol molecules, having both hydrophilic hydroxyl

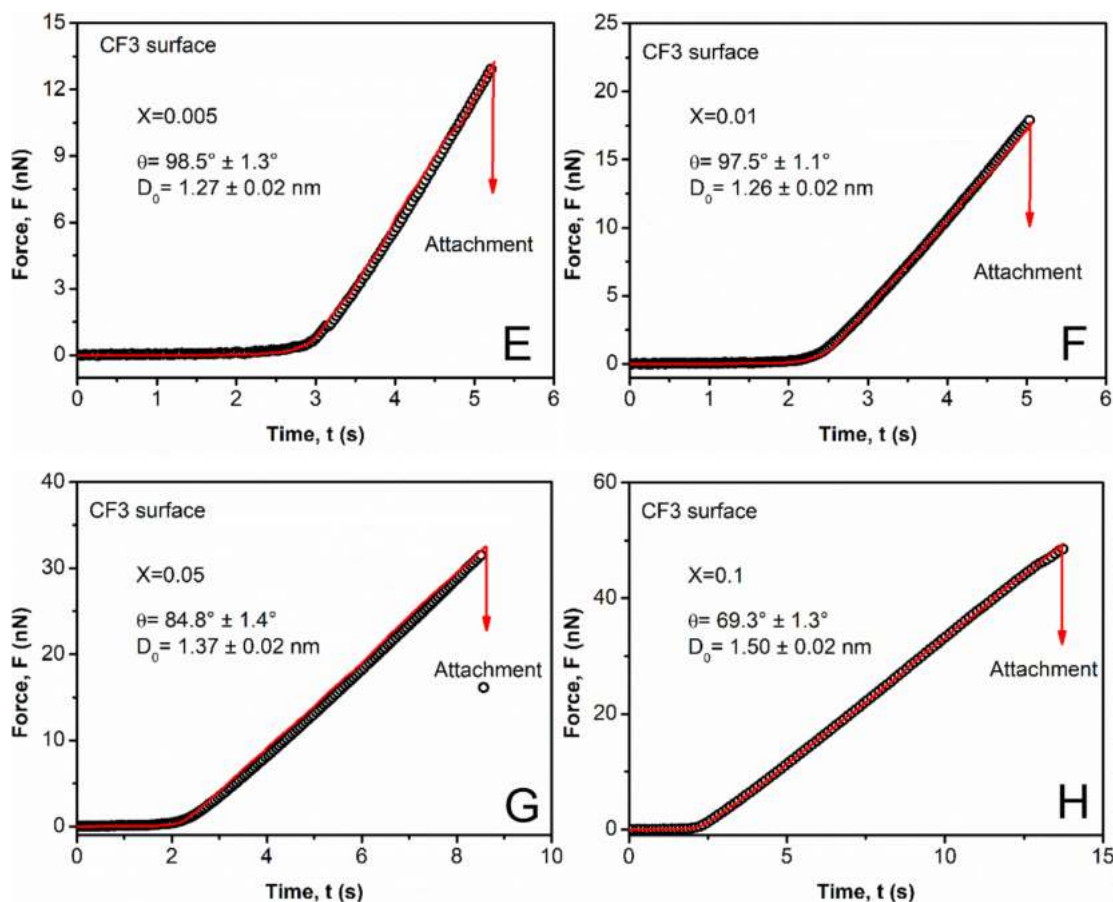


Fig. 5 (continued)

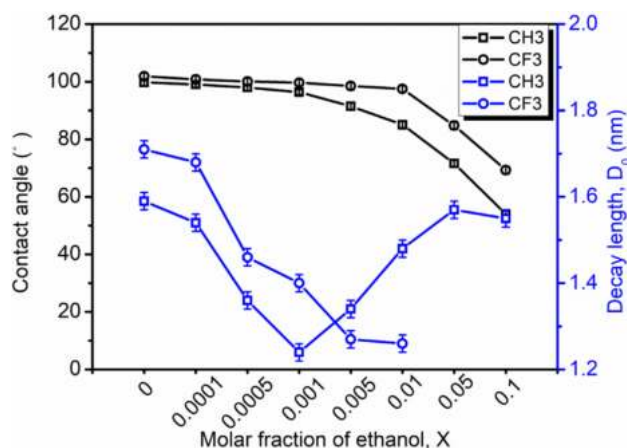


Fig. 6. Measured liquid contact angle in air and fitted HB decay length D_0 of hydrocarbon (CH3) and fluorinated (CF3) surface with ethanol molar fraction increasing from 0 to 0.1. At least five independent contact angle measurements have been conducted in each case.

group and hydrophobic ethyl group, could accumulate at water-hydrophobic surface (or air) interface [74–76] and form hydrogen bonds with interfacial water molecules: (1) directly forming hydrogen bonds with the free OH groups of the water molecules, or (2) breaking the water-water hydrogen bond to form a new hydrogen bond with one of the water molecules and generating one free OH group. At very dilute ethanol concentration, the former

case dominates and leads to reduced density of free OH groups at interface, hence contributing to the weakened HB interaction. However, as more ethanol is added, the latter case becomes more important and original interfacial hydrogen bond network could be altered. The ethanol–water hydrogen bond could restrict the conformation of water molecules and affect surrounding hydrogen bond structure, thus leading to reduced average hydrogen bonds of each water molecule [77–79]. Therefore, more free OH groups could be generated and stronger hydrophobic interaction could be observed. If ethanol content continues to increase, more ethanol molecules will adsorb at interface and interfacial water molecule density will keep reduced as well as free OH group density. Then, interfacial hydrogen bonding network will no more have influence in surface interactions. Therefore, the hydrophobic interaction will gradually become weakened till reaching its strength in pure ethanol [29,61,80]. Meanwhile, it is possible that ethanol molecules could be embedded between carbon chains of CH3 and CF3 surfaces to increase surface hydrophilicity, thus weakening the hydrophobic interactions.

It's also noted that the hydrophobic interaction decay length reaches its minimum at ethanol molar fraction of ~ 0.001 for CH3 surface and ~ 0.01 for CF3 surface, respectively (Fig. 6), indicating that CH3 surface is more sensitive to ethanol than CF3 surface. This result may be attributed to different hydrophobic effects of hydrocarbon and fluorinated surfaces. The strong attractive dispersion force between the hydrocarbons and ethyl groups of ethanol across depletion layer could promote the accumulation behavior of ethanol at interface [45,81,82]. However, the presence of ordered water layer on fluorinated surface could prevent direct contact with ethanol, and the VDW interaction between fluorocar-

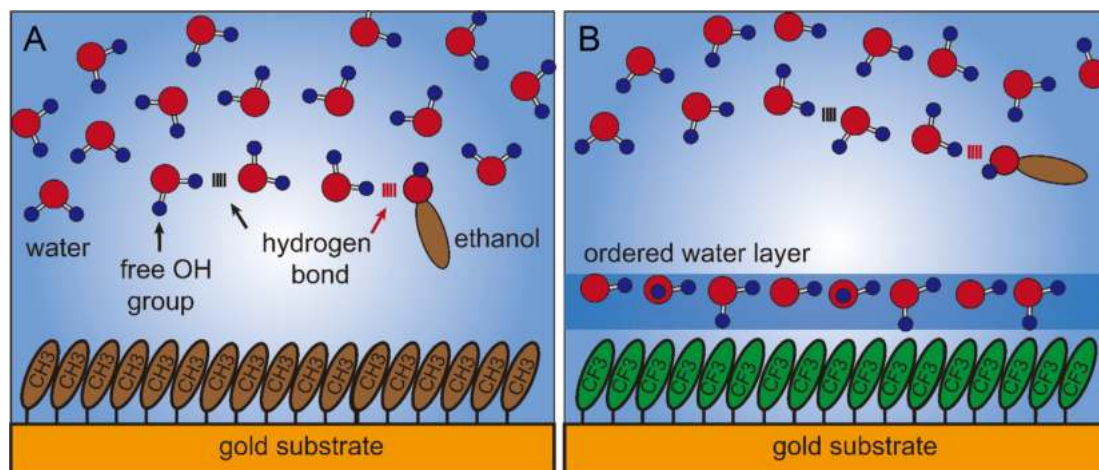


Fig. 7. Schematics of interfacial hydrogen bonding network on (A) hydrocarbon and (B) fluorinated surface.

bonds and ethanol across water layer is repulsive according to Lifshitz theory [45,83–85], which could inhibit the adsorption behavior of ethanol at interface (Fig. 7B). Conclusionally, CH₃ surface exhibits a more ethanol-sensitive behavior than CF₃ surface.

4. Conclusions

In this work, for the *first* time the hydrophobic interaction mechanisms between air bubbles and hydrocarbon and fluorinated surfaces in aqueous solutions have been quantitatively and systematically characterized. Ethanol was introduced to aqueous media to modulate the solution polarity. It was found that increasing the ethanol content in an aqueous medium could monotonically reduce the contact angles on hydrocarbon and fluorinated surfaces due to the decreased surface energy of aqueous medium. Larger contact angles were detected on fluorinated surface than that on hydrocarbon surface, suggesting higher hydrophobicity of fluorinated surface. Surface force measurements revealed that the hydrophobic interactions of air bubbles with hydrophobic surfaces (i.e., hydrocarbon and fluorinated surface) were firstly weakened and then strengthened when increasing the ethanol content (with its maximum molar fraction less than 0.1) in aqueous solutions, even though the contact angles were monotonically decreased. This ethanol-dependent behavior of hydrophobic interactions is attributed to the presence of ethanol affecting the hydrogen bonding network of water, which could firstly consume free dangling OH groups of water molecules in aqueous solutions with low ethanol content, and then break interfacial hydrogen bond network to generate more free OH groups under the conditions with relatively larger ethanol content. Meanwhile, hydrocarbon surface exhibited a higher sensitivity to ethanol content than fluorinated surface, which was attributed to the protective layer of ordered water molecules on fluorinated surface and repulsive VDW force of fluorocarbon with ethanol across water layer. These results have demonstrated that adjusting solution polarity could be a feasible way to modulate surface interactions between hydrophobic surfaces, and the hydrocarbon and fluorinated surfaces possess different hydrophobic interaction behaviors.

In previous studies, the influence of several factors such as surface hydrophobicity [25], surface chemical heterogeneity [24,85], nano-bubbles [86], temperature [6] and salts [26] on hydrophobic interactions were experimentally investigated. Simulation methods have also been employed to explore arrangement of water molecules on hydrophobic surfaces [87–89]. Nevertheless, the effects of material chemistry and solution polarity on hydrophobic

interactions have not been fully understood. This work has advanced the field by providing new insights on the fundamental surface interaction mechanisms of two major types of hydrophobic substrates (e.g., hydrocarbon and fluorinated surfaces) in aqueous solutions, which provides useful implications for material separation, mineral flotation, bubble/drop manipulation, micro-devices, and so on. Future work on water structures in the vicinity of various hydrophobic surfaces of varying surface chemistry under different conditions (e.g., water chemistry, temperature) will further advance the fundamental understanding of hydrophobic interaction mechanisms.

Author Contributions

All the authors have contributed to the investigation, methodology, resources, writing-reviewing & editing.

Data availability

Data will be made available on request.

Declaration of Competing Interest

The authors declare that they have no known competing financial interests or personal relationships that could have appeared to influence the work reported in this paper.

Acknowledgements

This work was supported by the Natural Sciences and Engineering Research Council of Canada (NSERC), the Canada Foundation for Innovation (CFI), and the Canada Research Chairs Program (H. Zeng).

Appendix A. Supplementary data

Supplementary data to this article can be found online at <https://doi.org/10.1016/j.jcis.2022.12.084>.

References

- [1] Z. Wu, X. Wang, H. Liu, H. Zhang, J.D. Miller, Some physicochemical aspects of water-soluble mineral flotation, *Adv. Colloid Interface Sci.* 235 (2016) 190–200.

- [2] S. Lu, Hydrophobic interaction in flocculation and flotation 3. Role of hydrophobic interaction in particle–bubble attachment, *Colloids Surf.* 57 (1) (1991) 73–81.
- [3] Y. Wang, S. Tao, Y. An, A reverse membrane emulsification process based on a hierarchically porous monolith for high efficiency water–oil separation, *J. Mater. Chem. A* 1 (5) (2013) 1701–1708.
- [4] Y. Wang, J. Wang, Y. Ding, S. Zhou, F. Liu, In situ generated micro-bubbles enhanced membrane antifouling for separation of oil-in-water emulsion, *J. Membr. Sci.* 621 (2021) 119005.
- [5] C. Yu, P. Zhang, J. Wang, L. Jiang, Superwettability of gas bubbles and its application: from bioinspiration to advanced materials, *Adv. Mater.* 29 (45) (2017) 1703053.
- [6] R.L. Baldwin, Temperature dependence of the hydrophobic interaction in protein folding, *Proc. Natl. Acad. Sci.* 83(21) (1986) 8069–8072.
- [7] R.D. Tilton, C.R. Robertson, A.P. Gast, Manipulation of hydrophobic interactions in protein adsorption, *Langmuir* 7 (11) (1991) 2710–2718.
- [8] M. Guo, Y. Yan, H. Zhang, H. Yan, Y. Cao, K. Liu, S. Wan, J. Huang, W. Yue, Magnetic and pH-responsive nanocarriers with multilayer core–shell architecture for anticancer drug delivery, *J. Mater. Chem.* 18 (42) (2008) 5104–5112.
- [9] J.C. Biffiger, H.W. Kim, S.G. DiMaggio, The polar hydrophobicity of fluorinated compounds, *ChemBiochem* 5 (5) (2004) 622–627.
- [10] D. Chandler, Interfaces and the driving force of hydrophobic assembly, *Nature* 437 (7059) (2005) 640–647.
- [11] M. Mao, J. Zhang, R.-H. Yoon, W.A. Ducker, Is there a thin film of air at the interface between water and smooth hydrophobic solids?, *Langmuir* 20 (5) (2004) 1843–1849.
- [12] J. Mittal, G. Hummer, Static and dynamic correlations in water at hydrophobic interfaces, *Proceedings of the National Academy of Sciences* 105(51) (2008) 20130–20135.
- [13] I. Hyla-Kryspin, G. Haufe, S. Grimme, Weak Hydrogen Bridges: A Systematic Theoretical Study on the Nature and Strength of C–H... F–C Interactions, *Chemistry–A, European Journal* 10 (14) (2004) 3411–3422.
- [14] D. Nelson Jr, G. Fraser, W. Klemperer, Electric dipole moments of HF–C₂H₂, HF–C₂H₄, and HF–C₃H₆, *J. Chem. Phys.* 82 (10) (1985) 4483–4485.
- [15] X. Li, J. Li, M. Eleftheriou, R. Zhou, Hydration and dewetting near fluorinated superhydrophobic plates, *J. Am. Chem. Soc.* 128 (38) (2006) 12439–12447.
- [16] M.P. Krafft, J.G. Riess, Chemistry, physical chemistry, and uses of molecular fluorocarbon–hydrocarbon diblocks, triblocks, and related compounds • unique “apolar” components for self-assembled colloid and interface engineering, *Chem. Rev.* 109 (5) (2009) 1714–1792.
- [17] G.A. Kimmel, N.G. Petrik, Z. Dohnálek, B.D. Kay, Crystalline ice growth on Pt (111): Observation of a hydrophobic water monolayer, *Phys. Rev. Lett.* 95 (16) (2005) 166102.
- [18] C. Wang, H. Lu, Z. Wang, P. Xiu, B. Zhou, G. Zuo, R. Wan, J. Hu, H. Fang, Stable liquid water droplet on a water monolayer formed at room temperature on ionic model substrates, *Phys. Rev. Lett.* 103 (13) (2009) 137801.
- [19] A. Akaishi, T. Yonemaru, J. Nakamura, Formation of water layers on graphene surfaces, *ACS Omega* 2 (5) (2017) 2184–2190.
- [20] C. Wang, C. Qi, Y. Tu, X. Nie, S. Liang, Ambient conditions disordered–ordered phase transition of two-dimensional interfacial water molecules dependent on charge dipole moment, *Phys. Rev. Mater.* 3 (6) (2019) 065602.
- [21] D.T. Limmer, A.P. Willard, P. Madden, D. Chandler, Hydration of metal surfaces can be dynamically heterogeneous and hydrophobic, *Proc. Natl. Acad. Sci.* 110 (11) (2013) 4200–4205.
- [22] J. Zhang, J. Tan, R. Pei, S. Ye, Y. Luo, Ordered Water Layer on the Macroscopically Hydrophobic Fluorinated Polymer Surface and Its Ultrafast Vibrational Dynamics, *J. Am. Chem. Soc.* (2021).
- [23] C. Shi, D.Y. Chan, Q. Liu, H. Zeng, Probing the hydrophobic interaction between air bubbles and partially hydrophobic surfaces using atomic force microscopy, *J. Phys. Chem. C* 118 (43) (2014) 25000–25008.
- [24] X. Cui, J. Liu, L. Xie, J. Huang, Q. Liu, J.N. Israelachvili, H. Zeng, Modulation of hydrophobic interaction by mediating surface nanoscale structure and chemistry, not monotonically by hydrophobicity, *Angew. Chem.* 130 (37) (2018) 12079–12084.
- [25] C. Shi, X. Cui, L. Xie, Q. Liu, D.Y. Chan, J.N. Israelachvili, H. Zeng, Measuring forces and spatiotemporal evolution of thin water films between an air bubble and solid surfaces of different hydrophobicity, *ACS Nano* 9 (1) (2015) 95–104.
- [26] X. Cui, J. Liu, L. Xie, J. Huang, H. Zeng, Interfacial ion specificity modulates hydrophobic interaction, *J. Colloid Interface Sci.* 578 (2020) 135–145.
- [27] L. Xie, X. Cui, L. Gong, J. Chen, H. Zeng, Recent advances in the quantification and modulation of hydrophobic interactions for interfacial applications, *Langmuir* 36 (12) (2020) 2985–3003.
- [28] J. Liu, X. Cui, L. Xie, J. Huang, L. Zhang, J. Liu, X. Wang, H. Zeng, Probing effects of molecular-level heterogeneity of surface hydrophobicity on hydrophobic interactions in air/water/solid systems, *J. Colloid Interface Sci.* 557 (2019) 438–449.
- [29] J. Wang, Z. Li, R.-H. Yoon, J.C. Eriksson, Surface forces in thin liquid films of n-alcohols and of water–ethanol mixtures confined between hydrophobic surfaces, *J. Colloid Interface Sci.* 379 (1) (2012) 114–120.
- [30] G.-H. Deng, Y. Shen, H. Chen, Y. Chen, B. Jiang, G. Wu, X. Yang, K. Yuan, J. Zheng, Ordered-to-Disordered Transformation of Enhanced Water Structure on Hydrophobic Surfaces in Concentrated Alcohol–Water Solutions, *The journal of physical chemistry letters* 10 (24) (2019) 7922–7928.
- [31] X. Zhang, R. Manica, Y. Tang, Q. Liu, Z. Xu, Bubbles with tunable mobility of surfaces in ethanol–NaCl aqueous solutions, *J. Colloid Interface Sci.* 556 (2019) 345–351.
- [32] J.C. Eriksson, X. Zhenbo, R.-H. Yoon, Thermodynamic Properties of Water–Ethanol Films Formed between Hydrophobic Surfaces, Part I, *Colloid Journal* 81 (6) (2019) 650–661.
- [33] M. Yaacobi, A. Ben-Naim, Hydrophobic interaction in water–ethanol mixtures, *J. Solution Chem.* 2 (5) (1973) 425–443.
- [34] D.M. Huang, D. Chandler, The hydrophobic effect and the influence of solute–solvent attractions, *J. Phys. Chem. B* 106 (8) (2002) 2047–2053.
- [35] W.-Y. Chuang, T.-H. Young, D.-M. Wang, R.-L. Luo, Y.-M. Sun, Swelling behavior of hydrophobic polymers in water/ethanol mixtures, *Polymer* 41 (23) (2000) 8339–8347.
- [36] R. Halder, B. Jana, Unravelling the composition-dependent anomalies of pair hydrophobicity in water–ethanol binary mixtures, *J. Phys. Chem. B* 122 (26) (2018) 6801–6809.
- [37] L. Chai, J. Klein, Large area, molecularly smooth (0.2 nm rms) gold films for surface forces and other studies, *Langmuir* 23 (14) (2007) 7777–7783.
- [38] S.H. Donaldson Jr, S. Das, M.A. Gebbie, M. Rapp, L.C. Jones, Y. Roiter, P.H. Koenig, Y. Gizaw, J.N. Israelachvili, Asymmetric electrostatic and hydrophobic–hydrophilic interaction forces between mica surfaces and silicone polymer thin films, *ACS Nano* 7 (11) (2013) 10094–10104.
- [39] L. Gong, L. Xiang, J. Zhang, L. Han, J. Wang, X. Wang, J. Liu, B. Yan, H. Zeng, Interaction mechanisms of zwitterions with opposite dipoles in aqueous solutions, *Langmuir* 35 (7) (2019) 2842–2853.
- [40] J.L. Hutter, J. Bechhoefer, Calibration of atomic-force microscope tips, *Rev. Sci. Instrum.* 64 (7) (1993) 1868–1873.
- [41] D.Y. Chan, E. Klaseboer, R. Manica, Film drainage and coalescence between deformable drops and bubbles, *Soft Matter* 7 (6) (2011) 2235–2264.
- [42] D.Y. Chan, E. Klaseboer, R. Manica, Theory of non-equilibrium force measurements involving deformable drops and bubbles, *Adv. Colloid Interface Sci.* 165 (2) (2011) 70–90.
- [43] S. Zhang, L. Zhang, X. Lu, C. Shi, T. Tang, X. Wang, Q. Huang, H. Zeng, Adsorption kinetics of asphaltene at oil/water interface: Effects of concentration and temperature, *Fuel* 212 (2018) 387–394.
- [44] I.S. Khattab, F. Bandarkar, M.A.A. Fakhree, A. Jouyban, Density, viscosity, and surface tension of water+ ethanol mixtures from 293 to 323K, *Korean J. Chem. Eng.* 29 (6) (2012) 812–817.
- [45] J.N. Israelachvili, Intermolecular and surface forces, *Academic press* 2011.
- [46] J. Israelachvili, R. Pashley, The hydrophobic interaction is long range, decaying exponentially with distance, *Nature* 300 (5890) (1982) 341–342.
- [47] S.H. Donaldson Jr, A. Røyne, K. Kristiansen, M.V. Rapp, S. Das, M.A. Gebbie, D.W. Lee, P. Stock, M. Valtiner, J. Israelachvili, Developing a general interaction potential for hydrophobic and hydrophilic interactions, *Langmuir* 31 (7) (2015) 2051–2064.
- [48] X. Cui, J. Liu, L. Xie, J. Huang, Q. Liu, J.N. Israelachvili, H. Zeng, Modulation of Hydrophobic Interaction by Mediating Surface Nanoscale Structure and Chemistry, not Monotonically by Hydrophobicity, *Angew. Chem. Int. Ed.* 57 (37) (2018) 11903–11908.
- [49] F. Bartell, J. Smith, Alteration of surface properties of gold and silver as indicated by contact angle measurements, *J. Phys. Chem.* 57 (2) (1953) 165–172.
- [50] L. Gong, L. Xiang, J. Zhang, L. Han, J. Wang, X. Wang, J. Liu, B. Yan, H. Zeng, Interaction Mechanisms of Zwitterions with Opposite Dipoles in Aqueous Solutions, *Langmuir* (2019).
- [51] A. Tlili, A. Abdelghani, K. Aguir, M. Gillet, N. Jaffrezic-Renault, Adsorption characteristics of self-assembled thiol and dithiol layer on gold, *Mater. Sci. Eng. C* 27 (4) (2007) 620–624.
- [52] T. Ederth, Substrate and solution effects on the long-range “hydrophobic” interactions between hydrophobized gold surfaces, *J. Phys. Chem. B* 104 (41) (2000) 9704–9712.
- [53] A.K. Cheng, D.M. Soolaman, H.-Z. Yu, Evaporation of Microdroplets of Ethanol–Water Mixtures on Gold Surfaces Modified with Self-Assembled Monolayers, *J. Phys. Chem. B* 110 (23) (2006) 11267–11271.
- [54] M. Lundgren, N.L. Allan, T. Cosgrove, N. George, Wetting of water and water/ethanol droplets on a non-polar surface: A molecular dynamics study, *Langmuir* 18 (26) (2002) 10462–10466.
- [55] K. Harper, B. Minofar, M.R. Sierra-Hernandez, N.N. Casillas-Iltuarte, M. Roeselova, H.C. Allen, Surface residence and uptake of methyl chloride and methyl alcohol at the air/water interface studied by vibrational sum frequency spectroscopy and molecular dynamics, *Chem. A Eur. J.* 113 (10) (2009) 2015–2024.
- [56] G. Gao, C.V. Nguyen, C.M. Phan, Molecular arrangement between electrolyte and alcohol at the air/water interface, *J. Mol. Liq.* 242 (2017) 859–867.
- [57] S. Vafaei, D. Wen, Modification of the Young–Laplace equation and prediction of bubble interface in the presence of nanoparticles, *Adv. Colloid Interface Sci.* 225 (2015) 1–15.
- [58] H. Peng, Synthesis and application of fluorine-containing polymers with low surface energy, *Polym. Rev.* 59 (4) (2019) 739–757.
- [59] B. Cao, O. Wang, J. Cai, W. Xie, S. Liu, J. Zhao, Silicone/fluorine-functionalized flow modifier with low surface energy for improving interfaces in highly filled composites, *Compos. Sci. Technol.* 214 (2021) 108994.
- [60] C. Shi, X. Cui, L. Xie, Q. Liu, D.Y. Chan, J.N. Israelachvili, H. Zeng, Measuring forces and spatiotemporal evolution of thin water films between an air bubble and solid surfaces of different hydrophobicity, *ACS Nano* 9 (1) (2014) 95–104.

- [61] A.V. Nguyen, J. Nalaskowski, J.D. Miller, H.-J. Butt, Attraction between hydrophobic surfaces studied by atomic force microscopy, *Int. J. Miner. Process.* 72 (1–4) (2003) 215–225.
- [62] V.H. Dalvi, P.J. Rossky, Molecular origins of fluorocarbon hydrophobicity, *Proceedings of the National Academy of Sciences* 107(31) (2010) 13603–13607.
- [63] E.E. Fileti, P. Chaudhuri, S. Canuto, Relative strength of hydrogen bond interaction in alcohol–water complexes, *Chem. Phys. Lett.* 400 (4–6) (2004) 494–499.
- [64] M. Heger, T. Scharge, M.A. Suhm, From hydrogen bond donor to acceptor: the effect of ethanol fluorination on the first solvating water molecule, *PCCP* 15 (38) (2013) 16065–16073.
- [65] O. Gereben, L. Pusztai, Hydrogen bond connectivities in water–ethanol mixtures: On the influence of the H-bond definition, *J. Mol. Liq.* 220 (2016) 836–841.
- [66] Q. Du, E. Freysz, Y.R. Shen, Vibrational spectra of water molecules at quartz/water interfaces, *Phys. Rev. Lett.* 72 (2) (1994) 238.
- [67] Y.R. Shen, V. Ostroverkhov, Sum-frequency vibrational spectroscopy on water interfaces: polar orientation of water molecules at interfaces, *Chem. Rev.* 106 (4) (2006) 1140–1154.
- [68] C. Tian, Y. Shen, Structure and charging of hydrophobic material/water interfaces studied by phase-sensitive sum-frequency vibrational spectroscopy, *Proc. Natl. Acad. Sci.* 106(36) (2009) 15148–15153.
- [69] Q. Du, E. Freysz, Y.R. Shen, Surface vibrational spectroscopic studies of hydrogen bonding and hydrophobicity, *Science* 264 (5160) (1994) 826–828.
- [70] F. Despa, A. Fernández, R.S. Berry, Dielectric modulation of biological water, *Phys. Rev. Lett.* 93 (22) (2004) 228104.
- [71] J.M.P. Kanth, S. Vemparala, R. Anishetty, Long-distance correlations in molecular orientations of liquid water and shape-dependent hydrophobic force, *Phys. Rev. E* 81 (2) (2010) 021201.
- [72] M.U. Hammer, T.H. Anderson, A. Chaimovich, M.S. Shell, J. Israelachvili, The search for the hydrophobic force law, *Faraday Discuss.* 146 (2010) 299–308.
- [73] R. Pazhianur, R.-H. Yoon, Model for the origin of hydrophobic force, *Mining, Metallurgy & Exploration* 20 (4) (2003) 178–184.
- [74] L. Fritz, D. Hofmann, Molecular dynamics simulations of the transport of water–ethanol mixtures through polydimethylsiloxane membranes, *Polymer* 38 (5) (1997) 1035–1045.
- [75] M. Alheshibri, V.S. Craig, Generation of nanoparticles upon mixing ethanol and water; Nanobubbles or Not?, *J. Colloid Interface Sci.* 542 (2019) 136–143.
- [76] R. Lu, W. Gan, B.-H. Wu, Z. Zhang, Y. Guo, H.-F. Wang, C–H stretching vibrations of methyl, methylene and methine groups at the vapor/alcohol (n=1–8) interfaces, *J. Phys. Chem. B* 109 (29) (2005) 14118–14129.
- [77] S.Y. Noskov, G. Lamoureux, B. Roux, Molecular dynamics study of hydration in ethanol–water mixtures using a polarizable force field, *J. Phys. Chem. B* 109 (14) (2005) 6705–6713.
- [78] A. Oleinikova, I. Brovchenko, A. Geiger, B. Guillot, Percolation of water in aqueous solution and liquid–liquid immiscibility, *J. Chem. Phys.* 117 (7) (2002) 3296–3304.
- [79] P. Wernet, D. Nordlund, U. Bergmann, M. Cavalleri, M. Odelius, H. Ogasawara, L.-Å. Näslund, T. Hirsch, L. Ojamäe, P. Glatzel, The structure of the first coordination shell in liquid water, *Science* 304 (5673) (2004) 995–999.
- [80] Z. Li, R.-H. Yoon, Thermodynamics of solvophobic interaction between hydrophobic surfaces in ethanol, *Langmuir* 30 (44) (2014) 13312–13320.
- [81] J.N. Israelachvili, van der Waals dispersion force contribution to works of adhesion and contact angles on the basis of macroscopic theory, *J. Chem. Soc. Faraday Trans. 2: Mol. Chem. Phys.* 69 (1973) 1729–1738.
- [82] F.M. Fowkes, Determination of interfacial tensions, contact angles, and dispersion forces in surfaces by assuming additivity of intermolecular interactions in surfaces, *J. Phys. Chem.* 66(2) (1962) 382–382.
- [83] P.M. Claesson, H.K. Christenson, Very long range attractive forces between uncharged hydrocarbon and fluorocarbon surfaces in water, *J. Phys. Chem.* 92 (6) (1988) 1650–1655.
- [84] L.Y. Clasohm, I.U. Vakarelski, R.R. Dagastine, D.Y. Chan, G.W. Stevens, F. Grieser, Anomalous pH dependent stability behavior of surfactant-free nonpolar oil drops in aqueous electrolyte solutions, *Langmuir* 23 (18) (2007) 9335–9340.
- [85] R.F. Tabor, C. Wu, F. Grieser, R.R. Dagastine, D.Y. Chan, Measurement of the hydrophobic force in a soft matter system, *J. Phys. Chem. Lett.* 4 (22) (2013) 3872–3877.
- [86] E.E. Meyer, K.J. Rosenberg, J. Israelachvili, Recent progress in understanding hydrophobic interactions, *Proceedings of the National Academy of Sciences* 103(43) (2006) 15739–15746.
- [87] R. Zangi, M. Hagen, B. Berne, Effect of ions on the hydrophobic interaction between two plates, *J. Am. Chem. Soc.* 129 (15) (2007) 4678–4686.
- [88] C. Pangali, M. Rao, B. Berne, A Monte Carlo simulation of the hydrophobic interaction, *J. Chem. Phys.* 71 (7) (1979) 2975–2981.
- [89] T.M. Raschke, J. Tsai, M. Levitt, Quantification of the hydrophobic interaction by simulations of the aggregation of small hydrophobic solutes in water, *Proc. Natl. Acad. Sci.* 98(11) (2001) 5965–5969.



Full Length Article

Characterizing foulants on slotted liner and probing the surface interaction mechanisms in organic media with implication for an antifouling strategy in oil production

Lu Gong^a, Jingyi Wang^a, Li Xiang^a, Jun Huang^a, Vahidoddin Fattahpour^b, Morteza Roostaei^b, Mahdi Mamoudi^b, Brent Fermaniuk^b, Jing-Li Luo^a, Hongbo Zeng^{a,*}

^a Department of Chemical and Materials Engineering, University of Alberta, Edmonton, Alberta T6G 1H9, Canada

^b RGL Reservoir Management Inc., 3735 6908 42nd Street, Leduc, Alberta T9E 0R8, Canada

ARTICLE INFO

Keywords:

Fouling
EN coating
AFM colloidal probe
Adhesion
Asphaltenes
Adsorption

ABSTRACT

Fouling phenomena are commonly observed in oil production processes, which have caused many challenging issues. Many previous studies focused on fouling in aqueous environment. However, the characterization of foulants and underlying interaction mechanism in organic media still remain limited, which is of fundamental and practical importance. In this work, the foulants on slotted liner samples were characterized, which have served in an oil wellbore based on steam-assisted gravity drainage (SAGD) operation for about six months. The foulants were demonstrated to be fine mineral solids (e.g., silica) and organic materials (e.g., asphaltenes). Atomic force microscope (AFM) colloidal probe technique was employed to quantify the interaction forces of silica particles or asphaltenes with carbon steel (L80) substrates with or without electroless nickel-phosphorus (EN) coating in organic media. The results demonstrated that the corrosion on L80 surface could significantly enhance the adhesion with silica particles and asphaltenes, aggravating the fouling phenomena; while the EN coating could effectively eliminate the corrosion and show good antifouling property. Quartz crystal microbalance with dissipation monitoring (QCM-D) technique was applied to investigate the dynamic adsorption behaviors of asphaltenes on iron (a major component of L80) and EN coating surfaces. The QCM-D results showed that much less asphaltenes were adsorbed on EN coating than that on iron, which agrees well with the force measurements. This work provides useful insights on the fouling processes and fundamental surface interaction mechanisms of fine solids, asphaltenes and substrates in oil, with implications on developing effective antifouling strategies (e.g., functional coatings) in oil production.

1. Introduction

Fouling problem has been one of the greatest challenges in engineering and industries, especially in oil and gas industries [1–6]. The steam-assisted gravity drainage (SAGD) technique has been widely used as the environment-friendly extraction method of crude oil for decades in Alberta, Canada [7–12]. In SAGD operation, two horizontal parallel wells are drilled, and completion tools with sand control devices such as slotted liners are installed in these wells [13,14]. Stream of high temperature and high pressure is continuously pumped into the formation through the upper well to heat the crude oil and liquidize it by reducing the oil viscosity. Subsequently, the complex mixture of steam, water, crude oil, and fine solids is pumped out via the lower well. The slotted

liners with proper sizes allow the passage of the production fluids and some of the fine solids but prevent the influx of sand particles larger than the liner slots. Obviously, the efficiency of bitumen extraction using SAGD operations significantly depends on the performance of the slotted liners. The undesired foulants deposited on the liner surfaces could cause serious plugging issues [15–22]. Once the slots are plugged, the collection rate of bitumen would be lowered and the service life of slotted liners could be reduced [23–26]. Besides, cleaning foulants from the liner surfaces is technically challenging and also significantly increases the operation costs [27–29]. In other oil production processes, the detrimental fouling and plugging problems due to the deposition of various organic/inorganic foulants can also cause undesired damages to pipelines and other equipment. Therefore, investigating the fouling

* Corresponding author.

E-mail address: hongbo.zeng@ualberta.ca (H. Zeng).

<https://doi.org/10.1016/j.fuel.2020.120008>

Received 15 October 2020; Received in revised form 11 December 2020; Accepted 13 December 2020

Available online 31 December 2020

0016-2361/© 2020 Elsevier Ltd. All rights reserved.

phenomena and developing efficient anti-fouling strategies are of fundamental and practical importance. To achieve these tasks, it is rational to firstly identify the components of foulants, determine the driving forces for the attachment of foulants on surfaces, and study the dynamic adsorption processes for the following fouling development.

Carbon steel is commonly applied as the construction material in oil wellbores and pipelines due to its low price, great constructive ability, and excellent extensive property [30–35]. However, millions of tons of pipes are consumed every year around the world due to the poor resistance of carbon steel to corrosion, abrasion and fouling, especially under the conditions of high temperature and high pressure during SAGD operations [3,36]. Over the last few decades, the electroless nickel-phosphorous (EN) coating on carbon steel has caught much attention due to its excellent anti-corrosion performance, wear resistance, uniform thickness, and great hardness [37–39]. Recently, the EN coated pipe surfaces show much less fouling phenomena than those without the coating [40–42]. The previous studies investigated the fouling behaviors of asphaltenes, fine solids, oil-in-water emulsions and water-in-oil emulsions on various substrates and the antifouling performance of EN coating in aqueous solutions [40,43–46]. The results demonstrate that the attractive van der Waals (VDW) force accounts for the fouling processes, while the repulsive electric double layer (EDL) force mainly contributes to the anti-fouling behavior of EN coating. The EDL repulsion can be significantly weakened in aqueous solutions with high salinity, acid pH and presence of divalent ions.

Asphaltenes are generally defined by the solubility in organic media, which can be well dissolved in good solvents (aromatic solvents, such as toluene), but aggregate and precipitate in poor solvents (e.g., heptane) thus inducing the instability of water-in-oil emulsions and leading to aggravated fouling problems in oil production [47–51]. In organic media, with the absence of electric double layer, many of the surface interactions of fine solids, asphaltenes and various substrates have not been systematically studied and the mechanistic understanding still remains limited. Investigating the interaction and adsorption behaviors of fine solids (e.g., silica) and asphaltenes on pipe surfaces and evaluating the antifouling performance of functional coating (e.g., EN coating) can improve the fundamental understandings of the underlying mechanism of fouling and antifouling phenomena, and facilitate the development of efficient antifouling strategies.

In this work, the foulants on the surface of slotted liners, which have served in the oil wellbore of the SGAD operation for about six months, were firstly characterized using the scanning electron microscopy (SEM) and energy dispersive X-ray spectroscopy (EDS) to identify the components of the foulants and their distributions. Then, the surface interactions of silica particles or asphaltene-coated silica particles with both carbon steel L80 and EN coating surfaces in organic media were quantitatively measured using the atomic force microscope (AFM) colloidal probe technique. Toluene (good solvent of asphaltenes), heptane (poor solvent of asphaltenes) and heptol (the mixture of toluene and heptane with certain volume ratios) were used as the model organic media. The measured force profiles during both approach and retraction processes were analyzed and correlated to the fouling phenomena. Finally, the dynamic adsorption processes of asphaltenes on both iron (major component of L80 carbon steel) surface and EN coating surface were investigated using the quartz crystal micro-balance with dissipation monitoring (QCM-D) technique. Our results improve the fundamental understanding of the adsorption behaviors and interaction mechanisms of fine solids and asphaltenes on liner surface and functional coatings in organic media with useful implications for the development of antifouling approaches in oil production.

2. Materials and experimental methods

2.1. Materials

L80 carbon steel substrates (8 mm × 8 mm × 5 mm) were supplied by

RGL Reservoir Management Inc. (RGL, Canada). Asphaltenes were extracted from Athabasca bitumen by following a reported procedure [52]. Toluene (C₇H₈, 99.9%, HPLC grade, Sigma-Aldrich, Canada) and Heptane (C₇H₁₆, 99.9%, HPLC grade, Sigma-Aldrich, Canada) were used as the organic solvents in this study. Heptols were prepared by mixing toluene and heptane with the toluene volume ratios of 0.2, 0.5 and 0.8. The asphaltenes solution with the concentration of 10,000 ppm was prepared by firstly dissolving asphaltenes in pure toluene, followed by sonicating for 30 min. Then, this solution was sealed as the stock solution and stored in the refrigerator. Before the experiments, the asphaltenes solution was prepared by diluting the stock solution to desired concentrations with pure toluene and sonicating for 30 min. Silica microsphere aqueous suspension (5% solids, microsphere diameter 5 μm, Sigma-Aldrich, Canada) was used to model fine solids. Silicon wafers with 0.5 μm thermal oxide layer were purchased from NanoFAB, University of Alberta (Canada). Ethanol (99.5%, anhydrous, ACROS Organics, Canada) was used as received.

2.2. Preparation of liner substrates

The slotted liner, provided by the RGL Inc. (Canada), has been served in a SAGD wellbore of Athabasca region for at least 6 months, which is operated under the temperature of ~250 °C and the pressure of ~4 MPa [42,53]. The liner substrates were prepared from the slotted liner using the thin section technique. Briefly, the small liner pieces with fouled slots were firstly cut using a diamond saw from the slotted liner, as shown in Fig. 1. One side of a liner piece was mounted on a glass slide using the epoxy glue for protection. The other side was polished with sandpapers to make the surface smooth and appropriate for the following SEM and EDS characterizations.

2.3. Electroless nickel-phosphorus (EN) coating on L80 substrates

In this work, the L80 carbon steel was used as the substrates for EN coating. The L80 substrates were firstly washed using toluene, acetone, ethanol and DI water, and dried by pure nitrogen. Subsequently, these substrates were immersed in 10 wt% sodium hydroxide solution and heated to 70 °C for 20 min to remove possible organic contaminants. The cleaned substrates were activated by immersed in 2 wt% hydrochloric acid for 30 s and washed with DI water. The EN coating bath solution contained 25 g/L NiSO₄·6H₂O, 16 g/L NaH₂PO₂·H₂O, 40 g/L NH₄Cl, 10 g/L CH₃COONa, 15 g/L citric acid, and 20 mg/L lactic acid. The pH was adjusted to 8.5 using the ammonium hydroxyl solution and hydrochloric acid. The bath solution was heated to 80 °C and stirred at 250 rpm. The EN coating process started by immersing the activated L80 substrates in the bath solution. After 60 min, the substrates were cleaned with DI water and ethanol. The success of EN coating on L80 substrate

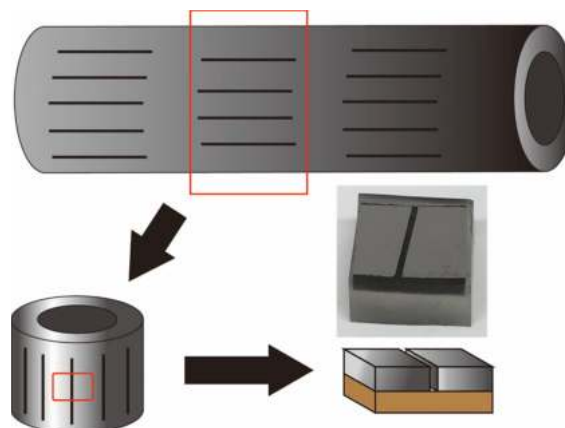


Fig. 1. Schematic of the sample preparation of liner substrates.

was confirmed by the AFM surface image, SEM image and X-ray diffraction (XRD).

2.4. Preparation of silica probe and asphaltene-coated silica probe

The silica probes were prepared before force measurements. A silica microsphere with the diameter of $\sim 5\ \mu\text{m}$ was carefully glued to the top position of the NP-O10 AFM tipless cantilever (Bruker, Santa Barbara, CA) using two-component epoxy glue (EP2LV, MasterBond). Then, the probes were placed in ambient conditions for at least 24 h. Asphaltene-coated silica probes were prepared by immersing the UV-treated silica probes in 20 ppm asphaltene-toluene solution for 2 days. Then, these probes were gently and repeatedly (at least three times) washed by pure toluene, ethanol and water for several seconds, followed by drying in pure nitrogen.

2.5. Force measurements using AFM colloidal probe technique

The interaction forces between silica probe or asphaltene-coated silica probe and L80 or EN-L80 substrate in organic media were directly and quantitatively measured using the AFM colloidal probe technique with a Dimension Icon AFM (Bruker, Santa Barbara, CA) [44,54,55]. The spring constant of the prepared probe was firstly calibrated using the Hutter and Bechhoefer method [56]. In a force measurement, both the probe and the substrate were immersed in the organic solvent with the probe placed above. This probe was driven by a piezo actuator to approach the substrate at the speed of $1\ \mu\text{m/s}$ till a

maximum loading force of 10 nN was reached, and then retract to original position, as shown in Fig. 2A. During the movement, the deflection of the cantilever was detected by the optical laser reflection system and the force was calculated using Hooke's Law. The data containing the separation and force profile between the particle and substrate was obtained from the AFM software. In the force measurement, multiple measurements (at least 50 times) have been conducted at the different locations on the substrate in the organic media and two independently prepared substrates have been tested under the same experimental condition, to ensure the repeatability and the accuracy of the adhesion results. The SEM image of a silica probe is shown in Fig. 2B. L80 substrates were polished with sandpapers just before immersed in organic solvent to avoid the effect of oxidation on L80 substrate.

2.6. Adsorption behavior of asphaltenes using QCM-D

The dynamic adsorption processes of asphaltenes on both iron and EN coating surfaces were investigated using quartz crystal microbalance with dissipation (QCM-D) monitoring technique. The iron sensor was prepared on the commercial gold sensor using the electron beam evaporation (EBE) technique. The Cr layer with the thickness of 10 nm and the Fe layer with the thickness of 90 nm were deposited on a gold sensor to prepare the iron sensor. The Cr layer was applied here to enhance the stability of iron layer on sensor surface. The EN sensor was prepared on iron sensor using the above EN coating process. Prior to QCM-D experiments, the iron or EN sensor was firstly cleaned by toluene, acetone, ethanol and DI water, and dried with pure nitrogen.

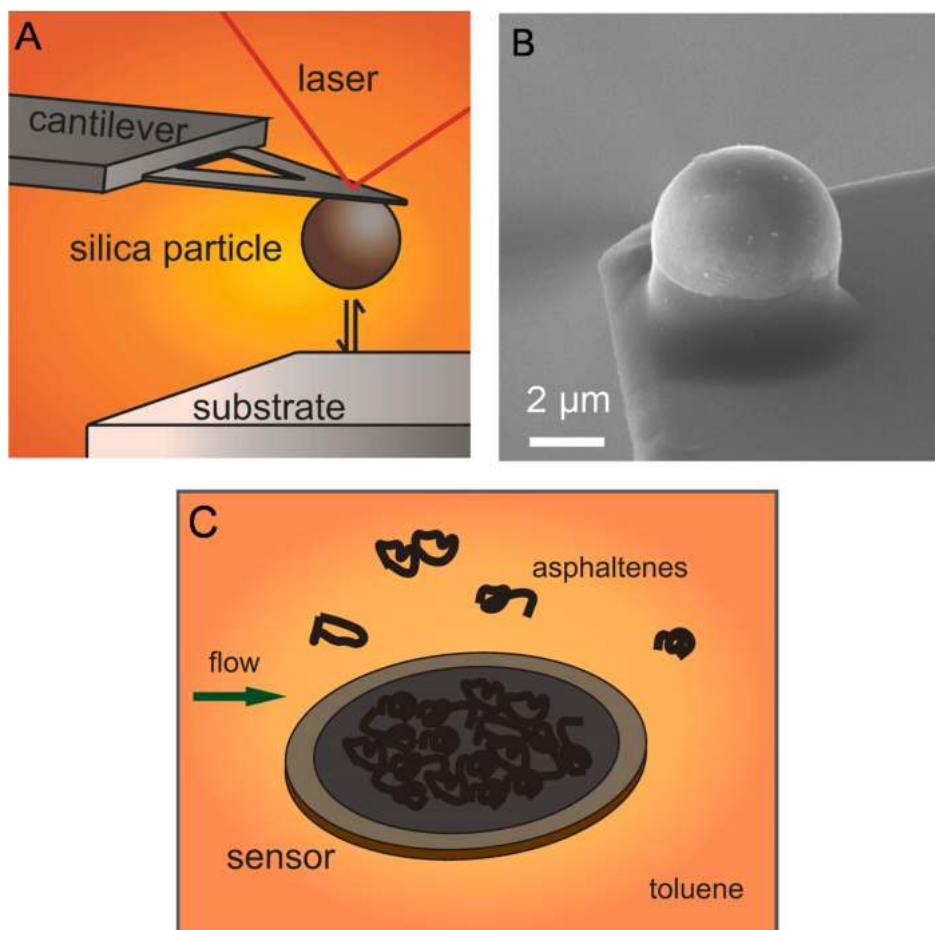


Fig. 2. (A) Schematic of the AFM colloidal probe technique to measure the surface interactions between the silica probe and a substrate in the organic medium. (B) SEM image of the prepared silica probe. The diameter was measured to be $\sim 5\ \mu\text{m}$. (C) Schematic of the QCM-D monitoring technique to investigate the dynamic adsorption process of asphaltenes on the sensor surface.

The cleaned sensor was installed in the QCM-D chamber and driven to oscillate at a series of specific frequencies by the machine. When the pure toluene was pumped in the chamber at a volume velocity of 350 $\mu\text{L}/\text{min}$, the baseline was established, where the signals of both frequency change and dissipation energy change of the sensor were defined as zero. Then, as-prepared asphaltene solution was pumped in the chamber at the volume velocity of 350 $\mu\text{L}/\text{min}$ and the adsorption of asphaltenes on sensor surface started, which resulted in the negative change in frequency signal and the positive change in dissipation energy signal. The schematic of QCM-D monitoring technique is shown in Fig. 2C. After the adsorption reached its equilibrium, pure toluene was finally pumped in the chamber to wash away the unstably adsorbed asphaltenes on sensor surface. The frequency change Δf and dissipation energy change ΔD were recorded. Since the adsorbed asphaltenes layer was quite thin and rigid, the Sauerbrey equation was used to calculate the adsorbed mass per area Δm of asphaltenes on the sensor surface, as in Eq. (1) [57].

$$\Delta m = -\frac{C}{n} \Delta f \quad (1)$$

where, C equals 17.1 $\text{ng}/(\text{Hz}\cdot\text{cm}^2)$ for a 5 MHz quartz crystal sensor, and n is the overtone number ($n = 1, 3, 5, 7, \dots$).

3. Results and discussion

3.1. Characterization of fouled liner slot

The as-prepared liner substrate containing a slot, which has been filled with foulants during oil production, has been characterized using SEM and EDS, as shown in Fig. 3.

In Fig. 3A, the SEM image shows that the slot is between the white continuous area in the top and bottom parts of the image, and has been filled with foulants, which are indicated as the black spots and non-continuous white spots. Besides, the upper and lower edges of the liner are in jagged shape, which indicates the serious damages of the liner material. This is possibly caused by the abrasion and/or corrosion during oil production. The EDS element mappings have been conducted in the chosen white rectangular box in Fig. 3A and the spatial distribution of detected elements including carbon (C), silicon (Si), oxygen (O), iron (Fe), sulfur (S), calcium (Ca), aluminum (Al), and zinc (Zn) are shown in Fig. 3B-I. Different colors have been assigned to different elements and a higher concentration of element resulted in a brighter color in these figures. It is noted that carbon element (yellow color) covers most part of the slot as in Fig. 3B, which mainly comes from the crude oil (e.g., asphaltenes). The bright yellow area is the concentrated organic materials, while the light-yellow area could be other materials with a few crude oil. Fig. 3C shows the distribution of silicon element in the slot, which represents fine solids (e.g., silica) from the ground.

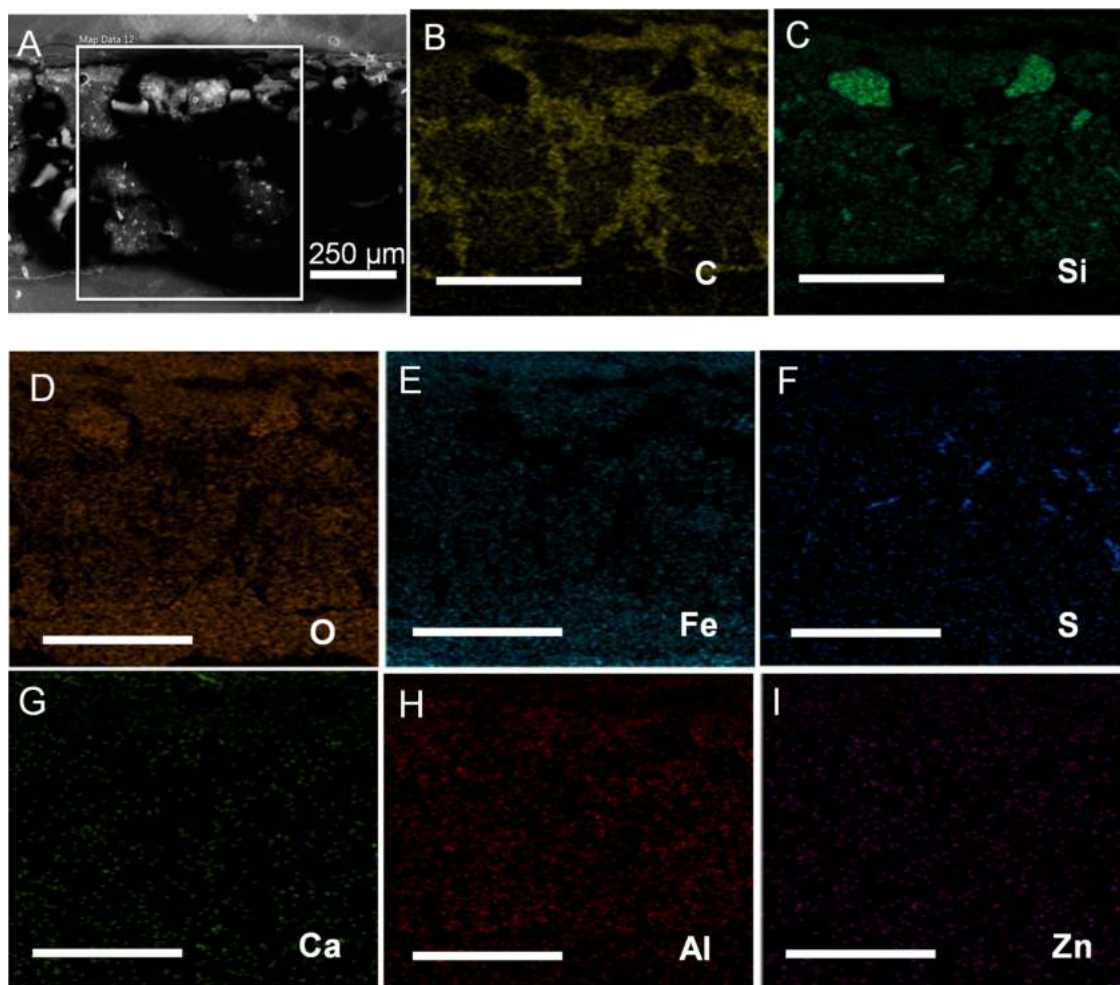


Fig. 3. (A) SEM image of the as-prepared liner substrate containing a slot with foulants. The white box in the image shows the area chosen for EDS element mapping. (B-I) EDS mapping results of the as-prepared liner substrate. The elements of carbon (C), silicon (Si), oxygen (O), iron (Fe), sulfur (S), calcium (Ca), aluminum (Al), and zinc (Zn) have been detected. The scale bar in Fig. 3B-I is 250 μm .

Similarly, the bright green area indicates the presence of silicon at high concentration, which is the bulk solids. Interestingly, the carbon and silicon mappings seem to match with each other. The high carbon content area shows low silicon concentration, while the low carbon content area exhibits high silicon concentration. This suggests that the foulants in the slot are mainly composed of crude oil and silica particles. Fig. 3D shows the presence of oxygen element. Since both crude oil and fine solids contain oxygen element, its distribution in the slot is relatively even. The iron element (Fig. 3E) is mainly from the liner material, and the sulfur element (Fig. 3F) mainly comes from the crude oil. The bright blue area in Fig. 3F indicates the distribution of concentrated sulfur, which could be the deposited asphaltene material and/or corrosion products. The calcium, alumina and zinc elements (Fig. 3G, H and I) mainly come from the fine solids.

Conclusionally, the major components of the foulants in the slotted liner are the organic materials (e.g., asphaltenes), and fine solids (e.g., silica). Hence, the silica particles and asphaltenes are used as the model foulants to investigate the fouling mechanisms in the following work. It is noted that, because of the different geological conditions and extraction techniques applied in oil production, the organic foulants could contain other crude oil components, such as naphthenates and resins [58], and the inorganic foulants could also include different mineral particles [59]. The methodologies applied in this work can be readily extended to characterize the foulants and the fouling mechanisms of other related systems in oil production.

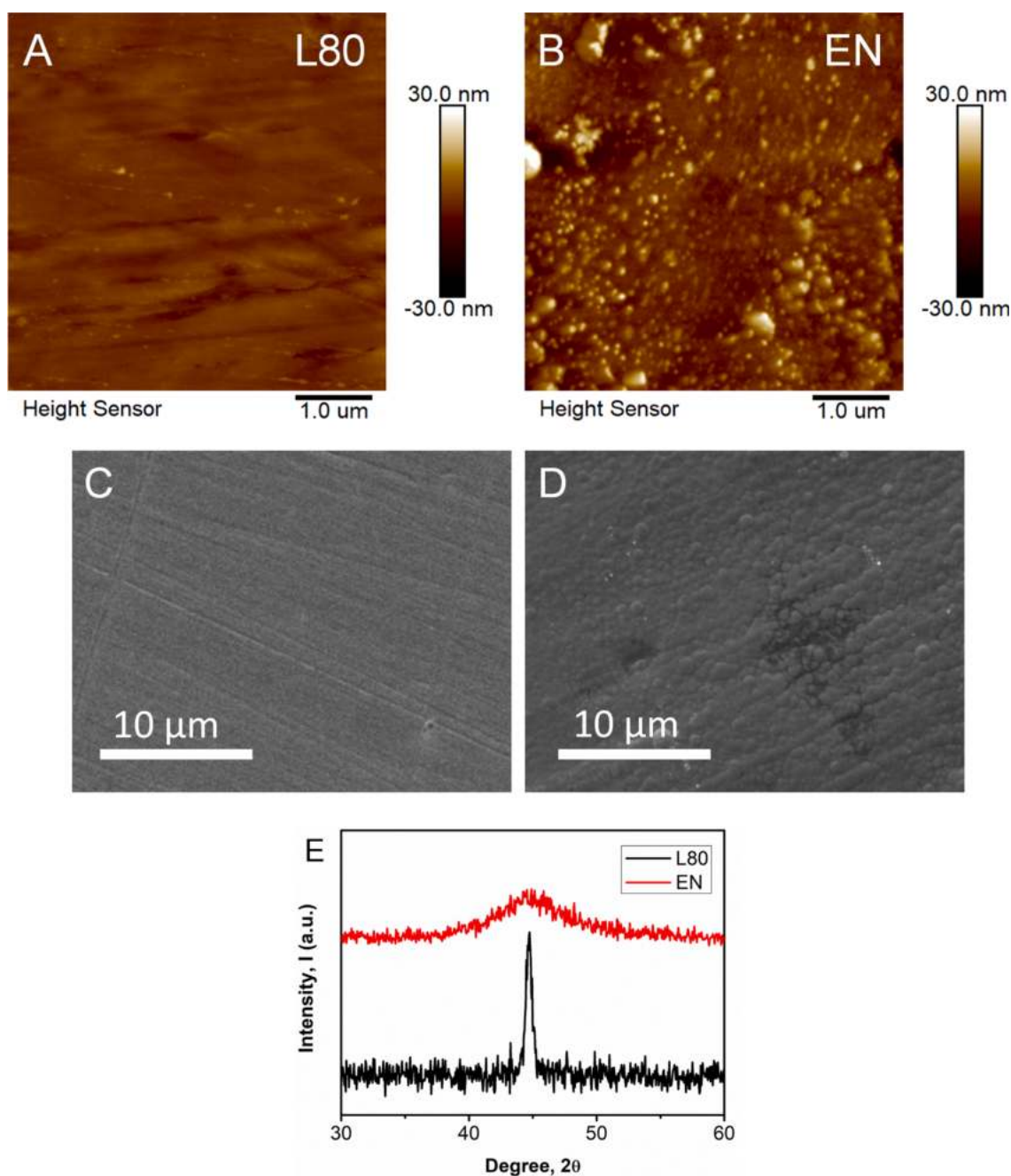


Fig. 4. The AFM surface images of (A) L80 substrate and (B) EN-L80 substrate. The SEM images of (C) L80 substrate and (D) EN-L80 substrate. (E) The XRD results of L80 and EN-L80 substrates.

3.2. Characterization of L80 and EN-L80 substrates

Fig. 4A and B show the AFM surface images of L80 and EN-L80 substrates, respectively. The L80 surface after polishing is quite smooth with a root-mean-square (RMS) roughness of 1.71 nm. However, the EN-L80 substrate shows a much rougher surface (RMS 5.06 nm) containing nodules with the sizes ranging from several nanometers to several hundred nanometers. Fig. 4C and D show the SEM images of L80 and EN-L80 substrates. The L80 substrate is very smooth with a few scratches on the surface, which could be originated from the polishing process. The EN-L80 substrate has a large number of aggregates on the surface, which confirms the successful deposition of nickel and phosphorus. Fig. 4E shows the XRD results of L80 and EN-L80 substrates. The diffraction peak at 45° indicates the crystal structure of carbon steel L80, while the broadened diffraction peak at $40\text{--}50^\circ$ indicates the amorphous matrix of EN coating.

3.3. Surface interactions of silica probe and L80 or EN-L80 substrate

The interaction forces between silica probe and L80 or EN-L80 substrate in toluene, heptane and heptols have been quantified using the AFM colloidal probe technique. The measured force profiles during approach are shown in Fig. 5. All the force profiles have been normalized by the radius of the silica probe.

Before force measurements with L80 and EN-L80 substrates, silica probe was firstly applied to interact with clean silica substrate in toluene, heptane and heptols (ω is the volume ratio of toluene, $\omega = 0.2, 0.5$, or 0.8), as shown in Fig. 5A. All the force curves during approaching show strong attraction when the separation distance becomes less than 10 nm, which is due to the dominant van der Waals (VDW) attraction

between the silica probe and silica substrate in these organic media [60]. It is noted that the attraction in toluene is much weaker than that in heptane, which suggests that the VDW force between the silica probe and silica substrate in toluene is weaker than that in heptane. Decreasing ω , the volume ratio of toluene in heptol, leads to the enhanced attraction between silica probe and silica substrate, indicating the strengthened VDW force.

The measured interaction forces can be analyzed by the theoretical model. Here, the VDW force F_{vdw} is calculated using the following Eq. (2) [60].

$$\frac{F_{vdw}}{R} = -\frac{A_H}{6D^2} \quad (2)$$

where A_H is the Hamaker constant for the silica probe and the silica substrate interacting in organic medium, R is the radius of spherical silica probe ($\sim 2.5 \mu\text{m}$), and D is the separation distance. The Hamaker constant can be calculated using the combining relation, as shown in Eq. (3) [60].

$$A_{132} = \left(\sqrt{A_{11}} - \sqrt{A_{33}} \right) \left(\sqrt{A_{22}} - \sqrt{A_{33}} \right) \quad (3)$$

where A_{132} is the Hamaker constant between probe 1 and substrate 2 in medium 3, and A_{11} , A_{22} , and A_{33} are the Hamaker constants of probe 1, substrate 2 and medium 3, respectively. In literatures, the Hamaker constant of silica is $6.6 \times 10^{-20} \text{ J}$ [60,61]. The Hamaker constants of toluene and heptane are calculated to be $5.4 \times 10^{-20} \text{ J}$ and $4.5 \times 10^{-20} \text{ J}$ with their dielectric constant and refractive index using the Lifshitz theory [62,63]. Therefore, the Hamaker constants between silica probe and silica substrate in toluene and heptane are calculated to be $0.6 \times 10^{-21} \text{ J}$ and $2.0 \times 10^{-21} \text{ J}$, respectively. The theoretical force curves are

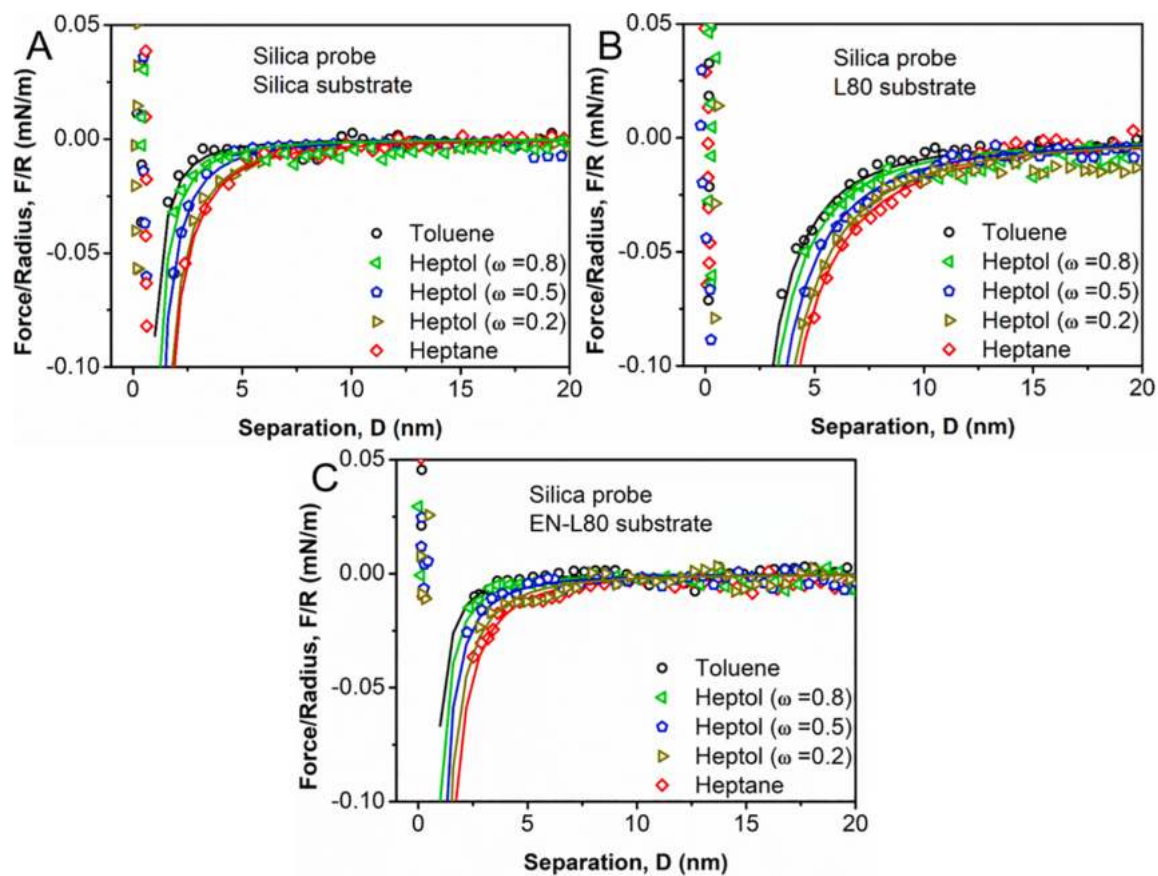


Fig. 5. Measured force profiles during approach of silica probes with (A) silica substrate, (B) L80 substrate and (C) EN-L80 substrate in toluene, heptane and heptols (ω is the volume ratio of toluene, $\omega = 0.2, 0.5$, or 0.8). Solid line curves are the theoretical force curves.

plotted as the red lines in Fig. 5A. The experimental data and the theoretical lines agree well with each other, which confirms the validation of the model. This theoretical model has also been applied to fit the measured force profiles in heptols and the correlated Hamaker constants of heptols with ω of 0.2, 0.5 and 0.8 could be calculated as 4.7×10^{-20} J, 4.9×10^{-20} J, and 5.2×10^{-20} J, respectively. These values will be used in following work.

The interaction forces of silica probe with L80 and EN-L80 were also measured in toluene, heptane and heptols, which are shown in Fig. 5B and C. The attractive VDW force dominates the surface interactions when the silica probe approaches the L80 or EN-L80 substrate. Similarly, increasing the toluene volume ratio in the organic media results in the weakened attraction between the silica probe and L80 or EN-L80 substrate. Comparing the force profiles in Fig. 5B and C, the attractive VDW forces measured with L80 substrate are much stronger than with EN-L80 substrate in the same medium. The force profiles have also been theoretically analyzed and the fitting curves are shown as the red lines in Fig. 5B and C. The Hamaker constants of L80 and EN-L80 substrates are calculated to be 20.0×10^{-20} J and 6.0×10^{-20} J, respectively, which are within the reported value range [43,44,60,61]. As the attractive VDW force is the major driving force for silica particles approaching substrate surface, the much smaller Hamaker constant of EN coating indicates the significantly lower possibility for the attachment of silica particles on the surface.

3.4. Surface interactions of asphaltene-coated silica probe and L80 or EN-L80 substrate

The surface interactions between the asphaltene-coated silica probe

and L80 or EN-L80 substrate during approaching in toluene, heptane and heptols ($\omega = 0.2, 0.5$, or 0.8) were measured, as in Fig. 6.

Similarly, asphaltene-coated silica probe has been firstly applied to interact with a clean silica substrate in toluene, heptane and heptols, as in Fig. 6A. It is noted that the interaction forces are repulsive in toluene and heptols ($\omega = 0.5$ and 0.8) when the separation distance is less than 10 nm. The forces are growing stronger while the asphaltene-coated probe is brought closer to the silica substrate. In heptol ($\omega = 0.2$) and heptane, the obtained force curves show a weak attraction when the separation is less than 7 nm. However, when the separation distance is less than 2 nm, the forces rapidly become repulsive, which is due to the structural repulsion between the rigid surfaces of the probe and the substrate [60,64]. Hence, decreasing the toluene content in organic solvent leads to the interaction force change from strong repulsion to weak attraction. This result is quite different from the force result in Fig. 5A. It has been reported that in a good solvent (e.g., toluene), asphaltenes adsorbed on the substrate surface could partially stretch into the bulk solvent with some functional groups anchoring at the substrate surface, which is very similar to polymer brushes [65–68]. These asphaltene “brushes” could prevent the approach and contact of other surface (e.g., silica surface) via the steric repulsion. As the solvent becomes poor (e.g., heptol), the adsorbed asphaltenes tend to aggregate on substrate surface. The steric repulsion originated from the stretched asphaltene “brushes” would be gradually weakened. In poor solvent (e.g., heptane), the aggregation of the adsorbed asphaltenes is so significant that the steric repulsion could be negligible. Thus, the attractive VDW force dominates in heptane, and the measured force curve turns to weak attraction. In this work, the steric repulsion F_{ste} can be calculated using Eq. (4) [69].

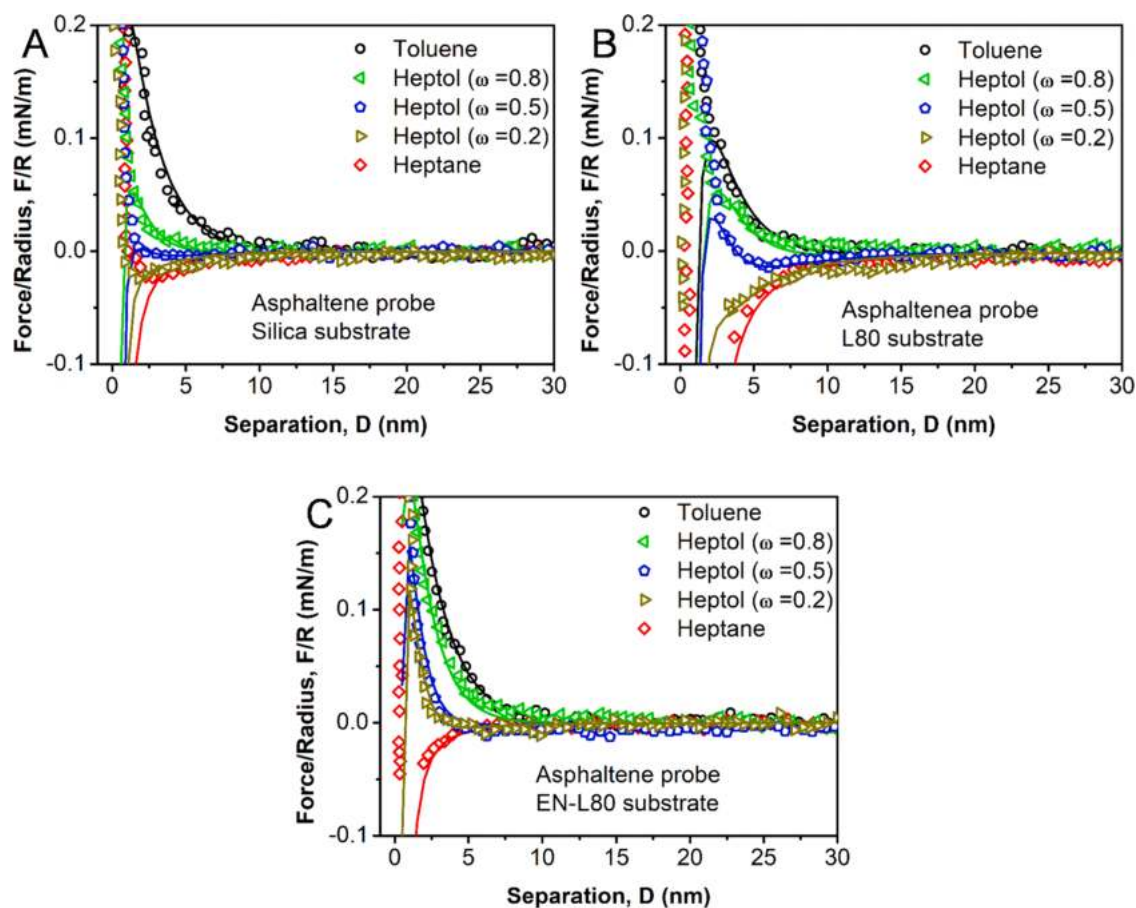


Fig. 6. Measured force profiles during approach of asphaltene-coated silica probes with (A) silica substrate, (B) L80 substrate and (C) EN-L80 substrate in toluene, heptane and heptols ($\omega = 0.2, 0.5$, or 0.8).

$$\frac{F_{ste}}{R} = 50 \frac{k_B T L_0}{s^3} \exp\left(-2\pi \frac{D}{L_0}\right) \quad (4)$$

where k_B is the Boltzmann constant, T is the temperature, L_0 is the characteristic length of adsorbed asphaltene “brushes” on the surface, and s is the average distance between two adsorbed asphaltene “brushes”. Since there is only a very thin layer of asphaltenes adsorbed on the silica probe, the attractive VDW force could be treated as the same between silica probe and silica substrate at relatively large separation [60,70]. The characteristic length L_0 and the average grafting distance s of asphaltenes adsorbed on silica surface in different organic media can be fitted and the results are listed in Table 1. These values are in consistence with the reported values [63,67]. It is noted that asphaltenes have the longest characteristic length L_0 in toluene since toluene is a good solvent. In heptols, decreasing the toluene content makes the solvent worse to asphaltenes, thus leading to the decreasing characteristic length L_0 of asphaltene “brushes”. Therefore, the steric repulsion gradually becomes weakened. In poor solvent (i.e., heptane), the steric repulsion can be ignored since asphaltenes are so significantly aggregated. The schematic of characteristic length L_0 of asphaltenes adsorbed on silica surface in toluene, heptane and heptols is shown in Fig. 7.

The force measurements between asphaltene-coated silica probes and L80 or EN-L80 substrates in toluene, heptane and heptols were also conducted as in Fig. 6B and C. It can be noted that in the case of L80 substrate (Fig. 6B), the force profile is repulsive in toluene and heptols ($\omega = 0.5$ and 0.8) and attractive in heptol ($\omega = 0.2$) and heptane, when the separation distance is less than 10 nm. In the case of EN-L80 substrate (Fig. 6C), the measured force is repulsive in toluene and heptols ($\omega = 0.2, 0.5$ and 0.8), and turns to be attractive in heptane. These results indicate that both VDW attraction and steric repulsion contribute to the surface interaction between L80 or EN-L80 substrate and asphaltene-coated silica particle, and the steric repulsion becomes strengthened as the toluene content in organic solvent increases. Meanwhile, the force curve between asphaltene-coated silica particle and L80 substrate is more attractive than that between asphaltene-coated silica particle and EN-L80 substrate in the same medium due to the much greater VDW attraction, suggesting less possibility for the asphaltenes approaching and attaching on the substrate surface in organic media (e.g., toluene, heptane and heptols).

3.5. Adhesion between silica or asphaltene-coated silica particle and L80 or EN-L80 substrate

The adhesion between silica or asphaltene-coated silica particle and L80 or EN-L80 substrate in toluene, heptols and heptane has also been recorded in the force measurements during retraction. The normalized adhesion is shown in Fig. 8. It is noted that the adhesion between silica particle and L80 or EN-L80 substrate becomes stronger as the toluene content in the organic medium decreases, which is attributed to the enhanced VDW attraction. The adhesion between asphaltene-coated silica particle and L80 or EN substrate is stronger than that of silica particles. When the toluene content in the organic medium decreases, the reduced steric repulsion and the enhanced VDW attraction can result in the strengthened adhesion between asphaltenes and substrates.

Table 1

The fitted characteristic length L_0 and average grafting distance s of asphaltenes “brushes” on silica surface in toluene, heptane and heptols.

Solvent	L_0 /nm	s /nm
Toluene	6.5	23
Heptol ($\omega = 0.8$)	4.5	21
Heptol ($\omega = 0.5$)	3.0	20
Heptol ($\omega = 0.2$)	2.5	19
Heptane	–	–

During the force measurements, the actual contact of asphaltenes and substrate surface could lead to the formation of the short-ranged interactions including hydrogen bond, acid/base interaction, and so on [44,65,67]. These short-ranged interactions combined with VDW attraction contribute to the measured adhesion between asphaltenes and substrate surfaces (i.e., L80 and EN surface). It is noticed that the measured adhesion F_{ad} for all the cases is unexpectedly very weak ($F_{ad}/R < 0.005$ mN/m), especially for the cases of L80 substrates. This seems to be contrary to the occurrence of serious fouling phenomena in oil industries. Here, this weak adhesion could be the consequence of the polishing treatment of L80 substrates before each force measurement, which erases the corrosion products from the surfaces. Corrosion products, such as oxides and sulfides of metals on liner surface could change the physical and chemical properties of the surface and provide numerous interaction sites for the development of fouling layers. In practical oil production, the corrosion of liner surface is inevitable, especially under extreme conditions (e.g., in SAGD operations). The presence of salinity, O_2 , CO_2 , and H_2S could significantly promote the corrosive reaction and cause damages to liner material [71]. The corrosion phenomena have also been detected by the EDS element mapping results of liner substrate in Fig. 3.

Herein, AFM force measurements between the silica or asphaltene-coated silica probe and L80 substrates at corroded and uncorroded area have been conducted accordingly to demonstrate the influence of corrosion. A newly polished L80 substrate was immersed in 100 mM NaCl solution for 6 h at ambient conditions and the corrosion on this L80 substrate was observed from the optical image shown in Fig. 9A. The black areas on the surface are the corrosion products. Two positions highlighted by the red circles have been chosen for the force measurements. The Position I is the corroded area, while the Position II is the uncorroded area. The measured force profiles with the silica probe or asphaltene-coated silica probe at Position I and Position II in toluene are shown in Fig. 9B–E.

In Fig. 9B and C, the strong adhesion has been measured between silica probe or asphaltene-coated silica probe and corroded L80 substrate in toluene, which is ~ 2.3 mN/m for silica probe and ~ 3.5 mN/m for asphaltene-coated silica probe, respectively. However, in the force curves on uncorroded L80 substrate, the measured force curves exhibit extremely low adhesion ($F_{ad}/R < 0.005$ mN/m), which agrees with the previous results. This results demonstrate that the corrosion products on L80 substrate could significantly enhance the adhesion between silica particle or asphaltene-coated silica particle and L80 substrate in organic media (e.g., toluene), hence leading to serious fouling phenomena. In literatures, iron oxides and sulfides due to the corrosive reaction could introduce the oxygen and sulfur atoms to iron surface, which could create strong attraction (e.g., hydrogen bonding and acid-base interaction) with silica particles or asphaltenes [72–74]. This result suggests that preventing the occurrence of corrosion on steel surface can effectively inhibit the fouling phenomena. In turn, the measured strong adhesion between the foulants and the steel surface could also indicate the occurrence of corrosion on the steel surface. Hence, determining the fouling phenomena via surface force measurements could be an alternative method to understand the corrosion processes of the steel surface, such as the influence of deposited asphaltenes and the corrosion inhibitors in the corrosion processes of the steel surface.

In Fig. 8, the adhesion of the silica or asphaltene-coated silica probe with L80 substrate is stronger than that with EN-L80 substrate, which suggests that silica particles and asphaltenes may be more difficult to be removed or cleaned from L80 surface than from EN coating surface. Previous work has reported that the larger surface roughness can lead to the enhanced fouling phenomena due to the relatively larger contact area and higher contacting possibility of foulants on the surface [75,76]. However, the EN coating surface, even though having a rougher surface (RMS roughness 5.06 nm) than the L80 substrate (RMS roughness 1.71 nm), still shows the relatively weaker adhesion with the foulants (e.g., silica particles and asphaltenes). The nonmetal phosphorus atoms in the

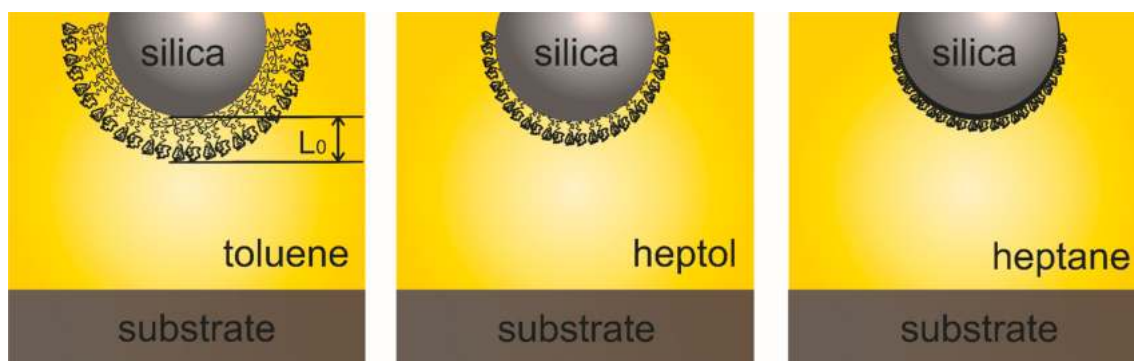


Fig. 7. Schematic of characteristic length L_0 change of asphaltenes on silica surface in toluene (left), heptols (middle) and heptane (right).

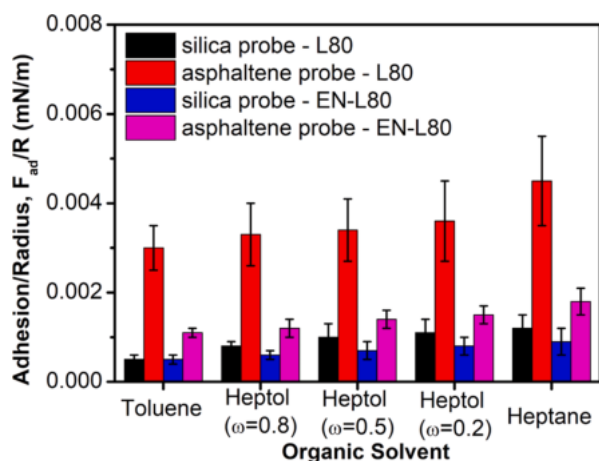


Fig. 8. Normalized adhesion between silica or asphaltene-coated silica probe and L80 or EN-L80 substrate in toluene, heptols and heptane.

EN coating could give rise to the amorphous structure of the coating, leading to the lower surface energy, while the metal nickel atoms have less chemical reactivity than iron atoms, endowing the surface with the anti-corrosion property, which subsequently limits the foulant adhesion [77,78]. Therefore, the EN coating shows the great antifouling property.

3.6. Dynamic adsorption behaviors of asphaltenes on iron and EN coating surface

The above force measurements have elucidated the surface interaction mechanisms of fouling phenomena of silica particles and asphaltenes on L80 surface and EN coating surface in organic media. After the first layer of foulants is deposited on the substrate surface, the continuous adsorption process of asphaltenes and solids would finally lead to the serious fouling phenomena. Hence, the quartz crystal microbalance with dissipation (QCM-D) monitoring technique has been applied to study the dynamic adsorption behaviors of asphaltenes on iron (major component of L80) and EN coating surfaces. The adsorption results of frequency change Δf and dissipation energy change ΔD are shown in Fig. 10.

Fig. 10A shows the dynamic adsorption process of 10 ppm asphaltene-toluene solution on iron surface. The frequency curve drops to negative when the asphaltenes solution is pumped to flow on the iron sensor surface, which suggests the adsorption of asphaltenes on iron surface. Even though the steric repulsion between asphaltenes and the substrate surface in toluene prevents the attachment of asphaltenes on sensor surface, the VDW attraction, hydrodynamic interaction by the flowing fluid and thermal motion of asphaltenes can overcome this repulsion and lead to the contact of asphaltenes on sensor surface. Once

the contact occurs, the adhesion between asphaltenes and sensor surface, contributed by interactions such as VDW, hydrogen bonding, and acid/base interaction [44,65,67], will prevent the detachment of asphaltenes from sensor surface, hence resulting in the observed adsorption behavior. The more the frequency curve drops, the more the asphaltenes are adsorbed on iron surface. Meanwhile, the dissipation energy curve becomes positive and increases as asphaltenes are adsorbed on iron surface. This is due to the fact that asphaltenes are relatively soft and the oscillation energy generated by QCM-D machine could be dissipated. After about 1200 s, both frequency curve and energy dissipation curve tend to be linear with only a little variation, suggesting that the adsorption process has reached its equilibrium, where the iron surface has almost been fully covered by asphaltenes and there are still limited asphaltenes continuously adsorbed on the surface at a very slow rate. This continuous adsorption is caused by the interactions between asphaltenes, such as VDW interactions, hydrogen bindings, and π - π interactions [79]. Then, pure toluene is used to replace the asphaltene solution. A very small increase of frequency curve and a decrease of energy dissipation curve have been observed, which indicates that only limited unstable asphaltenes are washed away. In Fig. 10B and C, the concentration of asphaltene solution has been increased to 100 and 500 ppm, respectively. Similar changes of frequency and energy dissipation curves have been observed. However, the frequency curve drops faster and the energy dissipation curve increases more rapidly in higher asphaltene concentration, indicating the quicker rate of asphaltenes adsorption. Besides, increasing asphaltene concentration also leads to a more negative value of frequency curve and a limited increase of energy dissipation curve at the equilibrium, suggesting more asphaltenes can be adsorbed on the iron surface. When introducing pure toluene, the frequency curve increases and energy dissipation curve decreases, indicating that the unstable asphaltenes are washed away. Moreover, the dynamic adsorption processes of asphaltenes on EN coating surfaces have also been investigated and the results are shown in Fig. 10D, E, and F. Similar adsorption process and trend of frequency curve and energy dissipation curve have been observed.

It is noted that the frequency change at the equilibrium on iron sensor is -35 Hz, -46 Hz, and -48 Hz for the asphaltene concentrations of 10, 100, and 500 ppm, respectively, while the frequency change on EN sensor is -18 Hz, -25 Hz, and -29 Hz, respectively. This suggests that more asphaltenes could be adsorbed on iron surface than on EN coating surface. Using the Sauerbrey equation [57,80–82], the adsorbed mass per area of asphaltenes on both iron and EN coating surface has been calculated and shown in Fig. 10G. It is noted that more asphaltenes could be adsorbed on the surface when the bulk concentration increases, and much less asphaltenes are adsorbed on EN coating surface than on iron surface, which is attributed to much weaker adhesion between asphaltenes and EN coating than that between asphaltenes and iron surface in toluene.

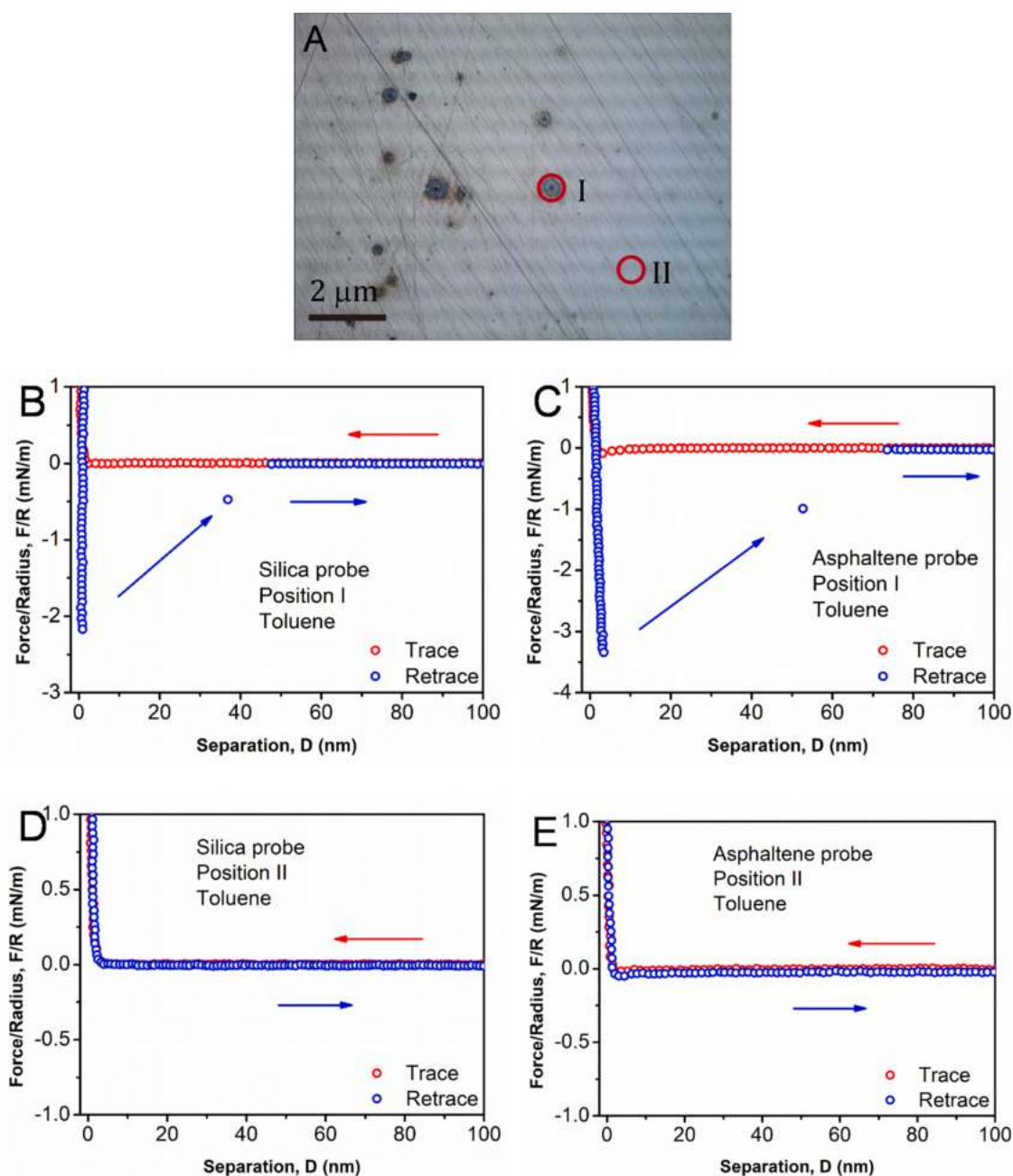


Fig. 9. (A) Optical image of a polished L80 substrate after immersed in 100 mM NaCl solution for 12 h. The red-circle Position I is the corroded area, while the red-circle Position II is the uncorroded area. (B-C) Measured force profiles with (B) silica probe and (C) asphaltene-coated silica probe at Position I in toluene. (D-E) Measured force profiles with (D) silica probe and (E) asphaltene-coated silica probe at Position II in toluene. (For interpretation of the references to color in this figure legend, the reader is referred to the web version of this article.)

4. Conclusions

In this work, the foulants on slotted liners, which have served in an oil wellbore for six months, have been characterized using SEM and EDS. The results show that the fine solids (e.g., silica) and organic materials (e.g., asphaltenes) are the major components of the foulants in the slot. The fouling mechanism of silica particles and asphaltenes on L80 and the antifouling property of EN-L80 substrates in organic media (e.g., toluene, heptane and heptols) have been investigated using the AFM colloidal probe technique. The measured force profiles show that in the case of silica particles, the attractive VDW force dominates the surface interactions and contributes to the attachment of silica particles on L80 and EN-L80. In the case of asphaltene-coated silica particles, both

attractive VDW force and repulsive steric force contribute to the surface interactions. In a good solvent (i.e., toluene), adsorbed asphaltenes would extend to the bulk solvent, hence leading to the strong steric repulsion between asphaltene-coated silica particle and substrate surface. The steric repulsion becomes weaker when the toluene content in organic medium decreases. In a poor solvent (i.e., heptane), the significant aggregation of adsorbed asphaltenes accounts for the much weakened steric repulsion. The force measurements also demonstrate that the corrosion on L80 substrate surfaces could significantly aggravate the adhesion with silica particles and asphaltene particles, leading to the fouling phenomena. In contrast, the EN coating can effectively enhance the corrosion resistance of substrate surface, thus preventing the attachment of foulants on the surface. The dynamic adsorption of

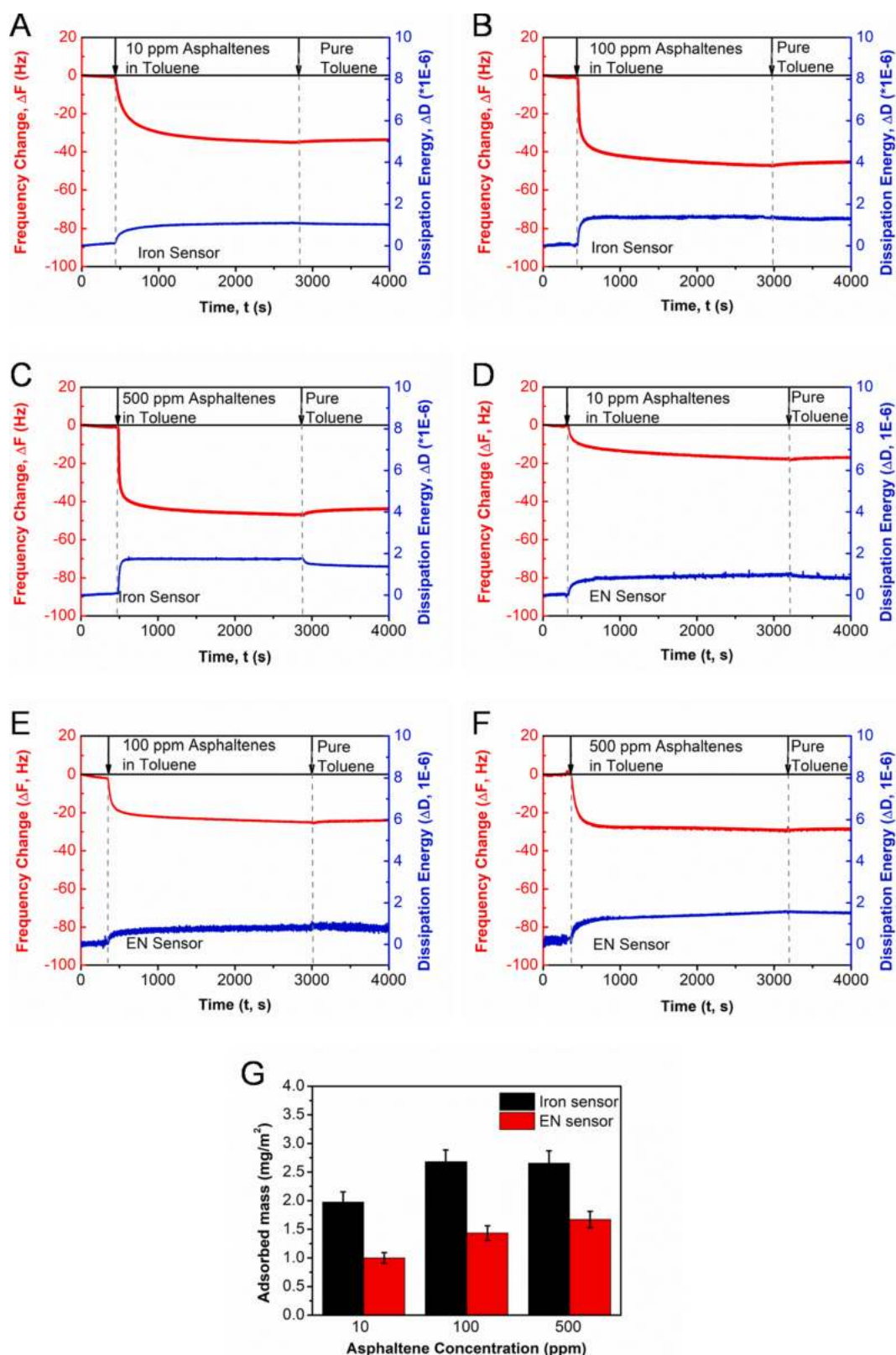


Fig. 10. QCM-D response, i.e., changes in frequency Δf and dissipation energy ΔD for the adsorption of asphaltenes on (A-C) iron and (D-F) EN coating surfaces in toluene. The asphaltene concentration is 10, 100, and 500 ppm. (G) The calculated mass per area of asphaltenes adsorbed on iron and EN coating surfaces.

asphaltenes on both iron and EN coating surface has also been studied using the QCM-D technique. The higher asphaltene concentration in the bulk could result in more and faster adsorption of asphaltenes on the surface. Less asphaltenes have been detected on EN coating surface than

on iron surface. These results demonstrate that the EN coating possesses good anti-fouling property in oil media. Our work sheds useful insights into the fundamental understanding of fouling phenomena of fine solids and asphaltenes in organic media and associated surface interaction

mechanisms, with implications on the development of efficient anti-fouling strategies (e.g., functional coatings) in oil and gas industries.

Declaration of Competing Interest

The authors declare that they have no known competing financial interests or personal relationships that could have appeared to influence the work reported in this paper.

Acknowledgement

The authors are grateful to the finance support from the Natural Sciences and Engineering Research Council of Canada (NSERC), RGL Reservoir Management Inc. (RGL), Canada Foundation for Innovation (CFI), and the Canada Research Chairs Program (H. Zeng).

References

- [1] Kotlyar L, Sparks B, Woods J, Chung K. Solids associated with the asphaltene fraction of oil sands bitumen. *Energy Fuels* 1999;13:346–50.
- [2] Qiao P, Harbottle D, Tchoukov P, Masliyah J, Sjoblom J, Liu Q, et al. Fractionation of asphaltenes in understanding their role in petroleum emulsion stability and fouling. *Energy Fuels* 2017;31:3330–7.
- [3] Pugsley T, Pernitsky D, Grundler J, Johnsen E. Fouling of heat transfer surfaces in a steam assisted gravity drainage (SAGD) in situ facility for the recovery of oil sands bitumen. *International Conference on Heat Exchanger Fouling and Cleaning*. 2013.
- [4] Watkinson AP. Deposition from crude oils in heat exchangers. *Heat Transfer Eng* 2007;28:177–84.
- [5] Zhao M, Song X, Zhou D, Lv W, Dai C, Yang Q, et al. Study on the reducing injection pressure regulation of hydrophobic carbon nanoparticles. *Langmuir* 2020;36:3989–96.
- [6] Zeng H, Tessoro N, Gonzalez D, Gramin P, Wicking C, Pietrobon M. “Sticky molecules” on rock surface might play an important role in formation damage due to asphaltene deposition. *Fuel* 2020;277:117983.
- [7] Edmunds N, Gittins SD. Effective application of steam assisted gravity drainage of bitumen to long horizontal well pairs. *J Can Pet Technol* 1993;32:49–55.
- [8] Hamm R, Ong T. Enhanced steam-assisted gravity drainage: a new horizontal well recovery process for peace river, Canada. *J Can Pet Technol* 1995;34.
- [9] Edmunds N, Kovalsky J, Gittins S, Pennacchioli E. Review of phase A steam-assisted gravity-drainage test. *SPE Reservoir Eng* 1994;9:119–24.
- [10] Gates I, Chakrabarty N. Optimization of steam-assisted gravity drainage in McMurray reservoir. *Canadian International Petroleum Conference*, Petroleum Society of Canada. 2005.
- [11] Nasr T, Law D, Beaulieu G, Golbeck H, Korpany G, Good W. SAGD application in gas cap and top water oil reservoirs. *J Can Pet Technol* 2003;42.
- [12] Giesy JP, Anderson JC, Wiseman SB. Alberta oil sands development. *Proc Natl Acad Sci* 2010;107:951–2.
- [13] Tan T, Butterworth E, Yang P. Application of a thermal simulator with fully coupled discretized wellbore simulation to SAGD. *J Can Pet Technol* 2002;41:25–30.
- [14] Stone TW, Brown G, Guyaguler B, Bailey WJ, Law DH. Practical control of SAGD wells with dual-tubing strings. *J Can Pet Technol* 2014;53:32–47.
- [15] Bott T. General fouling problems. In: *Fouling Science and Technology*. Springer; 1988. p. 3–14.
- [16] Allen EW. Process water treatment in Canada’s oil sands industry: II. A review of emerging technologies. *J Environ Eng Sci* 2008;7:499–524.
- [17] Bennett CA, Appleyard S, Gough M, Hohmann RP, Joshi HM, King DC, et al. Industry-recommended procedures for experimental crude oil preheat fouling research. *Heat Transfer Eng* 2006;27:28–35.
- [18] Zhu X, Tu W, Wee K-H, Bai R. Effective and low fouling oil/water separation by a novel hollow fiber membrane with both hydrophilic and oleophobic surface properties. *J Membr Sci* 2014;466:36–44.
- [19] Coletti F, Macchietto S. A dynamic, distributed model of shell-and-tube heat exchangers undergoing crude oil fouling. *Ind Eng Chem Res* 2011;50:4515–33.
- [20] Bennett CA, Kistler RS, Nangia K, Al-Ghawas W, Al-Hajji N, Al-Jemaz A. Observation of an isokinetic temperature and compensation effect for high-temperature crude oil fouling. *Heat Transfer Eng* 2009;30:794–804.
- [21] Dong S, Kim E-S, Alpatova A, Noguchi H, Liu Y, El-Din MG. Treatment of oil sands process-affected water by submerged ceramic membrane microfiltration system. *Sep Purif Technol* 2014;138:198–209.
- [22] Lightbown V. New SAGD technologies show promise in reducing environmental impact of oil sand production. *J Environ Solutions Oil Gas Min* 2015;1:47–58.
- [23] N. Board, Canada’s Oil Sands Opportunities and Challenges to 2015: An Update, An Energy Market Assessment, (2006).
- [24] Giacchetta G, Leporini M, Marchetti B. Economic and environmental analysis of a Steam Assisted Gravity Drainage (SAGD) facility for oil recovery from Canadian oil sands. *Appl Energy* 2015;142:1–9.
- [25] Butler R, McNab G, Lo H. Theoretical studies on the gravity drainage of heavy oil during in-situ steam heating. *Can J Chem Eng* 1981;59:455–60.
- [26] Howard P. Economic impacts of the petroleum industry in Canada, CERi, 2009.
- [27] Speight JG. Fouling in refineries. Gulf Professional Publishing; 2015.
- [28] Müller-Steinhagen H, Malayeri M, Watkinson A. Recent advances in heat exchanger fouling research, mitigation, and cleaning techniques. Taylor & Francis; 2007.
- [29] Costa ALH, Tavares VBG, Borges JL, Queiroz EM, Pessoa FLP, Liporace FdS, de Oliveira SG. Parameter estimation of fouling models in crude preheat trains. *Heat Transfer Eng* 2013;34:683–91.
- [30] Ogundele G, White W. Some observations on corrosion of carbon steel in aqueous environments containing carbon dioxide. *Corrosion* 1986;42:71–8.
- [31] Ogundele G, White W. Observations on the influences of dissolved hydrocarbon gases and variable water chemistries on corrosion of an API-L80 steel. *Corrosion* 1987;43:665–73.
- [32] Al-Hashem AH, Carew JA, Al-Sayegh A. The Effect of Water-Cut on the Corrosion Behavior of L80 Carbon Steel Under Downhole Conditions. *CORROSION* 2000. NACE International; 2000.
- [33] Choi HJ, Warnken D, Al Beheiri FI, Al-Bannai NS. Field Corrosion Assessment of L80 Carbon Steel Downhole Production Tubing at Khuff Gas Wells. *CORROSION* 2006. NACE International; 2006.
- [34] Sun W, Pugh D, Ling S, Reddy R, Pacheco J, Nisbet R, Nor N, Kersey M, Morshidi L. Understanding and quantifying corrosion of L80 carbon steel in sour environments. *CORROSION* 2011. NACE International; 2011.
- [35] Deyab MAM. Corrosion inhibition and adsorption behavior of sodium lauryl ether sulfate on L80 carbon steel in acetic acid solution and its synergism with ethanol. *J Surfactants Deterg* 2015;18:405–11.
- [36] Ameer ZO, Kudrashov V, Nasr-El-Din H, Forsyth J, Mahoney J, Daigle B. Stimulation of High Temperature SAGD Producer Wells Using a Novel Chelating Agent (GLDA) and Subsequent Geochemical Modeling Using PHREEQC. *SPE International Symposium on Oilfield Chemistry*. Society of Petroleum Engineers; 2015.
- [37] Parkinson R. Properties and applications of electroless nickel. *Nickel Dev Inst* 1997;37.
- [38] Keong K, Sha W. Crystallisation and phase transformation behaviour of electroless nickel-phosphorus deposits and their engineering properties. *Surf Eng* 2002;18:329–43.
- [39] Sudagar J, Lian J, Sha W. Electroless nickel, alloy, composite and nano coatings—a critical review. *J Alloys Compd* 2013;571:183–204.
- [40] Zhu D, Uzcategui A, Gong L, Qiu X, Huang J, Sun C, Luo J-L, Zeng H. Investigation of electroless nickel-phosphorus coating as an alternative to corrosion/fouling resistant alloys in downhole service. *OTC Brasil, Offshore Technology Conference*. 2017.
- [41] Zhu D, Gong L, Qiu X, Hu W, Huang J, Zhang L, et al. Application of electroless nickel coating as a scaling resistant alloy in thermal production. *SPE International Oilfield Scale Conference and Exhibition*. Society of Petroleum Engineers; 2018.
- [42] Zhu D, Leitch M, Wang J, Shi X, Gong L, Aghaie E, et al. Evaluation of an advanced metal bonded coating technology for improved SAGD performance. *SPE Latin America and Caribbean Heavy and Extra Heavy Oil Conference*. Society of Petroleum Engineers; 2016.
- [43] Gong L, Qiu X, Zhang L, Huang J, Hu W, Xiang L, et al. Probing the interaction mechanism between oil-in-water emulsions and electroless nickel-phosphorus coating with implications for antifouling in oil production. *Energy Fuels* 2018.
- [44] Gong L, Wang J, Zhang L, Fattahpour V, Mamoudi M, Roostaei M, et al. Fouling mechanisms of asphaltenes and fine solids on bare and electroless nickel-phosphorus coated carbon steel. *Fuel* 2019;252:188–99.
- [45] Gong L, Zhang L, Xiang L, Zhang J, Fattahpour V, Mamoudi M, et al. Surface interactions between water-in-oil emulsions with asphaltenes and electroless nickel-phosphorus coating. *Langmuir* 2020;36:897–905.
- [46] Vittoratos E. Flow regimes during cyclic steam stimulation at cold lake. *J Can Pet Technol* 1991;30.
- [47] Shi C, Zhang L, Xie L, Lu X, Liu Q, He J, et al. Surface interaction of water-in-oil emulsion droplets with interfacially active asphaltenes. *Langmuir* 2017;33:1265–74.
- [48] Czarnecki J, Tchoukov P, Dabros T, Xu Z. Role of asphaltenes in stabilisation of water in crude oil emulsions. *Can J Chem Eng* 2013;91:1365–71.
- [49] Gong L, Zhang L, Xiang L, Zhang J, Fattahpour V, Mamoudi M, et al. Surface interactions between water-in-oil emulsions with asphaltenes and electroless nickel-phosphorus coating. *Langmuir* 2020.
- [50] Xie L, Shi C, Cui X, Zeng H. Surface forces and interaction mechanisms of emulsion drops and gas bubbles in complex fluids. *Langmuir* 2017;33:3911–25.
- [51] Khammar M, Zhu Y, Xu Y. Centrifugal recovery of solvent-diluted bitumen from oil sands. *Miner Eng* 2019;136:8–17.
- [52] Zhang LY, Lawrence S, Xu Z, Masliyah JH. Studies of Athabasca asphaltene Langmuir films at air–water interface. *J Colloid Interface Sci* 2003;264:128–40.
- [53] Fermaniuk B, Claerhout M, Zhu D. In-Situ SAGD Thermal-Chemical Effects and Metal-Bond Coated Slotted Liner Design for Enhanced Sand Control, Flow and Long Term Performance. *SPE Thermal Well Integrity and Design Symposium*. Society of Petroleum Engineers; 2015.
- [54] Han L, Gong L, Chen J, Zhang J, Xiang L, Zhang L, et al. Universal mussel-inspired ultrastable surface-anchoring strategy via adaptive synergy of catechol and cations. *ACS Appl Mater Interfaces* 2018;10:2166–73.
- [55] Zou W, Gong L, Pan M, Zhang Z, Sun C, Zeng H. Effect of salinity on adsorption and interaction forces of hydrophobically modified polyacrylamide on silica and alumina surfaces. *Miner Eng* 2020;150:106280.
- [56] Hutter JL, Bechhoefer J. Calibration of atomic-force microscope tips. *Rev Sci Instrum* 1993;64:1868–73.
- [57] Tamiz Bakhtiar M, Harbottle D, Curran M, Ng S, Spence J, Siy R, et al. Role of caustic addition in bitumen–clay interactions. *Energy Fuels* 2015;29:58–69.

- [58] Arla D, Sinquin A, Palermo T, Hurtevent C, Graciaa A, Dicharry C. Influence of pH and water content on the type and stability of acidic crude oil emulsions. *Energy Fuels* 2007;21:1337–42.
- [59] Pernyeszi T, Patzkó Á, Berkesi O, Dékány I. Asphaltene adsorption on clays and crude oil reservoir rocks. *Colloids Surf, A* 1998;137:373–84.
- [60] Israelachvili JN. Intermolecular and surface forces. Academic press; 2011.
- [61] Chen G, Warmack R, Huang A, Thundat T. Harmonic response of near-contact scanning force microscopy. *J Appl Phys* 1995;78:1465–9.
- [62] Visser J. On Hamaker constants: a comparison between Hamaker constants and Lifshitz-van der Waals constants. *Adv Colloid Interface Sci* 1972;3:331–63.
- [63] Wang S, Liu J, Zhang L, Masliyah J, Xu Z. Interaction forces between asphaltene surfaces in organic solvents. *Langmuir* 2009;26:183–90.
- [64] Wang S, Liu J, Zhang L, Masliyah J, Xu Z. Interaction forces between asphaltene surfaces in organic solvents. *Langmuir* 2010;26:183–90.
- [65] Zhang L, Shi C, Lu Q, Liu Q, Zeng H. Probing molecular interactions of asphaltenes in heptol using a surface forces apparatus: implications on stability of water-in-oil emulsions. *Langmuir* 2016;32:4886–95.
- [66] Liu J, Cui X, Santander C, Tan X, Liu Q, Zeng H. Destabilization of fine solids suspended in oil media through wettability modification and water-assisted agglomeration. *Fuel* 2019;254:115623.
- [67] Liu J, Cui X, Huang J, Xie L, Tan X, Liu Q, et al. Understanding the stabilization mechanism of bitumen-coated fine solids in organic media from non-aqueous extraction of oil sands. *Fuel* 2019;242:255–64.
- [68] Natarajan A, Xie J, Wang S, Liu Q, Masliyah J, Zeng H, et al. Understanding molecular interactions of asphaltenes in organic solvents using a surface force apparatus. *J Phys Chem C* 2011;115:16043–51.
- [69] Butt H-J, Kappl M, Mueller H, Raiteri R, Meyer W, Rühle J. Steric forces measured with the atomic force microscope at various temperatures. *Langmuir* 1999;15: 2559–65.
- [70] Wang J, Li J, Xie L, Shi C, Liu Q, Zeng H. Interactions between elemental selenium and hydrophilic/hydrophobic surfaces: direct force measurements using AFM. *Chem Eng J* 2016;303:646–54.
- [71] Chen X. The Study of the Corrosion Behavior of Gas Nitriding Treated L80 Steel in Simulated Environment for the Slotted Liners of SAGD. University of Alberta; 2016.
- [72] Nalwaya V, Tantayakom V, Piumsomboon P, Fogler S. Studies on asphaltenes through analysis of polar fractions. *Ind Eng Chem Res* 1999;38:964–72.
- [73] Xing C, Hilts R, Shaw J. Sorption of Athabasca vacuum residue constituents on synthetic mineral and process equipment surfaces from mixtures with pentane. *Energy Fuels* 2010;24:2500–13.
- [74] Adams JJ. Asphaltene adsorption, a literature review. *Energy Fuels* 2014;28: 2831–56.
- [75] Elimelech M, Zhu X, Childress AE, Hong S. Role of membrane surface morphology in colloidal fouling of cellulose acetate and composite aromatic polyamide reverse osmosis membranes. *J Membr Sci* 1997;127:101–9.
- [76] Persson BN, Albohr O, Tartaglino U, Volokitin A, Tosatti E. On the nature of surface roughness with application to contact mechanics, sealing, rubber friction and adhesion. *J Phys: Condens Matter* 2004;17:R1.
- [77] Gong L, Qiu X, Zhang L, Huang J, Hu W, Xiang L, et al. Probing the interaction mechanism between oil-in-water emulsions and electroless nickel-phosphorus coating with implications for antifouling in oil production. *Energy Fuels* 2018;33: 3764–75.
- [78] Liu Y, Beckett D, Hawthorne D. Effect of heat treatment, top coatings and conversion coatings on the corrosion properties of black electroless Ni-P films. *Appl Surf Sci* 2011;257:4486–94.
- [79] Langevin D, Argillier J-F. Interfacial behavior of asphaltenes. *Adv Colloid Interface Sci* 2016;233:83–93.
- [80] Cho N-J, Kanazawa KK, Glenn JS, Frank CW. Employing two different quartz crystal microbalance models to study changes in viscoelastic behavior upon transformation of lipid vesicles to a bilayer on a gold surface. *Anal Chem* 2007;79: 7027–35.
- [81] Voinova MV, Rodahl M, Jonson M, Kasemo B. Viscoelastic acoustic response of layered polymer films at fluid-solid interfaces: continuum mechanics approach. *Phys Scr* 1999;59:391.
- [82] Zahabi A, Gray MR, Dabros T. Kinetics and properties of asphaltene adsorption on surfaces. *Energy Fuels* 2012;26:1009–18.



Full Length Article

Fouling mechanisms of asphaltenes and fine solids on bare and electroless nickel-phosphorus coated carbon steel

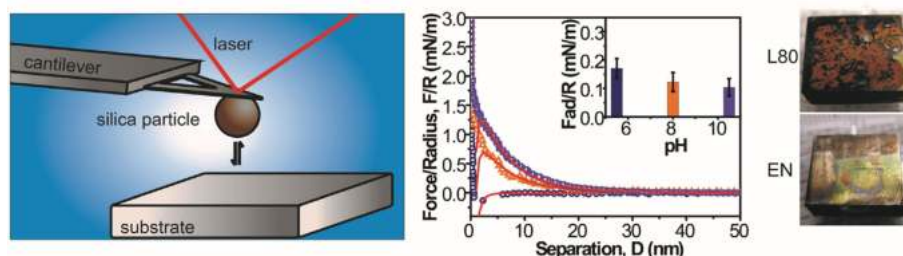


Lu Gong^{a,1}, Jingyi Wang^{a,1}, Ling Zhang^a, Vahidoddin Fattahpour^b, Mahdi Mamoudi^b, Morteza Roostaei^b, Brent Fermaniuk^b, Jing-Li Luo^a, Hongbo Zeng^{a,*}

^a Department of Chemical and Materials Engineering, University of Alberta, Edmonton, Alberta T6G 1H9, Canada

^b RGL Reservoir Management Inc., 3735 8th Street, Nisku, Alberta T9E 8J8, Canada

GRAPHICAL ABSTRACT



ARTICLE INFO

Keywords:

EN coating
AFM colloidal probe technique
Surface forces
Antifouling mechanism

ABSTRACT

Fouling is a critical issue faced by the chemical and oil industries in various operation processes, which has negative impact on the operational efficiency and generates significant economic losses, technical and environmental challenges. Investigating the interaction mechanisms between foulants (e.g., fine solids, asphaltenes) and different substrates is of both fundamental and practical importance in understanding the fouling mechanisms in chemical/petroleum engineering processes and developing antifouling strategies. In this work, atomic force microscope (AFM) colloidal probe technique was employed to directly quantify the interactions between silica or asphaltenes and selected substrates (i.e., carbon steel L80 and L80 with electroless nickel-phosphorus (EN) coating) in aqueous solutions. The effects of salinity, pH and presence of divalent ions (e.g., Ca^{2+}) on the surface interactions were investigated. The obtained force profiles showed that the interactions between silica or asphaltenes and L80 surface were more attractive than that between silica or asphaltenes and EN coating, in NaCl solutions. Bulk fouling tests in silica and asphaltenes-coated silica suspensions revealed that significant fouling of silica and asphaltenes were found on L80 substrates, while EN coating exhibited excellent antifouling performance. Our results provide useful insights into the fundamental understanding of the fouling mechanism of fine solids and asphaltenes, and the development of novel effective antifouling coatings in chemical and oil industries.

* Corresponding author.

E-mail address: hongbo.zeng@ualberta.ca (H. Zeng).

¹ L. Gong and J. Wang contribute equally to the work.

1. Introduction

Fouling, defined as the adsorption and build-up of undesired materials on the surfaces of related substrates or equipment through physical or/and chemical interactions [1–3], has caused significantly challenging problems to the chemical engineering and oil industries. The unexpected depositions of various materials on substrate surfaces in industrial operations result in negative impacts on the operational efficiency and generate significant economic losses.

Steam-Assisted Gravity Drainage (SAGD) technique is the most widely used in-situ recovery method to extract bitumen from the Canadian oil sands [4]. In the SAGD operations, fouling on facilities such as pipelines and heat exchangers can lead to plugged liners, increased pressure drop, enlarged heat resistance and reduced bitumen extraction efficiency [5–7]. Meanwhile, it costs billions of dollars for industries in the world to shut down and clean or replace related facilities [8]. Disposal of the fouled devices and the related foulants could also lead to potential negative impacts on the environment. Therefore, it is important to characterize the foulant components and understand the fouling mechanisms in related industrial processes.

In previous studies, it has been reported that the major components of plugging foulants identified in SAGD operations include corrosion products (e.g., iron oxide), clay particles (e.g., kaolinite), fine solids (e.g., silica) and organics (e.g., bitumen, asphaltenes) [1,9–11]. Among these foulants, asphaltenes are the heaviest molecular fractions of crude oil with complex ring structures, which are insoluble in alkane solvents (e.g., heptane), but soluble in aromatic solvents (e.g., toluene) [12–15]. Asphaltenes are considered to be one of the major causes for the fouling issues in oil production [16–20]. It was well known that asphaltenes can easily deposit on various surfaces, such as silica and iron surfaces, via the van der Waals force, hydrogen bonds, cation/anion- π interactions and so on [21,22]. Additionally, the aggregations of asphaltenes could act as the precursor for the coke formation, and the coke can lead to stronger fouling problems in oil production [23–27]. Fine solids, originated from the reservoir ground or oil sands [28,29], were often presented with asphaltenes in bitumen extraction [30,31]. Thus, the adsorption of fine solids (i.e., silica) and organics (e.g., asphaltenes) contributes significantly to the fouling in oil production processes.

L80 carbon steel is one of the commonly used materials in pipe and joints for oil and gas industry [32–34]. However, the limited corrosion and fouling resistance of L80 carbon steel makes antifouling treatments requisite for its service under harsh environment in industrial operations [34–36]. Over past decades, various protective coating techniques on steels have been developed to extend their applications in different industrial processes [37–42], such as plasma enhanced chemical vapor deposition, polymer coatings and electroless deposition [43–48]. Among them, the electroless nickel-phosphorus (EN) coating shows great potential applications for its remarkable properties, such as high corrosion resistance, high wear resistance, great hardness, uniform thickness, and good lubricity [49–51]. The EN coating on steel substrates could protect the steel during service under harsh operation environment [49]. Meanwhile, other materials, such as TiO_2 , Al_2O_3 , SiC , and ZrO_2 , have been added in the EN coating to improve its performances (e.g., corrosion resistance) [52–56]. However, the evaluation and understanding of the antifouling property of EN coating in chemical and oil industries still remains very limited, which is one of the major focuses of this work.

In this study, for the first time, the fouling and antifouling behaviors and the interaction mechanisms of silica and asphaltenes on L80 carbon steel and L80 with EN coating in aqueous solutions have been investigated via quantitative force measurements using the atomic force microscope (AFM) colloidal probe technique and bulk fouling tests. The effects of salinity, pH and divalent ions (i.e., Ca^{2+}) were also investigated. Our work studies the fundamental fouling and antifouling mechanisms of fine solids and organics on selected metal surfaces in chemical and oil industries, with implications for the development of

effective antifouling strategies.

2. Materials and methodology

2.1. Materials

L80 carbon steel (L80) substrates were supplied by RGL Reservoir Management Inc. (RGL, Alberta, Canada). Silica microsphere particles (diameter 5 μm , Sigma-Aldrich, Canada) were used as fine solids in the force measurements. Asphaltenes were extracted from Athabasca bitumen by following a procedure reported previously [57]. Toluene (C_7H_8 , 99.9%, HPLC grade, Sigma-Aldrich, Canada) was used as the solvent to dissolve asphaltenes. Silica wafers with 0.5 μm thermal oxide layer purchased from NanoFAB, University of Alberta, were used in force measurements for the force calibration of AFM probes. Sodium chloride (NaCl , $\geq 99.5\%$, Sigma-Aldrich, Canada) was used to prepare the aqueous solutions. Calcium chloride dihydrate ($\text{CaCl}_2 \cdot 2\text{H}_2\text{O}$, ACS reagent, $\geq 99\%$, Sigma-Aldrich, Canada) was used as the source of Calcium ions to investigate the effect of divalent cations on fouling. Sodium hydroxide (NaOH , ACS reagent, $\geq 97\%$, Sigma-Aldrich, Canada) and hydrochloric acid (HCl , certified ACS Plus, Fisher Scientific, Canada) were used as pH modifiers. Aqueous solutions were prepared using Milli-Q water with a resistivity of 18.2 $\text{M}\Omega \cdot \text{cm}$ (BARNSTEAD Smart2Pure, Thermo Scientific, Canada). Silica particles (size 0.5–10 μm , Sigma-Aldrich, Canada) were used to prepare the silica suspensions for fouling tests. Ethanol (99.5%, anhydrous, ACROS Organics, Canada) was used for washing and cleaning of the substrates.

2.2. Preparation of electroless nickel-phosphorus (EN) coating

The nickel-phosphorus (EN) coating used in this study was prepared by electroless deposition onto L80 carbon steel substrates from a piece of slotted liner using reported EN coating plating process [58,59]. First, the bare L80 steel was soaked in NaOH solution (20 wt%) at 70 $^\circ\text{C}$ for 15 min to remove all cutting fluids, grease and oil from the surface. Then, it was washed by DI water and ethanol, and dried using pure nitrogen. A solution of 10 wt% hydrochloric acid was used to activate the L80 surface for the plating process. The details of bath compositions and reaction conditions are listed in Table 1. The activated L80 substrates were placed in the electroless plating solution for EN coating. After the coating process was completed, the substrates were rinsed with DI water and ethanol, and dried using pure nitrogen.

2.3. Preparation of silica and asphaltenes probes

The silica probe was prepared using two-component epoxy glue (EP2LV, MasterBond, USA) to attach a silica microsphere (radius $\sim 2.5 \mu\text{m}$) to the end of a tipless AFM cantilever (NP-O10, Bruker, Santa Barbara, CA). This glued silica probe was placed at room temperature (23 $^\circ\text{C}$) for at least 24 h for epoxy curing. Before force measurements, the silica probe was treated in a UV-Ozone cleaner for 15 min to remove

Table 1
Bath compositions and reaction conditions for EN coating deposition.

Composition	Concentration
$\text{NiSO}_4 \cdot 6\text{H}_2\text{O}$	25 g L^{-1}
$\text{NaH}_2\text{PO}_4 \cdot \text{H}_2\text{O}$	30 g L^{-1}
Citric acid	20 g L^{-1}
Lactic acid	20 mL L^{-1}
Reaction Conditions:	
pH: 6.0	
Temperature: 85 $^\circ\text{C}$	
Agitation: 250 rpm	
Time: 30 min	

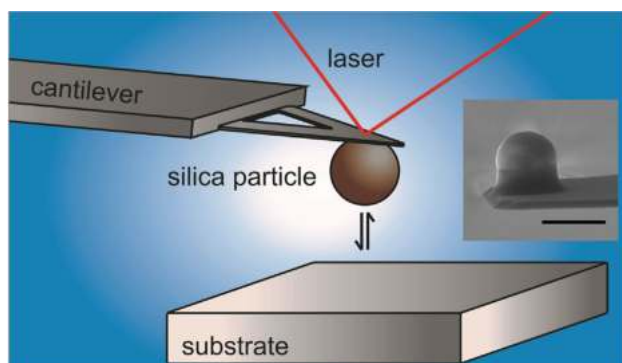


Fig. 1. Schematic of AFM colloidal probe technique in aqueous solution. The inset shows the SEM image of a typical silica probe (Scale bar: 5 μm).

the possible organic contaminants, and then rinsed with DI water and ethanol, followed by drying with pure nitrogen. Asphaltenes probe was prepared by immersing the cleaned silica probe in 20 ppm asphaltenes-in-toluene solution for 2 days. Fig. S1 shows the scanning electron microscopy (SEM) images of silica probe and asphaltenes-coated silica probe, demonstrating the successful deposition and full coverage of asphaltenes on the probe. Prior to force measurements, the asphaltenes probe was washed using toluene and dried with pure nitrogen.

2.4. Force measurements using colloidal probe technique

The force measurements between silica or asphaltenes-coated silica probe and different substrates (i.e., L80, L80 with EN coating) in NaCl solutions were conducted with a Dimension Icon AFM (Bruker, Santa Barbara, CA, USA) using the colloidal probe technique, as illustrated in Fig. 1. The details of experimental setup were reported elsewhere [7,60–66].

During the force measurements, the substrate was firstly immersed in the aqueous solution. A silica or asphaltenes probe was installed in the tip holder of the AFM and then placed in the aqueous solution. The piezo sensitivity was calibrated from the linear regime of the force curves between the probe and a clean silica surface, and the spring constant of this probe was calibrated using the thermal tune method [67]. During each force measurement, the silica or asphaltenes probe was driven by a piezo to approach the substrate at a velocity of $1 \mu\text{m s}^{-1}$ until a loading force of 10 nN was reached, and then it was retracted from the substrate. The deflection of the probe was detected by an optical laser beam detection system, and the interaction forces were calculated using the Hooke's law. The corresponding force profiles between the probe and the substrate were recorded by the AFM software. To obtain reproducible results, multiple force measurements were conducted with the probe on different positions (more than 50) of the same substrate, and two independently prepared substrates were tested. The measured force curves were analyzed and the average adhesion between the probe and the substrate was determined.

The force-separation profiles between the probe and substrate in NaCl solutions were measured and recorded by the AFM software. To theoretically analyze the measured interactions, the classical Derjaguin-Landau-Verwey-Overbeek (DLVO) model coupled with hydrodynamic interaction has been applied to fit the measured force data. The included van der Waals force (F_{vdw}) and electric double layer force (F_{edl}) are given by Eqs. (1) and (2), respectively [68,69].

$$F_{vdw} = -\frac{A_H R}{6D^2} \quad (1)$$

$$F_{edl} = \frac{\pi}{\epsilon \epsilon_0 \kappa^2} [(\sigma_p^2 + \sigma_s^2)(e^{-2\kappa D} + 2\kappa D - 1)e^{-2\kappa D} + 4\sigma_p \sigma_s (e^{-\kappa D} + \kappa D - 1)e^{-\kappa D}] \quad (2)$$

$$\sigma = \sqrt{8\epsilon \epsilon_0 \kappa_B T C N_A} \sinh\left(\frac{e\Psi}{2\kappa_B T}\right) \quad (3)$$

where A_H is the Hamaker constant, R is the radius of silica microsphere, D is the separation distance between the microsphere and flat substrate, ϵ is the relative permittivity of medium, ϵ_0 is the vacuum permittivity, κ is the Debye length, σ_p is the surface charge density of colloidal probe, σ_s is the charge density of the flat substrate, κ_B is the Boltzmann constant, T is the temperature, C is the bulk concentration of ions, N_A is the Avogadro's number, e is the elementary charge, and Ψ is the surface potential. In addition to the DLVO interactions, the hydrodynamic force (F_{hd}) was also included to analyze the measured force profile as given by Eq. (4) [70].

$$F_{hd} = -\frac{6\pi\eta R^2}{D} u, \text{ as } \frac{D}{R} \rightarrow 0 \quad (4)$$

where η is the fluid viscosity (0.001 N m^{-2} , 20°C), and u is the approaching velocity of microsphere ($u = 1 \mu\text{m s}^{-1} = 1.0 \times 10^{-6} \text{ m s}^{-1}$). Therefore, the total forces (F) can be given by Eq. (5).

$$F = F_{vdw} + F_{edl} + F_{hd} \quad (5)$$

2.5. Bulk fouling tests

The bulk fouling tests of L80 and EN coating in silica and asphaltenes-coated silica suspensions were conducted to evaluate their fouling and antifouling performances. Asphaltenes-coated silica particles were prepared by soaking silica particles ($0.5 \sim 10 \mu\text{m}$) in 20 ppm asphaltenes in toluene for 2 days. Then the liquid was removed after centrifugation. The solids were thoroughly washed by pure toluene and dried at room temperature (23°C). Silica or asphaltenes-coated silica suspensions were prepared by dispersing 0.1 g particles in 100 mL NaCl solutions with different water chemistries (e.g., salinity, pH and Ca^{2+} ions) using an ultrasonic bath for 1 h. L80 and EN substrates were separately immersed in the silica or asphaltenes-coated silica suspensions with a stirring speed of 300 rpm for 24 h at room temperature (23°C). Then the treated substrates were washed with DI water and dried with pure nitrogen, and characterized using optical imaging, Scanning Electron Microscopy (SEM) and Energy Dispersive X-Ray Spectroscopy (EDS). The intensity signal of silicon element in the EDS spectra was determined to show the fouling of silica particles, and that of carbon element was examined for the fouling of asphaltenes-coated silica particles. It is noted that although EDS characterizations could not quantify the total amount of foulants adsorbed on substrates, they provide useful data for direct comparison of antifouling performance of different substrates under same experimental condition.

3. Results and discussion

3.1. Characterization of EN coating

Fig. 2 shows the SEM and EDS results of EN coating on L80 substrate. The typical nodular structure of electroless nickel phosphorus [58] was detected on the flat substrate. The EDS element results of the EN coating show the presence of nickel and phosphorus elements, demonstrating the successful deposition of EN coating on L80 substrate. Fig. 2c shows the SEM image of the cross section of EN coating, and Fig. 2d–f show the EDS element mapping of iron, phosphate and nickel at the cross section. The thickness of the EN coating layer was determined to be $\sim 15 \mu\text{m}$. Fig. 3 shows the topographic AFM images of the EN and L80 substrates, which have root-mean-square (rms) roughness of 21.9 nm and 12.5 nm, respectively.

3.2. Effect of electrolyte (NaCl) concentration

The effects of electrolyte concentration on the surface interactions

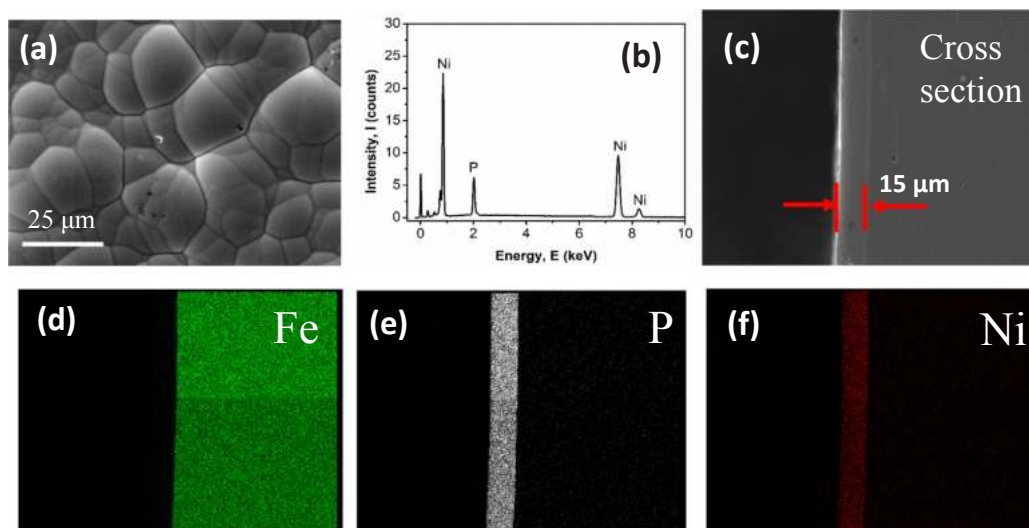


Fig. 2. (a) SEM image of EN coating deposited on L80. (b) EDS spectrum of EN coating. (c) SEM image of the cross section of the EN coating. (d, e, f) EDS elemental mapping of the cross section of EN coating for elements Fe, P and Ni.

were investigated. The interaction forces between silica or asphaltene-coated silica probe and L80 or EN substrates were measured in NaCl solutions of varying concentration: 1, 10, and 100 mM at natural pH of 5.8. The force results are shown in Fig. 4.

Fig. 4a shows the normalized force profiles between silica probe and L80 substrate in 1, 10 and 100 mM NaCl solutions. Pure repulsive forces were measured between silica probe and L80 substrate in 1 mM NaCl. At low salinity (i.e., 1 mM), the Debye length is about 9.6 nm, and the electrical double layer (EDL) interaction contributes significantly to the long-range repulsion. In 10 mM NaCl solution, the long-range repulsion disappeared and repulsion was detected only at very short distances of $D < 2$ nm. At high salinity condition (i.e., 100 mM NaCl), no noticeable repulsion was detected during approaching, while attraction was measured and an obvious “jump-in” behavior was observed at distance less than 10 nm. According to the classical DLVO theory, both the van der Waals (VDW) and electric double layer (EDL) interactions contribute to the surface interaction between the silica probe and L80 surface in NaCl solutions. Under high salinity (i.e., 100 mM) condition, the electric double layer was significantly compressed with a Debye length less than 1 nm, thus the VDW attraction dominates the interaction and leads to the “jump-in” behavior during approaching [68]. The inset in Fig. 4a shows the normalized adhesion F_{ad}/R measured during the separation between the silica probe and L80 substrate under different NaCl concentration conditions, which were all around 0.8 mN m^{-1} and did not change significantly with salt concentration.

To better understand the interactions between silica probe and L80

substrate in NaCl solutions, the experimental data was theoretically analyzed based on the DLVO theory, as shown in the solid red curves of Fig. 4a. For calibrating the surface property (i.e., surface potential) of silica, firstly, the interaction forces between silica probe and flat silica substrate were measured in 1, 10 and 100 mM NaCl solutions, as shown in Fig. S2a, which were fitted with the DLVO theory. The Hamaker constant between silica surfaces in NaCl solution was calculated as $6.28 \times 10^{-21} \text{ J}$ using the Lifshitz theory and assuming the dielectric constant and refractive index of silica and water [68,71,72]. It is found that the experimental data in 100 mM NaCl reasonably agrees with theoretical calculations based on the dominating VDW interactions, which validates the calculated Hamaker constant. Fitting the measured force curves between silica surfaces in 1 and 10 mM NaCl solutions using the DLVO theory gives the surface potentials of silica surface in 1 and 10 mM NaCl as -28.0 and -22.0 mV , respectively. The obtained surface potentials of silica fall within the value range reported previously [61,73,74], as in Table S1. The Hamaker constant and fitted surface potential values of silica were further applied to fit the measured force curves between silica probe and L80 surface in 1, 10 and 100 mM NaCl solutions. The fitted Hamaker constant between the silica probe and the L80 substrate in the 100 mM NaCl solution was $2.13 \times 10^{-20} \text{ J}$ based on the measured force curves. The reported Hamaker constants of silica, steel and water are $6.3 \times 10^{-20} \text{ J}$, $3.0 \times 10^{-19} \text{ J}$, and $3.7 \times 10^{-20} \text{ J}$, respectively [68,75]. The Hamaker constant between silica and steel in aqueous solution was calculated as $2.08 \times 10^{-20} \text{ J}$ based on the combination relation which is very close

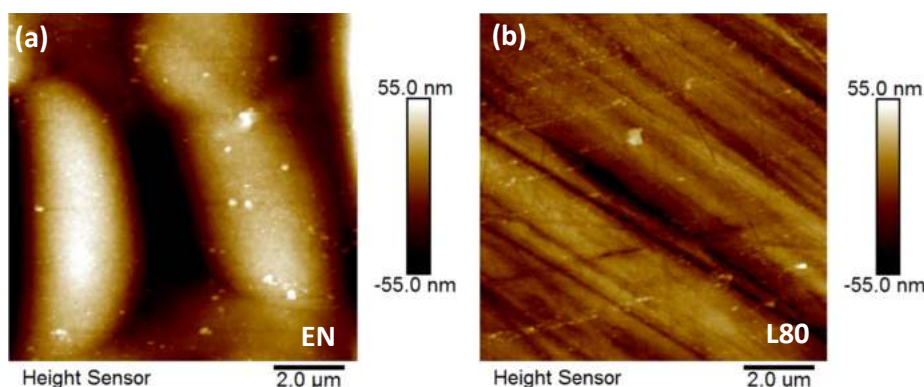


Fig. 3. Topographic AFM image of (a) EN coating and (b) L80 substrate. The root-mean-square (rms) roughness is 21.9 nm for EN and 12.5 nm for L80.

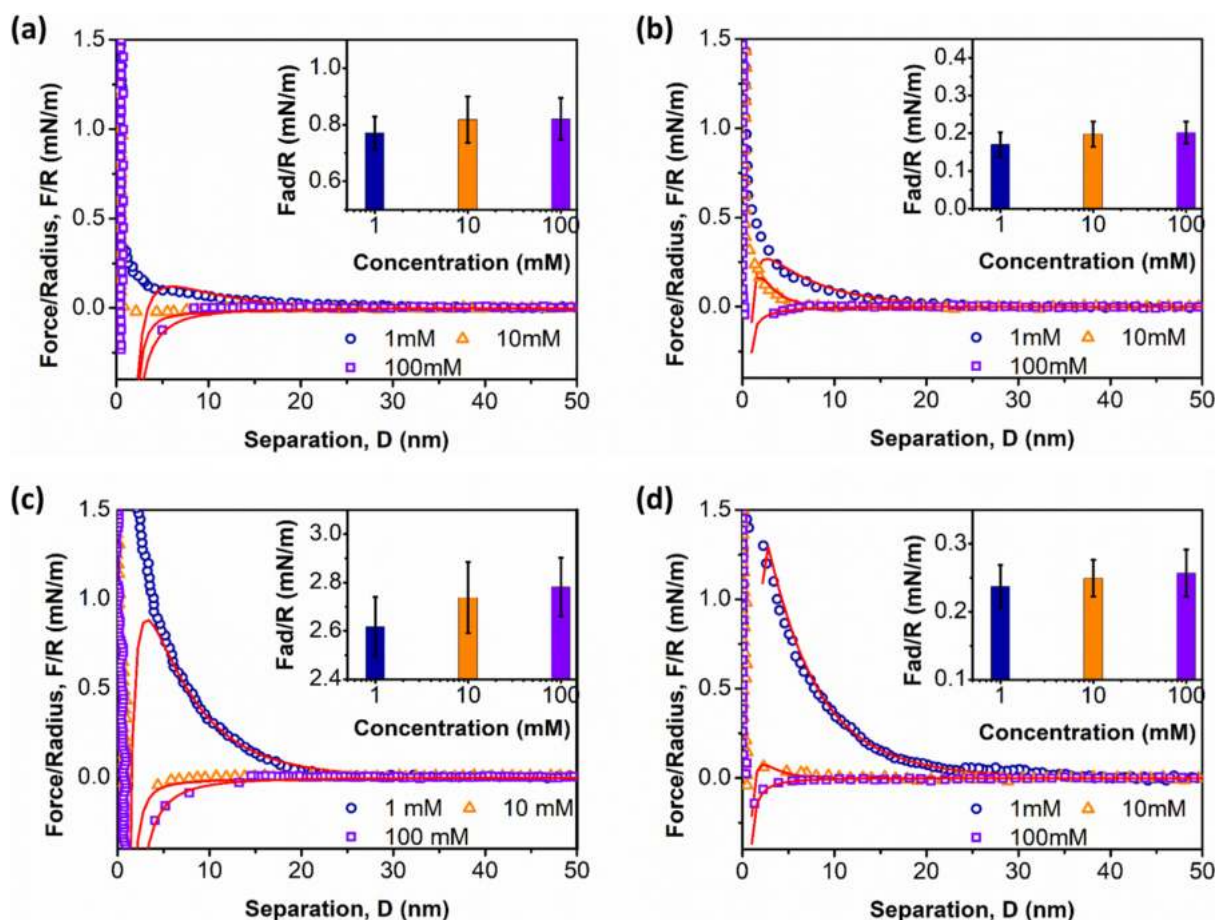


Fig. 4. Normalized surface interaction forces during approaching in 1, 10 and 100 mM NaCl solutions for (a) silica probe vs. L80 substrate, (b) silica probe vs. EN substrate, (c) asphaltenes-coated silica probe vs. L80 substrate, and (d) asphaltenes-coated probe vs. EN substrate.

Table 2

The Hamaker constants and surface potentials of silica, asphaltenes, L80 and EN in 1, 10 and 100 mM NaCl solutions.

Hamaker constant A_H			
Silica probe-water-L80 substrate	2.13×10^{-20} J		
Silica probe-water-EN substrate	3.3×10^{-21} J		
Asphaltenes probe-water-L80 substrate	2.31×10^{-20} J		
Asphaltenes probe-water-EN substrate	3.5×10^{-21} J		
Surface potentials Ψ			
	1 mM	10 mM	100 mM
Silica	−28.0 mV	−22.0 mV	−
Asphaltenes	−55.0 mV	−18.0 mV	−
L80	−5.5 mV	−3.0 mV	−
EN	−9.5 mV	−6.0 mV	−

to the fitted value. The surface potentials of L80 in 1 and 10 mM NaCl solutions were further fitted and calculated as −5.5 and −3.0 mV, respectively, as shown in Table 2, also close to the reported values [76,77]. It is noted that the surface potentials of silica and L80 surfaces in NaCl solutions become less negative when the solution salinity increases [68].

Fig. 4b shows the measured force curves between silica probe and EN substrate in 1, 10 and 100 mM NaCl solutions. Similar trend was observed as that in Fig. 4a that the measured forces changed from the repulsion to attraction when the salinity increased from 1 mM to 100 mM. This tendency was also due to the compressed electric double layer interaction under high salinity condition. The inset in Fig. 4b shows the normalized adhesion between silica probe and EN coating

surface measured during separation, which was all around 0.2 mN m^{-1} . Comparing the force curves in Fig. 4a and b, the interaction forces during approaching between silica probe and EN substrate are less attractive in 100 mM NaCl and more repulsive in 1 mM NaCl compared to those of the L80 substrate. Meanwhile the adhesion forces measured during separation are also much weaker. These results indicate that silica particles are more difficult to attach on EN coating than on L80 in NaCl solutions.

The measured force curves between silica probe and EN substrate in 1, 10 and 100 mM NaCl solutions were also theoretically analyzed using a similar approach used to obtain Fig. 4a, and are shown by the solid curves in Fig. 4b. The Hamaker constant between silica and EN substrate was determined to be 3.3×10^{-21} J from the force results under high salinity condition (i.e., 100 mM). This value was much smaller than the Hamaker constant between silica and L80 substrate, indicating that the VDW attraction between silica and EN substrate in NaCl solutions was weaker than that between silica and L80 substrate. The surface potentials of EN coating in 1 and 10 mM NaCl solutions were fitted to be −9.5 mV and −6.0 mV, respectively. These surface potentials were more negative than those of L80 substrate in NaCl solutions, demonstrating that the EDL repulsion between silica and EN substrate was stronger than that between silica and L80 substrate. The EN coating has nickel atoms and phosphorus atoms on its surface, which could attract more hydroxyl groups in aqueous solutions. Therefore, the more negative surface potentials, as well as the stronger EDL repulsions between EN substrate and silica probe, could be obtained.

Fig. 4c and d show the measured force curves and theoretical fittings for interactions of asphaltenes probe with L80 and EN substrate in

1, 10 and 100 mM NaCl solutions, respectively. Under low salinity (i.e., 1 mM NaCl), the force curves were repulsive due to the strong EDL repulsion. Under high salinity (i.e., 100 mM NaCl), the force curves became attractive because of the dominant role of VDW attraction. The measured adhesion between asphaltenes and L80 (around 2.7 mN m^{-1}) was much stronger than that between asphaltenes and EN coating (around 0.25 mN m^{-1}), suggesting that the asphaltenes was more difficult to attach to EN coating surface.

The measured force profiles were also theoretically analyzed based on the classic DLVO theory which is shown in the solid red curves of Fig. 4c and d. For calibrating the surface property (i.e., surface potential) of asphaltenes-coated silica probe, the interaction forces between asphaltenes-coated silica probe and silica substrate were measured in 1, 10 and 100 mM NaCl solutions, as shown in Fig. S2b. The Hamaker constant between asphaltenes and silica in NaCl solution was found through fitting to be $6.55 \times 10^{-21} \text{ J}$ from the force curve at high salinity (i.e., 100 mM), which is close to the reported values [78,79]. Then, fitting the force curves at 1 and 10 mM NaCl solutions gives the surface potentials of asphaltenes surface as -55.0 mV and -18.0 mV , respectively, as in Table S1. The obtained surface potentials of asphaltenes were within the reported value range [73,80]. The Hamaker constant and fitted surface potentials were further used in the theoretical analysis of measured force curves between asphaltenes-coated silica probe and L80 or EN substrate. The Hamaker constants between asphaltenes-coated silica probe and L80 or EN substrates in NaCl solution were also found through fitting to be $2.31 \times 10^{-20} \text{ J}$ and $3.5 \times 10^{-21} \text{ J}$, respectively. Based on the measured interaction forces at high salinity (i.e., 100 mM). The smaller Hamaker constant between asphaltenes-coated silica and EN substrate indicated a weaker VDW attraction than that between asphaltenes-coated silica and L80 substrate. With the fitted surface potentials of asphaltenes, L80 and EN substrates, it is noted that the experimental force curves between asphaltenes-coated silica and L80 or EN substrate in 1 and 10 mM NaCl solutions agree well with theoretical calculations based on the classical DLVO theory. These results further validate the fitted Hamaker constants and surface potentials.

3.3. Effect of pH

The effect of solution pH on the surface interactions was also investigated. The interaction forces between silica probe or asphaltenes-coated silica probe and L80 or EN substrate were measured in 1 mM NaCl solution at pH of 5.5, 8.0 and 10.5. The force results are shown in Fig. 5.

Fig. 5a shows the normalized interaction forces between a silica probe and L80 substrate in 1 mM NaCl solutions at different pH of 5.5, 8.0 and 10.5. The long-range repulsive forces were detected at pH of 8.0 and 10.5. At pH of 5.5, the “jump-in” behavior was observed at distance less than 10 nm and attraction was measured. At alkaline pH (i.e., pH 10.5), more OH^- ions in the bulk solution could induce more adsorption of OH^- ions on the surface or promote the deprotonation of related surface chemical groups, which makes the substrate surface more negatively charged [68]. Therefore, alkaline pH of the NaCl solution induced stronger EDL repulsion between silica probe and L80 substrate. The inset in Fig. 5a shows the normalized adhesions F_{ad}/R between silica probe and L80 substrate in 1 mM NaCl solutions at pH of 5.5, 8.0 and 10.5. The normalized adhesion F_{ad}/R decreases from 0.78 mN m^{-1} at pH 5.5 to 0.60 mN m^{-1} at pH 8.0 and finally to 0.58 mN m^{-1} at pH 10.5, indicating that the alkaline pH leads to weaker adhesion between silica and L80 substrate. Thus, the solution pH has an influence on the adhesion between two surfaces. Fig. 5b shows the normalized interaction forces between silica probe and EN substrate in 1 mM NaCl solutions at pH of 5.5, 8.0 and 10.5. A similar trend as in Fig. 5a was observed. The measured normalized adhesions decreased from 0.17 mN m^{-1} at pH 5.5 to 0.11 mN m^{-1} at pH 10.5, which was also due to the alkaline pH. It was noticed that the adhesion forces between silica

probe and EN substrate were weaker than those between silica and L80 substrate in NaCl solutions, indicating that it would be more difficult for silica particles to attach to EN surface.

Fig. 5c and d show the normalized interaction forces between asphaltenes-coated silica probe and L80 or EN substrate in 1 mM NaCl solutions at pH 5.5, 8.0 and 10.5. The obtained force curves are repulsive, except for the case of asphaltenes-coated silica probe and L80 substrate in 1 mM NaCl solution at pH 5.5, which showed a “jump-in” behavior at distances less than 4 nm. It was observed that the interaction forces between asphaltenes-coated silica probe and EN substrate were more repulsive than those between asphaltenes-coated silica probe and L80 substrate. This result was also due to the more negatively charged asphaltene surface at alkaline pH. Moreover, the normalized adhesion between asphaltenes and L80 or EN substrates became weaker at alkaline solution (i.e. pH 10.5), as shown in the insets of Fig. 5c and d. Additionally, the adhesion between asphaltenes and EN coating was much weaker than that between asphaltenes and L80, suggesting the higher possibility for asphaltenes to adsorb on L80 surface.

The measured force profiles were also theoretically analyzed using the similar approach, as shown by the solid red curves in Fig. 5. For calibrating the surface property (i.e. surface potential) of silica and asphaltenes-coated silica, the interaction forces between silica probe or asphaltenes-coated silica probe and silica substrate in 1 mM NaCl solution at pH of 5.5, 8.0 and 10.5 were measured, as shown in Fig. S3. Since the Hamaker constants between silica probe or asphaltenes-coated silica probe and silica substrate in NaCl solution were known, the surface potentials of silica and asphaltenes were fitted and the results were listed in Table S2. These values were within the value ranges reported previously [68,73,78,80]. Afterwards, the surface potentials of silica and asphaltenes were applied in the theoretical analysis of the measured interaction forces between silica probe or asphaltenes-coated silica probe and L80 or EN substrate. Thus, the surface potentials of L80 and EN substrates were fitted, as shown in Table 3. It was noted that the surface potentials of L80 and EN substrates became more negative when the solution pH turned to be alkaline, and the surface potentials of EN substrate were more negative than those of L80 substrate, suggesting a stronger EDL repulsion between silica or asphaltenes and EN substrate in NaCl solutions.

3.4. Effect of calcium ion

Previous studies show that the presence of divalent ions could influence the aggregation behaviors and conformations of asphaltenes adsorbed at the oil–water interfaces, which would further impact the emulsion stability [81–83]. The effect of divalent ions (i.e., calcium ions) was also investigated. The interaction forces between silica probe or asphaltenes-coated silica probe and L80 or EN substrate in 1 mM NaCl at pH = 8.0 with the addition of 0, 1 and 10 mM Ca^{2+} were measured, and the force results are shown in Fig. 6.

Fig. 6a and b show the normalized interaction forces between the silica probe and L80 or EN substrate in 1 mM NaCl solution with the addition of 0, 1, and 10 mM Ca^{2+} ions. The measured force profiles exhibited a tremendously weakened repulsion with the addition of Ca^{2+} ions, which could be due to the significantly compressed electrical double layer force. Divalent calcium ion has the stronger charge-shielding effect than monovalent sodium ions, which results in the more neutralized surface potentials and the weaker EDL repulsion [84]. It was also noted that the force profiles between the silica probe and L80 substrate in 1 and 10 mM Ca^{2+} ions were more attractive than those between silica probe and EN substrate, which was due to the stronger VDW attraction between silica and L80. Fig. 6c and d show the normalized interaction forces between asphaltenes-coated silica probe and L80 or EN substrate in 1 mM NaCl solutions with the addition of 0, 1, and 10 mM Ca^{2+} ions. Similar trend of the force profiles with silica probe cases could be observed. The insets in Fig. 6 show the normalized adhesions F_{ad}/R between silica probe or asphaltenes-coated silica probe

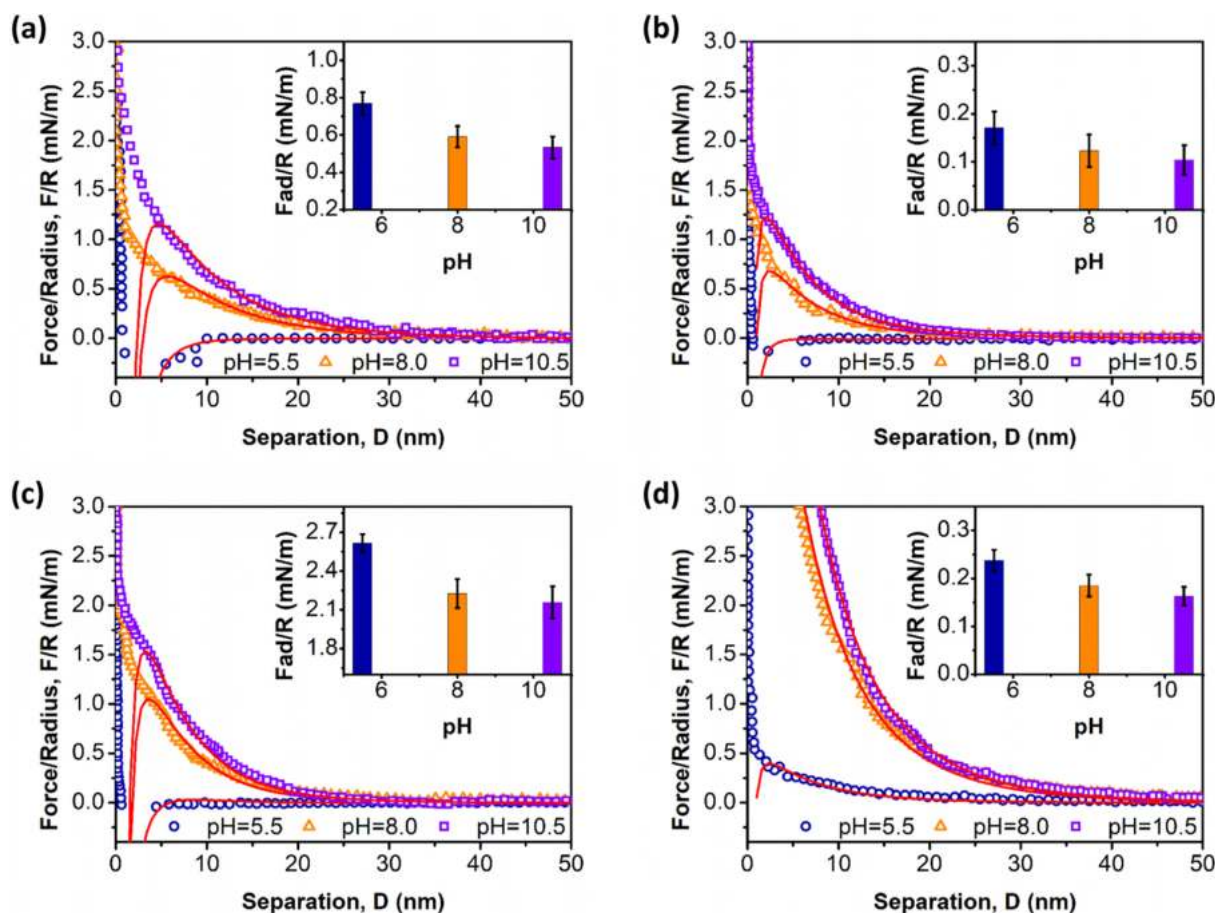


Fig. 5. Normalized surface interaction forces during approaching in 1 mM NaCl solution at pH of 5.5, 8.0 and 10.5 for (a) silica probe vs. L80 substrate, (b) silica probe vs. EN substrate, (c) asphaltenes-coated silica probe and L80 substrate, and (d) asphaltenes-coated silica probe and EN substrate.

Table 3

The surface potentials of silica, asphaltenes, L80 and EN in 1 mM NaCl solutions at pH of 5.5, 8.0 and 10.5.

	pH = 5.5	pH = 8.0	pH = 10.5
Silica	−25.0 mV	−32.0 mV	−39.5 mV
Asphaltenes	−52.0 mV	−63.0 mV	−68.5 mV
L80	−3.0 mV	−6.0 mV	−6.5 mV
EN	−7.0 mV	−18.0 mV	−19.0 mV

and L80 or EN substrate in the presence of 0, 1 and 10 mM Ca^{2+} ions. The increased adhesion with the addition of Ca^{2+} ions demonstrates the significant influence of divalent ions (i.e., Ca^{2+} ions) in the surface interactions. The increased adhesion with the addition of Ca^{2+} ions demonstrates the significant influence of divalent ions (i.e., Ca^{2+} ions) in the surface interactions as the result of the strong shielding effect to weaken electric double layer interaction and bridging effect of Ca^{2+} ions between two negatively charged surfaces [83]. The relatively smaller adhesion between silica or asphaltenes and EN substrate than those between silica or asphaltenes and L80 substrate suggests the greater possibility to lower the fouling of silica and asphaltenes on EN coating surface.

The measured force profiles were also analyzed by the theoretical approach discussed above, as shown by the solid red curves in Fig. 6. The surface potentials of silica probe and asphaltenes-coated silica probe in 1 mM NaCl solutions with 0, 1 and 10 mM Ca^{2+} ions were firstly calibrated via force measurements with the silica substrate, as shown in Fig. S4. Based on the classical DLVO theory, the surface potentials of silica and asphaltenes were fitted and listed in Tables S3 and

4. Then, the surface potentials of L80 and EN were fitted from the measured force profiles and the results are also listed in Table 4. It is noted that the surface potentials became less negative when Ca^{2+} ions were added to the NaCl solution. The surface potentials of EN substrate was more negative than L80 substrate, suggesting a stronger EDL repulsion between EN coating and silica probe or asphaltenes-coated silica probe in NaCl solutions.

3.5. Bulk fouling tests in silica and asphaltenes-coated silica suspensions

To examine the fouling and antifouling performances of L80 and EN substrates in NaCl solutions, bulk fouling tests in silica and asphaltenes-coated silica suspensions were conducted under the effects of salinity, pH and Ca^{2+} ions. The optical images of L80 and EN substrates before the bulk fouling tests are shown in Fig. S5.

Fig. 7a and c show the bulk fouling test results of L80 substrates in silica and asphaltenes-coated silica suspensions with 1, 10 and 100 mM NaCl, respectively. After performing the fouling tests, the L80 substrates showed increased corrosion and fouling products (yellow and black domains) on the surface with increasing solution salinity, indicating that the fouling of L80 substrate by silica particles and asphaltenes was aggravated under higher salinity conditions. Therefore, high salinity (i.e., 100 mM NaCl) promoted the fouling of silica and asphaltenes-coated silica particles on L80 surface. Fig. 7b and d show the optical images of EN substrates after the bulk fouling tests in silica and asphaltenes-coated silica suspensions with 1, 10 and 100 mM NaCl. Unlike L80 substrates, there was no obvious fouling on EN substrates, suggesting that EN coating may possess an excellent antifouling property compared to L80.

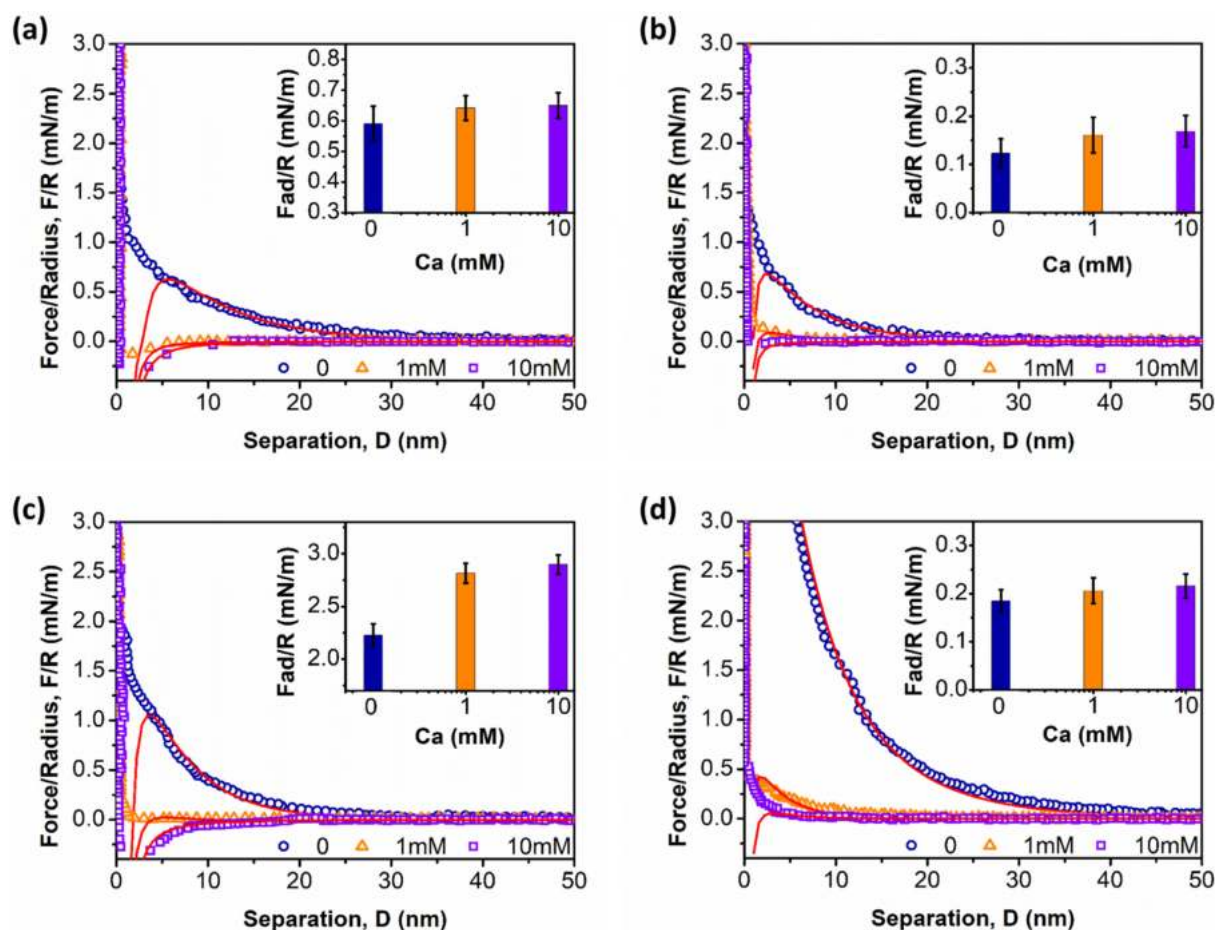


Fig. 6. Normalized surface interaction forces during approaching in 1 mM NaCl solutions at pH 8.0 with the addition of 0, 1 and 10 mM Ca^{2+} for (a) silica probe vs. L80 substrate, (b) silica probe and EN substrate, (c) asphaltenes-coated silica probe and L80 substrate, and (d) asphaltenes-coated silica probe and EN substrate.

Table 4

The surface potentials of silica, asphaltenes, L80 and EN in 1 mM NaCl solutions at pH 8.0 with the addition of 0, 1 and 10 mM Ca^{2+} .

	0	1 mM	10 mM
Silica	−32.0 mV	−15.0 mV	−5.0 mV
Asphaltenes	−63.0 mV	−28.0 mV	−16.0 mV
L80	−6.0 mV	−4.0 mV	−2.0 mV
EN	−18.0 mV	−6.0 mV	−3.0 mV

To evaluate the fouling phenomena, SEM and EDS were conducted to characterize L80 and EN substrates after the bulk fouling tests in silica and asphaltenes suspensions with 100 mM NaCl, and the results are shown in Fig. 8. The SEM images of L80 substrates (Fig. 8a and e) showed that there were particles adsorbed on the substrate surfaces, and the EDS results (Fig. 8b and f) confirmed the presence of silicon element. It was noted that no silicon signal was detected from the EDS result of L80 substrate before fouling tests (Fig. S4c). Thus, the fouling of silica and asphaltenes-coated silica occurred on L80 surfaces. Fig. 8c and g show the SEM images of EN substrates after bulk fouling tests. The EDS results (Fig. 8d and h) show that only a very limited amount of

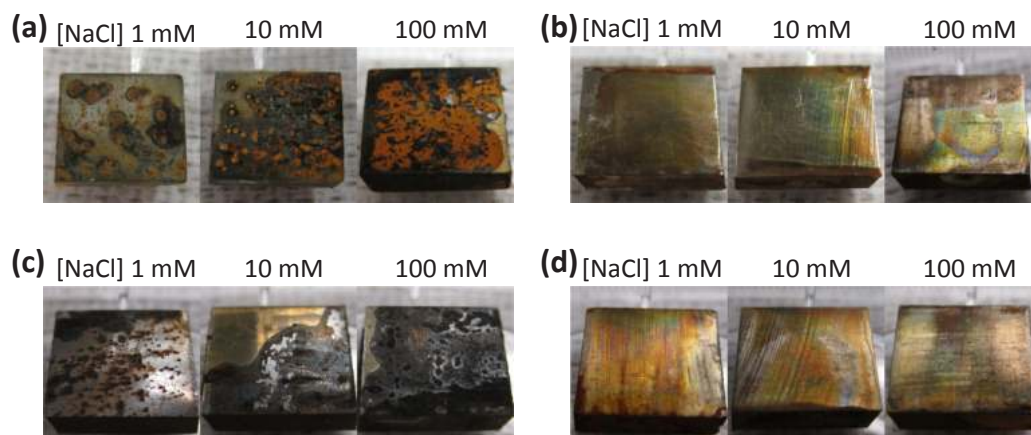


Fig. 7. Optical images of L80 and EN substrates after bulk fouling tests in silica and asphaltenes suspensions with 1, 10 and 100 mM NaCl. (a) L80 substrates in silica suspensions. (b) EN substrates in silica suspensions. (c) L80 substrates in asphaltenes-coated silica suspensions. (d) EN substrates in asphaltenes-coated silica suspensions. (The size of substrates is $8 \times 8 \times 3$ mm.)

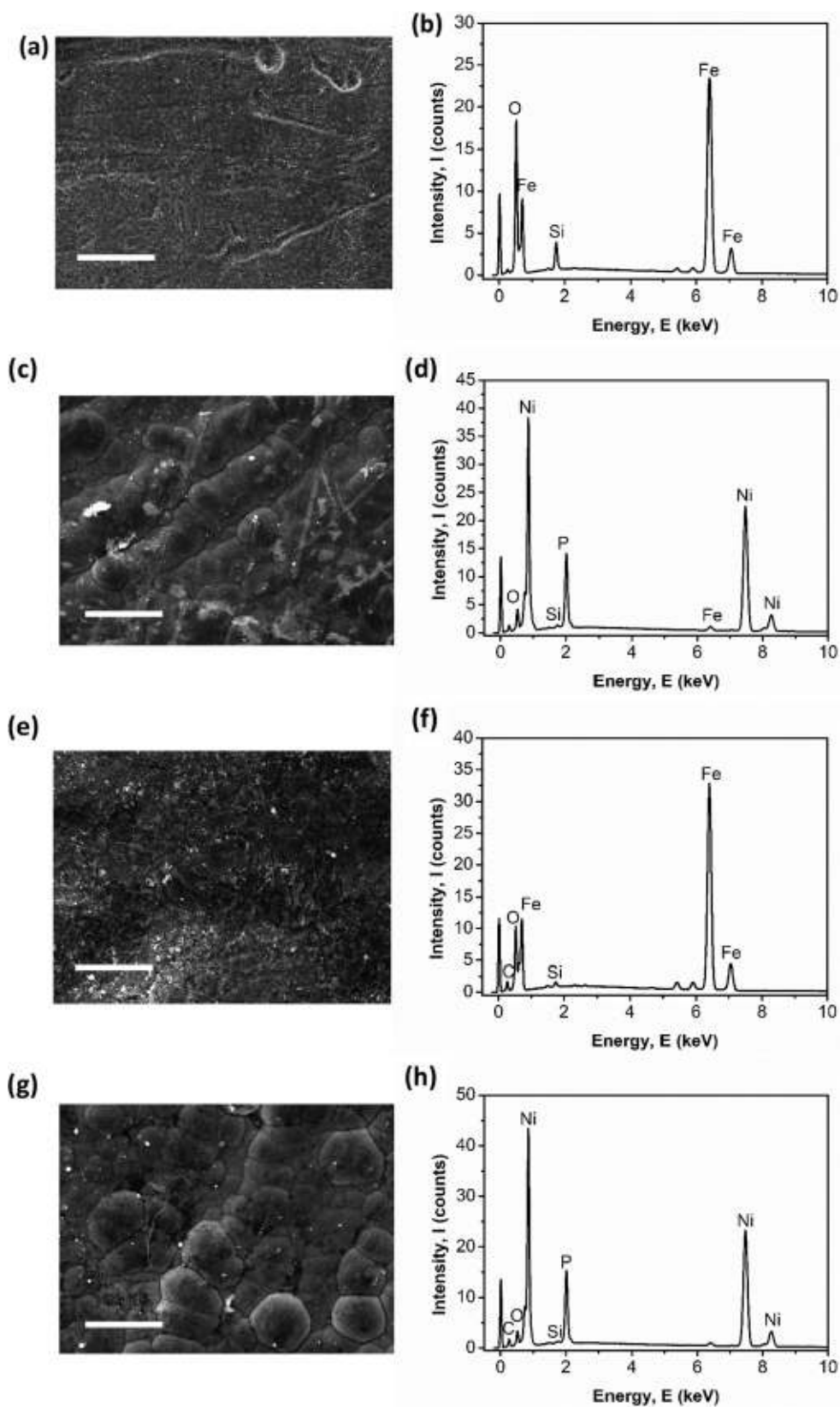


Fig. 8. SEM and EDS results of L80 and EN substrates after bulk fouling tests in silica and asphaltenes suspensions with 100 mM NaCl. (a, b) L80 substrate in silica suspensions. (c, d) EN substrate in silica suspensions. (e, f) L80 substrate in asphaltenes suspensions. (g, h) EN substrate in asphaltenes suspensions. (Scale bar: 25 μ m).

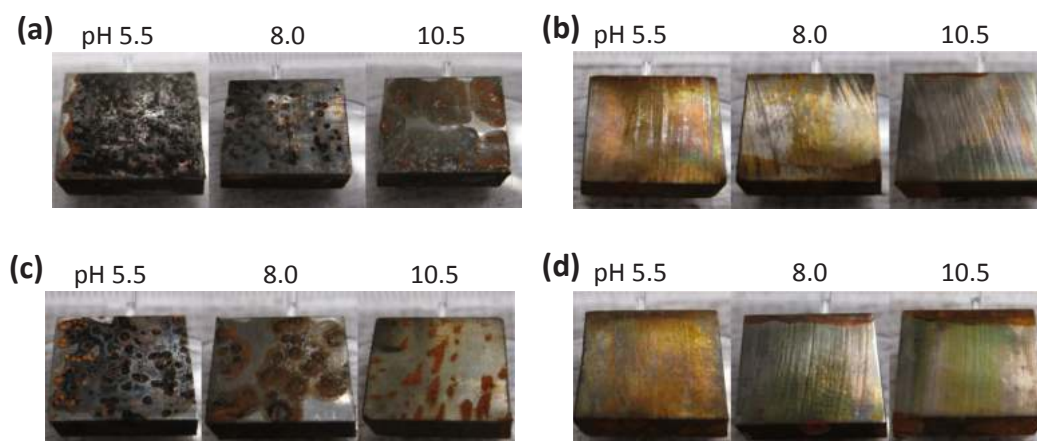


Fig. 9. Optical images of L80 and EN substrates after bulk fouling tests in silica and asphaltene suspensions with 1 mM NaCl solution and pH of 5.5, 8.0 and 10.5. (a) L80 substrates in silica suspensions. (b) EN substrates in silica suspensions. (c) L80 substrates in asphaltene-coated silica suspensions. (d) EN substrates in asphaltene-coated silica suspensions. (The dimensions of substrates are: $8 \times 8 \times 3$ mm.)

silicon could be detected on the EN surfaces. The SEM and EDS results were consistent with the optical images in Fig. 7. Therefore, these results demonstrate that the EN coating possesses a much better antifouling performance than L80 in silica and asphaltene suspensions with different salinities. It is noted that EN coating (RMS roughness 21.9 nm) has the rougher surface morphology and lower surface energy than L80 substrate (RMS roughness 12.5 nm) [77]. Previous reports demonstrated that large surface roughness and high surface energy could aggravate fouling phenomena [85,86]. With relatively high surface roughness and low surface energy, EN coating shows much better antifouling property than L80.

Fig. 9a and c show the optical images of L80 substrates after the bulk fouling tests in silica and asphaltene suspensions with 1 mM NaCl and pH of 5.5, 8.0 and 10.5. It was observed that all the L80 substrates displayed yellow and black domains on the surfaces, indicating fouling occurrence. The fouling aggravated when the solution pH decreased to 5.5, suggesting that low acidic pH promoted the fouling of silica and asphaltene-coated silica particles on L80 surface. Fig. 9b and d show the optical images of EN substrates after the bulk fouling tests in silica and asphaltene suspensions with 1 mM NaCl and pH of 5.5, 8.0 and 10.5. No obvious change was observed on EN surfaces. Therefore, EN coating possesses a better antifouling performance than L80 in silica and asphaltene suspensions at different pH.

Fig. 10a and c show the optical images of L80 substrates after the bulk fouling tests in silica and asphaltene suspensions in 1 mM NaCl solutions with 0, 1 and 10 mM Ca^{2+} ions. Fouling was visually detected on L80 surfaces and aggravated fouling could be detected when more Ca^{2+} ions were added in the NaCl solutions. Thus, the presence of Ca^{2+} ions promoted the fouling of silica and asphaltene particles on the L80 surfaces. Fig. 10b and d show the optical images of EN surfaces after the

bulk fouling tests. Similarly, no obvious fouling was observed on the EN surfaces. Thus, EN coating shows a better antifouling performance than L80 in silica and asphaltene suspensions in the presence of Ca^{2+} ions.

4. Conclusions

In this work, the fouling mechanisms and antifouling property of silica and asphaltene-coated silica on L80 and EN substrates in NaCl solutions were directly quantified using the AFM colloidal probe technique. The effects of solution salinity, pH and presence of Ca^{2+} ions were investigated. The measured force curves were theoretically analyzed using the classic DLVO theory. The force results indicate that the attractive VDW interactions between silica probe or asphaltene-coated silica probe and L80 or EN substrate in NaCl solutions contribute to the fouling phenomena, and the repulsive EDL interactions play an important role in their antifouling property. The surface force measurements also demonstrated that the EDL repulsion became weakened under high salinity condition, at low acidic pH and with the presence of divalent ions (i.e., Ca^{2+}). Compared with the L80 substrate, EN coating surface showed weaker VDW attraction and stronger EDL repulsion with silica and asphaltene-coated silica in NaCl solutions. EN coating has nickel atoms and non-metal phosphorus atoms on its surface, which could adsorb more hydroxyl ions to carry more negative surface potential. Therefore, the stronger EDL repulsion, as well as the weaker VDW attraction, led to the excellent antifouling properties of EN coating. Furthermore, bulk fouling tests of L80 and EN substrates in silica and asphaltene suspensions were also conducted to evaluate their fouling and antifouling performances. The bulk fouling results agreed well with the surface force measurement results, which demonstrated that EN coating possessed excellent antifouling property.

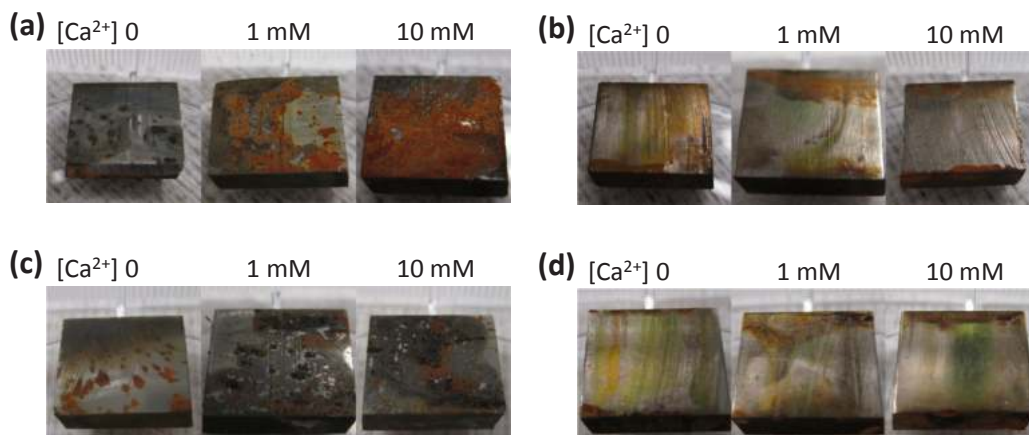


Fig. 10. Images of L80 and EN substrates after bulk fouling tests in silica and asphaltene suspensions in 1 mM NaCl solution with 0, 1 mM and 10 mM Ca^{2+} ions. (a) L80 substrates in silica suspensions. (b) EN substrates in silica suspensions. (c) L80 substrates in asphaltene-coated silica suspensions. (d) EN substrates in asphaltene-coated silica suspensions. (The dimensions of substrates are: $8 \times 8 \times 3$ mm.)

Our work has improved the fundamental understandings of the fouling mechanisms of silica particles and asphaltenes on bare and EN-coated L80 surfaces in NaCl solutions, which provides useful insights on the antifouling behaviors of the EN coatings and the development of anti-fouling strategies for chemical and petroleum industries.

Author contributions

The manuscript was written through contributions of all authors. All authors have given approval to the final version of the manuscript.

Notes

The authors declare no competing financial interest.

Acknowledgement

The authors are grateful to the financial support from the Natural Sciences and Engineering Research Council of Canada (NSERC), RGL Reservoir Management Inc (RGL), Canada Foundation for Innovation (CFI), and the Canada Research Chairs Program (H. Zeng).

Appendix A. Supplementary data

Supplementary data to this article can be found online at <https://doi.org/10.1016/j.fuel.2019.04.113>.

References

- [1] Watkinson AP. Deposition from crude oils in heat exchangers. *Heat Transfer Eng* 2007;28(3):177–84.
- [2] Hu B, Scott K. Microfiltration of water in oil emulsions and evaluation of fouling mechanism. *Chem Eng J* 2008;136(2–3):210–20.
- [3] Amin INHM, Mohammad AW. Adsorptive fouling of organic solutes simulating sweetwater solutions on ultrafiltration membranes. *Chem Eng J* 2015;264:470–8.
- [4] Acosta E. Achieving sustainable, optimal SAGD operations. *J Petrol Technol* 2010;62(11):24–8.
- [5] Munoz V, Elliott G, Afara M, Mikula R. microscopy of heat exchanger fouling during SAGD operations. *Microsc Microanal* 2011;17(S2):1906.
- [6] Pugsley T, Pernitsky D, Grundler J, Johnsen E. Fouling of heat transfer surfaces in a steam assisted gravity drainage (SAGD) in situ facility for the recovery of oil sands bitumen. *Int Conf Heat Exchanger Fouling Clearing* 2013.
- [7] Zhu D, Leitch M, Wang J, Shi X, Gong L, Aghaie E, et al. Evaluation of an advanced metal bonded coating technology for improved SAGD Performance SPE Latin America and caribbean heavy and extra heavy oil conference Society of Petroleum Engineers; 2016.
- [8] MacAdam J, Parsons SA. Calcium carbonate scale formation and control. *Rev Environ Sci Biotechnol* 2004;3(2):159–69.
- [9] Das SK, Butler RM. Mechanism of the vapor extraction process for heavy oil and bitumen. *J Petrol Sci Eng* 1998;21(1):43–59.
- [10] Srinivasan M. Heat exchanger fouling of some Canadian crude oils. University of British Columbia; 2008.
- [11] Lalchan CA, Wiggins CB, Moriyama C. Formulation of an emulsified thermal acid blend for SAGD applications in Eastern Alberta Canadian Unconventional Resources Conference Society of Petroleum Engineers; 2011.
- [12] Adams JJ. Asphaltene adsorption, a literature review. *Energy Fuels* 2014;28(5):2831–56.
- [13] Yarranton HW, Masliyah JH. Molar mass distribution and solubility modeling of asphaltenes. *AIChE J* 1996;42(12):3533–43.
- [14] Hoepfner MP, Limsakoune V, Chuenmeechao V, Maqbool T, Fogler HS. A fundamental study of asphaltene deposition. *Energy Fuels* 2013;27(2):725–35.
- [15] Goual L, Firoozabadi A. Measuring asphaltenes and resins, and dipole moment in petroleum fluids. *AIChE J* 2002;48(11):2646–63.
- [16] Wang J, Buckley JS, Creek JL. Asphaltene deposition on metallic surfaces. *J Dispersion Sci Technol* 2004;25(3):287–98.
- [17] Deshannavar U, Rafeen M, Ramasamy M, Subbarao D. Crude oil fouling: a review. *J Appl Sci(Faisalabad)* 2010;10(24):3167–74.
- [18] Zhang L, Xie L, Shi C, Huang J, Liu Q, Zeng H. Mechanistic understanding of asphaltene surface interactions in aqueous media. *Energy Fuels* 2016;31(4):3348–57.
- [19] Rocha J, Baydak E, Yarranton H, Zsukowski D, Ali-Marciano V, Gong L, et al. Role of aqueous phase chemistry, interfacial film properties, and surface coverage in stabilizing water-in-bitumen emulsions. *Energy Fuels* 2016;30(7):5240–52.
- [20] Mao X, Gong L, Xie L, Qian H, Wang X, Zeng H. Novel Fe3O4 based super-hydrophilic core-shell microspheres for breaking asphaltenes-stabilized water-in-oil emulsion. *Chem Eng J* 2019;358:869–77.
- [21] Mullins OC. The asphaltenes. *Annu Rev Anal Chem* 2011;4:393–418.
- [22] Mullins OC, Sheu EY. Structures and dynamics of asphaltenes. Springer Science & Business Media; 2013.
- [23] Harji A, Koppel P, Mazurek W, Meysami P. Processing options for bitumen upgrading Canadian International Petroleum Conference Petroleum Society of Canada; 2003.
- [24] Jian C, Tang T, Bhattacharjee S. Probing the effect of side-chain length on the aggregation of a model asphaltene using molecular dynamics simulations. *Energy Fuels* 2013;27(4):2057–67.
- [25] Jian C, Zeng H, Liu Q, Tang T. Probing the adsorption of polycyclic aromatic compounds onto water droplets using molecular dynamics simulations. *J Phys Chem C* 2016;120(26):14170–9.
- [26] Goual L, Sedghi M, Zeng H, Mostowfi F, McFarlane R, Mullins OC. On the formation and properties of asphaltene nanoaggregates and clusters by DC-conductivity and centrifugation. *Fuel* 2011;90(7):2480–90.
- [27] Kim S-H, Kim K-D, Lee H, Lee Y-K. Beneficial roles of H-donors as diluent and H-shuttle for asphaltenes in catalytic upgrading of vacuum residue. *Chem Eng J* 2017;314:1–10.
- [28] Thompson D, Taylor A, Graham D. Emulsification and demulsification related to crude oil production. *Colloids Surf* 1985;15:175–89.
- [29] Bobicki ER, Liu Q, Xu Z. Ligand-promoted dissolution of serpentine in ultramafic nickel ores. *Miner Eng* 2014;64:109–19.
- [30] Chalaturnyk RJ, Don Scott J, Özüm B. Management of oil sands tailings. *Pet Sci Technol* 2002;20(9–10):1025–46.
- [31] Liu X, Cui X, Huang J, Xie L, Tan X, Liu Q, et al. Understanding the stabilization mechanism of bitumen-coated fine solids in organic media from non-aqueous extraction of oil sands. *Fuel* 2019;242:255–64.
- [32] Carew J, Al-Sayegh A, Al-Hashem A. The effect of water-cut on the corrosion behaviour L80 carbon steel under downhole conditions. NACE; 2000. Corrosion-National Association of Corrosion Engineers Annual Conference.
- [33] Choi HJ, Warnken D, Al Beheiri FI, Al-Bannai NS. Field corrosion assessment of L80 carbon steel downhole production tubing at Khuff gas wells. *CORROSION* 2006. NACE International; 2006.
- [34] Sun W, Pugh D, Ling S, Reddy R, Pacheco J, Nisbet R, et al. Understanding and quantifying corrosion of L80 carbon steel in sour environments. *CORROSION* 2011. NACE International; 2011.
- [35] Deyab MAM. Corrosion Inhibition and Adsorption Behavior of Sodium Lauryl Ether Sulfate on L80 Carbon Steel in Acetic Acid Solution and Its Synergism with Ethanol. *J Surfactants Deterg* 2015;18(3):405–11.
- [36] Ye Y, Liu Z, Liu W, Zhang D, Zhao H, Wang L, et al. Superhydrophobic oligoaniline-containing electroactive silica coating as pre-process coating for corrosion protection of carbon steel. *Chem Eng J* 2018;348:940–51.
- [37] Lalonde M, Tissier J-P, Corrieu G. Fouling of a plate heat exchanger used in ultra-high-temperature sterilization of milk. *J Dairy Res* 1984;51(04):557–68.
- [38] Changani S, Belmar-Beiny M, Fryer P. Engineering and chemical factors associated with fouling and cleaning in milk processing. *Exp Therm Fluid Sci* 1997;14(4):392–406.
- [39] Visser J, Jeurnink TJ. Fouling of heat exchangers in the dairy industry. *Exp Therm Fluid Sci* 1997;14(4):407–24.
- [40] Bansal B, Chen XD. A critical review of milk fouling in heat exchangers. *Compr Rev Food Sci Food Saf* 2006;5(2):27–33.
- [41] Genzer J, Marmur A. Biological and synthetic self-cleaning surfaces. *MRS Bull* 2008;33(08):742–6.
- [42] Mérian T, Goddard JM. Advances in nonfouling materials: perspectives for the food industry. *J Agric Food Chem* 2012;60(12):2943–57.
- [43] Beuf M, Rizzo G, Leuliet J, Müller-Steinhagen H, Yiantsios S, Karabelas A, et al. Fouling and cleaning of modified stainless steel plate heat exchangers processing milk products; 2003.
- [44] Rosmaninho R, Melo LF. Calcium phosphate deposition from simulated milk ultrafiltrate on different stainless steel-based surfaces. *Int Dairy J* 2006;16(1):81–7.
- [45] Premathilaka S, Hyland M, Chen X, Bansal B. A study of the effects of surface chemistry on the initial deposition mechanisms of dairy fouling. *Food Bioprod Process* 2006;84(4):265–73.
- [46] Rosmaninho R, Santos O, Nylander T, Paulsson M, Beuf M, Benezech T, et al. Modified stainless steel surfaces targeted to reduce fouling—evaluation of fouling by milk components. *J Food Eng* 2007;80(4):1176–87.
- [47] Balasubramanian S, Puri V. Thermal energy savings in pilot-scale plate heat exchanger system during product processing using modified surfaces. *J Food Eng* 2009;91(4):608–11.
- [48] Lin J, Wang C, Wang S, Chen Y, He W, Xiao D. Initiation electroless nickel plating by atomic hydrogen for PCB final finishing. *Chem Eng J* 2016;306:117–23.
- [49] Gu C, Lian J, Li G, Niu L, Jiang Z. High corrosion-resistant Ni-P/Ni-Ni-P multilayer coatings on steel. *Surf Coat Technol* 2005;197(1):61–7.
- [50] Cheng Y, Zou Y, Cheng L, Liu W. Effect of the microstructure on the anti-fouling property of the electroless Ni-P coating. *Mater Lett* 2008;62(27):4283–5.
- [51] Wu Y, Liu T, Luo S. Corrosion characteristics of electroless Ni-P coating in sulfur-bearing solution. *Mater Corros* 2009;60(12):987–90.
- [52] Karthikeyan S, Ramamoorthy B. Effect of reducing agent and nano Al₂O₃ particles on the properties of electroless Ni-P coating. *Appl Surf Sci* 2014;307:654–60.
- [53] Bigdeli F, Allahkaram SR. An investigation on corrosion resistance of as-applied and heat treated Ni-P/nanoSiC coatings. *Mater Des* 2009;30(10):4450–3.
- [54] Xu H, Yang Z, Li M-K, Shi Y-L, Huang Y, Li H-L. Synthesis and properties of electroless Ni-P-Nanometer Diamond composite coatings. *Surf Coat Technol* 2005;191(2–3):161–5.
- [55] Ranganatha S, Venkatesha T, Vathsala K. Process and properties of electroless Ni-Cu-P-ZrO₂ nanocomposite coatings. *Mater Res Bull* 2012;47(3):635–45.
- [56] Sadreddini S, Afshar A. Corrosion resistance enhancement of Ni-P-nano SiO₂ composite coatings on aluminum. *Appl Surf Sci* 2014;303:125–30.

- [57] Zhang LY, Lawrence S, Xu Z, Masliyah JH. Studies of Athabasca asphaltene Langmuir films at air–water interface. *J Colloid Interface Sci* 2003;264(1):128–40.
- [58] Luo H, Leitch M, Behnamian Y, Ma Y, Zeng H, Luo J-L. Development of electroless Ni–P/nano-WC composite coatings and investigation on its properties. *Surf Coat Technol* 2015;277:99–106.
- [59] Kar KK, Sathiyamoorthy D. Influence of process parameters for coating of nickel–phosphorous on carbon fibers. *J Mater Process Technol* 2009;209(6):3022–9.
- [60] Xie L, Wang J, Shi C, Huang J, Zhang H, Liu Q, et al. Probing surface interactions of electrochemically active galena mineral surface using atomic force microscopy. *J Phys Chem C* 2016;120(39):22433–42.
- [61] Wang J, Li J, Xie L, Shi C, Liu Q, Zeng H. Interactions between elemental selenium and hydrophilic/hydrophobic surfaces: direct force measurements using AFM. *Chem Eng J* 2016;303:646–54.
- [62] Xie L, Wang J, Shi C, Cui X, Huang J, Zhang H, et al. Mapping the nanoscale heterogeneity of surface hydrophobicity on the sphalerite mineral. *J Phys Chem C* 2017;121(10):5620–8.
- [63] Liu J, Wang J, Huang J, Cui X, Tan X, Liu Q, et al. Heterogeneous Distribution of Adsorbed Bitumen on Fine Solids from Solvent-Based Extraction of Oil Sands Probed by AFM. *Energy Fuels* 2017;31(9):8833–42.
- [64] Wang J, Xie L, Zhang H, Liu Q, Liu Q, Zeng H. Probing interactions between sphalerite and hydrophobic/hydrophilic surfaces: effect of water chemistry. *Powder Technol* 2017;320:511–8.
- [65] Yang D, Xie L, Bobicki E, Xu Z, Liu Q, Zeng H. Probing anisotropic surface properties and interaction forces of chrysotile rods by atomic force microscopy and rheology. *Langmuir* 2014;30(36):10809–17.
- [66] Gao Z, Xie L, Cui X, Hu Y, Sun W, Zeng H. Probing anisotropic surface properties and surface forces of fluorite crystals. *Langmuir* 2018;34(7):2511–21.
- [67] Hutter JL, Bechhoefer J. Calibration of atomic-force microscope tips. *Rev Sci Instrum* 1993;64(7):1868–73.
- [68] Israelachvili JN. Intermolecular and surface forces. Academic press; 2011.
- [69] Cappella B, Dietler G. Force-distance curves by atomic force microscopy. *Surf Sci Rep* 1999;34(1–3):1–104.
- [70] Tulpur A, Walz J. Simultaneous measurement of structural and hydrodynamic forces between colloidal surfaces in complex fluids. *Colloids Surf A* 2007;300(3):268–80.
- [71] Prieve DC, Russel WB. Simplified predictions of Hamaker constants from Lifshitz theory. *J Colloid Interface Sci* 1988;125(1):1–13.
- [72] Bergstrom L, Meurk A, Arwin H, Rowcliffe DJ. Estimation of Hamaker constants of ceramic materials from optical data using Lifshitz theory. *J Am Ceram Soc* 1996;79(2):339–48.
- [73] Wang M, Revil A. Electrochemical charge of silica surfaces at high ionic strength in narrow channels. *J Colloid Interface Sci* 2010;343(1):381–6.
- [74] Wang S, Liu J, Zhang L, Xu Z, Masliyah J. Colloidal interactions between asphaltene surfaces in toluene. *Energy Fuels* 2008;23(2):862–9.
- [75] Chen G, Warmack R, Huang A, Thundat T. Harmonic response of near-contact scanning force microscopy. *J Appl Phys* 1995;78(3):1465–9.
- [76] Boulangé-Petermann L, Doren A, Baroux B, Bellon-Fontaine M-N. Zeta potential measurements on passive metals. *J Colloid Interface Sci* 1995;171(1):179–86.
- [77] Gong L, Qiu X, Zhang L, Huang J, Hu W, Xiang L, et al. Probing the Interaction Mechanism between Oil-in-Water Emulsions and Electroless Nickel-Phosphorus Coating with Implications for Antifouling in Oil Production. *Energy Fuels* 2018.
- [78] Liu J, Xu Z, Masliyah J. Studies on bitumen – silica interaction in aqueous solutions by atomic force microscopy. *Langmuir* 2003;19(9):3911–20.
- [79] Wu J, Prausnitz JM, Firoozabadi A. Molecular thermodynamics of asphaltene precipitation in reservoir fluids. *AIChE J* 2000;46(1):197–209.
- [80] Das S, Thundat T, Mitra SK. Analytical model for zeta potential of asphaltene. *Fuel* 2013;108:543–9.
- [81] Wang J, Lu Q, Harbottle D, Sjöblom J, Xu Z, Zeng H. Molecular interactions of a polyaromatic surfactant C5Pe in aqueous solutions studied by a surface forces apparatus. *J Phys Chem B* 2012;116(36):11187–96.
- [82] Chaisoontornyotin W, Haji-Akbari N, Fogler HS, Hoepfner MP. Combined asphaltene aggregation and deposition investigation. *Energy Fuels* 2016;30(3):1979–86.
- [83] Shi C, Zhang L, Xie L, Lu X, Liu Q, Mantilla CA, et al. Interaction mechanism of oil-in-water emulsions with asphaltenes determined using droplet probe AFM. *Langmuir* 2016;32(10):2302–10.
- [84] Mo H, Tay KG, Ng HY. Fouling of reverse osmosis membrane by protein (BSA): effects of pH, calcium, magnesium, ionic strength and temperature. *J Membr Sci* 2008;315(1–2):28–35.
- [85] Elimelech M, Zhu X, Childress AE, Hong S. Role of membrane surface morphology in colloidal fouling of cellulose acetate and composite aromatic polyamide reverse osmosis membranes. *J Membr Sci* 1997;127(1):101–9.
- [86] Hamza A, Pham V, Matsuura T, Santerre J. Development of membranes with low surface energy to reduce the fouling in ultrafiltration applications. *J Membr Sci* 1997;131(1–2):217–27.

Interaction Mechanisms of Zwitterions with Opposite Dipoles in Aqueous Solutions

Lu Gong,[†] Li Xiang,[†] Jiawen Zhang,[†] Linbo Han,^{†,‡} Jingyi Wang,[†] Xiaogang Wang,[§] Jifang Liu,^{†,||} Bin Yan,^{*,†,⊥} and Hongbo Zeng^{*,†}

[†]Department of Chemical and Materials Engineering, University of Alberta, Edmonton, Alberta T6G 1H9, Canada

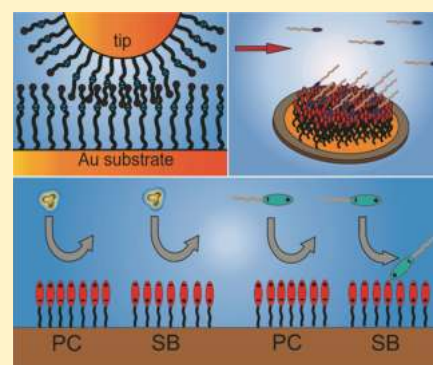
[‡]College of Health Science and Environmental Engineering, Shenzhen Technology University, Shenzhen 518118, China

[§]College of Material Science & Engineering, Heavy Machinery Engineering Research Center of Education Ministry, Taiyuan University of Science and Technology, Taiyuan 030024, China

^{||}The Fifth Affiliated Hospital, Guangzhou Medical University, Guangzhou, Guangdong 510700, China

[⊥]College of Light Industry, Textile & Food Engineering, Sichuan University, Chengdu 610065, China

ABSTRACT: Zwitterionic groups have been widely used in antibiofouling surfaces to resist nonspecific adsorption of proteins and other biomolecules. The interactions among zwitterionic groups have attracted considerable attention in bioengineering, whereas the understanding of their nanomechanical mechanism still remains limited. In this work, the interaction mechanisms between two zwitterionic groups with opposite dipoles, i.e., phosphorylcholine (PC) and sulfobetaine (SB), have been investigated via direct force measurements using an atomic force microscope (AFM) and dynamic adsorption tests using the quartz crystal microbalance with dissipation monitoring technique (QCM-D) in aqueous solutions. The AFM force measurements show that the adhesive forces between contacted zwitterionic surfaces during separation in both symmetric and asymmetric configurations were close, mainly due to the enforced alignment of opposing dipole pairs via complementary orientations under confinement. The solution salinity and pH had almost negligible influence on the adhesion measured during surface separation. The QCM-D adsorption tests of PC-headed lipid on PC and SB surfaces showed some degree of adsorption of lipid molecules on the SB surface, whereas not on the PC surface. The different adsorption behaviors indicate that because the outermost negatively charged sulfonic group on the SB faced the aqueous solution, this configuration could facilitate it to form an attractive electrostatic interaction with the PC head of lipid molecules in the solution. This work shows that in addition to hydration and steric interactions, the zwitterionic dipole-induced interactions play an important role in the adhesion and antifouling behaviors of the zwitterionic molecules and surfaces. The improved fundamental understanding provides useful insights into the development of new functional materials and coatings with antifouling applications.



INTRODUCTION

Functional materials with zwitterionic groups, inspired by the bioinert nature of the cell membrane surface, have received considerable attention because of their effective nonfouling capability to resist nonspecific protein adsorption in aqueous solutions.^{1–4} The developed zwitterionic materials, with excellent antibiofouling and biocompatible properties,^{5–11} have been utilized in different bioengineering areas such as antifouling coatings and biomedical devices.^{12–16} Much effort has been devoted to the experimental and theoretical understandings of the protein resistance properties of zwitterions or zwitterionic surfaces in aqueous solutions,^{17–19} which is considered mainly due to the hydration repulsion associated with surfaces.^{19–21}

Zwitterions or zwitterionic groups can be generally divided into two types. (1) The first type has a structure like phosphorylcholine (PC) with a positively charged choline group facing the surrounding aqueous medium and a

negatively charged phosphate group linked to the main body of the molecule or the substrate. (2) The second type shows reversed dipole moment as the first type such as the sulfobetaine (SB) group with the negatively charged sulfonic group directly facing the medium.^{20,22–24} Zwitterionic polar head groups of lipid molecules can influence the properties of the lipid membrane, such as protein adsorption, ion binding, and membrane fluidity.^{20,25–30} Many previous studies have investigated the interactions between both types of zwitterionic groups and the surrounding molecules such as proteins and other biomolecules. However, the understanding of interaction mechanisms among the zwitterionic groups still remains very limited. Thus, understanding the interactions between the

Received: December 9, 2018

Revised: January 28, 2019

Published: January 29, 2019

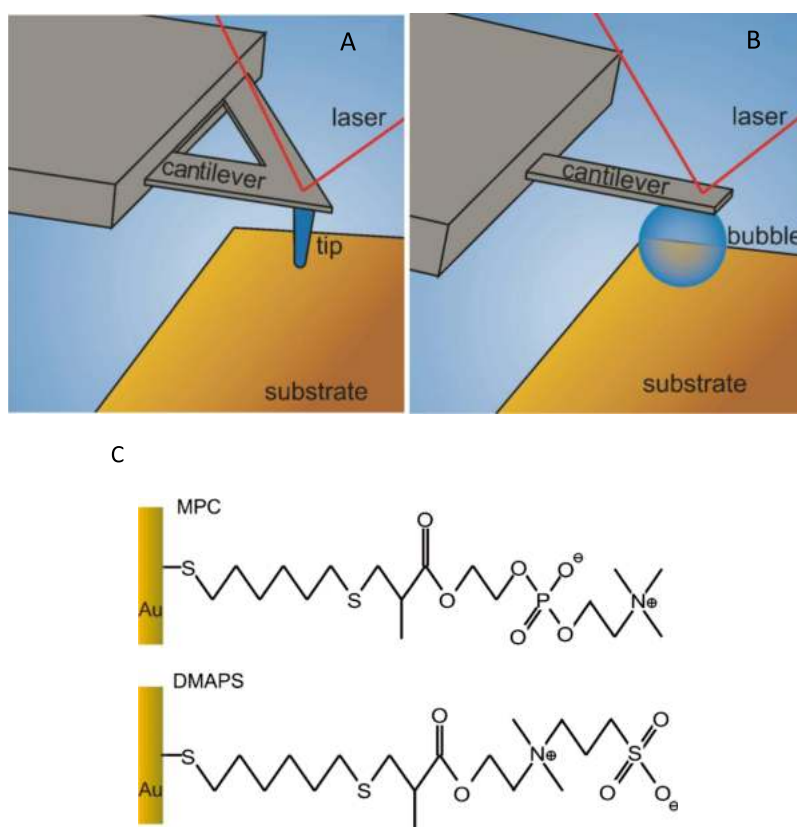


Figure 1. Schematic illustration of (A) the AFM tip probe technique and (B) the AFM bubble probe technique for measuring surface forces. (C) Schematic illustration of MPC and DMAPS surfaces on the gold substrate.

zwitterions with opposite dipoles is of both fundamental and practical importance.

In this work, for the first time, the interactions between two zwitterionic groups carrying the opposite dipoles (i.e., PC and SB groups) in aqueous solutions have been quantified using atomic force microscope (AFM) force measurements and the quartz crystal microbalance with dissipation monitoring (QCM-D). The influences of solution salinity and pH were also investigated. To this end, a small molecule with the PC group and the thiol group (MPC-SH) was synthesized from 2-methacryloyloxyethyl phosphorylcholine (MPC) and 1,6-hexanedithiol, whereas a small molecule with the SB group and the thiol group (DMAPS-SH) was synthesized from 3-[dimethyl(2-methacryloyloxyethyl)ammonium]propane sulfonate (DMAPS) and 1,6-hexanedithiol. Zwitterionic PC and SB groups were grafted on gold surfaces through the Au–S bond. The force measurements between the zwitterionic groups were conducted in both symmetric and asymmetric configurations to elucidate the interaction mechanisms with the opposite dipole. The surface charge properties of MPC and DMAPS surfaces in aqueous solutions were quantitatively probed using the AFM bubble probe technique. Besides, the dynamic adsorption behaviors of PC-headed lipids on the zwitterionic PC and SB surfaces have been explored using the QCM-D. Our work provides useful insights into the fundamental understanding of the intermolecular interactions of zwitterions and the related fouling/antifouling behaviors, with implications for developing new functional materials and coatings with antifouling applications.

MATERIALS AND METHODS

Materials. Sodium chloride, potassium chloride, and potassium hydroxide were purchased from Sigma-Aldrich, Canada. Milli-Q water with a resistivity of 18.2 MΩ cm (BARNSTEAD Smart2Pure, Thermo Scientific, Canada) was used to prepare aqueous solutions. Gold wafer was purchased from Sigma-Aldrich and used as received. Sodium hydroxide (ACS reagent, Sigma-Aldrich, Canada) and hydrochloric acid (certified ACS Plus, Fisher Scientific, Canada) were used to adjust solution pH. 2-Methacryloyloxyethyl phosphorylcholine, 3-[dimethyl(2-methacryloyloxyethyl)ammonium]propane sulfonate, methanol, and diisopropylamine were purchased from Sigma-Aldrich, Canada. 1,6-Hexanedithiol (SH(CH₂)₆SH) and hexane was purchased from Fisher Scientific, Canada.

Synthesis of MPC-SH and DMAPS-SH. The chemical synthesis of MPC-SH and DMAPS-SH followed a reported procedure.³¹ The typical synthesis for MPC-SH was shown as follows. 2-Methacryloyloxyethyl phosphorylcholine (1.8 g) and 1,6-hexanedithiol (1.2 μL) were dissolved in 50 mL methanol (Sigma-Aldrich, Canada) and the solution was degassed using pure nitrogen for 30 min. With the addition of 50 μL diisopropylamine (Sigma-Aldrich, Canada), the reaction was kept at room temperature overnight. The solution was then dried at 50 °C with a rotary evaporator and the white solids obtained were washed with hexane (Fisher Scientific, Canada) several times to remove the excess 1,6-hexanedithiol and diisopropylamine. After drying in a vacuum desiccator overnight, the MPC-SH solids were collected and stored in a glass vial. According to the reported results, the product efficiency of the reaction reached almost 88 mol %.³¹ The DMAPS-SH was synthesized using the same procedure except that 3-[dimethyl(2-methacryloyloxyethyl)ammonium]propane sulfonate was used. The successful synthesis of MPC-SH and DMAPS-SH was confirmed using ¹H NMR analysis.

MPC-SH ¹H NMR spectrum (400 MHz, in DMSO-*d*₆). δ = (ppm): 1.12–1.14 (3H, –CH₃), 1.32–1.49 (8H, –CH₂CH₂CH₂CH₂–), 2.48 (9H, –N(CH₃)₃), 2.53–2.69 (6H,

–SCH₂–; 1H, –CH–COO–), 3.11 (2H, –CH₂–N–), 3.48–3.50 (2H, –COO–CH₂–), 4.00–4.13 (4H, –CH₂–PO₄–CH₂–).

DMAPS-SH ¹H NMR spectrum (400 MHz, in DMSO-*d*₆). δ = (ppm): 1.20–1.22 (3H, –CH₃), 1.35–1.57 (8H, –CH₂CH₂CH₂CH₂–; 2H, –CH₂–CH₂–SO₃), 2.41–2.46 (6H, –SCH₂–; 1H, –CH–COO–), 2.48 (9H, –N(CH₃)₃), 3.34–3.43 (4H, –CH₂–N–CH₂–), 3.79 (2H, –COO–CH₂–), 4.03–4.10 (4H, –CH₂–SO₃–).

Preparation of the Surfaces with Zwitterionic PC and SB Groups. The surfaces with zwitterionic PC and SB groups were prepared on gold wafers. First, MPC-SH and DMAPS-SH solutions were prepared by dissolving the solids in methanol to prepare 5 mM solutions. Gold wafers were washed using Milli-Q water and ethanol and dried with pure nitrogen. Then, the cleaned gold wafers were treated in UV ozone for 15 min prior to use. MPC and DMAPS surfaces were prepared by immersing gold wafers in 5 mM MPC-SH and DMAPS-SH solutions for 12 h at room temperature (23 °C). It should be noted that the excess 1,6-hexanedithiol was washed and removed using pure hexane, and the side product, 1,6-hexanedithiol with MPC or DMAPS at both ends, cannot adsorb on the gold surface due to the absence of the thiol group. Only MPC-SH or DMAPS-SH could graft onto the gold substrate to prepare the zwitterionic substrates.³¹ Thereafter, the wafers were washed using Milli-Q water and pure ethanol, and dried using pure nitrogen. The PC and SB surfaces were kept in a vacuum desiccator before other experiments. The scheme of PC and SB surfaces are shown in Figure 1.

Cyclic Voltammetry (CV) for Determining MPC or DMAPS Graft Density. The electrochemical experiments were performed to determine the surface density of MPC and DMAPS on the substrates using a CHI 920c scanning electrochemical microscope (CH Instruments Inc., Austin TX). The detailed experimental setup has been reported previously.^{31–34} The three-electrode cell was constructed using a platinum wire as the counter electrode, an Ag/AgCl/3.4 M KCl microelectrode as the reference electrode, and the prepared MPC or DMAPS substrate as the working electrode. The electrochemical experiments of CV were conducted in the solution of 0.5 M KOH and 3.3 M KCl within the range of –0.2 and –1.3 V at a scanning speed of 0.5 V/s. The solution was first purged using pure nitrogen for 30 min. The CV curves were then obtained. The reduction peaks at –0.8 to –1.0 V in the CV profiles were attributed to the transformation of charges from the electrode to the thiol during the reductive adsorption. The number density of alkanethiol was calculated using eq 1

$$\gamma = \frac{Q_{\text{SAM}} \times N_A}{F} \quad (1)$$

where γ is the surface number density of alkanethiol, Q_{SAM} is the total surface charge density determined by the reductive peak area, scan speed and electrode surface area, N_A is the Avogadro constant, and F is the Faraday constant.

Force Measurements between MPC and DMAPS Surfaces in Aqueous Solutions. The interactions between MPC and DMAPS surfaces in aqueous solutions were investigated using an atomic force microscope (AFM) tip probe technique in symmetric and asymmetric configurations, as illustrated in Figure 1A. The force measurements were conducted using an MFP-3D-BIO AFM (Asylum Research, Santa Barbara, CA). The detailed force measurement procedures have been reported previously.³⁵ Before experiments, the gold AFM probes (NPG-10, Bruker, Santa Barbara, CA) were immersed in 5 mM MPC or DMAPS solutions for 12 h to prepare the PC and SB surfaces, respectively, followed by a thorough washing with Milli-Q water and ethanol. The spring constants of these AFM probes were calibrated using the thermal tune method.

In each force measurement, both the AFM probe and the prepared MPC/DMAPS substrate were first immersed in the aqueous solutions. The AFM probe was driven by a piezo to approach the substrate at a velocity of 1 $\mu\text{m/s}$ until a maximum loading force of 5 nN was reached and then retracted from the substrate. The interaction force was measured via detecting the deflection of the cantilever and recorded as a function of the surface separation. For

each case, force measurements were conducted at 20 different spots on a selected substrate and at least two independently prepared substrates were tested.

Surface Potentials of MPC and DMAPS Surfaces in NaCl Solutions. The surface potentials of PC and SB surfaces in NaCl solutions were quantified using the bubble probe AFM technique, as illustrated in Figure 1B. The detailed experimental setup has been reported previously.^{36–41} Briefly, prior to the experiments, a circular glass slide of the AFM fluid cell was immersed in 5 mM octadecyltrichlorosilane in ethanol solution for ~15 s to obtain a slight hydrophobicity of ~50° water contact angle (WCA), which was suitable to attach an air bubble on the substrate in aqueous solutions. A custom-made rectangular silicon AFM cantilever with a gold patch was also hydrophobized to allow it to pick up the air bubble. The spring constant of the AFM cantilever was calibrated and determined using the thermal tune method in the aqueous solution before the bubble loading. An air bubble was carefully generated in the aqueous solution on the hydrophobic glass slide using an ultra-sharp glass pipet. The prepared MPC/DMAPS substrate was carefully immersed in the fluid cell and placed near the air bubble. The hydrophobized cantilever was moved to pick the air bubble off the glass slide to generate a bubble probe and then moved over the substrate for force measurements in aqueous solutions.

During force measurements, the bubble probe was driven by a piezo to approach the substrate at a velocity of 1 $\mu\text{m/s}$ until a certain deflection of 1 μm was reached and then the cantilever was lifted up. The moving velocity of 1 $\mu\text{m/s}$ was set to reduce the hydrodynamic effects. The deflection of the cantilever was monitored using an optical laser beam detection system. Therefore, the time and force profiles were obtained and recorded, which were further analyzed using a theoretical model described below.

To quantitatively analyze the surface potentials of MPC and DMAPS surfaces in NaCl solutions, a theoretic model based on the Reynolds lubrication theory and augmented Young–Laplace equation was used to fit the AFM force profiles. To describe the shape deformation of the bubble responding to the external pressure, such as hydrodynamic pressure and disjoining pressure, the augmented Young–Laplace equation given by eq 2 was applied.⁴²

$$\frac{\sigma}{r} \frac{\partial}{\partial r} \left(r \frac{\partial h}{\partial r} \right) = \frac{2\sigma}{R} - \Pi - p \quad (2)$$

where σ is the interfacial tension between the bubble and aqueous solution, r is the radial coordinate, h is the thickness of the confined liquid film between the bubble and the solid substrate, R is the radius of the bubble, Π is the disjoining pressure, and p is the excess hydrodynamic pressure. To describe the drainage phenomena of confined fluid between the bubble and the substrate, Reynolds lubrication theory shown in eq 3 was applied.⁴²

$$\frac{\partial h}{\partial t} = \frac{1}{12\mu r} \frac{\partial}{\partial r} \left(rh^3 \frac{\partial p}{\partial r} \right) \quad (3)$$

Here, t is the time and μ is the viscosity of the aqueous solution. The overall interaction force between the bubble and the substrate $F(t)$ was calculated from the integration of the hydrodynamic pressure and the disjoining pressure based on the Derjaguin approximation given by eq 4.

$$F(t) = 2\pi \int_0^\infty [p(r, t) + \Pi(r, t)] \cdot r \, dr \quad (4)$$

Dynamic Adsorption of PC-Headed Lipids on MPC and DMAPS Surfaces. The dynamic adsorption behaviors of PC-headed lipid, i.e., 1,2-dipalmitoyl-*sn*-glycerol-3-phosphocholine (DPPC), on MPC and DMAPS surfaces in aqueous solution were studied using the QCM-D (Biolin Scientific, Sweden). Before the experiments, gold-coated quartz sensors were cleaned using Milli-Q water and ethanol and dried with pure nitrogen, and then treated in UV ozone for 30 min. Thereafter, the treated sensors were placed in the 5:1:1 solution of Milli-Q water, ammonia (25%), and hydrogen peroxide (30%) at 75 °C for 15 min. Finally, these sensors were treated with

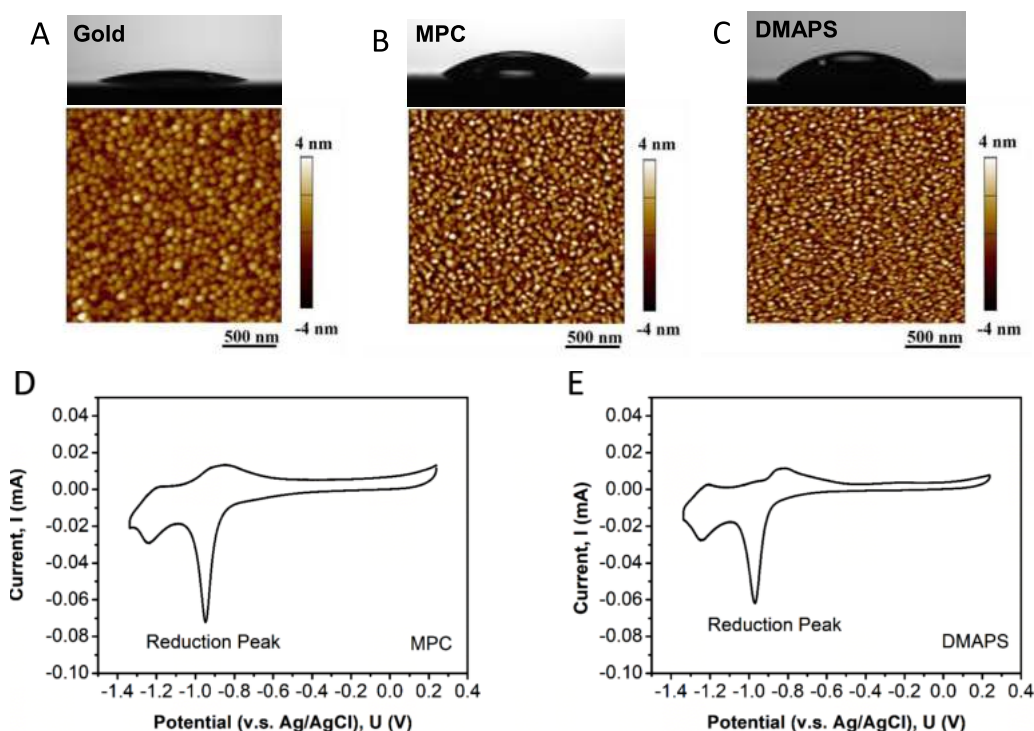


Figure 2. (A–C) Water contact angle (WCA) and AFM topographic images of bare gold (A), MPC (B), and DMAPS (C) surfaces in air. The WCAs of bare gold, MPC, and DMAPS surfaces are $<5^\circ$, $10.2^\circ \pm 0.8^\circ$, and $18.4^\circ \pm 0.7^\circ$, respectively. The root-mean-square roughness (rms) of bare gold, MPC, and DMAPS surfaces are measured to be 0.95, 1.55, and 1.49 nm, respectively. (D, E) Cyclic voltammetry (CV) curves of MPC (D) and DMAPS (E) substrates on gold substrates.

UV ozone for another 10 min. The MPC and DMAPS surfaces were prepared by immersing the cleaned gold sensors in 5 mM of MPC-SH and DMAPS-SH solution, respectively. The PC-headed DPPC solution was prepared in 1 mM NaCl solutions with a concentration of 20 ppm. In the experiments, the DPPC solution was driven using a pump to flow onto the MPC or DMAPS sensor mounted in the QCM-D chamber at a rate of 350 $\mu\text{L}/\text{min}$. Meanwhile, the changes of frequency (Δf) and energy dissipation (ΔD) were simultaneously monitored as a function of time by the QCM-D controller and recorded by the Q-sense software.

RESULTS AND DISCUSSION

Characterization of MPC and DMAPS Surfaces. Figure 2A–C show the water contact angles (WCAs) and AFM topographic images of bare gold, MPC, and DMAPS surfaces in air, respectively. The WCAs of bare gold, MPC, DMAPS surfaces were measured to be $<5^\circ$, $10.2^\circ \pm 0.8^\circ$, and $18.4^\circ \pm 0.7^\circ$, respectively. The AFM topographic images in Figure 2 show that the root-mean-square roughness (rms) of bare gold, MPC, and DMAPS substrates are 0.95, 1.55, and 1.49 nm, respectively. The changes of the WCAs and surface morphologies of the substrates indicate the successful deposition of the MPC and DMAPS on gold substrates.

The surface densities of MPC and DMAPS on gold wafer were determined using the cyclic voltammetry (CV) method.^{33,34} Figure 2C,D show the measured cyclic voltammetry curves of MPC and DMAPS surfaces in the solution of 0.5 M KOH and 3.3 M KCl. The reduction peaks indicate the electron transferring due to the desorption process of the thiol group on the gold surface, which were determined at around -0.95 V in the first scan. The surface densities of MPC and DMAPS on the substrates were then calculated from

these reduction peaks to be 3.2 and 2.8 chains/ nm^2 , respectively, which are very close to the reported values.³¹

Force Measurements between PC and SB Groups in Aqueous Solutions. Prior to the force measurements, MPC and DMAPS were deposited on both AFM probes and gold substrates. The force measurements between PC and SB groups were conducted in both symmetric and asymmetric configurations in 1 mM NaCl solutions (natural pH 5.6) and the results are shown in Figure 3.

Figure 3B shows the measured force curves in a symmetric configuration in 1 mM NaCl solution, where the MPC probe interacts with the MPC substrate and the DMAPS probe interacts with the DMAPS substrate. Repulsive forces were detected during approaching (or tracing) for both cases. According to the classical Derjaguin–Landau–Verwey–Overbeek theory, the van der Waals (VDW) force and electric double layer (EDL) force contribute to the interactions between the two surfaces in aqueous solutions. Since the VDW force was attractive for the symmetric system here,⁴³ the detected repulsion was mainly attributed to the repulsive EDL interaction. Generally, the zwitterionic group is stoichiometrically neutral. However, the previous study demonstrated that both PC and SB groups are negatively charged in electrolyte solutions, due to the different binding abilities of the positively charged group and the negatively charged group of the zwitterionic groups to the surrounding counterions.⁴⁴ The positively charged quaternary ammonium group possesses a stronger binding ability with anions (such as Cl^- , OH^-) than that of the negatively charged phosphate group or the sulfonate group with cations (such as Na^+ , H^+).⁴⁵ Therefore, the repulsion measured in 1 mM NaCl mainly arise from the EDL interaction between the negatively charged MPC and DMAPS surfaces. Figure 3B also shows that the repulsion between two

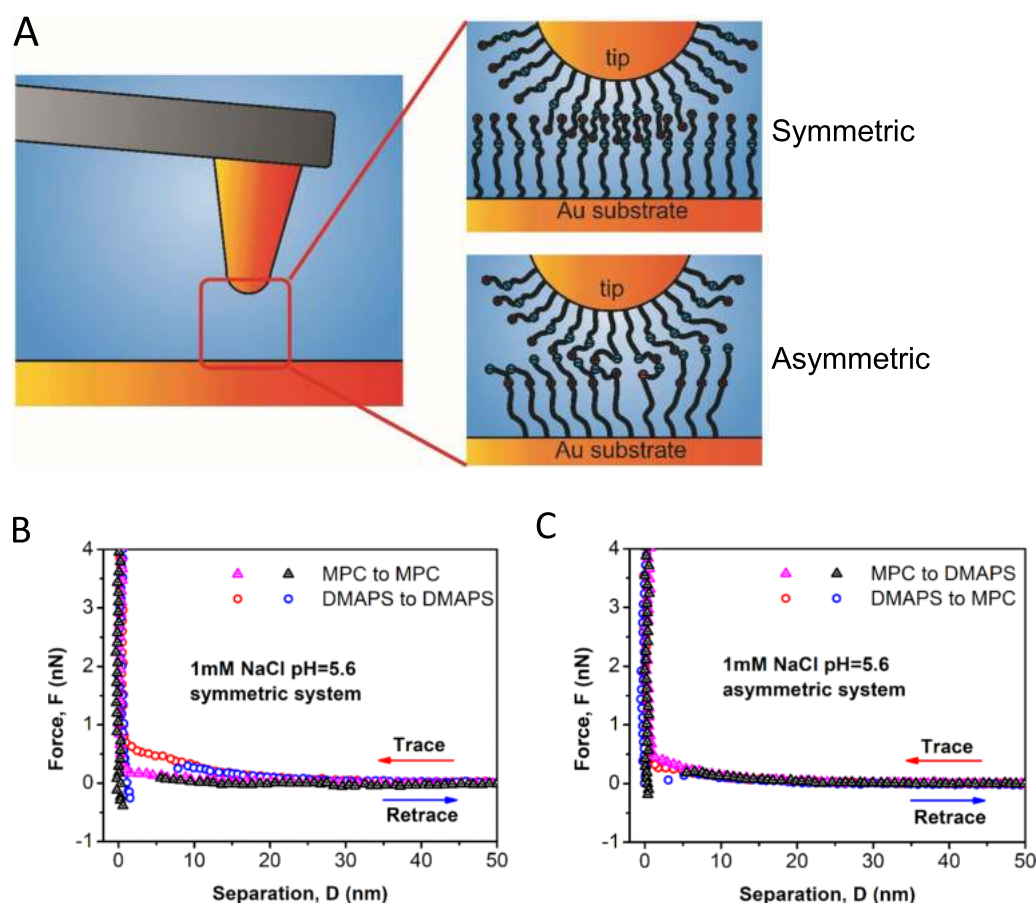


Figure 3. (A) Schematic illustration of the interactions between zwitterionic groups in both symmetric and asymmetric configurations in AFM force measurements. (B) Measured force curves in symmetric configurations (i.e., MPC vs MPC and DMAPS vs DMAPS) in 1 mM NaCl solution. (C) Measured force curves in asymmetric configuration (i.e., MPC vs DMAPS) in 1 mM NaCl solution.

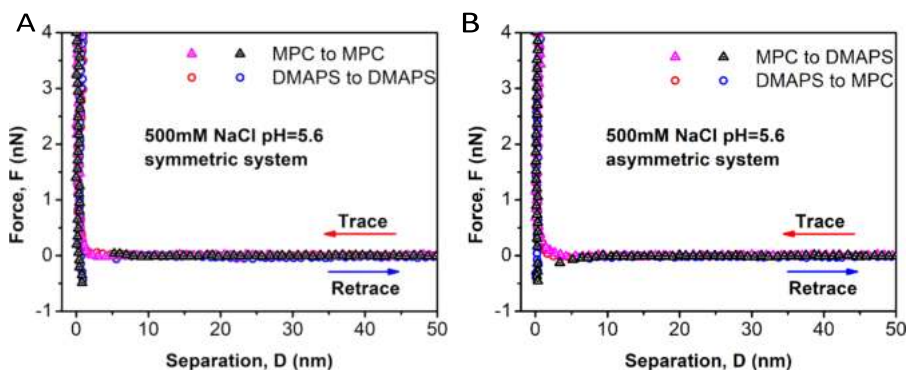


Figure 4. (A) Measured force profiles in symmetric configuration between the two MPC surfaces and two DMAPS surfaces in 500 mM NaCl solution. (B) Measured force curves of asymmetric systems (MPC vs DMAPS) in 500 mM NaCl solution.

DMAPS surfaces is stronger than that between two MPC surfaces, indicating that the DMAPS surface has more negative surface potential than the MPC surface.

During the retraction process (Figure 3B), adhesion has been detected in both MPC and DMAPS symmetric systems with a similar force magnitude. The measured adhesion is most likely originated from the attractive electrostatic interactions between the zwitterionic groups aligned during contact (Figure 3A). During the force measurement, the MPC and DMAPS layers on the substrate could be interpenetrated by the opposing MPC or DMAPS molecules on the AFM probe,²⁰ leading to close contact of the zwitterionic groups. Therefore,

the contacted zwitterionic groups with the same dipoles could be forced to align in an antiparallel orientation showing that an attractive electrostatic interaction occurs.⁴⁶ Since the dipole momentums of the PC and SB groups are very close to each other,⁴⁷ similar adhesion was measured for the two symmetric cases. It should be noted that the type of ions has been reported to affect the behaviors of the zwitterionic groups in aqueous solutions and also their dipole momentum.^{48,49} Stronger binding affinity of the zwitterionic groups with the surrounding counterions results in the greater screening effect and weakened electrostatic attraction between the positive charge and the negative charge of the zwitterionic group, which

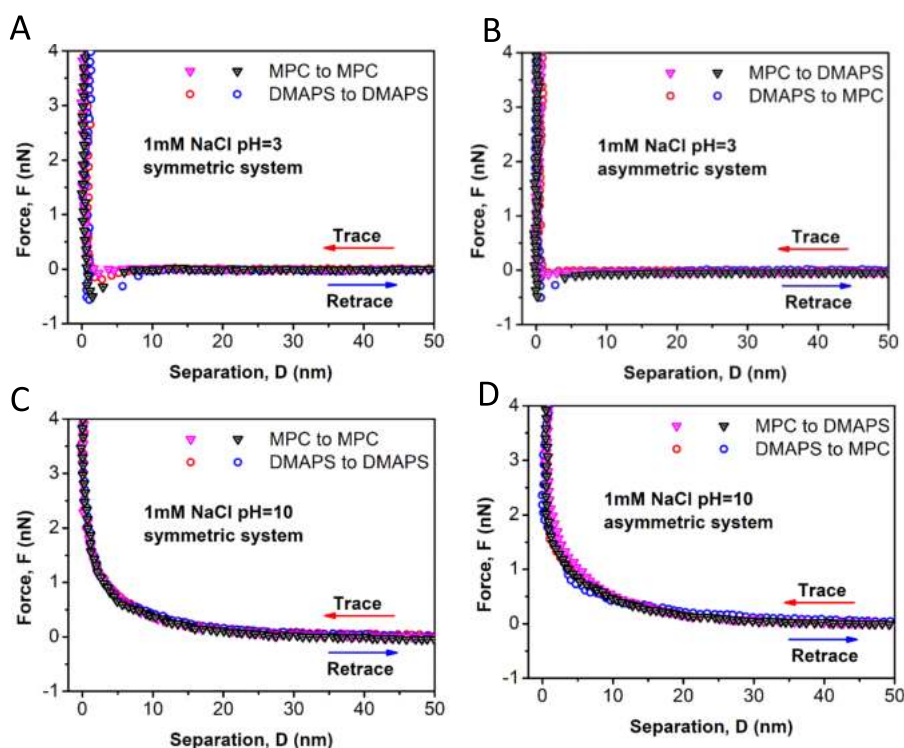


Figure 5. (A, B) Measured force curves of symmetric (A) and asymmetric (B) systems of MPC and DMAPS surfaces in 1 mM NaCl solution with pH 3. (C, D) Measured force curves of symmetric (C) and asymmetric (D) systems of MPC and DMAPS surfaces in 1 mM NaCl solution with pH 10.

leads to the changes of the dipole momentum. Therefore, the interaction behaviors between zwitterionic groups could be affected by the ion types in the aqueous solutions. In this work, only NaCl was present in the aqueous solutions to investigate the effects of salinity and pH.

Figure 3C shows that the measured force curves in asymmetric configurations, where the MPC probe interacts with the DMAPS substrate and the DMAPS probe interacts with the MPC substrate in 1 mM NaCl solution. Both force curves appear to be almost the same. Similar to the symmetric system, repulsion was detected during approaching, which was mainly due to the electrostatic repulsion of the negatively charged MPC and DMAPS surfaces in 1 mM NaCl solution. Adhesion was measured during the retraction process, which was almost the same for the two measurements (Figure 3C). In the asymmetric system, the opposing zwitterionic groups with opposite dipoles could be forced to induce alignment shown in Figure 3A, resulting in the adhesion measured.

Effect of Salt Concentration on the Interactions between PC and SB Groups. As discussed above, the repulsive EDL force plays an important role in the measured interactions during the approaching of zwitterionic surfaces in aqueous solution of low salinity (i.e., 1 mM NaCl). It is well-known that high salinity conditions could significantly influence the interfacial interactions by compressing the electrical double layer.⁴³ Thus, the interactions between MPC and DMAPS surfaces have been also investigated in 500 mM NaCl solution and the force profiles are shown in Figure 4.

Figure 4A shows the measured force curves of symmetric systems in 500 mM NaCl solution. Under such high salinity conditions, the Debye length is reduced to be less than 1 nm and the repulsive EDL force is negligible, which agrees with the

short-range repulsion measured during approaching (Figure 4A). The short-range repulsion at <3 nm could be mainly attributed to the hydration repulsion between the zwitterionic surfaces, which is considered as the major reason for the antibiofouling properties of zwitterionic surfaces. Adhesion was measured during surface retraction, which was close to the adhesion measured in dilute solution (i.e., 1 mM NaCl) and caused by the interactions between the aligned zwitterionic groups with the same dipoles. Figure 4B shows the measured force curves of the asymmetric system in 500 mM NaCl solution, which are similar to that for the symmetric system. The hydration repulsion contributes to the short-range surface repulsion of the measured force profiles, whereas the adhesion measured during surface separation are caused by the aligned zwitterionic groups with opposite dipoles during contact.

Effect of pH on the Interaction Forces between PC and SB Groups. The pH of aqueous solution generally plays an important role in the interactions of two charged surfaces in aqueous solutions. Adjusting solution pH could result in changes of the surface potentials, which thereby strengthens or weakens the EDL interactions between the two surfaces.⁴³ To better understand the interaction behaviors among zwitterionic groups, the interactions between MPC and DMAPS surfaces have also been investigated in 1 mM NaCl solutions under acidic (pH = 3) and alkaline (pH = 10) pH conditions, and the force profiles are shown in Figure 5.

Figure 5A shows the measured force curves of the symmetric system in 1 mM NaCl solution with acidic pH (pH = 3). It is noted that no repulsion was detected during surface approaching in symmetric configuration compared to the force profiles in 1 mM NaCl solution with pH 5.6 (Figure 3A). Under acidic conditions (i.e., pH 3), negatively charged zwitterionic PC or SB surfaces would be mostly neutralized by

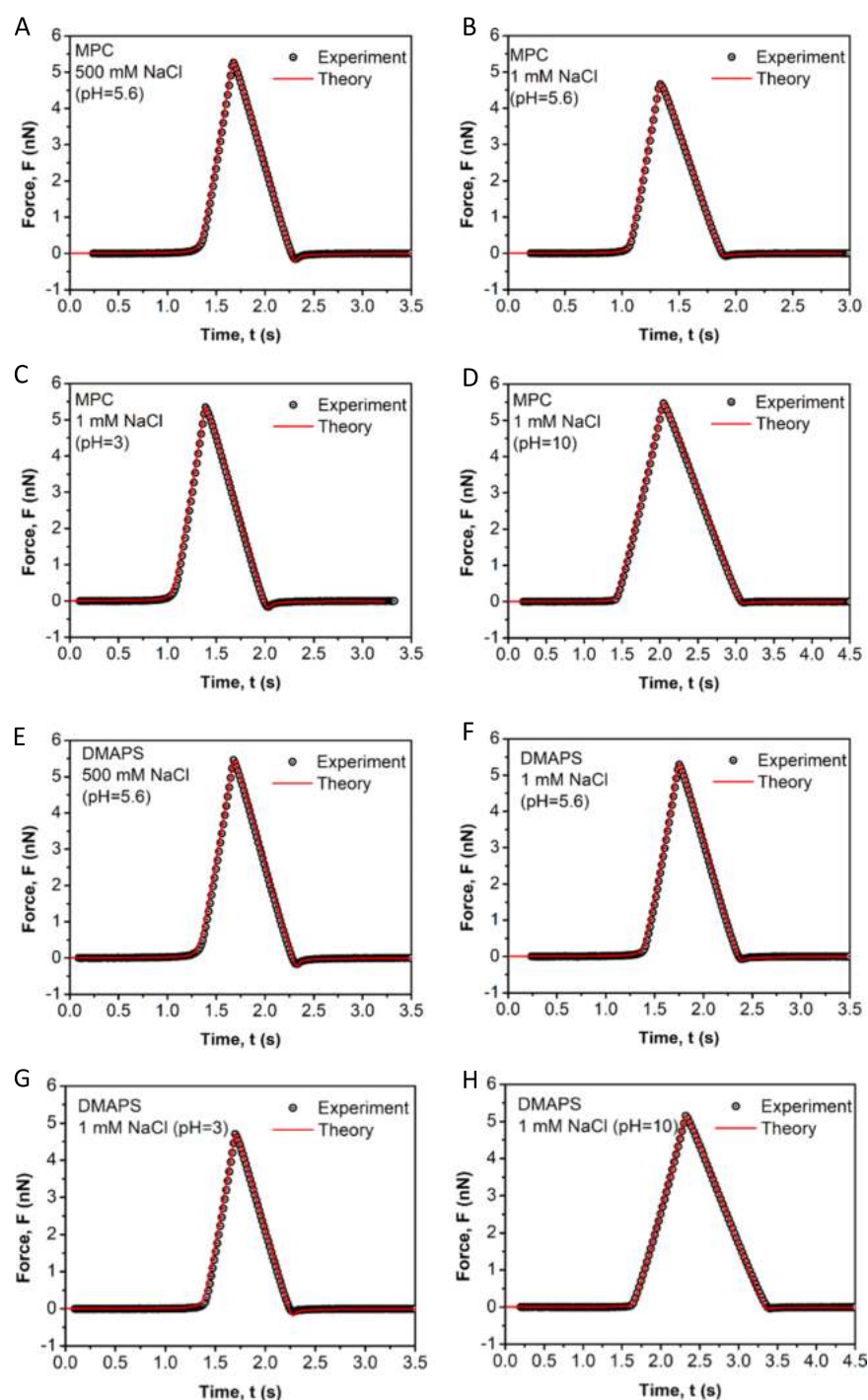


Figure 6. (A–D) Measured force curves (black open symbols) and theoretically calculated curves (red solid curves) between the air bubble and (A) MPC in 500 mM NaCl solution with pH 5.6, (B) in 1 mM NaCl solution with pH 5.6, (C) in 1 mM NaCl solution with pH 3, and (D) in 1 mM NaCl solution with pH 10. (E–H) Measured force curves and theoretical curves between the air bubble and (E) DMAPS in 500 mM NaCl solution with pH 5.6, (F) in 1 mM NaCl solution with pH 5.6, (G) in 1 mM NaCl solution with pH 3, and (H) in 1 mM NaCl solution with pH 10.

protons (H^+) from the bulk solution,^{50,51} leading to less negative surface potentials, thus the repulsive EDL interaction would be weakened. Therefore, the attractive VDW force would become dominant during the approaching process which led to “jump in” behavior as shown in Figure 5A,B. Since the adhesion measured in both symmetric and asymmetric configurations in acidic pH is close to that measured under natural pH (Figure 3A,B), lowering the pH of the solution

would not significantly affect the enforced complementary alignment of the zwitterionic groups.

Figure 5C,D show the measured force curves of symmetric systems (i.e., MPC vs MPC and DMAPS vs DMAPS) and asymmetric systems (i.e., MPC vs DMAPS), respectively, in 1 mM NaCl solution with alkaline pH (pH = 10). Different from the force curves measured at pH 3, stronger repulsive forces have been detected at pH 10, indicating the strengthened

repulsive EDL forces between two zwitterionic surfaces.⁴³ In the presence of such strong EDL repulsion, MPC and DMAPS surfaces would not be able to contact with each other and attractive dipole–dipole interactions of the zwitterionic PC and SB groups would not be achieved. Thus, no adhesion was detected during the retraction process.

Surface Potentials of MPC and DMAPS Surfaces in Aqueous Solutions. The above force measurements show that the MPC and DMAPS surfaces in NaCl solutions become more negatively charged with increasing pH of aqueous solutions, which is consistent with previous reports.^{52,53} The AFM bubble probe technique has been applied to quantify the surface potentials of MPC and DMAPS surfaces in aqueous solutions. This method has been widely used to investigate the interfacial interactions and surface properties of minerals, polymer surfaces, bubbles, and drops.^{36,38,54} The force profiles between the air bubble and MPC or DMAPS surface in NaCl solutions have been measured, as shown in Figure 6, which were analyzed using the theoretical model based on the Reynolds lubrication theory and augmented Young–Laplace equation. Using the reported surface potentials of air bubbles in NaCl solutions of different salinities and pH conditions (Table 1),^{36,37,55} the surface potentials of MPC and DMAPS surfaces were determined. The experimental (black dots) and theoretically calculated (red line) force curves are shown in Figure 6.

Table 1. Hamaker Constants (for Air Bubble–Water–Substrate) and Surface Potentials of Air Bubble and MPC/DMAPS Surfaces in NaCl Solutions

substrate	Hamaker constant (J)	1 mM NaCl		
		pH = 3	pH = 5.6	pH = 10
bubble		−1 mV	−28 mV	−50 mV
MPC	-2.0×10^{-20}	−5 mV	−11 mV	−19 mV
DMAPS	-1.6×10^{-20}	−5 mV	−18 mV	−27 mV

Figure 6A shows the measured force profile between the air bubble and MPC substrate in 500 mM NaCl solution. Under such high salinity, electric double layer is significantly compressed and the repulsive EDL force is negligible. Therefore, only van der Waals force is considered and the Hamaker constant (for air bubble–water–substrate) was calculated to be -2.0×10^{-20} J (Table 1). The negative Hamaker constant between the air bubble and the MPC surface in 500 mM NaCl solution indicates that the VDW interaction in this case was repulsive, which is in consistent with the fact that the MPC substrate is superhydrophilic and the air bubble is repelled from the substrate. Figure 6B–D show the measured force profiles between the air bubble and MPC substrate in 1 mM NaCl solutions with pH 5.6, 3 and 10, respectively. The surface potentials of the MPC surface in the NaCl solutions of pH 3, 5.6, and 10 were determined to be −5, −11, and −19 mV, respectively (Table 1). It is noted that the surface potential becomes more negative with increasing solution pH, which is consistent with previous reports.^{50,56} Figure 6E–H show the measured force curves between the air bubbles and DMAPS substrate in 500 mM NaCl solution and 1 mM NaCl solutions with pH 5.6, 3 and 10, respectively. Similarly, the Hamaker constant between the air bubble and DMAPS substrate in 500 mM NaCl solution was first calculated to be -1.6×10^{-20} J (Table 1). The surface potentials of DMAPS surface in 1 mM NaCl solutions with pH

of 3, 5.6, and 10 were determined to be −5, −18, and −29 mV (Table 1), respectively. The above results indicate that the DMAPS surface are more negatively charged than the MPC substrate under the same aqueous solution conditions, which is consistent with previous reports.^{57–59}

Dynamic Adsorption Behavior of Zwitterionic Lipids on MPC and DMAPS Surfaces in Aqueous Solution. To better understand the interaction and adsorption behaviors between zwitterionic groups with opposite dipoles, zwitterionic PC-headed lipid, 1,2-dipalmitoyl-*sn*-glycerol-3-phosphocholine (DPPC), has been employed to investigate its dynamic adsorption on MPC and DMAPS surfaces using the quartz crystal microbalance with dissipation monitoring technique (QCM-D), as shown in Figure 7A. The DPPC lipid is one of the most common phospholipids in biological organisms, which consists of two hydrophobic tail chains and a zwitterionic PC head group,⁶⁰ having the same dipole orientation with MPC and the opposite dipole orientation with DMAPS.

Figure 7B shows the frequency change and energy dissipation change associated with the adsorption of DPPC on the MPC surface in 1 mM NaCl of pH 5.6. When 20 ppm DPPC solution was introduced into the QCM-D chamber, the frequency slowly decreased with time, indicating the adsorption of DPPC molecules on the MPC surface, approaching a plateau at $t \sim 7200$ s. The background solution 1 mM NaCl without DPPC was then introduced and the frequency change recovered back to about −5 Hz, indicating that the adsorption of DPPC on MPC was weak and the lipid molecules were almost all washed off by the background solution. Figure 7C shows the changes of frequency and energy dissipation associated with the adsorption of DPPC on the DMAPS surface. Similarly, the frequency slowly decreased with time and did not reach a plateau even after 8200 s, upon the introduction of 20 ppm DPPC solution, indicating the adsorption of DPPC lipid molecules on the DMAPS surface. However, after introducing the background solution 1 mM NaCl without DPPC, the frequency change only recovered slightly ($\Delta F \sim -40$ Hz), indicating that most adsorbed DPPC molecules remained on the DMAPS surface.

The different adsorption behaviors of DPPC lipids on MPC and DMAPS surfaces could be mainly attributed to the different interaction behaviors of the zwitterionic PC head group of DPPC with the zwitterionic PC groups on MPC and the SB groups (with the opposite dipole orientation as PC groups) on the DMAPS surface. The negatively charged sulfonic group of the SB group on DMAPS faces the aqueous solution, which would allow it to relatively more easily form an attractive electrostatic interaction with the PC head (with the opposite dipole orientation as SB) of the DPPC lipid molecule in the aqueous solution. From the first glance, the QCM-D results do not seem to directly agree with the approaching force curves measured in Figure 3A,B. However, it should be noted that the interactions between the dissolved individual DPPC molecules and DMAPS or MPC in QCM-D measurements have some difference with the interaction configurations of DMAPS and MPC surfaces in AFM force measurements. The AFM force measurements in this work detected the surface–surface interactions (functionalized AFM tip surface vs substrate surface) which demonstrated (1) the collective behaviors of the zwitterionic dipoles during surface approaching as well as (2) the enforced alignment of the zwitterionic dipoles under confinement (Figure 3C) between the AFM tip

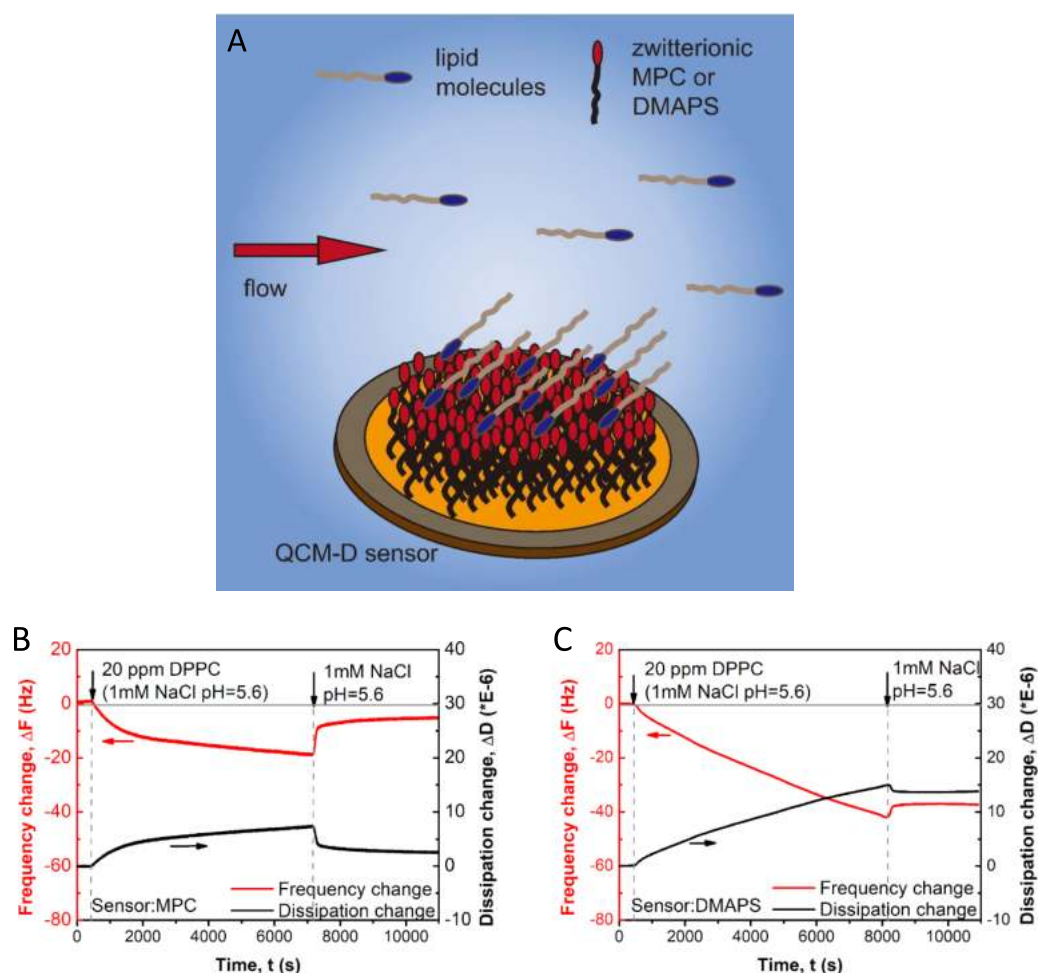


Figure 7. (A) Schematic illustration of dynamic adsorption of DPPC lipid on the zwitterionic surface in aqueous solution (1 mM NaCl, pH 5.6) using QCM-D. (B) Dynamic adsorption results (i.e., changes of frequency and energy dissipation with time) of 20 ppm DPPC lipid on the MPC surface in 1 mM NaCl solution. (C) Dynamic adsorption results (i.e., changes of frequency and energy dissipation with time) of 20 ppm DPPC lipid on the DMAPS surface in 1 mM NaCl solution.

and the substrate, thus leading to adhesion during surface separation, whereas during QCM-D measurements, individual dissolved DPPC molecules would diffuse to the vicinity of the zwitterionic SAM surfaces and the adsorption of the individual DPPC molecule would be largely influenced by the interaction of the single PC group and the zwitterionic PC or SB groups on the sensor surfaces, but without any confinement. Thereby, the QCM-D results that DPPC molecules show higher adsorption on DMAPS with the opposite dipole orientation actually agree well with the AFM force results in both Figure 3A,B that adhesion was measured during surface separation due to the enforced alignment of opposing dipole pairs via complementary orientations as illustrated in Figure 3C.

Implication of Interactions between Zwitterionic Groups with Opposite Dipoles. In previous reports, zwitterionic MPC and DMAPS surfaces show excellent antibiofouling performance,^{19,20,61–63} as illustrated in Figure 8A. The previous research studies reported protein adsorption results of fibrinogen and lysozyme on zwitterionic PC-headed and SB-headed self-assembled monolayer surfaces in aqueous solutions using surface plasmon resonance spectroscopy.³ The results demonstrate that there are limited proteins adsorbed on the zwitterionic surfaces. It is reported that under higher alkaline pH, the protein adsorption for fibrinogen and

lysozyme on both zwitterionic SAM surfaces decreased, which could be due to the strong hydration effect and strengthened surface potential at higher pH conditions. The protein adsorption results of fibrinogen and lysozyme on polymeric PMPC and PSBMA brush surfaces in aqueous solution have also been reported.⁶⁴ Very limited protein adsorption was detected on these zwitterionic polymer brush surfaces. It is also reported in these previous studies that the protein adsorption decreases with increasing polymer layer thickness (<65 nm) of the zwitterionic polymeric brush surfaces, indicating the important contribution of steric interaction associated with hydration interaction of the hydrophilic polymer brushes in antifouling performance compared to zwitterionic SAM surfaces.^{64–66} The antifouling properties of zwitterionic surfaces (e.g., MPC and DMAPS) are mainly attributed to the collective hydration interaction of many zwitterions on the surfaces.

Figure 8B shows the QCM-D adsorption results of DPPC lipids on PC (with the same dipole orientation) and SB (with the opposite dipole orientation) surfaces in aqueous solution, with more lipid adsorption detected on the SB surface than on the PC surface. The QCM-D results are consistent with the adhesion results detected during separation in the AFM measurements (Figures 3, 4, and 5) that under confinement,

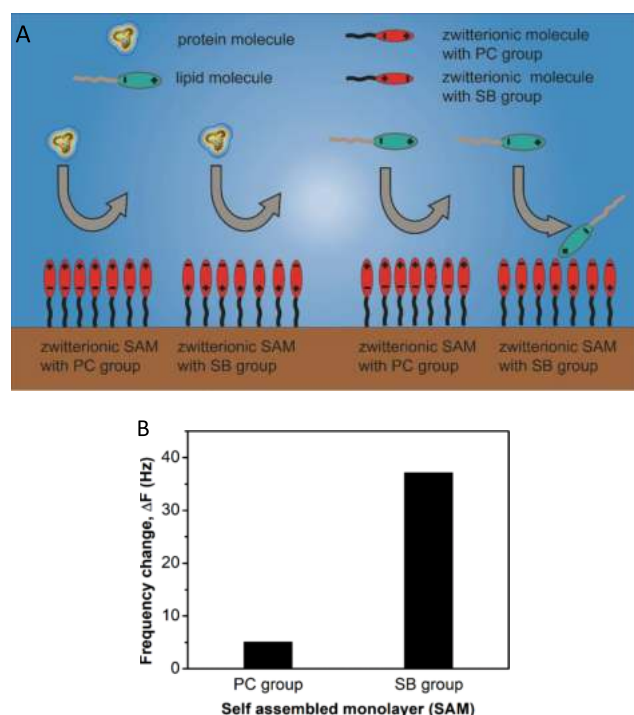


Figure 8. (A) Schematic illustration of the adsorptions of proteins and lipids on zwitterionic PC-headed and SB-headed SAM surfaces in aqueous solutions. (B) The adsorption results of DPPC lipid on MPC and DMAPS surfaces in aqueous solution using QCM-D in this work.

aligned zwitterionic group pairs with opposite dipoles could lead to intermolecular attraction. It is noted that many proteins, lipid molecules, and other types of biomolecules generally carry various zwitterionic groups with different dipole orientations, some of which may result in the adsorption or fouling behavior on zwitterionic surfaces. For example, in recent reports, the C-reactive protein (CRP), a nonspecific plasma protein produced by hepatocytes in the liver, has been discovered to specifically bind with the PC head groups in the presence of calcium ions.^{67,68} This specific CRP–PC interaction suggest the potential applications of zwitterionic groups as a biosensor to monitor CRP protein levels.⁶⁹ The findings in this work, together with the aforementioned previous reports, imply that the aligned zwitterionic groups with opposite dipoles can contribute to the attractive interactions of the lipid molecules, other biomolecules and related surfaces. These results further imply that the zwitterionic dipole-induced interactions together with other intermolecular interactions (e.g., hydration, electrostatic, and steric interactions)^{70,71} play an important role in the adhesion and antifouling behaviors of the zwitterionic molecules and surfaces, providing useful insights into the development of new antifouling surfaces.

CONCLUSIONS

In this work, the interaction mechanisms between the zwitterionic groups with opposite dipole orientations (i.e., PC and SB groups) in aqueous solutions have been quantitatively investigated via direct force measurements using AFM and adsorption tests using QCM-D. The effects of solution salinity and pH on the interactions of the zwitterionic surfaces were investigated. The AFM force measurement results showed that the adhesion measured

during separation between PC and SB groups in both symmetric and asymmetric configurations were close, mainly due to the attractive electrostatic interactions between the aligned zwitterionic groups. The solution salinity and pH did not significantly influence surface adhesion. QCM-D tests were conducted to monitor the dynamic adsorption of PC-headed lipid DPPC on PC and SB surfaces, which showed that the adsorption of DPPC could be detected on the SB surface, whereas not on the PC surface. The different adsorption behaviors could be because of the fact that the outmost negatively charged sulfonic group of the SB group on DMAPS faced the aqueous solution, which would facilitate it to form an attractive electrostatic interaction with the PC head of DPPC lipid molecules in the solution. Our results indicate that the adhesion behaviors are mainly due to the alignment of opposing dipole pairs via complementary orientations under confinement (i.e., in AFM force measurement). Without enforced confinement, the electrostatic interaction of the outermost charged group of individual hydrophilic zwitterionic molecules (e.g., zwitterionic lipid) with the opposing zwitterionic surface would play an important role in their interaction behaviors. The excellent antifouling performance of zwitterionic surfaces or zwitterionic polymers to biomolecules is mainly attributed to the strong hydration and steric interactions of the grafted chains carrying zwitterionic groups collectively on the substrates. This work shows that the zwitterionic dipole-induced interactions contribute significantly to the adhesion and antifouling behavior of the zwitterionic molecules and surfaces, which should be taken into consideration in the development of effective antifouling materials and coatings in related engineering and bioengineering applications.

AUTHOR INFORMATION

Corresponding Authors

*E-mail: yanbinscu@126.com (B.Y.).

*E-mail: hongbo.zeng@ualberta.ca. Phone: +1-780-492-1044 (H.Z.).

ORCID

Hongbo Zeng: 0000-0002-1432-5979

Author Contributions

This manuscript was written through contributions of all authors. All authors have given approval to the final version of the manuscript.

Notes

The authors declare no competing financial interest.

ACKNOWLEDGMENTS

This work was supported by the Natural Sciences and Engineering Research Council of Canada (NSERC), the Canada Foundation for Innovation (CFI), the Alberta Advanced Education & Technology Small Equipment Grants Program (AET/SEGP), and the Canada Research Chairs Program (H.Z.).

REFERENCES

- (1) Lewis, A. L. Phosphorylcholine-based polymers and their use in the prevention of biofouling. *Colloids Surf., B* **2000**, *18*, 261–275.
- (2) Vermette, P.; Meagher, L. Interactions of phospholipid-and poly(ethylene glycol)-modified surfaces with biological systems: relation to physico-chemical properties and mechanisms. *Colloids Surf., B* **2003**, *28*, 153–198.

- (3) Holmlin, R. E.; Chen, X.; Chapman, R. G.; Takayama, S.; Whitesides, G. M. Zwitterionic SAMs that resist nonspecific adsorption of protein from aqueous buffer. *Langmuir* **2001**, *17*, 2841–2850.
- (4) Mi, L.; Jiang, S. Integrated antimicrobial and nonfouling zwitterionic polymers. *Angew. Chem., Int. Ed.* **2014**, *53*, 1746–1754.
- (5) Mi, L.; Jiang, S. Synchronizing nonfouling and antimicrobial properties in a zwitterionic hydrogel. *Biomaterials* **2012**, *33*, 8928–8933.
- (6) Zhang, L.; Cao, Z.; Bai, T.; Carr, L.; Ella-Menye, J.-R.; Irvin, C.; Ratner, B. D.; Jiang, S. Zwitterionic hydrogels implanted in mice resist the foreign-body reaction. *Nat. Biotechnol.* **2013**, *31*, 553.
- (7) Bai, T.; Liu, S.; Sun, F.; Sinclair, A.; Zhang, L.; Shao, Q.; Jiang, S. Zwitterionic fusion in hydrogels and spontaneous and time-independent self-healing under physiological conditions. *Biomaterials* **2014**, *35*, 3926–3933.
- (8) Zhang, P.; Sun, F.; Tsao, C.; Liu, S.; Jain, P.; Sinclair, A.; Hung, H.-C.; Bai, T.; Wu, K.; Jiang, S. Zwitterionic gel encapsulation promotes protein stability, enhances pharmacokinetics, and reduces immunogenicity. *Proc. Natl. Acad. Sci. U.S.A.* **2015**, *112*, 12046–12051.
- (9) Chou, Y.-N.; Sun, F.; Hung, H.-C.; Jain, P.; Sinclair, A.; Zhang, P.; Bai, T.; Chang, Y.; Wen, T.-C.; Yu, Q.; Jiang, S. Ultra-low fouling and high antibody loading zwitterionic hydrogel coatings for sensing and detection in complex media. *Acta Biomater.* **2016**, *40*, 31–37.
- (10) Han, X.; Hung, H.-C.; Jain, P.; Sun, F.; Xu, X.; Yang, W.; Bai, T.; Jiang, S. Sterilization, hydration-dehydration and tube fabrication of zwitterionic hydrogels. *Biointerphases* **2017**, *12*, No. 02C411.
- (11) Han, L.; Xiang, L.; Zhang, J.; Chen, J.; Liu, J.; Yan, B.; Zeng, H. Biomimetic Lubrication and Surface Interactions of Dopamine-Assisted Zwitterionic Polyelectrolyte Coatings. *Langmuir* **2018**, *34*, 11593–11601.
- (12) Iwasaki, Y.; Ishihara, K. Phosphorylcholine-containing polymers for biomedical applications. *Anal. Bioanal. Chem.* **2005**, *381*, 534–546.
- (13) Shen, C.-H.; Lin, J.-C. Improving the surface biocompatibility with the use of mixed zwitterionic self-assembled monolayers prepared by a proper solvent. *Langmuir* **2011**, *27*, 7091–7098.
- (14) Fan, H.; Li, B.; Yan, Y.; Huang, J.; Kang, W. Phase behavior and microstructures in a mixture of anionic Gemini and cationic surfactants. *Soft Matter* **2014**, *10*, 4506–4512.
- (15) Zhang, J.; Zhang, L.; Cui, X.; Gong, L.; Xiang, L.; Shi, C.; Hu, W.; Zeng, H. Scalable polyzwitterion–polydopamine coating for regenerable oil/water separation and underwater self-cleaning of stubborn heavy oil fouling without pre-hydration. *Chem. Commun.* **2018**, *54*, 9734–9737.
- (16) Mao, X.; Gong, L.; Xie, L.; Qian, H.; Wang, X.; Zeng, H. Novel Fe₃O₄ based superhydrophilic core-shell microspheres for breaking asphaltene-stabilized water-in-oil emulsion. *Chem. Eng. J.* **2019**, *358*, 869–877.
- (17) Nagumo, R.; Ito, T.; Akamatsu, K.; Miura, R.; Suzuki, A.; Tsuboi, H.; Hatakeyama, N.; Takaba, H.; Miyamoto, A. Molecular dynamics simulations for microscopic behavior of water molecules in the vicinity of zwitterionic self-assembled monolayers. *Polym. J.* **2012**, *44*, 1149.
- (18) Nomura, K.; Mikuni, S.; Nakaji-Hirabayashi, T.; Gemmei-Ide, M.; Kitano, H.; Noguchi, H.; Uosaki, K. Water structure at the interfaces between a zwitterionic self-assembled monolayer/liquid water evaluated by sum-frequency generation spectroscopy. *Colloids Surf., B* **2015**, *135*, 267–273.
- (19) He, Y.; Hower, J.; Chen, S.; Bernards, M. T.; Chang, Y.; Jiang, S. Molecular simulation studies of protein interactions with zwitterionic phosphorylcholine self-assembled monolayers in the presence of water. *Langmuir* **2008**, *24*, 10358–10364.
- (20) Chen, S.; Zheng, J.; Li, L.; Jiang, S. Strong resistance of phosphorylcholine self-assembled monolayers to protein adsorption: insights into nonfouling properties of zwitterionic materials. *J. Am. Chem. Soc.* **2005**, *127*, 14473–14478.
- (21) Luk, Y.-Y.; Kato, M.; Mrksich, M. Self-assembled monolayers of alkanethiolates presenting mannitol groups are inert to protein adsorption and cell attachment. *Langmuir* **2000**, *16*, 9604–9608.
- (22) Zhao, Y.-H.; Wee, K.-H.; Bai, R. Highly hydrophilic and low-protein-fouling polypropylene membrane prepared by surface modification with sulfobetaine-based zwitterionic polymer through a combined surface polymerization method. *J. Membr. Sci.* **2010**, *362*, 326–333.
- (23) Laughlin, R. G. Fundamentals of the zwitterionic hydrophilic group. *Langmuir* **1991**, *7*, 842–847.
- (24) Azzaroni, O.; Brown, A. A.; Huck, W. T. UCST wetting transitions of polyzwitterionic brushes driven by self-association. *Angew. Chem., Int. Ed.* **2006**, *45*, 1770–1774.
- (25) Disalvo, E.; Lairion, F.; Martini, F.; Tymoczysyn, E.; Frías, M.; Almaleck, H.; Gordillo, G. Structural and functional properties of hydration and confined water in membrane interfaces. *Biochim. Biophys. Acta, Biomembr.* **2008**, *1778*, 2655–2670.
- (26) Gawrisch, K.; Ruston, D.; Zimmerberg, J.; Parsegian, V.; Rand, R.; Fuller, N. Membrane dipole potentials, hydration forces, and the ordering of water at membrane surfaces. *Biophys. J.* **1992**, *61*, 1213–1223.
- (27) Boggs, J. M.; Rangaraj, G.; Koshy, K. M. Effect of hydrogen-bonding and non-hydrogen-bonding long chain compounds on the phase transition temperatures of phospholipids. *Chem. Phys. Lipids* **1986**, *40*, 23–34.
- (28) Boggs, J. M. Lipid intermolecular hydrogen bonding: influence on structural organization and membrane function. *Biochim. Biophys. Acta, Rev. Biomembr.* **1987**, *906*, 353–404.
- (29) Aikawa, T.; Okura, H.; Kondo, T.; Yuasa, M. Comparison of Carboxybetaine with Sulfobetaine as Lipid Headgroup Involved in Intermolecular Interaction between Lipids in the Membrane. *ACS Omega* **2017**, *2*, 5803–5812.
- (30) Marra, J.; Israelachvili, J. Direct measurements of forces between phosphatidylcholine and phosphatidylethanolamine bilayers in aqueous electrolyte solutions. *Biochemistry* **1985**, *24*, 4608–4618.
- (31) Goda, T.; Tabata, M.; Sanjoh, M.; Uchimura, M.; Iwasaki, Y.; Miyahara, Y. Thiolated 2-methacryloyloxyethyl phosphorylcholine for an antifouling biosensor platform. *Chem. Commun.* **2013**, *49*, 8683–8685.
- (32) Tsai, C.-C.; Wang, G.-J. A Glucose Biosensor Based on a 3D Nanostructured Gold Electrode. *J. Electrochem. Soc.* **2013**, *160*, B1–B5.
- (33) Xiao, X.; Li, H.; Wang, M.; Zhang, K.; Si, P. Examining the effects of self-assembled monolayers on nanoporous gold based amperometric glucose biosensors. *Analyst* **2014**, *139*, 488–494.
- (34) Péter, M.; Lammertink, R. G.; Hempenius, M. A.; Vancso, G. J. Electrochemistry of surface-grafted stimulus-responsive monolayers of poly(ferrocenyldimethylsilane) on gold. *Langmuir* **2005**, *21*, 5115–5123.
- (35) Xie, L.; Wang, J.; Shi, C.; Huang, J.; Zhang, H.; Liu, Q.; Liu, Q.; Zeng, H. Probing surface interactions of electrochemically active galena mineral surface using atomic force microscopy. *J. Phys. Chem. C* **2016**, *120*, 22433–22442.
- (36) Shi, C.; Cui, X.; Xie, L.; Liu, Q.; Chan, D. Y.; Israelachvili, J. N.; Zeng, H. Measuring forces and spatiotemporal evolution of thin water films between an air bubble and solid surfaces of different hydrophobicity. *ACS Nano* **2015**, *9*, 95–104.
- (37) Xie, L.; Shi, C.; Wang, J.; Huang, J.; Lu, Q.; Liu, Q.; Zeng, H. Probing the interaction between air bubble and sphalerite mineral surface using atomic force microscope. *Langmuir* **2015**, *31*, 2438–2446.
- (38) Shi, C.; Cui, X.; Zhang, X.; Tchoukov, P.; Liu, Q.; Encinas, N.; Paven, M.; Geyer, F.; Vollmer, D.; Xu, Z.; Butt, H. J. Interaction between air bubbles and superhydrophobic surfaces in aqueous solutions. *Langmuir* **2015**, *31*, 7317–7327.
- (39) Xie, L.; Shi, C.; Cui, X.; Zeng, H. Surface forces and interaction mechanisms of emulsion drops and gas bubbles in complex fluids. *Langmuir* **2017**, *33*, 3911–3925.

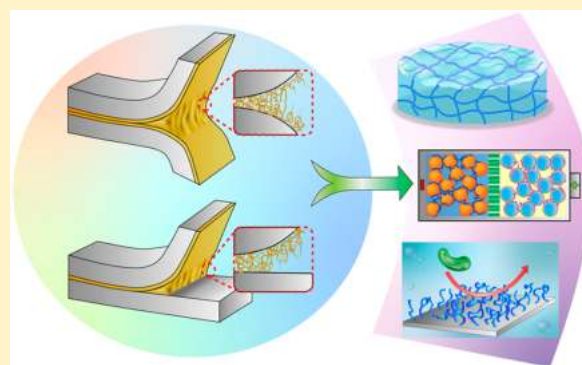
- (40) Cui, X.; Liu, J.; Xie, L.; Huang, J.; Liu, Q.; Israelachvili, J. N.; Zeng, H. Modulation of Hydrophobic Interaction by Mediating Surface Nanoscale Structure and Chemistry, not Monotonically by Hydrophobicity. *Angew. Chem., Int. Ed.* **2018**, *57*, 11903–11908.
- (41) Gong, L.; Qiu, X.; Zhang, L.; Huang, J.; Hu, W.; Xiang, L.; Zhu, D.; Sabbagh, R.; Mahmoudi, M.; Fattahpour, V.; Luo, J. L. Probing the interaction mechanism between oil-in-water emulsions and electrodeless nickel-phosphorus (EN) coating with implications for antifouling in oil production. *Energy Fuels* **2018**, DOI: 10.1021/acs.energyfuels.8b03132.
- (42) Carnie, S. L.; Chan, D. Y.; Lewis, C.; Manica, R.; Dagastine, R. R. Measurement of dynamical forces between deformable drops using the atomic force microscope. I. Theory. *Langmuir* **2005**, *21*, 2912–2922.
- (43) Israelachvili, J. N. *Intermolecular and Surface Forces*; Academic Press, 2011.
- (44) Liaw, D. J.; Lee, W. F.; Whung, Y. C.; Lin, M. C. Aqueous solution properties of poly [3-dimethyl (methacryloyloxyethyl) ammonium propane sulfonate]. *J. Appl. Polym. Sci.* **1987**, *34*, 999–1011.
- (45) Virtanen, J.; Arot car na, M.; Heise, B.; Ishaya, S.; Laschewsky, A.; Tenhu, H. Dissolution and aggregation of a poly (NIPA-block-sulfobetaine) copolymer in water and saline aqueous solutions. *Langmuir* **2002**, *18*, 5360–5365.
- (46) Georgiev, G. S.; Kamenska, E. B.; Vassileva, E. D.; Kamenova, I. P.; Georgieva, V. T.; Iliev, S. B.; Ivanov, I. A. Self-assembly, antipolyelectrolyte effect, and nonbiofouling properties of polyzwitterions. *Biomacromolecules* **2006**, *7*, 1329–1334.
- (47) Chevalier, Y.; Storet, Y.; Pourchet, S.; Le Perchec, P. Tensioactive properties of zwitterionic carboxybetaine amphiphiles. *Langmuir* **1991**, *7*, 848–853.
- (48) He, Y.; Shao, Q.; Chen, S.; Jiang, S. Water mobility: A bridge between the Hofmeister series of ions and the friction of zwitterionic surfaces in aqueous environments. *J. Phys. Chem. C* **2011**, *115*, 15525–15531.
- (49) Zhang, Z.; Moxey, M.; Alswieleh, A.; Morse, A. J.; Lewis, A. L.; Geoghegan, M.; Leggett, G. J. Effect of salt on phosphorylcholine-based zwitterionic polymer brushes. *Langmuir* **2016**, *32*, 5048–5057.
- (50) Jiang, W.; Fischer, G.; Girmay, Y.; Irgum, K. Zwitterionic stationary phase with covalently bonded phosphorylcholine type polymer grafts and its applicability to separation of peptides in the hydrophilic interaction liquid chromatography mode. *J. Chromatogr. A* **2006**, *1127*, 82–91.
- (51) Wu, L.; Jasinski, J.; Krishnan, S. Carboxybetaine, sulfobetaine, and cationic block copolymer coatings: A comparison of the surface properties and antibiofouling behavior. *J. Appl. Polym. Sci.* **2012**, *124*, 2154–2170.
- (52) Jiang, W.; Irgum, K. Synthesis and evaluation of polymer-based zwitterionic stationary phases for separation of ionic species. *Anal. Chem.* **2001**, *73*, 1993–2003.
- (53) Alswieleh, A. M.; Cheng, N.; Canton, I.; Ustbas, B.; Xue, X.; Ladmiral, V.; Xia, S.; Ducker, R. E.; El Zubir, O.; Cartron, M. L.; Hunter, C. N. Zwitterionic Poly (amino acid methacrylate) Brushes. *J. Am. Chem. Soc.* **2014**, *136*, 9404–9413.
- (54) Cui, X.; Shi, C.; Xie, L.; Liu, J.; Zeng, H. Probing Interactions between Air Bubble and Hydrophobic Polymer Surface: Impact of Solution Salinity and Interfacial Nanobubbles. *Langmuir* **2016**, *32*, 11236–11244.
- (55) Yang, C.; Dabros, T.; Li, D.; Czarnecki, J.; Masliyah, J. H. Measurement of the zeta potential of gas bubbles in aqueous solutions by microelectrophoresis method. *J. Colloid Interface Sci.* **2001**, *243*, 128–135.
- (56) Zhou, Y.; Raphael, R. M. Solution pH alters mechanical and electrical properties of phosphatidylcholine membranes: relation between interfacial electrostatics, intramembrane potential, and bending elasticity. *Biophys. J.* **2007**, *92*, 2451–2462.
- (57) Perttu, E. K.; Szoka, F. C. Zwitterionic sulfobetaine lipids that form vesicles with salt-dependent thermotropic properties. *Chem. Commun.* **2011**, *47*, 12613–12615.
- (58) Mary, P.; Bendejacq, D. D.; Labeau, M.-P.; Dupuis, P. Reconciling low-and high-salt solution behavior of sulfobetaine polyzwitterions. *J. Phys. Chem. B* **2007**, *111*, 7767–7777.
- (59) Azari, S.; Zou, L. Fouling resistant zwitterionic surface modification of reverse osmosis membranes using amino acid L-cysteine. *Desalination* **2013**, *324*, 79–86.
- (60) Prates Ramalho, J. P.; Gkeka, P.; Sarkisov, L. Structure and phase transformations of DPPC lipid bilayers in the presence of nanoparticles: insights from coarse-grained molecular dynamics simulations. *Langmuir* **2011**, *27*, 3723–3730.
- (61) Wang, T.; Wang, Y.-Q.; Su, Y.-L.; Jiang, Z.-Y. Antifouling ultrafiltration membrane composed of polyethersulfone and sulfobetaine copolymer. *J. Membr. Sci.* **2006**, *280*, 343–350.
- (62) Leng, C.; Hung, H.-C.; Sun, S.; Wang, D.; Li, Y.; Jiang, S.; Chen, Z. Probing the surface hydration of nonfouling zwitterionic and PEG materials in contact with proteins. *ACS Appl. Mater. Interfaces* **2015**, *7*, 16881–16888.
- (63) Krause, J. E.; Brault, N. D.; Li, Y.; Xue, H.; Zhou, Y.; Jiang, S. Photoiniferter-mediated polymerization of zwitterionic carboxybetaine monomers for low-fouling and functionalizable surface coatings. *Macromolecules* **2011**, *44*, 9213–9220.
- (64) Liu, L.; Li, W.; Liu, Q. Recent development of antifouling polymers: structure, evaluation, and biomedical applications in nano/micro-structures. *Wiley Interdiscip. Rev.: Nanomed. Nanobiotechnol.* **2014**, *6*, 599–614.
- (65) Feng, W.; Zhu, S.; Ishihara, K.; Brash, J. L. Adsorption of fibrinogen and lysozyme on silicon grafted with poly (2-methacryloyloxyethyl phosphorylcholine) via surface-initiated atom transfer radical polymerization. *Langmuir* **2005**, *21*, 5980–5987.
- (66) Yang, W.; Chen, S.; Cheng, G.; Vaisocherova, H.; Xue, H.; Li, W.; Zhang, J.; Jiang, S. Film thickness dependence of protein adsorption from blood serum and plasma onto poly (sulfobetaine)-grafted surfaces. *Langmuir* **2008**, *24*, 9211–9214.
- (67) Volanakis, J. E.; Wirtz, K. W. Interaction of C-reactive protein with artificial phosphatidylcholine bilayers. *Nature* **1979**, *281*, 155.
- (68) Chang, M.-K.; Binder, C. J.; Torzewski, M.; Witztum, J. L. C-reactive protein binds to both oxidized LDL and apoptotic cells through recognition of a common ligand: phosphorylcholine of oxidized phospholipids. *Proc. Natl. Acad. Sci. U.S.A.* **2002**, *99*, 13043–13048.
- (69) Christopeit, T.; Gossas, T.; Danielson, U. H. Characterization of Ca²⁺ and phosphocholine interactions with C-reactive protein using a surface plasmon resonance biosensor. *Anal. Biochem.* **2009**, *391*, 39–44.
- (70) Li, L.; Yan, B.; Zhang, L.; Tian, Y.; Zeng, H. Mussel-inspired antifouling coatings bearing polymer loops. *Chem. Commun.* **2015**, *51*, 15780–15783.
- (71) Zeng, H. *Polymer Adhesion, Friction, and Lubrication*; John Wiley & Sons, 2013.

Fundamentals and Advances in the Adhesion of Polymer Surfaces and Thin Films

Lu Gong,[†] Li Xiang,[†] Jiawen Zhang, Jingsi Chen, and Hongbo Zeng^{*†}

Department of Chemical and Materials Engineering, University of Alberta, Edmonton, Alberta T6G 1H9, Canada

ABSTRACT: Polymer materials have been widely used in industrial, agricultural, engineering, medical, electronic, and biological fields because of their excellent and diverse properties (e.g., mechanical, optical, electrical, and adhesive properties). The adhesion of polymer materials can affect the stability, alter the surface chemistry, change the surface structure, and influence the performance of the materials. It is of both fundamental and practical importance to understand the adhesion behaviors and interaction mechanisms of polymer surfaces and thin films for the development of new functional polymers and their applications. In this article, the fundamentals of surface energy, adhesion energy, and classical contact mechanics models are presented first, and the commonly used nanomechanical techniques for quantifying the intermolecular and surface interactions of polymers, including the surface forces apparatus (SFA) and atomic force microscope (AFM), are introduced. The advances in the adhesion of surfaces and thin films of various polymers (e.g., elastomers, glassy polymers) are reviewed. The effects of various factors, including the molecular weight, temperature, separation rate, and surface roughness, on the adhesion behaviors of these polymer surfaces and thin films are discussed. Their liquid- to solid-like behaviors during approach and detachment processes are shown. Several commonly applied methodologies used to modulate polymer adhesion are also introduced. Some recent applications based on polymer adhesion, remaining challenging issues, and future perspectives are also presented.



1. INTRODUCTION

Polymer materials ubiquitously exist in our everyday life and have been extensively exploited in industrial, agricultural, engineering, medical, electronic, and biological fields, taking advantage of their low cost as well as diverse and excellent properties.^{1–4} Every year, an uncountable number of polymers with various molecular structures and on-demand properties are synthesized along with the exploration of their applications in novel fields. Many studies have been conducted to test their outstanding performance and investigate their correlated properties, including adhesive, biocompatible, conductive, optical, and mechanical properties.^{5–10} Among all of these properties, the adhesive properties have become more and more important and have attracted much attention because the adhesion between polymer surfaces and thin films can affect the stability of polymer materials on the substrates, the surface structure and chemistry of the deposited polymer films, and the related performance when applied.^{11–15}

The adhesive phenomena between two surfaces are usually categorized into two configurations. When the two contacting surfaces are different, the force needed to separate them is usually identified as the “adhesion”. On the contrary, if the two adhering surfaces are the same, then the separating force is generally referred to as “cohesion”. In some situations, both adhesion and cohesion exist simultaneously.^{16–18} For example, when a liquid glue is applied to stick two surfaces together, the polymer molecules in the glue tend to graft onto the target

substrate surfaces upon coating and interact with each other during the following drying process. The excellent gluing performance depends not only on the strong adhesion between the polymer molecules and target surfaces but also on the strong cohesion among the glue polymer molecules.¹⁹ In this review, “polymer adhesion” involves both the adhesion of polymer–substrate and the cohesion between the same polymer surfaces.

With the increasing number of applications of various polymer materials under complicated and varied conditions, polymers with controllable adhesive properties have aroused great interest in recent years for the development of the “smart” materials, especially in biological and biomedical engineering.^{20–22} For example, the formation and dissociation of drug-loaded polymer capsules can be modulated by adjusting the adhesion of polymer molecules, leading to controlled drug delivery systems.^{23–26} On the basis of the previous studies, it is well accepted that the adhesive behaviors of the polymer materials can be facilely adjusted by parameters such as the polymer properties (e.g., molecular weight, molecular chemistry, and viscoelastic properties), surface

Special Issue: Intermolecular Forces and Interfacial Science

Received: July 8, 2019

Revised: August 22, 2019

Published: August 22, 2019

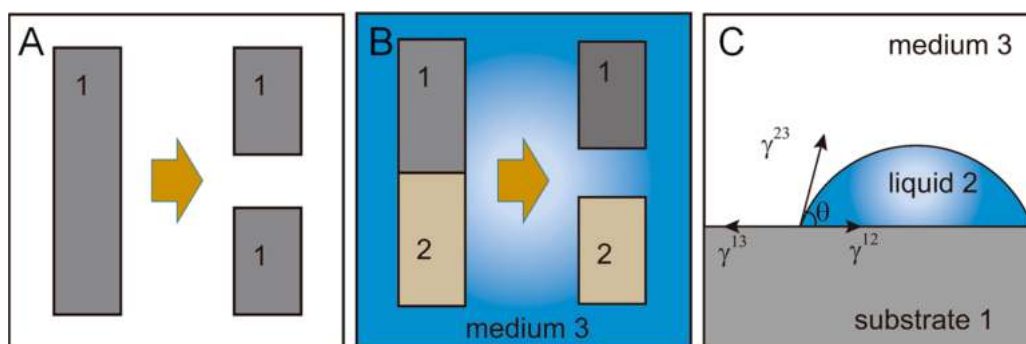


Figure 1. (A) Cohesion energy of two identical surfaces separated in vacuum. (B) Adhesion energy of two different surfaces separated in a medium. (C) Contact angle of liquid 2 on substrate 1 in medium 3.

properties (e.g., surface nanostructure and surface wettability), external loading conditions (e.g., loading force and loading/unloading rate), temperature, electromagnetic field, and light.^{27–36} Hence, investigating the adhesive properties of polymers and revealing the adhesion mechanisms under different effects can pave the way for the rational design of new polymer materials and their novel applications.

In previous work, the intra- and intermolecular interactions of polymer surfaces and thin films have been quantitatively measured to characterize the polymer adhesive behaviors.^{37–45} Different types of interactions have been identified to contribute to the polymer adhesion. For example, the strong electrostatic attraction between negative charges from one polymer and positive charges from another one plays a major role in the formation of some polymeric hydrogels.⁴⁶ Hydrogen bonding could contribute to the self-assembly and cross-linking of polymer structures.^{47,48} The hydrophobic interaction between polystyrene (PS) surfaces results in strong cohesion in aqueous environments.^{38,49,50} Weak attraction and even repulsive interaction have also been investigated and play important roles in the applications of polymer materials. For example, the weak interaction between water drops and the lotus leaf surface due to the surface structures plays a critical role in the drop-rolling and self-cleaning phenomena and has inspired numerous methods of fabrication of structural surfaces.^{51–54} Hydration repulsion between zwitterionic polymers and protein molecules in aqueous solutions makes it difficult for proteins to adhere to the zwitterionic surfaces, contributing to their nonbiofouling property.^{55–57} Therefore, understanding the adhesion behaviors and interaction mechanisms of polymer surfaces and thin films is of both practical and fundamental importance to the development of new functional polymers.

In this article, the fundamentals and advances in the understanding of adhesion mechanisms of polymer surfaces and thin films are presented and discussed. First, we introduce the fundamentals and classical contact mechanics models, followed by the commonly used experimental techniques for quantifying the surface forces and adhesion of polymers. We then discuss the adhesion and fracture behaviors of various polymers (e.g., elastomers, glassy polymers) and the influence of molecular weight, temperature, separation rate and surface roughness. We have also presented the typical strategies for the strengthening or weakening of polymer adhesion, several applications of polymer adhesion, some remaining challenges, and future perspectives.

2. ADHESION ENERGY AND CONTACT MECHANICS MODELS

2.1. Surface Energy and Adhesion Energy. Adhesion plays an important role in the separation processes of two polymer surfaces, which is very common in our daily life and in industrial production. The minimum force required for the detachment of two surfaces is referred as the adhesion force F_{ad} , and the free-energy change during the process is denoted as the adhesion energy W_{ad} . Typically, the adhesion between two surfaces is determined by the interactions between the molecules on the two surfaces, the number density of the molecules, and the contact area.^{11,58,59} Surface energy γ , which is defined as the energy change dW with the surface area A increasing by dA in vacuum (eq 1),¹¹ has become one of the most fundamental and important parameters in polymer science.⁶⁰

$$\gamma = \frac{dW}{dA} \quad (1)$$

When two identical surfaces with surface energy γ_1 are separated in vacuum (Figure 1A), the cohesion energy W_{11} per unit area can be calculated by the creation of two surfaces, which is presented in eq 2.¹¹

$$W_{11} = 2\gamma_1 \quad (2)$$

In the case of separating two dissimilar surfaces 1 and 2 in medium 3 as indicated in Figure 1B, the adhesion energy W_{132} is related to the interfacial energies γ_{12} , γ_{13} , and γ_{23} , as shown in eq 3.¹¹

$$W_{132} = \gamma_{13} + \gamma_{23} - \gamma_{12} \quad (3)$$

Several methods have been employed to measure or calculate the surface energy of a polymer substrate, among which the contact angle (CA) prediction is dominant.^{60–62} As depicted in Figure 1C, once the contact angle θ of one drop of liquid 2 on substrate surface 1 in medium 3 is determined, the adhesion energy W_{132} can be quantitatively derived from the surface energies (i.e., γ_{12} , γ_{13} , and γ_{23}) and contact angle following the Young–Dupré equation (eq 4) can be derived from Young’s eq (eq 5).^{63,64}

$$W_{132} = \gamma_{23}(1 + \cos \theta) \quad (4)$$

$$\gamma_{13} = \gamma_{12} + \gamma_{23} \cos \theta \quad (5)$$

Generally, the surface energy of a substrate is regarded as consisting of polar γ^p and apolar γ^d components, where γ^p is

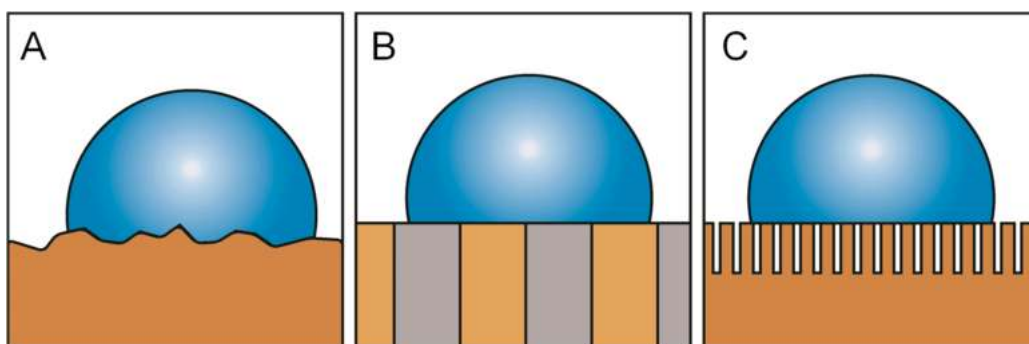


Figure 2. Schematic of contact angles of the (A) Wenzel model, (B) Cassie model, and (C) Cassie–Baxter model.

contributed by electron donor γ^- and electron acceptor γ^+ parts, as described in eq 6.^{65–67}

$$\gamma = \gamma^d + \gamma^p = \gamma^d + 2\sqrt{\gamma^+ \cdot \gamma^-} \quad (6)$$

According to the Lifshitz–van der Waals/acid–base approach, the surface energy of a substrate S can be calculated by measuring the contact angles of three different probe liquids (L_1 , L_2 , and L_3) with known surface energies, as shown in eq 7.⁶⁰ It should be noted that the property of the probe liquids, the preparation process of the substrates, and the specific interactions between liquids and surfaces have a considerable influence on the measured values of the surface energy.^{68–71}

$$\begin{bmatrix} 2\sqrt{\gamma_{L1}^d} & 2\sqrt{\gamma_{L1}^+} & 2\sqrt{\gamma_{L1}^-} \\ 2\sqrt{\gamma_{L2}^d} & 2\sqrt{\gamma_{L2}^+} & 2\sqrt{\gamma_{L2}^-} \\ 2\sqrt{\gamma_{L3}^d} & 2\sqrt{\gamma_{L3}^+} & 2\sqrt{\gamma_{L3}^-} \end{bmatrix} \cdot \begin{bmatrix} \sqrt{\gamma_S^d} \\ \sqrt{\gamma_S^+} \\ \sqrt{\gamma_S^-} \end{bmatrix} = \begin{bmatrix} \gamma_{L1}(1 + \cos \theta_{L1}) \\ \gamma_{L2}(1 + \cos \theta_{L2}) \\ \gamma_{L3}(1 + \cos \theta_{L3}) \end{bmatrix} \quad (7)$$

In practical terms, the prepared surfaces are rarely perfectly flat or chemically homogeneous. Therefore, the apparent contact angle (θ^*) of a liquid measured in experiments would be different from that on the ideal surfaces. In 1936, Wenzel discussed the effect of surface roughness on the value of the measured contact angle (Figure 2A), which is known as the Wenzel model.⁷²

$$\cos(\theta^*) = f \cos(\theta) \quad (8)$$

Here, θ is the contact angle calculated from Young's equation on the ideal surface, and f , the surface roughness ratio, is defined as the ratio of the real surface area to the apparent surface area. For a smooth surface with chemical heterogeneity, the apparent contact angle of a liquid is determined by the composite materials, which was reported by Cassie in 1948. When the flat surface is composed of two different materials (Figure 2B), the contact angle can be described using Cassie's model by eq 9.⁷³

$$\cos(\theta^*) = \varphi_1 \cos(\theta_1) + \varphi_2 \cos(\theta_2) \quad (9)$$

Here, θ_1 and θ_2 are the contact angles of the particular liquid on the flat surfaces consisting of pure materials 1 and 2, respectively, and φ_1 and φ_2 are the area fractions of materials 1 and 2 over the whole surface area, respectively. In some cases, the surface is so rough that the liquid cannot wet all of the grooves with air trapped on the surface, resulting in both a rough and heterogeneous surface, such as a lotus leaf. The Cassie–Baxter equation derived in 1944 is commonly used to

describe the synergic influence of both surface roughness and heterogeneity in this case of Figure 2C, as shown in eq 10.^{73,74}

$$\cos(\theta^*) = f\varphi \cos(\theta) + \varphi - 1 \quad (10)$$

Here, f is the surface roughness ratio of the wet surface, and φ is the fraction of the surface area wet by the liquid.

2.2. Contact Mechanics Models. Numerous experimental and theoretical studies have been conducted to elucidate the adhesion mechanics or contact mechanics of two surfaces over the past century. In 1882, Hertz investigated the deformation of two elastic spherical surfaces in contact under an applied load force,⁷⁵ assuming that there was no adhesion between the two surfaces. Hence, when two spheres with radii R_1 and R_2 are pressed into contact by a force F , the radius r of the contact area can be described by eq 11.

$$r^3 = \frac{RF}{K} \quad (11)$$

Here, $R = R_1 R_2 / (R_1 + R_2)$, and K is the equivalent elastic modulus which is related to Young's moduli E_1 and E_2 and Poisson's ratios ν_1 and ν_2 of the interacting materials by eq 12.

$$\frac{1}{K} = \frac{3}{4} \left[\frac{1 - \nu_1^2}{E_1} + \frac{1 - \nu_2^2}{E_2} \right] \quad (12)$$

Although Hertz contact mechanics is not directly applicable to many practical cases, particularly for polymer systems showing strong adhesion with other substrates, it has been utilized to investigate various tribological phenomena.^{76–78}

In 1971, Hertz's theory was modified by Johnson, Kendall, and Roberts (JKR) with a consideration of the surface energies of the contacting surfaces.^{76,79} It is noted that, in the JKR model, surface adhesion was treated to only occur within the contact region, while the surface forces outside the contact area (e.g., at very small surface separation) were still ignored. When two spheres of radii R_1 and R_2 , equivalent elastic modulus K , and adhesion energy W are pressed together under external force F , the radius r of the contact area can be given by eq 13.

$$\begin{aligned} r^3 &= \frac{R}{K} \left[F + 3\pi RW + \sqrt{6\pi RWF + (3\pi RW)^2} \right] \\ &= \frac{R}{K} \left(\sqrt{F + \frac{3}{2}\pi RW} + \sqrt{\frac{3}{2}\pi RW} \right)^2 \end{aligned} \quad (13)$$

The adhesion force F_{ad} or pull-off force is correlated to the adhesion energy W by eq 14, where $W = 2\gamma$ if the two surfaces are made of identical material.

$$F_{\text{ad}} = \frac{3}{2}\pi RW \quad (14)$$

In 1975, Derjaguin, Muller, and Toporov (DMT) proposed a model by employing the contact profiles of the Hertz model and taking surface interactions into account.^{77,80} Therefore, when two spheres (radii R_1 and R_2 , equivalent elastic modulus K , and adhesion energy W) are brought into contact under external force F , the radius r of the contact area can be given by eq 15.

$$r^3 = \frac{R}{K}(F + 2\pi RW) \quad (15)$$

Upon separation, the adhesion force is given by eq 16.

$$F_{\text{ad}} = 2\pi RW \quad (16)$$

The classical Hertz, JKR, and DMT models are usually applied to describe the surface deformation and adhesion between two elastic surfaces.^{81,82} Generally, the JKR model is suitable for soft materials with high surface energy and a large contact area, and the DMT theory is applicable in the cases of small and rigid surfaces with low surface energy.^{11,34} It is noted that although glassy polymers are commonly so rigid that the JKR model cannot be directly applied to analyze the measured adhesion, when the polymers are deposited as thin films on elastic substrates (e.g., mica), the systems comply with the JKR model.^{83,84}

Most polymer materials are viscoelastic. The loading and separating processes during contact mechanics tests of polymer surfaces are normally irreversible, which is due to the significant bulk deformation and the complex interactions (e.g., interpenetration and entanglement) of polymer chains across the contact interface.^{85–89} For interactions between two polymer surfaces of the same material, the adhesion hysteresis $\Delta\gamma$ describing this irreversibility and the energy dissipation is defined in eq 17.

$$\Delta\gamma = (\gamma_{\text{R}} - \gamma_{\text{A}}) \quad (17)$$

Here, γ_{R} is the so-called receding surface energy during separation and γ_{A} is the advancing surface energy on loading. For the reversible adhesion process without hysteresis, the adhesion hysteresis $\Delta\gamma$ is zero, and $\gamma_{\text{R}} = \gamma_{\text{A}}$ is the equilibrium thermodynamic surface energy γ . For viscoelastic polymers, the loading and unloading processes are irreversible, and the adhesion hysteresis is $\Delta\gamma > 0$. It is noted that the effects of surface (i.e., surface-energy-dependent) and bulk (i.e., modulus-dependent) hysteresis are often difficult to distinguish. Therefore, the effective surface energy γ_{eff} is usually used to describe the hysteretic adhesion property of viscoelastic polymers based on the adhesion force measured, as shown in eq 18.

$$\gamma_{\text{eff}} = \frac{F_{\text{ad}}}{3\pi R} \quad (18)$$

When an elastic sphere (radius R and modulus K) is in contact with a flat surface under loading force F with a contact area of radius r , the strain energy release rate G is often used to quantitatively analyze the unloading process, as shown in eq 19.

$$G = \frac{\left(F - \frac{Kr^3}{R}\right)^2}{6\pi Kr^3} = \frac{(F - L_{\text{H}})^2}{6\pi RL_{\text{H}}} \quad (19)$$

Here, $L_{\text{H}} = Kr^3/R$ is the so-called Hertz load for a contact radius r without surface adhesion (Hertz model). When the loading and separation processes (or loading–unloading cycle) are in equilibrium and no adhesion hysteresis exists, G is equal to the adhesion energy or work of adhesion W_{ad} . For the case in which the two contacting surfaces are made of the same materials, $G = W_{\text{ad}} = 2\gamma$.

In 1975, Gent and co-workers investigated the adhesion of viscoelastic polymers with glass using peel and tear tests under the effects of different peeling rates and temperatures.^{90,91} The Williams–Landel–Ferry (WLF) model was applied to describe such effects, as given by eq 20.⁹²

$$\log(a_T) = -\frac{8.86(T - T_g - 50)}{101.6 + T - (T_g + 50)} \quad (20)$$

Here, a_T is the WLF temperature shift factor, T is the temperature, and T_g is the glass-transition temperature of the polymer. On the basis of the results, the strain energy release rate G at a given peeling rate V can be empirically related to the thermodynamic adhesion energy W using eqs 21 and 22.^{93–96}

$$G = W(1 + \phi(a_TV)) \quad (21)$$

$$G = G_0 \left(1 + \left(\frac{V}{V^*}\right)^n\right) \quad (22)$$

$\phi(a_TV)$ is a dimensionless dissipation function used to describe the viscoelastic property of the polymer system, which has an empirical relation with the interfacial crack propagation velocity V during peeling, G_0 is the intrinsic adhesion energy (also referred to as the threshold toughness) when the peeling velocity is zero, and V^* is a characteristic critical velocity for crack propagation during peeling. Polymer toughness G is one of the most important mechanical properties of polymer materials and describes the ability of the polymer to withstand the applied loading force before fracture occurs.^{97–99} It is dependent on the geometry of the polymer material, environmental conditions (e.g., temperature and pressure), loading rate of the applied force, and intrinsic properties of the polymer including the molecular weight, polydispersity, bonding force between polymer chains, and packing structure. On the basis of the equation, the threshold toughness G_0 of a polymer material can be measured at the sufficiently low velocity (the so-called threshold rate).^{28,31,100,101} The value of G_0 could be higher than the thermodynamic adhesion energy, which is caused by the rearrangement of polymer chains at the interface and some physical and/or chemical interactions between polymer chains, such as hydrogen bonding.^{102–104}

It should also be noted that when the interfacial crack propagation velocity during peeling is quite small ($V \leq V^*$), the un-cross-linked polymer chains across the contact interface can be separated directly with zero dissipation in the adhesion energy. However, when the velocity is high ($V > V^*$), the pulling-out behavior of polymer chains at the interfacial crack tip is viscous and time-dependent, and significant energy dissipation could occur. For cross-linked polymers or elastomers, the pulling-out process of polymer chains around the interfacial crack propagation tip is also viscous, and the energy dissipation is practically viscoelastic and time-dependent. If chain scission is not involved at $V \leq V^*$, then the total energy for crack propagation would be equal to the

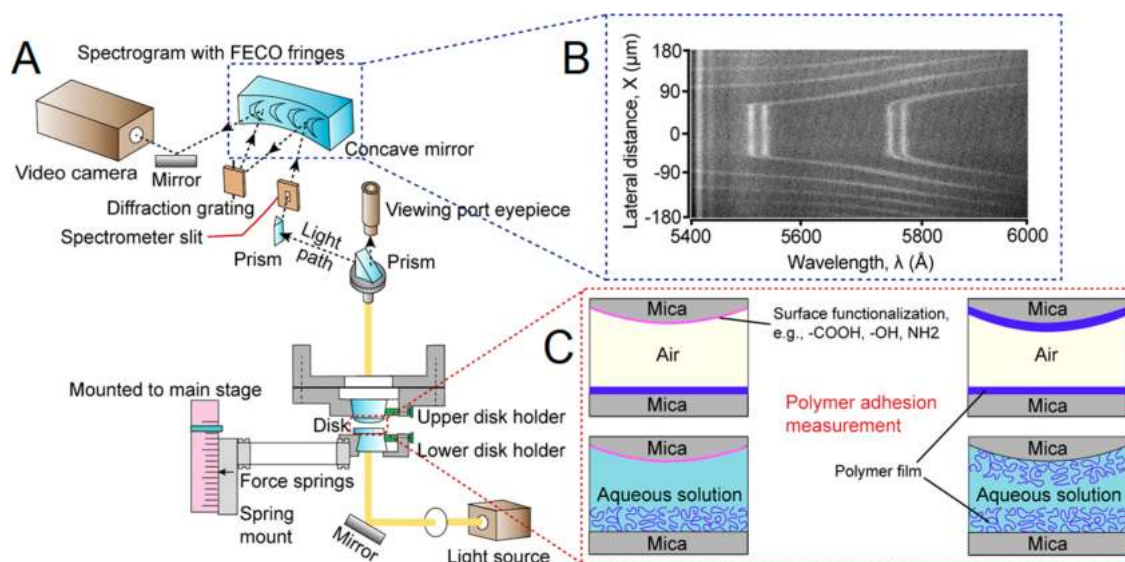


Figure 3. (A) Schematic of a typical experimental setup using a surface forces apparatus (SFA) to quantify the interaction forces between two surfaces. (B) Typical fringes of equal chromatic order (FECO) associated with the contact of two mica surfaces. (C) Selected experimental configurations (e.g., symmetric polymer–polymer case and asymmetric polymer–substrate case) used to measure the surface forces and adhesion in air and aqueous media.

thermodynamic adhesion energy value, with $W_{\text{ad}} = 2\gamma$ for the interactions of the same materials.^{104–107}

3. ADHESION MEASUREMENT TECHNIQUES

In the early 1950s, Derjaguin and co-workers measured the surface interaction between a hemispherical glass surface and a flat glass substrate in vacuum, which was proven to be due to attractive van der Waals forces.^{108,109} Since then, various experimental techniques have been developed and applied to quantify the interaction forces between different molecules and surfaces in vapors and liquid media, such as the surface forces apparatus (SFA), atomic force microscope (AFM), optical tweezers, magnetic tweezers, total internal reflection microscopy, and JKR apparatus.^{110–114} Among these techniques, SFA and AFM are probably the most widely used tools for measuring the intermolecular and surface forces of different material systems, as demonstrated by high force sensitivity and distance resolution.

3.1. Surface Forces Apparatus. The SFA was originally developed by Tabor, Winterton, and Israelachvili to quantitatively evaluate the van der Waals (VDW) forces between molecularly smooth mica surfaces in air and vacuum.^{115–117} Since then, significant advances have been achieved in improving the SFA technique by Israelachvili and co-workers, which have been widely employed to quantify a variety of intermolecular and surface forces including VDW forces, the electrostatic force, the hydrophobic interaction, biological-specific ligand–receptor interactions, and nanotribological forces (e.g., friction or lubrication forces under nanoconfinement).^{110,118–123} SFA is able to monitor the absolute separation distance between the two interacting surfaces, the thickness of the confined thin film, and the deformation of the interacting surfaces in situ and in real time on the basis of multiple beam interferometry (MBI) by using fringes of equal chromatic order (FECO).

Figure 3A shows a schematic of the typical setup of SFA experiments,¹¹⁰ which mainly consists of a light source, spectrometer, camera, SFA main chamber with a main stage,

micrometer, upper disk holder, and lower disk holder attached to the force spring. In a typical SFA experiment, two back-silvered (thickness ~ 50 nm) mica sheets (thickness $1\text{--}5$ μm) are glued onto two cylindrical silica disks with radius R (1 to 2 cm), followed by mounting them into the upper and lower disk holders in the SFA chamber in a crossed-cylinder configuration. In a typical force measurement, the two surfaces are first brought into contact for a certain time, followed by a separation process, during which the interaction region is simultaneously monitored by using the FECO fringes for the determination of surface deformation and their separation distance. The interaction forces are calculated by the deflection of the force spring following Hooke's law

$$F = k\Delta X \quad (23)$$

where F is the measured force, ΔX is the spring deflection, and k is the spring constant. The interaction between two crossed cylindrical surfaces with radius R is locally equivalent to that of a sphere of the same radius against a flat surface when their separation is $D \ll R$ on the basis of the Derjaguin approximation, which correlates the force $F(D)$ between the two curved surfaces with the interaction energy $E(D)$ per unit area between two flat surfaces as shown in eq 24.¹¹

$$E(D) = \frac{F(D)}{2\pi R} \quad (24)$$

The adhesion energy per unit area W_{ad} between two flat surfaces was usually related to the adhesion force F_{ad} between the two curved surfaces by the JKR model for soft elastic polymer materials with strong adhesion and a large contact area.^{76,124} Mica has served as the most commonly used supporting substrate for SFA experiments because of its transparent nature and molecularly smooth basal plane. The surface modification of mica can be realized via the deposition of a thin layer of other materials such as metal, metal oxides, polymers, lipid layers, and proteins.^{125,126} When the interacting substrates in the SFA experiments show multilayer structures consisting of the deposited material, mica, glue, and a silica

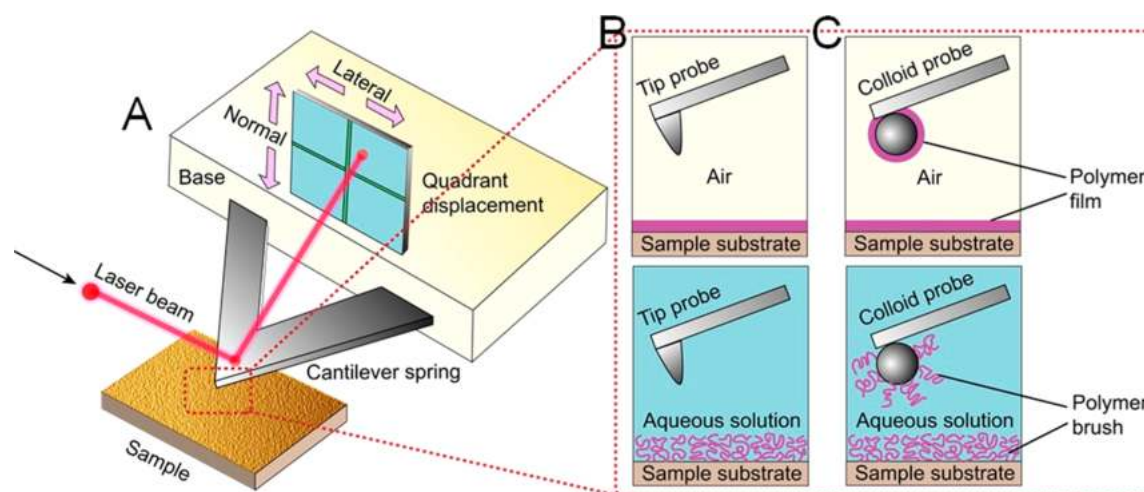


Figure 4. (A) Schematic of the typical experiment setup using an atomic force microscope (AFM) for force measurement. (B) Asymmetric experimental configuration used to probe the surface interaction between an AFM tip and a polymer film in air and aqueous solution. (C) Symmetric experimental configuration for the investigation of the interaction between two polymer films/polymer brushes in air and aqueous solution.

disk, the effective bulk modulus of the substrate is affected by the mechanical properties of the layers.

Over the past four decades, various interactions between polymer surfaces in air, vapor, and aqueous and nonaqueous media have been quantified using SFA.¹¹ The oscillatory solvation force, which plays an important role in polymer applications involving tribology, rheology, and adhesion properties, has been determined using an SFA to arise from the confinement of fluids between substrate surfaces.^{127–131} The interaction forces and adhesion between polyelectrolyte brushes have been measured by SFA, and the results suggest that both the type and concentration of ions can remarkably affect the brush structure and adhesion behavior.^{132–134} The rheological properties of confined water films and polystyrene (PS) films have been characterized using SFA.^{135,136} X-ray scattering and fluorescence imaging have been coupled with SFA to allow the simultaneous characterization of the structures of confined molecules and thin films during force measurements.^{137–140} Electrochemical modulation and external field (e.g., electric field) can also be coupled with SFA to tune and measure surface potentials and interfacial electrochemical reactions associated with force measurements and to investigate the influence of the external field on both normal and lateral forces.^{42,141–143} Despite the high resolution of <0.1 nm in the vertical displacement direction, it is noted that SFA is not an imaging technique and it is operated mostly with transparent or semitransparent materials with limited lateral resolution. The molecular orientation and composition of the confined thin films between interacting surfaces generally are not directly detected but can be characterized by coupling SFA with other techniques such as X-ray scattering and fluorescence imaging.

3.2. Atomic Force Microscope. The first atomic force microscope (AFM) was developed in 1982 by Binnig and Rohrer to investigate the substrate surface on the atomic scale.^{144,145} Since then, this technique has been widely used for applications such as surface imaging, force measurement, and molecular manipulation.^{146,147} Here, we briefly introduce the typical force measurement methodologies using AFM.

Figure 4A shows the schematic of the experiment setup for measuring the interaction forces between an AFM probe and a substrate surface using an AFM.³⁴ Commonly, the AFM probe is a sharp tip on the cantilever spring, as shown in Figure 4B. During the force measurement, the AFM probe is driven by a piezo to move toward and away from the substrate surface. The interaction between the tip and substrate could induce the bending of the cantilever. The deflection of the cantilever is monitored through the position displacement of a laser beam reflected from the back side of the cantilever using a position sensor (e.g., quartered photodiode). The spring constant of the AFM cantilever is usually determined using the Hutter and Bechhoefer method.¹⁴⁸ Thus, the interaction force between the AFM tip and substrate surface is obtained from the deflection of the cantilever and its spring constant using Hooke's law.

Except for the sharp AFM tip, the colloidal probes, which are prepared by attaching microsized particles (e.g., silica spheres, gold particles, and polymer spheres) to the AFM tipless cantilevers (as in Figure 4C), have also been exploited to measure the interaction force between the colloidal particle and the substrate surface.^{111,149} For example, the AFM probe with a PS microsphere has been utilized to investigate the adhesion mechanisms between the PS polymer and other substrates including silicon, mica, and polyurethane surfaces.¹⁵⁰ The impacts of the applied load, contact time, and surface roughness on the adhesion property of various polymers (e.g., polystyrene, poly(ethylene glycol), and polypropylene) with substrate surfaces (e.g., glass, metal, and silica) were also studied using the AFM colloidal probe technique.^{151–153} Typically, the radius of an AFM probe ranges from several nanometers to micrometers. Thus, the contact area between the AFM tip and the substrate surface is much smaller than that in an SFA experiment, which lowers the possibility of contamination during measurements. It is noted that the preparation of feasible AFM probes, such as the polymer-grafted silica probe, usually requires multiple steps. AFM can measure the forces of molecules and surfaces on the piconewton (pN) scale. The surface separation between the probe and substrate is determined by the displacement of the probe and the deflection of the cantilever, which might deviate

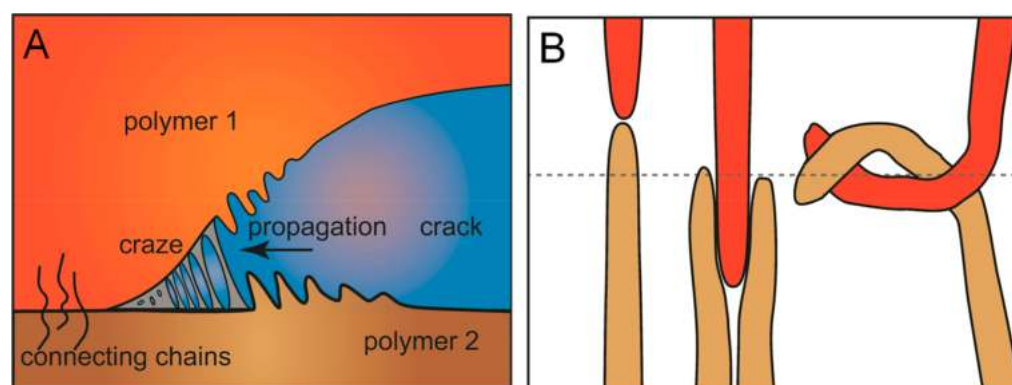


Figure 5. (A) Schematic of crack propagation at the polymer–polymer interface with the occurrence of crazing. (B) Schematic of the interpenetration, interdigitation, and entanglement of polymer chains across the contact interface.

from the actual separation distance between the surfaces, especially when the surfaces are soft and their deformation is not negligible.

4. ADHESION MECHANISMS OF POLYMER SURFACES AND THIN FILMS

The adhesion properties of polymer surfaces and thin films have been investigated for decades, and significant progress has been achieved in understanding the adhesion mechanisms. The adhesive interaction between a polymer surface and another identical or different substrate surface is largely determined by the physical (e.g., VDW) and/or chemical interactions (e.g., disulfide bond) of the polymer chains across the contact interface. The molecular weight, temperature, contact time, detachment velocity, and surrounding media have been found to play important roles in determining the adhesion properties of polymers. In this section, the advances in understanding the adhesion mechanisms of elastomers and glassy polymers and the influence of various parameters are reviewed.

4.1. Adhesion of Elastomers and Glassy Polymers.

Under external tensile stress, the fracture of bulk polymers and the separation of two polymer surfaces and thin films (i.e., elastomeric and glassy polymer) generally initiate from the occurrence of a crack on the microscale (Figure 5A). As the applied tensile stress increases, the crack would propagate. Eventually, the growth of the crack leads to material failure. For glassy polymers, crack propagation could also be associated with the formation of crazing. Crazing commonly refers to the formation of a network consisting of stretched polymer fibrils and the void space between these fibrils under tensile stress. For elastomeric polymers, it has been found that the measured adhesion energy between two polymer surfaces greatly depends on the crack propagation velocity V . Increasing the propagation velocity during the surface fracture leads to enhanced adhesion energy and fracture toughness.^{154,155} The adhesion can also be enhanced by physical and/or chemical interactions of interfacial polymer chains and connecting diblock polymers associated with the interdigitation, interpenetration, and entanglement of polymer chains across the contacting surfaces (Figure 5B).^{156,157}

A previous study by Gent and co-workers showed that the intrinsic adhesion energy (threshold toughness G_0) between two elastomeric polymer sheets increased linearly with the number of chemical bonds across the contacting interface with a fixed cross-linking density of each polymer film.^{91,154,158} This result demonstrated the important role of chemical interlinking

between the polymer surfaces in enhancing the adhesion energy. His following study showed that at the threshold rate, adding the component with no cross-linking bond created in a cross-linked elastomer could not affect the cohesion energy, which on the other hand could be significantly enhanced when increasing the crack propagation velocity.^{159,160} At the threshold rate, the pulling-out process of the un-cross-linked polymer chains was supposed to have almost no energy dissipation and thus could not influence the adhesion energy. However, when the crack propagation velocity was higher than the threshold rate, the pulling out of these un-cross-linked polymers would make a contribution to the adhesion energy between cross-linked elastomeric polymer surfaces and thin films.

A couple of models have been developed to describe the relation of the pulling-out process of polymer chains to the interfacial adhesion between contacting polymer surfaces, and most of the models are based on two assumptions.^{154,155,158,161–164} First, there is a threshold stress at the polymer interface below which the pulling-out process of polymer chains and surface separation could not happen. Second, when applied stress at the interface increases to be higher than the threshold stress, pulling-out rates of chains as well as the measured adhesion energy would increase. However, in different models, the properties of the partially pulled-out polymer chains are proposed differently.^{158,161} If the polymer chains that are partially pulled out are treated as straight chains, then the scale of the crack tip should be the same as that of these partially pulled-out chains, and the propagation of the crack is allowed. Thus, under a certain crack propagation velocity, the pulling-out process of chains would be relatively slow, and the critical propagation velocity V^* for the corresponding threshold toughness is relatively high. If the partially pulled-out polymer chains are supposed to collapse, then with the same crack propagation velocity the pull-out process would be relatively fast and the critical propagation velocity V^* would be slower. de Gennes and co-workers assumed that the polymer chains during the partial pulling-out process could form chain fibrils in the craze region to achieve the lowest surface energy and stretching energy of the polymer chains.^{103,165} Thus, the threshold toughness G_0 is proposed to be approximately related to the thermodynamic adhesion work W ($W = 2\gamma$) as demonstrated in eq 25.

$$G_0 - W \approx \gamma Na^2 \Sigma \approx k_B T N \Sigma \quad (25)$$

Here, γ is the surface energy of polymer chains, N is the degree of polymerization of the connecting chains, a is the length of the monomer, and Σ is the areal density of connecting chains. If the polymer chains are straight and fully stretched, then the critical propagation velocity V^* and threshold toughness G_0 can be expressed as in eqs 26 and 27, respectively.³¹

$$V^* \approx \frac{E}{3\zeta N \Sigma} \quad (26)$$

$$G_0 \approx \gamma N a^2 \Sigma \quad (27)$$

Here, E is Young's modulus of the polymer material, and ζ is the monomer friction coefficient. It can be observed that the threshold toughness G_0 increases linearly with the areal density of connecting polymer chains Σ . If the partially pulled-out chains collapse, then the critical propagation velocity V^* should be modified with multiplication by $a^4 \Sigma^2$.

A different model was proposed by Brown to describe the threshold toughness G_0 and thermodynamic adhesion work W as in eq 28.¹⁶⁶

$$G_0 - W \approx h f^* \Sigma \quad (28)$$

$$f^* \approx \gamma a \approx \frac{k_B T}{a} \quad (29)$$

Here, h is the maximum height of the crack zone, which is proportional to the pulled-out polymer chain length, and f^* is the minimum force for the existence of a fibril. If the pulled-out polymer chains are assumed to be completely extended (i.e., $h = Na$) and f^* is approximated using eq 29, then eq 27 can be transformed to be the same as eq 25 in de Gennes' model.¹⁶¹ However, the limitation for the application of de Gennes' model is that the density of the connecting polymer chain at the interface Σ should be low because high Σ can interfere with the free interpenetration of connecting polymer chains across the interface. So far, a feasible model for describing the adhesion property and chain behavior at the crazing zone between contacting polymer surfaces over the whole range of connecting polymer chain density remains to be developed.

For glassy polymers, the pulling-out process and/or chain scission at the crack tip could also contribute to the adhesion energy, which is quite similar to that of elastomeric polymers. However, the different properties (e.g., viscosity and elasticity) of glassy polymers and elastomers lead to different strengths of noncovalent interactions between polymer chains and dissimilar energy dissipation during the pulling-out process. Thus, the adhesive property of glassy polymers is different from that of elastomers.

4.2. Adhesion of Polymers from the Glassy State to Viscoelastic and Viscous States. Chain scission and disentanglement are usually believed to be involved in the surface fracture of glassy polymers.^{28,102,164,167–171} Because of the breaking of polymer chains during chain scission, the generated fragments are supposed to carry terminal radicals and react with other nearby polymer molecules and form cross-links. Although numerous experiments and simulations have been conducted, the understanding of the intrinsic mechanism of polymer fracture involving chain scission remains incomplete.^{34,163,164,167,171–173} A classical model was developed by Lake and Thomas to describe the chain scission phenomenon of elastomer and obtained threshold toughness G_0 by calculating the energy of breaking all of the connecting polymer chains present at the interface as shown in eq 30.¹⁷⁴

$$G_0 = \Sigma n U \quad (30)$$

Here, n is the number of main chain bonds in a single monomer, and U is the dissociation energy needed for each main chain bond. In this model, it is worth noting that at low crack propagation velocity, the viscoelastic contribution to the adhesion energy has been ignored.

In the bulk of glassy polymers, entanglements of polymer chains can transfer most of the endured stress. It has been found that when the average polymerization degree N of the polymer molecules is less than twice the average number of monomers involved in the entanglements N_e , the polymer chains can be pulled out easily instead of forming a craze and the disentanglement makes almost no contribution to the fracture toughness. When N/N_e is greater than 2, as revealed by theoretical simulation results, a stable craze zone starts to form, indicating the contribution of polymer entanglements to adhesion energy.^{173,175} Simulation results also suggested that most of the work dissipated during the crazing and surface fracture was mostly converted to heat because of the polymer chain friction. In the case of PS, the temperature of the fracture surface was estimated to be around 150–368 °C.¹⁷⁵ It was also found that when N/N_e was increased to beyond 8, the behavior of interfacial PS chains during fracture could change from pulling-out behavior to chain scission. In a previous study, the changing from chain pulling-out to the occurrence of crazing was observed at the interface between immiscible PS and PVP surfaces with connecting block polymer PS-*b*-PVP and tethered chains at the interface for reinforcement.^{28,176} Thus, the entanglements of polymer chains can significantly enhance the polymer material toughness.

Xu and co-workers have studied the behavior of interfacial polymer chains between two contacting homopolymer surfaces reinforced by a diblock polymer (e.g., PS/PVP/PS-*b*-PVP system).¹⁰¹ Figure 6 shows the failure mechanism map of

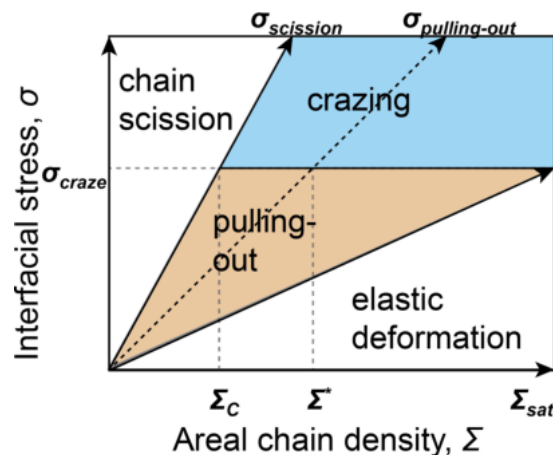


Figure 6. Map of failure mechanisms on different polymer chain behaviors with different normal tensile stress σ and areal chain density Σ .

different polymer chain behaviors under different normal tensile stress σ and areal chain density Σ . Here, σ_{craze} is the constant stress for the polymer system under which craze propagation could occur in the polymer. It has been discovered that when the polymer degree N is greater than $\sigma_{\text{craze}}/f_{\text{monomer}} \Sigma_c$ ($\Sigma_c = \sigma_{\text{craze}}/f_b$), chain scission can happen when $\Sigma < \Sigma_c$. With $\Sigma > \Sigma_c$, the craze will be formed during the fracture.

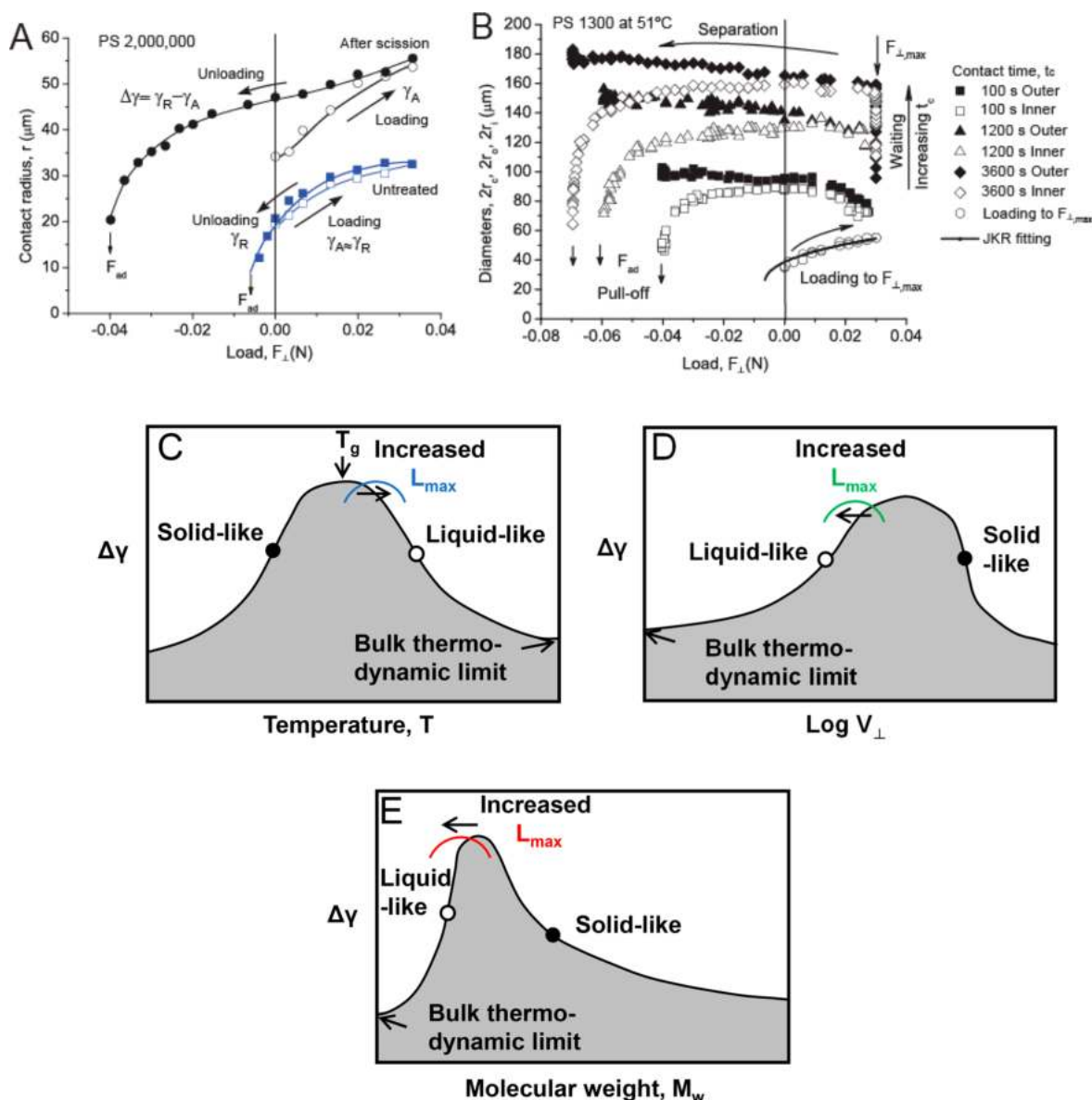


Figure 7. (A) Loading and unloading plots for PS (MW 2 000 000) surfaces with and without UV radiation treatment in air. (B) Loading and unloading plots for PS (MW 1 300) surfaces at 51 °C with different contact times. Effects of (C) temperature, (D) detachment velocity, and (E) molecular weight on the adhesion hysteresis. Reprinted from refs 12 and 33. Copyright American Chemistry Society.

Here, f_{monomer} is the static friction force needed to pull one monomer out of the polymer bulk, and f_b is the force needed to break one C–C bond of the polymer backbone. When N is intermediate ($\sigma_{\text{craze}}/f_{\text{monomer}}\Sigma_{\text{sat}} < N < \sigma_{\text{craze}}/f_{\text{monomer}}\Sigma_c$, where $\Sigma^* = \sigma_{\text{craze}}/f_{\text{monomer}}N$), the interfacial polymer chains exhibit pulling-out behavior during surface fracture with $\Sigma < \Sigma^*$, while craze will be formed with $\Sigma > \Sigma^*$. Σ_{sat} is the maximum areal chain density when the saturation of connecting block polymer chains at the contacting interface is achieved. When N is lower than $\sigma_{\text{craze}}/f_{\text{monomer}}\Sigma_{\text{sat}}$, the behavior of the interfacial polymer chains is being pulled out. It has been found by Creton and other researchers that when $N > \sigma_{\text{craze}}/f_{\text{monomer}}\Sigma_{\text{sat}}$, the plastic zone precedes the crack at two homopolymer interfaces reinforced by diblock copolymers.^{28,161,173} Meanwhile, the relation of interfacial toughness G and areal chain density Σ has been found to transit from $G \propto \Sigma$ to $G \propto \Sigma^2$.

When there is no connecting diblock copolymer at the interface between two homopolymers, a similar transition of

the fracture mechanism can still happen because of the entanglements of the two homopolymers. Typically, the static interface width (a_1) of the entangled interfacial region is used to describe the degree of entanglement of two polymers (i.e., the equilibrium width of the interface with the two entangled polymers present), which is given by eq 31.^{168,177–180}

$$a_1 \approx 2 \sqrt{\frac{a_1^2 + a_2^2}{12\chi}} \quad (31)$$

Here, a_1 and a_2 are the monomer lengths of polymers 1 and 2, respectively, and χ is the Flory–Huggins interaction parameter. The characteristic entanglement number N_{ent} and the entanglement length L_{ent} of polymers are given by eqs 32 and 33.

$$N_{\text{ent}} = \frac{a_1}{L_{\text{ave}}} \quad (32)$$

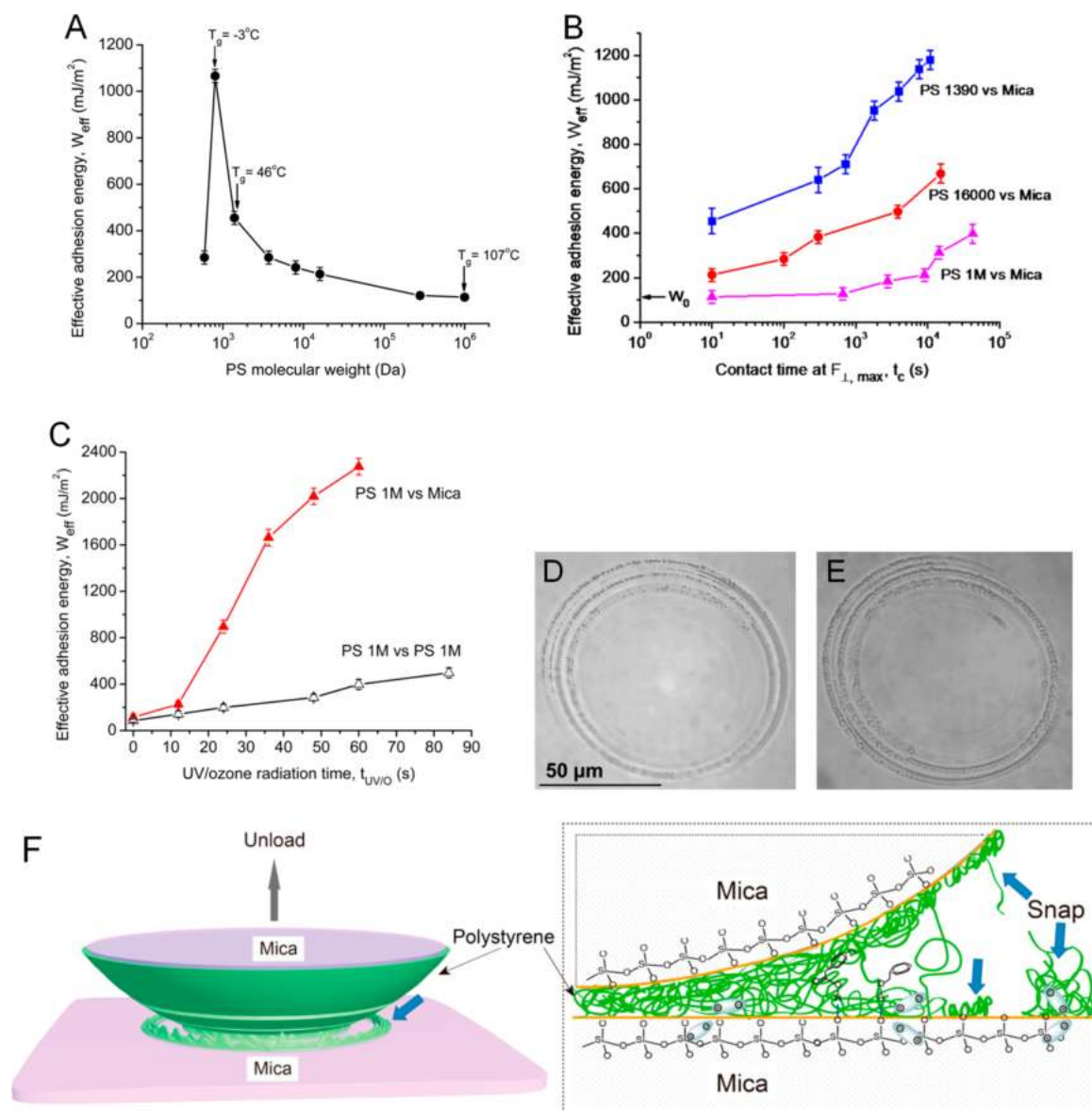


Figure 8. Effects of (A) molecular weight, (B) contact time, and (C) UV/ozone treatment on the adhesion energy between PS polymer and the mica surface. Optical images of concentric ring patterns of PS polymer residues on (D) the mica surface and (E) the PS surface after the surface fracture with the PS surface. (F) Schematic of the adhesive detachment of the mica surface and the PS polymer surface after UV/ozone treatment. Reprinted from ref 185. Copyright American Chemistry Society.

$$L_{\text{ent},i} = a_i \sqrt{\frac{n_{\text{ent},i}}{6}} \quad (33)$$

Here, L_{ave} is the average entanglement length of the polymer pair interacting with each other, $n_{\text{ent},i}$ is the degree of polymerization of the entanglement in the polymer, and i stands for the polymer species (i.e., 1 or 2). The characteristic number of entanglements can then be expressed as in eq 34.

$$N_{\text{ent}} = \sqrt{\frac{2(a_1^2 + a_2^2)}{\chi a_1 a_2 \sqrt{n_{\text{ent},1} n_{\text{ent},2}}}} \quad (34)$$

Brown and co-workers developed a model that was substantiated by the experiment results of Creton, Macosko, and co-workers. According to this model, the surface toughness G of the contacting interface of two homopolymers is

proportional to N_{ent}^2 when $N/N_e \geq 6$ to 8. Then eq 35 can be obtained as follows.

$$G \propto \frac{2(a_1^2 + a_2^2)}{\chi a_1 a_2 \sqrt{n_{\text{ent},1} n_{\text{ent},2}}} \quad (35)$$

This model was examined with experiments by Creton, Schnell, Macosko, and other researchers by using the asymmetric double cantilever beam (ADCB) method.^{169,181} Various kinds of polymers were employed in the polymer tests, such as PS, poly(ethylene oxide) (PEO), polyethylene (PE), and polycarbonate. For the interactions at the interface of PS–PS and PS-modified PS (i.e., poly(bromostyrene–styrene) or poly(*p*-methylstyrene)) with varied Flory–Huggins parameter χ , three regimes with different static interfacial widths a_i were detected.^{168,169} When a_i increased from regime I ($a_i < 6$ nm) to regime II ($6 \text{ nm} < a_i < 11$ nm), the behavior of polymer chains changed from pure pulling out to chain scission and the

interfacial toughness G increased significantly with the increasing interfacial width. When a_i was increase to regime III ($a_i > 11$ nm), the craze was formed during the surface fracture.

In recent publications, it has been found that the areal density of chain ends across the contacting interface, the bulk viscoelasticity indicating polymer chain mobility, and the specific physical and/or chemical interactions between polymer chains can affect the polymer entanglements at the interface and thus govern the adhesive properties between polymer surfaces and thin films.^{12,32,33,172,182,183} For example, Israelachvili and co-workers investigated the interactions between the PS polymers (e.g., MW 2 000 000) with different treatment.¹² It was found that treating a PS surface with ultraviolet (UV) radiation in an inert gas (i.e., nitrogen) could induce the cross-linking of polymer chains on the surface and thus reduced the density of chain ends. The adhesion between PS surfaces after the treatment was relatively weak. On the contrary, UV treatment in air (in the presence of oxygen) for PS polymers resulted in chain scission, and the density of chain ends could be increased. Thus, adhesion between the as-treated PS surfaces was significantly enhanced, as shown in Figure 7A. For PS polymers with low molecular weight or at temperature higher than or equal to T_g (e.g., molecular weight of 1300, temperature of 51 °C), which could increase the mobility of polymer chains, strong adhesion between PS surfaces and significant adhesion hysteresis were observed, as shown in Figure 7B.^{33,184} The T_g of PS polymer with a molecular weight of 1300 was reported at around 45 °C. For PS polymers with a high molecular weight (280 000–2 000 000), for which T_g was higher than room temperature, the adhesion energy was measured to decrease with increasing molecular weight at room temperature.¹⁸⁵ Zeng and co-workers also studied the separation velocity (V_L) effect on the adhesion between PS surfaces (molecular weight of less than 10 000) at a temperature of around T_g .³³ It was found that there was a critical separation velocity. When the separation velocity V_L was lower than the critical velocity, the surface energies (γ_R) of PS exhibited a velocity-independent property. However, when the separation velocity was higher than the critical value, the surface energies of PS were enhanced with increasing detachment velocity, which showed a power law dependence of $\gamma_R \propto V_L^n$ and $n = 0.15$ – 0.36 .³³ Such a scaling correlation could be compared with the reported values in the range of 0.1–0.8 by Muller, Li, Barthel, and Roux.^{94,186,187}

The schematics of temperature, separation velocity, and molecular weight effects on adhesion hysteresis $\Delta\gamma$ between two polymer surfaces are shown in Figure 7C–E. For glassy polymers with high molecular weights (for testing temperature $T < T_g$), the relaxation time of the polymer chains is long. Thus, the behaviors of the polymer surfaces are “solid-like” without significant involvement of bulk flow. Moreover, polymer loops are exposed at the surface with the relatively small density of short chain ends, leading to a very limited interdigitation or interpenetration between two surfaces, which results in a low adhesion hysteresis $\Delta\gamma$ during separation. The adhesion forces can be determined using the equation of $F_{ad} = 3\pi R\gamma$ according to the JKR theory. When the polymer molecular weight is low and/or the testing temperature is $T > T_g$, the polymers are liquid-like, with a low bulk viscosity and a short relation time of the polymer chains. The large surface deformation that arose from the macroscopic flow of polymer during approach and separation fails to be explained by the

JKR theory. Thus, thermodynamic parameter γ is used to determine the adhesion through the equation $F_{ad} = 4\pi R\gamma$ for the case of a liquid bridge between two surfaces under a low separation velocity. For a certain polymer (e.g., PS), the largest adhesion hysteresis $\Delta\gamma$ can be obtained when the temperature is around the glass-transition temperature, T_g . At zero or low load, the peak of adhesion hysteresis is at T_g or slightly below T_g , while the peak will shift to the position above T_g for several degrees at high loads. It is noted that the T_g for a polymer thin film may be higher or lower than the T_g for bulk polymer according to previous studies.¹⁸⁴

The adhesion and detachment mechanisms between polymer and solid substrate surfaces have also been investigated using SFA, and the asymmetric PS–mica system was selected as a model system.¹⁸⁵ The PS molecular weight, contact time, and polarity-enhancing UV/ozone treatment were found to significantly influence the adhesion between PS and the mica surface, as shown in Figure 8A–C. The adhesion between PS and the mica surface was mainly due to the polar interactions between the phenyl rings of PS and the polar –Si–OH and –Si–O–Si– groups on the mica surface. PS with a low molecular weight (T_g close to the experimental temperature to maximize the contribution of viscous forces) with high chain-end density and chain mobility could promote the rearrangement of polymer chains to facilitate the formation of more polar interactions between PS and mica surface, which thereby enhances the adhesion. A longer contact time could allow more effective polar interactions to be developed between rearranged polymer chains and the mica surface, leading to the enhanced adhesion property. UV/ozone treatment could increase the polarity of PS, strengthening its polar interactions with the mica surface and increasing the adhesion. Interestingly, the polymer material transfer was also observed during the separation of the UV/ozone-treated PS films (MW 1 M or 1 000 000). As shown in Figure 8D,E, the concentric ring polymer fracture pattern was on the mica surface and the opposing PS surface, revealing that the fracture occurred within the PS film. Such a fracture was discovered to occur locally (i.e., at different radial position in the “contact zone”), resulting in a “stick–slip” detachment. This phenomenon was mainly ascribed to the UV/ozone-induced chain scission and the enhanced polar interactions between PS chains/segments and the substrate surface, resulting in chain transfer and leading to the concentric ringlike polymer residues left on mica (Figure 8F).

4.3. Polymer Adhesion and Fracture from Liquid- to Solid-like Behavior. The fracture mechanisms of polymer thin films have been investigated using an SFA coupled with visualization techniques by Zeng and co-workers, suggesting a continuous process from liquid-like snapping to solid-like failure on the micro- and nanoscales.^{42,157,188–191} Fingering instabilities and cavities were observed upon the separation of confined thin films (thickness 10–1000 nm) of viscous PS with low molecular weight (i.e., 800 and 590) or glassy PS around the glass-transition temperature, which was in good agreement with the phenomena detected by macroscopic peeling or probe-tack tests for relatively thick adhesive films (0.01–1 mm).^{157,188,190–192} The Saffman–Taylor (ST) model was exploited to describe fingering instabilities of viscoelastic materials, with the prediction of the wavelength of fingering patterns.^{193–195} When a liquid with shear viscosity η_1 is gently introduced to a more viscous liquid with shear viscosity η_2 , patterned fingers with a wavelength larger than the critical

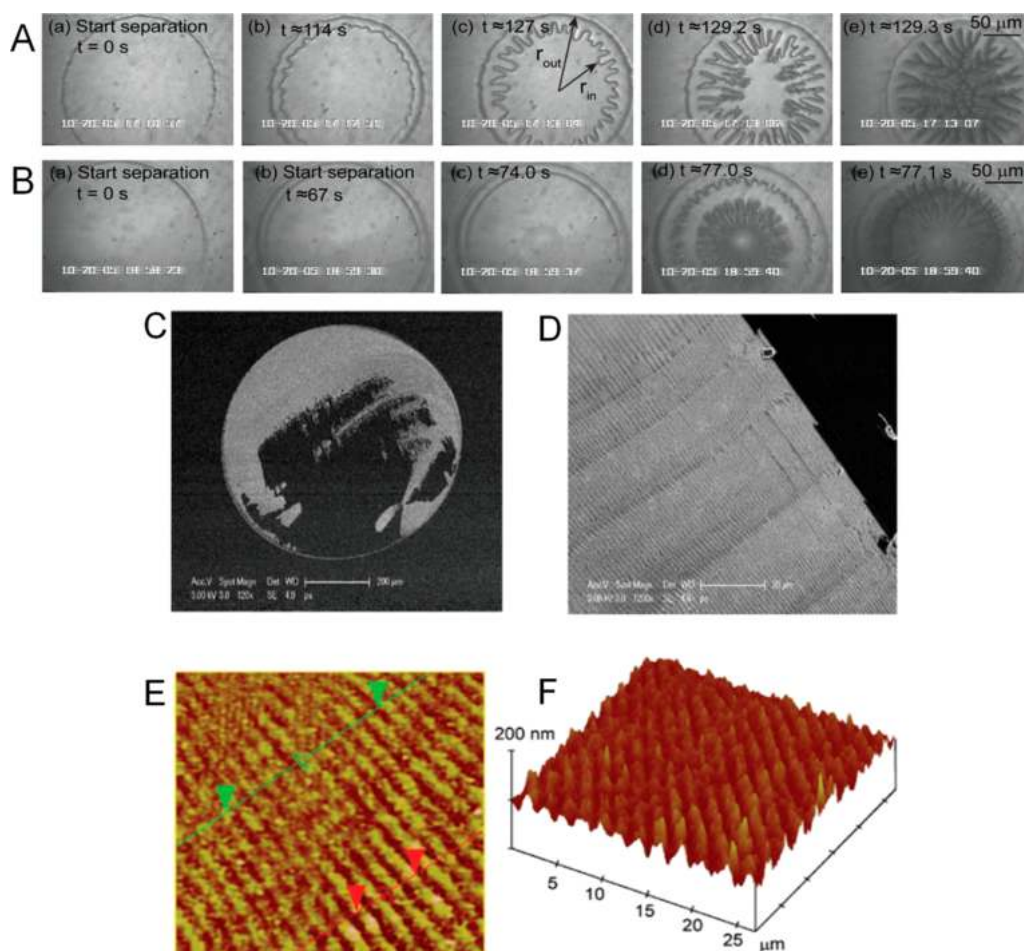


Figure 9. (A, B) Top-view microscopy images during the detachment between two PS thin films (molecular weight 590) after (A) keeping in contact for 10 min at 0.5 $\mu\text{m/s}$ and (B) keeping in contact for 30 min, with the first separation for 25 s, followed by waiting for 42 s and then separating again at a velocity of $\sim 3 \mu\text{m/s}$. (C–F) SEM and AFM images of the formed neck structure after the surface fracture of PS polymers (molecular weight 1390) at room temperature. Reprinted from ref 189. Copyright American Chemistry Society.

finger wavelength λ_C are generated by the interfacial instability, which is given by eq 36.^{189,193}

$$\lambda_C = 2\pi b \sqrt{\gamma / 12V(\eta_2 - \eta_1)} \quad (36)$$

Here, b is the gap height between the parallel plates, γ is the interfacial tension, and V is the fluid interface velocity.

The typical fingering patterns between two PS (molecular weight 590) melt thin films during the separation process are shown in Figure 9A,B.¹⁸⁹ With a short contact time (10 min) and low detachment velocity (0.5 $\mu\text{m/s}$) (Figure 9A), the pattern changed from the smooth and round fingering shape to the sharp tips before failure, exhibiting a transition of the fracture process. When the contact time was enhanced to 30 min and the separation velocity was increased to 3 $\mu\text{m/s}$ (Figure 9B), cavities appeared in the center of the neck, which expanded outward as cavity fingers before rupture.

The fracture pattern of glassy PS (molecular weight 1390) films was also examined by SEM and AFM, displaying parallel bands and sharp cracks as presented in Figure 9C–F.¹⁸⁹ Compared to the radial fingers of the viscous/viscoelastic polymers, the linear fracture bands are most likely attributed to the rapid propagation of the originated nanocracks along the direction of the crack tip. According to the definition, the viscosity of a material can be presented by the ratio of shear stress σ to shear rate V/b , and the ST equation is further

expressed as eq 37, where the critical wavelength is contributed by the surface tension, thickness of the polymer film, and shear stress rather than the viscosity and pulling velocity.¹⁸⁹ Experimental results of the failure of elastic and fully cross-linked PDMS films are in agreement with this relation.¹⁹⁶ Therefore, the continuous process of the failure of polymer thin films from the viscous liquid-like state to the elastic solid-like state can be described by the ST fingering equation.

$$\lambda_C = 2\pi b \sqrt{\frac{\gamma}{12V} \frac{V/b}{\sigma}} = 2\pi \sqrt{\frac{\gamma b}{12\sigma}} \quad (37)$$

It is noted that the polymer films tend to deform during the approach process between both symmetric polymer–polymer surfaces and asymmetric polymer–substrate surfaces.^{85,88,197} For viscous and viscoelastic polymers, the mobility of polymer chains can facilitate the deformation of surfaces, leading to the coalescence of symmetric polymer films and the spreading of polymers on a certain substrate. Zeng et al. reported the formation of highly ordered surface fingering patterns during the adhesive contact of two viscous or viscoelastic polymer films (e.g., PS, PDMS, and polybutadiene (PBD)), and the transient fingering instability could disappear after a certain time.⁸⁵ The schematic formation of fingering patterns and the associated macroscopic image, AFM image, and FECO fringes are shown in Figure 10. When the two surfaces approached

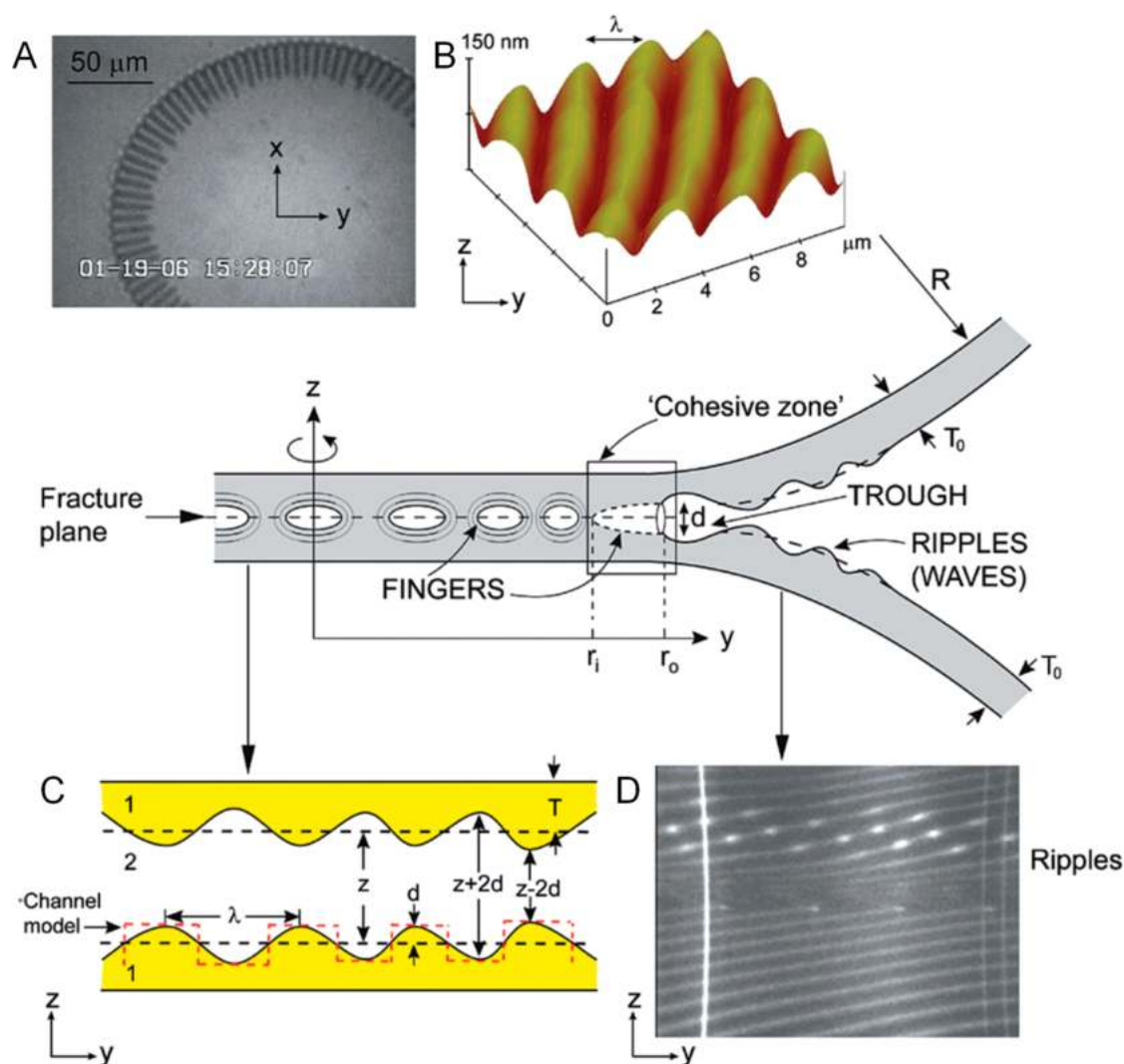


Figure 10. Schematic of adhesion junction and contact zone and the corresponding adhesion and coalescence of two viscoelastic polymers. (A) Microscopy image of the radial fingering patterns in the xy plane. (B) AFM three-dimensional topographic image of a typical fingering pattern. (C) Schematic of two polymer surfaces 1 and 2 approaching and interacting with each other in medium 2. (D) Typical FECO fringe for the concentric ripples propagating away from the contact zone. Reprinted from ref 85. Copyright American Chemistry Society.

each other below a critical rate, the appearance of fingering patterns was not affected by the approach velocity. For symmetric polymer–polymer coalescence, the average radius r of the fingering pattern was proportional to t^n , and the value of n varied in the range of 0.15–0.3 associated with the viscoelastic properties of the materials. The lifetime τ of the fingering patterns was dependent on the polymer properties, such as film thickness and viscosity, showing a maximum value at a certain film thickness and increasing with the polymer viscosity η as $\tau \propto \eta^n$, where n was determined to be 1.6 ± 0.2 for polymer–polymer adhesion and 2.1 ± 0.2 for polymer–substrate adhesion. For example, at a thickness of 200 nm, the fingering patterns generated by PBD films with a viscosity of ~ 5 Pa·s disappeared within 1 s, whereas the PS film with a viscosity of ~ 2900 Pa·s could form fingering patterns lasting for longer than 2 h. Moreover, for glassy polymers at the glass-transition temperature, the lifetime could be extended several days or even weeks.⁸⁵ The effect of applied loading force on the adhesion property and contact dynamics of viscoelastic polymers (e.g., PS with a molecular weight 900) was

investigated. When the applied loading force was gradually increased to around 30 mN and then kept unchanged for 1 week, a round contact boundary was first observed. But in 2 h highly ordered fingering patterns started to appear and became distinguishable in ~ 24 h.

It was proposed that the fluid mechanics coupled with the intermolecular and surface forces (e.g., VDW force) could be the interaction mechanism for the transient fingering patterns and interfacial instabilities. As shown in the schematic of Figure 10, during the growth of the contact area of the polymer thin films, the polymer melt outside the contact meniscus is driven by the Laplace pressure to move toward the contact zone. In this situation, air with low viscosity is introduced into the polymer melt with high viscosity in a local “trough” region outside of the contact meniscus where the polymer film thins. The transient fingering patterns could be induced by this indirect ST mechanism. The interaction forces between two surfaces (symmetric polymer–polymer case and asymmetric polymer–substrate case), including the attractive VDW force, repulsive surface tension, and elastic force, also contribute to

the surface deformation of polymer thin films. The attraction induces the formation of trough structure, while the repulsion prevents the formation. When the attraction is stronger than the repulsion, the surface deformation is aggravated, resulting in the formation and growth of the fingering patterns and instabilities. Otherwise, the surface deformation will be diminished. This type of adhesion behavior and transient fingering phenomenon may generally exist for a wide range of soft materials.

4.4. Surface Roughness on Polymer Adhesion. In practical applications, the surfaces of the polymer materials are barely atomically smooth, and the surface roughness can dramatically affect the adhesion properties of the polymeric materials in both positive and negative ways depending on the properties of the materials and the actual contact phenomenon. On the basis of the fundamental understanding of the classical contact mechanics in Section 2.1, various models have been developed by including the effect of roughness on the adhesion of a polymer surface with another surface of the same material or a different substrate.

Greenwood and Williamson investigated the contact behavior between a plane and a flat surface consisting of many uniformly distributed asperities with spherical summits of the same radius.¹⁹⁸ The contact of each asperity with the plane was assumed to be independent, and the real contact area was found to be enhanced by the increase in the normal loading force between the nonadhesive surfaces. In 1975, Fuller and Tabor studied the adhesion between a smooth rubber sphere and hard flat surfaces with different surface roughness.¹⁹⁹ The results indicated that the surface roughness, which was very small compared to the deformation within the contact area, could weaken the adhesion force even to a negligible value because of the decreased real contact area. Generally, for nonadhesive elastic or plastic surfaces, the real contact area between rough surfaces is much smaller than the apparent contact area, which tends to increase with increasing applied normal loading force due to surface deformation.^{200–206}

Benz and co-workers measured the adhesion properties of both randomly rough and patterned surfaces.²⁰⁷ The surfaces with random roughness ranging from 3 to 220 nm were prepared using poly(vinylidene fluoride-trifluoroethylene) (P(VDF-TrFE)), whereas the patterned surfaces were fabricated from poly(styrene-*b*-2-vinylpyridine) P(PS-PVP). For the randomly rough surfaces, the measured adhesion between identical polymer surfaces decreased slightly with increasing surface roughness and was enhanced by the increased loading force. Interestingly, the adhesion between the patterned surfaces dramatically decreased with higher surface roughness. Zappone and co-workers investigated the adhesion between the polymer surfaces (i.e., polyurethane (PU) and poly(vinylidene fluoride) (PVDF)) with different roughnesses and the smooth, bare mica surface both in air and in lubricating oil (Cargille).²⁰⁸ When the surface roughness was within the range of several nanometers (~ 7 nm), the measured adhesion in air decreased remarkably with the increasing roughness because of the reduced real contact area. As the roughness continued to increase, the influence of roughness became less significant because of the deformation of the asperities on polymer surfaces. Besides, the presence of lubricating oil between the surfaces could eliminate the adhesion by reducing the real contact area between the

major asperities of the rough polymer and smooth mica surface.

Surface roughness can also enhance the adhesion between two surfaces. The polymer surfaces with gecko-inspired hierarchical fibrillary structures can significantly increase the adhesion with other surfaces, which is generally believed to be due to the VDW attraction and increased real contact area.^{209–213} However, because of the limitation of effectively fabricating the specific surface structure or surface roughness, it still remains a challenge to establish a thorough understanding of the effect of surface roughness on polymer adhesion.

4.5. Common Strategies to Modulate Polymer Adhesion. Because the adhesion between polymer surfaces and thin films not only depends on the chemical and physical properties of the polymers but also is affected by surface roughness and environmental conditions, various methods have been developed to modulate the adhesion between two surfaces, and some commonly employed strategies are briefly introduced.

To increase the adhesion strength between two hard, solid surfaces, the most widely used strategy is to modify the substrates with a layer of relatively soft polymers, which results in an increased contact area between the two surfaces owing to the deformation of polymers during contact and compression. Moreover, the interactions between polymer chains including the physical interactions and chemical bonds can make a direct contribution to the enhancement of adhesion. Modulating the polymer entanglements at the interface while controlling the density and the mobility of the polymer chains can also tune the adhesion between two surfaces. When two polymer films are in contact, the flexible polymer chains on one surface can diffuse into the opposite one and entangle with the polymers on the other surface, yielding a significant enhancement of the adhesion strength. By adjusting the environmental conditions, such as temperature and UV radiation, the diffusion of polymer chains can be well-regulated and can lead to tunable adhesion between polymer surfaces. To effectively increase the polymer adhesion, specific physical and/or chemical interactions between polymer chains, such as the hydrophobic interaction between long carbon chains, hydrogen bonds, and dynamic chemical bonds (e.g., the Schiff-base bond), are commonly introduced into the systems.

Besides the direct coating and grafting of polymers, a pseudobrush layer of polymers can be established on the substrate by adsorbing polymer molecules from polymer melts or semidilute solutions.²¹⁴ For example, a pseudobrush layer of PDMS was formed on a silica surface by pressing bulk PDMS on the solid surface for more than 24 h,²¹⁵ and the bound PDMS layer could improve the adhesion of the silica substrate to other surfaces. It should be noted that the pseudobrush layer is different from the polymer brush grafted through specific chemical bonds because the polymer molecules in the pseudobrush layer can form multiple interaction points with the substrate, resulting in a restricted conformation of the polymer chains.

The design and modification of the molecular architecture have been recognized as an interesting and promising method for modulating the polymer adhesion. Previous studies on polymer adhesion are mainly focused on linear polymers. Recently, the effect of molecular architecture (i.e., linear, grafted, bottle-brush, branched, and highly branched) on the adhesion between the polymers and the substrates has been examined.^{216,217} It was found that for mobile polymers without

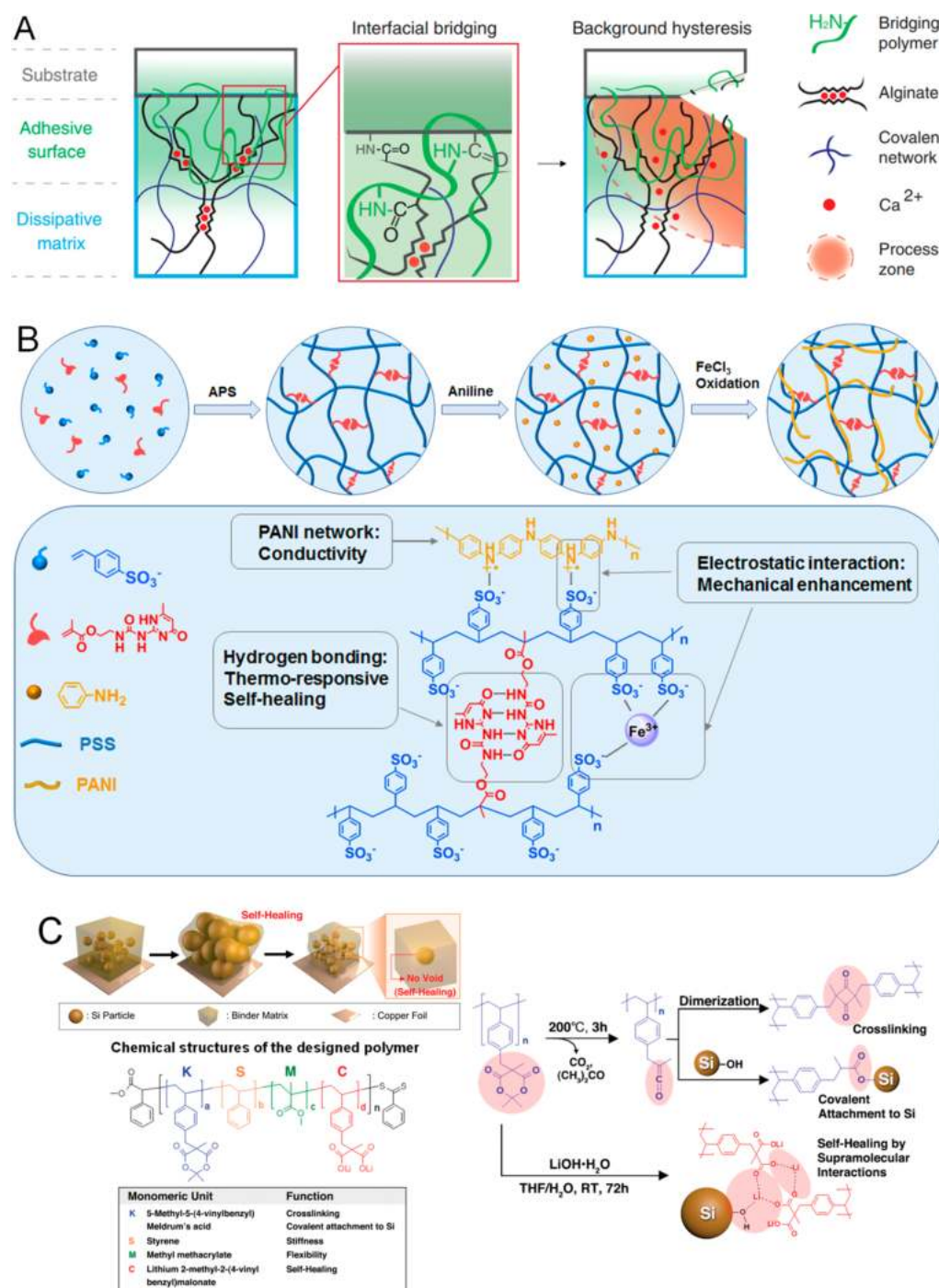


Figure 11. Design and development of polymeric materials for engineering and bioengineering applications. (A) Design of polymer-based tough bioadhesives containing an adhesive surface (green) and a dissipative matrix (light blue). (B) Schematic of supramolecular conductive PANI/PSS-UPy hydrogel for flexible bioelectronic application. (C) Development of polymeric binders of the silicon anode featuring a self-healing capacity based on the reversible ion-dipole interaction in lithium rechargeable batteries. Reprinted from refs 227, 240, and 245. Copyright American Association for the Advancement of Science, American Chemical Society, and John Wiley & Sons.

specific binding to the substrate, the adhesion was hardly affected by the side chains or molecular architecture; however, when the mobility of the polymer decreased and specific interactions (e.g., hydrogen bonds) were involved, the significant increase in the polymer adhesion was detected with the introduction of side chains, which was ascribed to the synergistic effect of the enhanced polymer entanglement and the increased real contact area.²¹⁶ The fabrication of polymer loops with both ends of a polymer chain anchored on the

substrate surface has been demonstrated to be a more effective strategy for reducing the polymer adhesion compared to the linear polymer brushes by hindering the penetration and interpenetration of the polymer with other components.^{218,219}

Recently, the gecko-inspired patterned adhesive surfaces have attracted considerable attention because of their robust and reversible adhesion on various surfaces, great adaptability to rough surfaces, excellent stability in both dry and wet environments, and good self-cleaning property.^{209,220–223} The

gecko-inspired adhesive surfaces possess hierarchical structures typically consisting of micro-/nanofibrils, which can enhance the adhesion with other surfaces by increasing the real contact area and dispersing the applied stress.^{212,224} It is believed that the strong adhesion strength between the hierarchical surfaces and substrate surfaces is dominated by the van der Waals force and other interactions.^{213,222} By applying peeling or shearing forces, the attachment and detachment processes can be reversible as well as controllable.^{213,224} Because of their universal adhesion and versatility, gecko-inspired patterned surfaces have been applied to various applications such as climbing robot feet and grippers, adhesive gloves in space, flexible wearable devices, and medical skin patches.^{224–226}

5. APPLICATIONS

5.1. Hydrogels. Hydrogels, as three-dimensional polymer networks with high water content, have served as promising candidates for many established and emerging applications in engineering and bioengineering, such as wound dressings,²²⁷ tissue scaffolds,²²⁸ bioelectronics,²²⁹ and soft ionotronics,²³⁰ because of their flexibility, biocompatibility, and stimuli-responsiveness. The mechanical properties of the as-fabricated hydrogel and its adhesion capability to various materials not only depend on the physical/chemical interactions but also are affected by the topology of networks and the energy dissipation mechanism.^{227,230–232} On the basis of the fundamental understanding of the adhesion between polymer surfaces and thin films, a series of hydrogels with desirable mechanical properties and adhesion behaviors have been developed via the rational design of molecular interactions and topologies.^{233–239}

The strong and robust bonding between the adhesive hydrogels and human tissues is a prerequisite for wound dressing applications. Recently, Mooney et al. reported a family of tough adhesives showing high adhesion energies to wet biological tissues via a two-layer strategy.²²⁷ The adhesive surface consisting of bridging polymers (e.g., chitosan, polyallylamine, polyethylenimine, collagen, and gelatin) was utilized to stably and firmly adhere to the tissues, and the tough double-network hydrogel matrix consisting of a covalently cross-linked polyacrylamide network and ionically cross-linked alginate network was employed to dissipate energy upon deformation. As presented in Figure 11A, when the hydrogel was separated from the substrate, the energy could be significantly dissipated via the breakage of alginate and calcium complexation at the tip of the crack, preventing the propagation of the crack.

The development of multifunctional hydrogels is also facilitated by the modulation of interactions between polymer chains, holding great promise for advanced bioelectronic devices. By introducing 2-ureido-4[1H]-pyrimidinone (UPy) groups as cross-linking points into the polyaniline/poly(4-styrenesulfonate) (PANI/PSS) network, Zeng and co-workers developed a conductive hydrogel with outstanding stretchability and a rapid self-healing capability for wearable bioelectronics, as depicted in Figure 11B.²⁴⁰ The dynamic and reversible multiple hydrogen bonding of UPy endows the hydrogel with stretchable and self-healing properties due to the formation of complementary hydrogen bonding, and the electrostatic interaction between the interpenetrated polymers can not only enhance the mechanical properties but also improve the conductivity of the hydrogel, leading to the fabrication of highly sensitive strain sensors.

5.2. Polymer Binder. Polymer binders play a critical role in maintaining the structural integrity and original capacity of the silicon (Si) anode, contributing to the high capacity of next-generation Li ion batteries.²⁴¹ The pulverization of Si is fatal to batteries with Si anodes, and even with the addition of polymer binders, the batteries still suffer from chronic capacity fading. The volume expansion of Si during charging can easily break the chemical/physical bonds between the polymer and Si as well as between polymers, leading to the undesired void formation around Si after the volume shrinkage during the following discharging, which thereby severely impairs the electrochemical performance.²⁴² Therefore, the improvement of the mechanical stability of the electrode through the polymer binder is essentially dependent on the adhesion between the polymer and Si particles as well as the cohesion between polymer chains,^{243,244} and the strong and reversible interactions such as specific noncovalent bonds and dynamic covalent bonds can be exploited in the binders to improve the cycling performances of the batteries. By copolymerizing 5-methyl-5-(4-vinylbenzyl) Meldrum's acid (M), styrene (S), methyl methacrylate (M), and lithium 2-methyl-2-(4-vinylbenzyl)malonate (C), Coskun and co-workers designed a self-healing polymeric binder featuring noncovalent ion–dipole interactions, as shown in Figure 11C.²⁴⁵ The lithium ions on polymer chains could form reversible ion–dipole interactions not only with the dicarboxyl groups on polymers but also with the silanol moieties on the Si particle surface, which facilitated the recovery of the binder–Si and binder–binder interactions, repairing the voids and maintaining the structural integrity of the electrode over a long cycling period.

5.3. Surface-Modification Technique. A surface-modification technique has been widely applied to modulate the surface properties (e.g., wettability) of a substrate through both physical and chemical approaches. A rational surface-modification technique by functional polymers has been commonly exploited in membrane engineering, oil–water separation, and bioengineering. Polydopamine, as a mussel-inspired polymer, is drawing increasing attention in surface modification because of its universal adhesion on diverse surfaces and its simple preparation processes.^{246–251} In spite of numerous studies on polydopamine-based polymers and their applications, it is still under debate whether the structure of polydopamine is a true polymer or a supramolecular assembly, which is mainly due to the auto-oxidation of dopamine and the following complex chemical reactions to form polydopamine.^{252–254} Owing to the insolubility of polydopamine in both aqueous solutions and organic solvents, it is challenging to experimentally determine the structure of polydopamine.²⁵²

The adhesion between a polydopamine surface and the substrates with varying wettability has been measured using an AFM.²⁵⁵ The substrate surfaces were prepared by grafting –OH groups or –CH₃ groups on gold surfaces via thiol–Au bonds. The results indicated that the polydopamine could deposit on all of the substrate surfaces, attributed to the hydrogen bonds and hydrophobic interactions provided by the catechol groups. Besides, the removal of the trapped air/vapor layer on the hydrophobic surface enhanced the adhesion between the polydopamine surface and the substrate, which was contributed by the strengthened hydrophobic attraction.

On the basis of the universal adhesion of polydopamine, a polyelectrolyte–polydopamine coating was developed to modify the surface properties of different substrates.²⁵⁶ Zwitterionic poly(3-[dimethyl(2-methacryloyloxyethyl) am-

monium] propanesulfonate) (PMAPS) was utilized as the functional coating material, and polydopamine was used to facilitate the coating process on both the silica substrate and polyurethane (PU) sponge. The obtained superoleophobic surface was successfully employed for water–oil separation and possessed an underwater self-cleaning property against heavy oil fouling. Moreover, the amine-modified catechol group has been designed as the anchoring ligand associated with the 2-methacryloyloxyethyl phosphorylcholine (PC) moiety for the surface modification of a variety of substrates including mica, glass, polypropylene (PP), polystyrene (PS), and TiO_2 .²⁵⁷ This facile, robust, and substrate-independent anchoring strategy endowed the surfaces with hydrophilicity and an bioantifouling property.

6. SUMMARY AND FUTURE PERSPECTIVES

Significant advances have been achieved in unraveling the adhesion mechanisms of polymer surfaces and thin films in the last few decades, and both fundamental and practical insights have been provided for the development of novel polymer materials for various applications such as hydrogel adhesives, polymer binders, and surface coatings. However, several challenges remain for the establishment of complete and comprehensive understanding in this field.

First, the impact of surface roughness on the adhesion between polymer surfaces is not systematically studied, and the precise modulation of adhesion via the control of surface roughness is still limited. Studying the adhesion mechanisms between surfaces of both random roughness and designed patterns could broaden our understanding of the surface structure with respect to the adhesion property and behavior and facilitate the development of surface-modification techniques using specific surface structure. Second, adhesion mechanisms of polymeric systems under extreme conditions (e.g., at extremely high or low temperature, in air or vacuum, and in extremely acid or alkaline solutions) are rarely reported. Such extreme conditions are expected to induce the variation of the physical/chemical properties of polymers and lead to distinct adhesion behaviors in both polymer–polymer and polymer–substrate systems, which is essentially important in the performance improvement of polymer materials. Third, the adhesion mechanisms of biomaterials and biological systems mostly remain to be systematically investigated in related biological processes or bioengineering applications. Investigating and mimicking the structure and property of biomaterials and biological systems is one of the most efficient strategies for developing new functional polymers and enhancing their properties. Fourth, the adhesion behavior of “smart” polymer materials with stimuli-responsive properties requires more characterization. Understanding the variation in polymer states and corresponding adhesion behavior under external stimuli provides fundamental insight into the dynamic mechanisms of polymer adhesion. Finally, with the development of theoretical methodologies and experimental techniques, the molecular mechanisms and nanomechanisms underlying the adhesion of polymer surfaces and thin films could be further elucidated, which facilitates the improvement of theoretical models and provides fundamental guidance for the evolution and application of polymer materials.

AUTHOR INFORMATION

Corresponding Author

*E-mail: hongbo.zeng@ualberta.ca. Phone: +1-780-492-1044.

ORCID

Hongbo Zeng: 0000-0002-1432-5979

Author Contributions

[†]These authors contributed equally to this work.

Notes

The authors declare no competing financial interest.

ACKNOWLEDGMENTS

The authors are grateful for financial support from the Natural Sciences and Engineering Research Council of Canada (NSERC), the Canada Foundation for Innovation (CFI), the NSERC E. W. R. Steacie Memorial Fellowship, and the Canada Research Chairs Program (H.Z.).

REFERENCES

- (1) Ekebaf, L.; Ogbeifun, D.; Okieimen, F. Polymer applications in agriculture. *Biokemistri* **2011**, *23* (2), 81–89.
- (2) Shahinpoor, M.; Kim, K. J. Ionic polymer–metal composites: IV. Industrial and medical applications. *Smart Mater. Struct.* **2005**, *14* (1), 197.
- (3) Green, R. A.; Baek, S.; Poole-Warren, L. A.; Martens, P. J. Conducting polymer-hydrogels for medical electrode applications. *Sci. Technol. Adv. Mater.* **2010**, *11* (1), 014107.
- (4) Alrifai, A.; Lindahl, O. A.; Ramser, K. Polymer-based microfluidic devices for pharmacy, biology and tissue engineering. *Polymers* **2012**, *4* (3), 1349–1398.
- (5) Jeong, H. E.; Lee, J.-K.; Kim, H. N.; Moon, S. H.; Suh, K. Y. A nontransferring dry adhesive with hierarchical polymer nanohairs. *Proc. Natl. Acad. Sci. U. S. A.* **2009**, *106* (14), 5639–5644.
- (6) Asadirad, A. M.; Boutault, S. p.; Erno, Z.; Branda, N. R. Controlling a polymer adhesive using light and a molecular switch. *J. Am. Chem. Soc.* **2014**, *136* (8), 3024–3027.
- (7) Chen, H.; Yuan, L.; Song, W.; Wu, Z.; Li, D. Biocompatible polymer materials: role of protein–surface interactions. *Prog. Polym. Sci.* **2008**, *33* (11), 1059–1087.
- (8) Nicolas, J.; Mura, S.; Brambilla, D.; Mackiewicz, N.; Couvreur, P. Design, functionalization strategies and biomedical applications of targeted biodegradable/biocompatible polymer-based nanocarriers for drug delivery. *Chem. Soc. Rev.* **2013**, *42* (3), 1147–1235.
- (9) Al-Saleh, M. H.; Sundararaj, U. A review of vapor grown carbon nanofiber/polymer conductive composites. *Carbon* **2009**, *47* (1), 2–22.
- (10) Yang, Y.; Yu, G.; Cha, J. J.; Wu, H.; Vosgueritchian, M.; Yao, Y.; Bao, Z.; Cui, Y. Improving the performance of lithium–sulfur batteries by conductive polymer coating. *ACS Nano* **2011**, *5* (11), 9187–9193.
- (11) Israelachvili, J. N. *Intermolecular and Surface Forces*; Academic Press: 2011.
- (12) Maeda, N.; Chen, N.; Tirrell, M.; Israelachvili, J. N. Adhesion and friction mechanisms of polymer-on-polymer surfaces. *Science* **2002**, *297* (5580), 379–382.
- (13) Shull, K. R. Contact mechanics and the adhesion of soft solids. *Mater. Sci. Eng., R* **2002**, *36* (1), 1–45.
- (14) Klein, J.; Kamiyama, Y.; Yoshizawa, H.; Israelachvili, J. N.; Fredrickson, G. H.; Pincus, P.; Fetters, L. J. Lubrication forces between surfaces bearing polymer brushes. *Macromolecules* **1993**, *26* (21), 5552–5560.
- (15) Israelachvili, J. N.; Tirrell, M.; Klein, J.; Almog, Y. a. Forces between two layers of adsorbed polystyrene immersed in cyclohexane below and above the θ temperature. *Macromolecules* **1984**, *17* (2), 204–209.
- (16) Kanitpong, K.; Bahia, H. Relating adhesion and cohesion of asphalts to the effect of moisture on laboratory performance of asphalt mixtures. *Transp. Res. Rec.* **2005**, *1901* (1), 33–43.
- (17) Lee, D. W.; Lim, C.; Israelachvili, J. N.; Hwang, D. S. Strong adhesion and cohesion of chitosan in aqueous solutions. *Langmuir* **2013**, *29* (46), 14222–14229.

- (18) Moropoulou, A.; Bakolas, A.; Bisbikou, K. Physico-chemical adhesion and cohesion bonds in joint mortars imparting durability to the historic structures. *Construction and Building Materials* **2000**, *14* (1), 35–46.
- (19) Wilker, J. J. Biomaterials: Redox and adhesion on the rocks. *Nat. Chem. Biol.* **2011**, *7* (9), 579.
- (20) Lepage, M.; Jiang, J.; Babin, J.; Qi, B.; Tremblay, L.; Zhao, Y. MRI observation of the light-induced release of a contrast agent from photo-controllable polymer micelles. *Phys. Med. Biol.* **2007**, *52* (10), N249.
- (21) Roberts, D. L.; Ma, Y.; Bowles, S. E.; Janczak, C. M.; Pyun, J.; Saavedra, S. S.; Aspinwall, C. A. Polymer-stabilized phospholipid vesicles with a controllable, pH-dependent disassembly mechanism. *Langmuir* **2009**, *25* (4), 1908–1910.
- (22) Li, H.; Lee, T.; Dziubla, T.; Pi, F.; Guo, S.; Xu, J.; Li, C.; Haque, F.; Liang, X.-J.; Guo, P. RNA as a stable polymer to build controllable and defined nanostructures for material and biomedical applications. *Nano Today* **2015**, *10* (5), 631–655.
- (23) Huo, M.; Yuan, J.; Tao, L.; Wei, Y. Redox-responsive polymers for drug delivery: from molecular design to applications. *Polym. Chem.* **2014**, *5* (5), 1519–1528.
- (24) Kim, S.; Kim, J.-H.; Jeon, O.; Kwon, I. C.; Park, K. Engineered polymers for advanced drug delivery. *Eur. J. Pharm. Biopharm.* **2009**, *71* (3), 420–430.
- (25) Haag, R. Supramolecular drug-delivery systems based on polymeric core-shell architectures. *Angew. Chem., Int. Ed.* **2004**, *43* (3), 278–282.
- (26) Jia, H.-Z.; Zhang, W.; Zhu, J.-Y.; Yang, B.; Chen, S.; Chen, G.; Zhao, Y.-F.; Feng, J.; Zhang, X.-Z. Hyperbranched-hyperbranched polymeric nanoassembly to mediate controllable co-delivery of siRNA and drug for synergistic tumor therapy. *J. Controlled Release* **2015**, *216*, 9–17.
- (27) Tirrell, M. Measurement of interfacial energy at solid polymer surfaces. *Langmuir* **1996**, *12* (19), 4548–4551.
- (28) Creton, C.; Kramer, E. J.; Hui, C. Y.; Brown, H. R. Failure mechanisms of polymer interfaces reinforced with block copolymers. *Macromolecules* **1992**, *25* (12), 3075–3088.
- (29) Horn, R.; Israelachvili, J. Molecular organization and viscosity of a thin film of molten polymer between two surfaces as probed by force measurements. *Macromolecules* **1988**, *21* (9), 2836–2841.
- (30) Patel, S. S.; Tirrell, M. Measurement of forces between surfaces in polymer fluids. *Annu. Rev. Phys. Chem.* **1989**, *40* (1), 597–635.
- (31) Brown, H. R. Effects of chain pull-out on adhesion of elastomers. *Macromolecules* **1993**, *26* (7), 1666–1670.
- (32) Chen, N.; Maeda, N.; Tirrell, M.; Israelachvili, J. Adhesion and friction of polymer surfaces: the effect of chain ends. *Macromolecules* **2005**, *38* (8), 3491–3503.
- (33) Zeng, H.; Maeda, N.; Chen, N.; Tirrell, M.; Israelachvili, J. Adhesion and friction of polystyrene surfaces around T g. *Macromolecules* **2006**, *39* (6), 2350–2363.
- (34) Zeng, H. *Polymer Adhesion, Friction, and Lubrication*; John Wiley & Sons: 2013.
- (35) Creton, C.; Kramer, E. J.; Hadziioannou, G. Critical molecular weight for block copolymer reinforcement of interfaces in a two-phase polymer blend. *Macromolecules* **1991**, *24* (8), 1846–1853.
- (36) Crosby, A. J.; Shull, K. R. Adhesive failure analysis of pressure-sensitive adhesives. *J. Polym. Sci., Part B: Polym. Phys.* **1999**, *37* (24), 3455–3472.
- (37) Zhang, X.; Liu, C.; Wang, Z. Force spectroscopy of polymers: Studying on intramolecular and intermolecular interactions in single molecular level. *Polymer* **2008**, *49* (16), 3353–3361.
- (38) Faghihnejad, A.; Zeng, H. Hydrophobic interactions between polymer surfaces: using polystyrene as a model system. *Soft Matter* **2012**, *8* (9), 2746–2759.
- (39) Faghihnejad, A.; Feldman, K. E.; Yu, J.; Tirrell, M. V.; Israelachvili, J. N.; Hawker, C. J.; Kramer, E. J.; Zeng, H. Adhesion and surface interactions of a self-healing polymer with multiple hydrogen-bonding groups. *Adv. Funct. Mater.* **2014**, *24* (16), 2322–2333.
- (40) Allara, D.; Fowkes, F.; Noolandi, J.; Rubloff, G.; Tirrell, M. Bonding and adhesion of polymer interfaces. *Mater. Sci. Eng.* **1986**, *83* (2), 213–226.
- (41) Kelley, T. W.; Schorr, P. A.; Johnson, K. D.; Tirrell, M.; Frisbie, C. D. Direct force measurements at polymer brush surfaces by atomic force microscopy. *Macromolecules* **1998**, *31* (13), 4297–4300.
- (42) Zeng, H.; Tian, Y.; Anderson, T. H.; Tirrell, M.; Israelachvili, J. N. New SFA techniques for studying surface forces and thin film patterns induced by electric fields. *Langmuir* **2008**, *24* (4), 1173–1182.
- (43) Mansky, P.; Liu, Y.; Huang, E.; Russell, T.; Hawker, C. Controlling polymer-surface interactions with random copolymer brushes. *Science* **1997**, *275* (5305), 1458–1460.
- (44) Raviv, U.; Giasson, S.; Kampf, N.; Gohy, J.-F.; Jérôme, R.; Klein, J. Lubrication by charged polymers. *Nature* **2003**, *425* (6954), 163.
- (45) Taunton, H. J.; Toprakcioglu, C.; Fetters, L. J.; Klein, J. Interactions between surfaces bearing end-adsorbed chains in a good solvent. *Macromolecules* **1990**, *23* (2), 571–580.
- (46) Appel, E. A.; Tibbitt, M. W.; Greer, J. M.; Fenton, O. S.; Kreuels, K.; Anderson, D. G.; Langer, R. Exploiting electrostatic interactions in polymer-nanoparticle hydrogels. *ACS Macro Lett.* **2015**, *4* (8), 848–852.
- (47) Sherrington, D. C.; Taskinen, K. A. Self-assembly in synthetic macromolecular systems via multiple hydrogen bonding interactions. *Chem. Soc. Rev.* **2001**, *30* (2), 83–93.
- (48) Chen, J.; Wu, M.; Gong, L.; Zhang, J.; Yan, B.; Liu, J.; Zhang, H.; Thundat, T.; Zeng, H. Mechanistic Understanding and Nanomechanics of Multiple Hydrogen-Bonding Interaction in Aqueous Environment. *J. Phys. Chem. C* **2019**, *123*, 4540.
- (49) Sánchez-Iglesias, A.; Grzelczak, M.; Altantzis, T.; Goris, B.; Perez-Juste, J.; Bals, S.; Van Tendeloo, G.; Donaldson, S. H., Jr; Chmelka, B. F.; Israelachvili, J. N. Hydrophobic interactions modulate self-assembly of nanoparticles. *ACS Nano* **2012**, *6* (12), 11059–11065.
- (50) Zhu, D.; Wang, F.; Gao, C.; Xu, Z. Construction of PS/PNIPAM core-shell particles and hollow spheres by using hydrophobic interaction and thermosensitive phase separation. *Front. Chem. Eng. China* **2008**, *2* (3), 253–256.
- (51) Cheng, Y.-T.; Rodak, D. E. Is the lotus leaf superhydrophobic? *Appl. Phys. Lett.* **2005**, *86* (14), 144101.
- (52) Jiang, L.; Zhao, Y.; Zhai, J. A lotus-leaf-like superhydrophobic surface: a porous microsphere/nanofiber composite film prepared by electrohydrodynamics. *Angew. Chem., Int. Ed.* **2004**, *43* (33), 4338–4341.
- (53) Ensikat, H. J.; Ditsche-Kuru, P.; Neinhuis, C.; Barthlott, W. Superhydrophobicity in perfection: the outstanding properties of the lotus leaf. *Beilstein J. Nanotechnol.* **2011**, *2* (1), 152–161.
- (54) Zhang, L.; Zhou, Z.; Cheng, B.; DeSimone, J. M.; Samulski, E. T. Superhydrophobic behavior of a perfluoropolyether lotus-leaf-like topography. *Langmuir* **2006**, *22* (20), 8576–8580.
- (55) Zhao, J.; Shi, Q.; Luan, S.; Song, L.; Yang, H.; Shi, H.; Jin, J.; Li, X.; Yin, J.; Stagnaro, P. Improved biocompatibility and antifouling property of polypropylene non-woven fabric membrane by surface grafting zwitterionic polymer. *J. Membr. Sci.* **2011**, *369* (1–2), 5–12.
- (56) Shi, Q.; Su, Y.; Zhao, W.; Li, C.; Hu, Y.; Jiang, Z.; Zhu, S. Zwitterionic polyethersulfone ultrafiltration membrane with superior antifouling property. *J. Membr. Sci.* **2008**, *319* (1–2), 271–278.
- (57) Chen, S.; Zheng, J.; Li, L.; Jiang, S. Strong resistance of phosphorylcholine self-assembled monolayers to protein adsorption: insights into nonfouling properties of zwitterionic materials. *J. Am. Chem. Soc.* **2005**, *127* (41), 14473–14478.
- (58) Butt, H.-J.; Graf, K.; Kappl, M. *Physics and Chemistry of Interfaces*; Wiley Online Library: 2003; Vol. 138.
- (59) Berg, J. C. *An Introduction to Interfaces & Colloids: The Bridge to Nanoscience*; World Scientific: 2010.
- (60) Owens, D. K.; Wendt, R. Estimation of the surface free energy of polymers. *J. Appl. Polym. Sci.* **1969**, *13* (8), 1741–1747.

- (61) Janssen, D.; De Palma, R.; Verlaak, S.; Heremans, P.; Dehaen, W. Static solvent contact angle measurements, surface free energy and wettability determination of various self-assembled monolayers on silicon dioxide. *Thin Solid Films* **2006**, *515* (4), 1433–1438.
- (62) Chibowski, E.; Perea-Carpio, R. Problems of contact angle and solid surface free energy determination. *Adv. Colloid Interface Sci.* **2002**, *98* (2), 245–264.
- (63) Good, R. J. A thermodynamic derivation of Wenzel's modification of young's equation for contact angles; together with a theory of hysteresis. *J. Am. Chem. Soc.* **1952**, *74* (20), 5041–5042.
- (64) White, L. R. On deviations from Young's equation. *J. Chem. Soc., Faraday Trans. 1* **1977**, *73*, 390–398.
- (65) van Oss, C. J.; Good, R. J. Surface tension and the solubility of polymers and biopolymers: the role of polar and apolar interfacial free energies. *J. Macromol. Sci., Chem.* **1989**, *26* (8), 1183–1203.
- (66) van Oss, C. J. Use of the combined Lifshitz–van der Waals and Lewis acid–base approaches in determining the apolar and polar contributions to surface and interfacial tensions and free energies. *J. Adhes. Sci. Technol.* **2002**, *16* (6), 669–677.
- (67) Sharma, A. Equilibrium contact angles and film thicknesses in the apolar and polar systems: Role of intermolecular interactions in coexistence of drops with thin films. *Langmuir* **1993**, *9* (12), 3580–3586.
- (68) Radelczuk, H.; Holysz, L.; Chibowski, E. Comparison of the Lifshitz–van der Waals/acid–base and contact angle hysteresis approaches for determination of solid surface free energy. *J. Adhes. Sci. Technol.* **2002**, *16* (12), 1547–1568.
- (69) Chen, H.; Li, L.; Jones, P. M.; Hsia, Y.-T.; Jhon, M. S. Lifshitz–van der Waals and Lewis acid–base approach for analyzing surface energy of molecularly thin lubricant films. *IEEE Trans. Magn.* **2007**, *43* (6), 2226–2228.
- (70) Hwang, G.; Yang, J.-h.; Lee, C.-H.; Ahn, I.-S.; Mhin, B. J. New selection criterion for a base polar liquid in the Lifshitz–van der Waals/Lewis acid–base approach. *J. Phys. Chem. C* **2011**, *115* (25), 12458–12463.
- (71) Balkenende, A.; Van de Boogaard, H.; Scholten, M.; Willard, N. Evaluation of different approaches to assess the surface tension of low-energy solids by means of contact angle measurements. *Langmuir* **1998**, *14* (20), 5907–5912.
- (72) Wenzel, R. N. Resistance of solid surfaces to wetting by water. *Ind. Eng. Chem.* **1936**, *28* (8), 988–994.
- (73) Cassie, A. Contact angles. *Discuss. Faraday Soc.* **1948**, *3*, 11–16.
- (74) Cassie, A.; Baxter, S. Wettability of porous surfaces. *Trans. Faraday Soc.* **1944**, *40*, 546–551.
- (75) Hertz, H. Ueber die Berührung fester elastischer Körper. *J. Reine Angew. Math.* **1882**, *92*, 156–171.
- (76) Johnson, K. L.; Kendall, K.; Roberts, A. Surface energy and the contact of elastic solids. *Proc. R. Soc. London, Ser. A* **1971**, *324* (1558), 301–313.
- (77) Derjaguin, B.; Muller, V.; Toporov, Y. P. Effect of contact deformations on the adhesion of particles. *Prog. Surf. Sci.* **1994**, *45* (1–4), 131–143.
- (78) Zhang, W.; Jin, F.; Zhang, S.; Guo, X. Adhesive contact on randomly rough surfaces based on the double-Hertz model. *J. Appl. Mech.* **2014**, *81* (5), 051008.
- (79) Kendall, K. The adhesion and surface energy of elastic solids. *J. Phys. D: Appl. Phys.* **1971**, *4* (8), 1186.
- (80) Derjaguin, B. V.; Muller, V. M.; Toporov, Y. P. Effect of contact deformations on the adhesion of particles. *J. Colloid Interface Sci.* **1975**, *53* (2), 314–326.
- (81) Johnson, K. L.; Johnson, K. L. *Contact Mechanics*; Cambridge University Press: 1987.
- (82) Horn, R.; Israelachvili, J.; Pribac, F. Measurement of the deformation and adhesion of solids in contact. *J. Colloid Interface Sci.* **1987**, *115* (2), 480–492.
- (83) Mangipudi, V. S.; Huang, E.; Tirrell, M.; Pocius, A. V. *Measurement of Interfacial Adhesion between Glassy Polymers Using the JKR Method Macromolecular Symposia*; Wiley Online Library: 1996; pp 131–143.
- (84) Ahn, D.; Shull, K. R. JKR studies of acrylic elastomer adhesion to glassy polymer substrates. *Macromolecules* **1996**, *29* (12), 4381–4390.
- (85) Zeng, H.; Tian, Y.; Zhao, B.; Tirrell, M.; Israelachvili, J. Transient surface patterns and instabilities at adhesive junctions of viscoelastic films. *Macromolecules* **2007**, *40* (23), 8409–8422.
- (86) Kausch, H. H.; Tirrell, M. Polymer interdiffusion. *Annu. Rev. Mater. Sci.* **1989**, *19* (1), 341–377.
- (87) Hui, C.-Y.; Baney, J.; Kramer, E. Contact mechanics and adhesion of viscoelastic spheres. *Langmuir* **1998**, *14* (22), 6570–6578.
- (88) Zeng, H.; Tian, Y.; Zhao, B.; Tirrell, M.; Israelachvili, J. Transient interfacial patterns and instabilities associated with liquid film adhesion and spreading. *Langmuir* **2007**, *23* (11), 6126–6135.
- (89) Webber, R. E.; Creton, C.; Brown, H. R.; Gong, J. P. Large strain hysteresis and Mullins effect of tough double-network hydrogels. *Macromolecules* **2007**, *40* (8), 2919–2927.
- (90) Ahagon, A.; Gent, A. Threshold fracture energies for elastomers. *J. Polym. Sci., Polym. Phys. Ed.* **1975**, *13* (10), 1903–1911.
- (91) Ahagon, A.; Gent, A. Effect of interfacial bonding on the strength of adhesion. *J. Polym. Sci., Polym. Phys. Ed.* **1975**, *13* (7), 1285–1300.
- (92) Ferry, J. D. *Viscoelastic Properties of Polymers*; John Wiley & Sons: 1980.
- (93) Li, L.-H.; Macosko, C.; Korba, G. L.; Pocius, A. V.; Tirrell, M. Interfacial energy and adhesion between acrylic pressure sensitive adhesives and release coatings. *J. Adhes.* **2001**, *77* (2), 95–123.
- (94) Li, L.; Tirrell, M.; Korba, G. A.; Pocius, A. V. Surface energy and adhesion studies on acrylic pressure sensitive adhesives. *J. Adhes.* **2001**, *76* (4), 307–334.
- (95) Li, L.; Mangipudi, V. S.; Tirrell, M.; Pocius, A. V. Direct Measurement of Surface and Interfacial Energies of Glassy Polymers and PDMS. *Fundamentals of Tribology and Bridging the Gap Between the Macro-and Micro/Nanoscales*; Springer: 2001; pp 305–329.
- (96) Xu, D. B.; Hui, C. Y.; Kramer, E. J. Interface fracture and viscoelastic deformation in finite size specimens. *J. Appl. Phys.* **1992**, *72* (8), 3305–3316.
- (97) Dai, C.-A.; Kramer, E. J.; Washiyama, J.; Hui, C.-Y. Fracture toughness of polymer interface reinforced with diblock copolymer: effect of homopolymer molecular weight. *Macromolecules* **1996**, *29* (23), 7536–7543.
- (98) Xiao, F.; Hui, C.-Y.; Washiyama, J.; Kramer, E. J. Phase angle effects on fracture toughness of polymer interfaces reinforced with block copolymers. *Macromolecules* **1994**, *27* (15), 4382–4390.
- (99) Perkins, W. G. Polymer toughness and impact resistance. *Polym. Eng. Sci.* **1999**, *39* (12), 2445–2460.
- (100) Gent, A. N.; Tobias, R. Threshold tear strength of elastomers. *J. Polym. Sci., Polym. Phys. Ed.* **1982**, *20* (11), 2051–2058.
- (101) Xu, D.-B.; Hui, C.-Y.; Kramer, E.; Creton, C. A micro-mechanical model of crack growth along polymer interfaces. *Mech. Mater.* **1991**, *11* (3), 257–268.
- (102) Kramer, E. J.; Norton, L. J.; Dai, C.-A.; Sha, Y.; Hui, C.-Y. Strengthening polymer interfaces. *Faraday Discuss.* **1994**, *98*, 31–46.
- (103) Raphael, E.; De Gennes, P. Rubber-rubber adhesion with connector molecules. *J. Phys. Chem.* **1992**, *96* (10), 4002–4007.
- (104) O'Connor, K.; McLeish, T. Entangled dynamics of healing end-grafted chains at a solid/polymer interface. *Faraday Discuss.* **1994**, *98*, 67–78.
- (105) Aubouy, M.; Léger, L.; Marciano, Y.; Raphaël, E.; Brown, H. *Adhesion between a Polydisperse Polymer Brush and an Elastomer*; AIP Conference Proceedings CONF- 950119, AIP1996; pp 3–13.
- (106) Deruelle, M.; Leger, L.; Tirrell, M. Adhesion at the solid-elastomer interface: influence of the interfacial chains. *Macromolecules* **1995**, *28* (22), 7419–7428.
- (107) Hui, C. Y.; Xu, D. B.; Kramer, E. J. A fracture model for a weak interface in a viscoelastic material (small scale yielding analysis). *J. Appl. Phys.* **1992**, *72* (8), 3294–3304.

- (108) Derjaguin, B. A theory of the heterocoagulation, interaction and adhesion of dissimilar particles in solutions of electrolytes. *Discuss. Faraday Soc.* **1954**, *18*, 85–98.
- (109) Derjaguin, B.; Titijevskaia, A.; Abricossova, I.; Malkina, A. Investigations of the forces of interaction of surfaces in different media and their application to the problem of colloid stability. *Discuss. Faraday Soc.* **1954**, *18*, 24–41.
- (110) Israelachvili, J.; Min, Y.; Akbulut, M.; Alig, A.; Carver, G.; Greene, W.; Kristiansen, K.; Meyer, E.; Pesika, N.; Rosenberg, K. Recent advances in the surface forces apparatus (SFA) technique. *Rep. Prog. Phys.* **2010**, *73* (3), 036601.
- (111) Kappl, M.; Butt, H. J. The colloidal probe technique and its application to adhesion force measurements. *Part. Part. Syst. Charact.* **2002**, *19* (3), 129–143.
- (112) Briscoe, B.; Fiori, L.; Pelillo, E. Nano-indentation of polymeric surfaces. *J. Phys. D: Appl. Phys.* **1998**, *31* (19), 2395.
- (113) Fällman, E.; Schedin, S.; Jass, J.; Andersson, M.; Uhlin, B. E.; Axner, O. Optical tweezers based force measurement system for quantitating binding interactions: system design and application for the study of bacterial adhesion. *Biosens. Bioelectron.* **2004**, *19* (11), 1429–1437.
- (114) Rundlöf, M.; Karlsson, M.; Wågberg, L.; Poptoshev, E.; Rutland, M.; Claesson, P. Application of the JKR method to the measurement of adhesion to Langmuir–Blodgett cellulose surfaces. *J. Colloid Interface Sci.* **2000**, *230* (2), 441–447.
- (115) Israelachvili, J.; Tabor, D. Measurement of van der Waals dispersion forces in the range 1.4 to 130 nm. *Nature, Phys. Sci.* **1972**, *236* (68), 106.
- (116) Israelachvili, J. N.; Tabor, D. The measurement of van der Waals dispersion forces in the range 1.5 to 130 nm. *Proc. R. Soc. London, Ser. A* **1972**, *331* (1584), 19–38.
- (117) Tabor, D.; Winterton, R. The direct measurement of normal and retarded van der Waals forces. *Proc. R. Soc. London, Ser. A* **1969**, *312* (1511), 435–450.
- (118) Israelachvili, J. Direct measurements of forces between surfaces in liquids at the molecular level. *Proc. Natl. Acad. Sci. U. S. A.* **1987**, *84* (14), 4722.
- (119) Israelachvili, J. N.; Adams, G. E. Measurement of forces between two mica surfaces in aqueous electrolyte solutions in the range 0–100 nm. *J. Chem. Soc., Faraday Trans. 1* **1978**, *74*, 975–1001.
- (120) Israelachvili, J. N.; McGuiggan, P. M. Adhesion and short-range forces between surfaces. Part I: New apparatus for surface force measurements. *J. Mater. Res.* **1990**, *5* (10), 2223–2231.
- (121) Raviv, U.; Laurat, P.; Klein, J. Fluidity of water confined to subnanometre films. *Nature* **2001**, *413* (6851), 51.
- (122) Raviv, U.; Klein, J. Fluidity of bound hydration layers. *Science* **2002**, *297* (5586), 1540–1543.
- (123) Klein, J.; Kumacheva, E.; Mahalu, D.; Perahia, D.; Fetters, L. J. Reduction of frictional forces between solid surfaces bearing polymer brushes. *Nature* **1994**, *370* (6491), 634.
- (124) Helm, C. A.; Knoll, W.; Israelachvili, J. N. Measurement of ligand-receptor interactions. *Proc. Natl. Acad. Sci. U. S. A.* **1991**, *88* (18), 8169–8173.
- (125) Horn, R.; Smith, D.; Haller, W. Surface forces and viscosity of water measured between silica sheets. *Chem. Phys. Lett.* **1989**, *162* (4–5), 404–408.
- (126) Vigil, G.; Xu, Z.; Steinberg, S.; Israelachvili, J. Interactions of silica surfaces. *J. Colloid Interface Sci.* **1994**, *165* (2), 367–385.
- (127) Horn, R. G.; Israelachvili, J. N. Direct measurement of structural forces between two surfaces in a nonpolar liquid. *J. Chem. Phys.* **1981**, *75* (3), 1400–1411.
- (128) Christenson, H.; Gruen, D.; Horn, R.; Israelachvili, J. Structuring in liquid alkanes between solid surfaces: Force measurements and mean-field theory. *J. Chem. Phys.* **1987**, *87* (3), 1834–1841.
- (129) Horn, R. G.; Israelachvili, J.; Perez, E. Forces due to structure in a thin liquid crystal film. *J. Phys. (Paris)* **1981**, *42* (1), 39–52.
- (130) Chan, D. Y.; Horn, R. The drainage of thin liquid films between solid surfaces. *J. Chem. Phys.* **1985**, *83* (10), 5311–5324.
- (131) Israelachvili, J. N.; McGuiggan, P. M.; Homola, A. M. Dynamic properties of molecularly thin liquid films. *Science* **1988**, *240* (4849), 189–191.
- (132) Balastre, M.; Li, F.; Schorr, P.; Yang, J.; Mays, J. W.; Tirrell, M. V. A study of polyelectrolyte brushes formed from adsorption of amphiphilic diblock copolymers using the surface forces apparatus. *Macromolecules* **2002**, *35* (25), 9480–9486.
- (133) Marra, J.; Israelachvili, J. Direct measurements of forces between phosphatidylcholine and phosphatidylethanolamine bilayers in aqueous electrolyte solutions. *Biochemistry* **1985**, *24* (17), 4608–4618.
- (134) Yu, J.; Jackson, N. E.; Xu, X.; Brettmann, B. K.; Ruths, M.; de Pablo, J. J.; Tirrell, M. Multivalent ions induce lateral structural inhomogeneities in polyelectrolyte brushes. *Science advances* **2017**, *3* (12), No. eaao1497.
- (135) Granick, S. Motions and relaxations of confined liquids. *Science* **1991**, *253* (5026), 1374–1379.
- (136) Israelachvili, J.; Berman, A. D. Surface forces and micro-rheology of molecularly thin liquid films. *CRC Handbook of Micro/Nanotribology* **1998**, *2*.
- (137) Chen, Y. L.; Chen, S.; Frank, C.; Israelachvili, J. Molecular mechanisms and kinetics during the self-assembly of surfactant layers. *J. Colloid Interface Sci.* **1992**, *153* (1), 244–265.
- (138) Drummond, C.; Israelachvili, J. Surface forces and wettability. *J. Pet. Sci. Eng.* **2002**, *33* (1–3), 123–133.
- (139) Mukhopadhyay, A.; Zhao, J.; Bae, S. C.; Granick, S. An integrated platform for surface forces measurements and fluorescence correlation spectroscopy. *Rev. Sci. Instrum.* **2003**, *74* (6), 3067–3072.
- (140) Wong, J. S.; Hong, L.; Bae, S. C.; Granick, S. Fluorescence recovery after photobleaching measurements of polymers in a surface forces apparatus. *J. Polym. Sci., Part B: Polym. Phys.* **2010**, *48* (24), 2582–2588.
- (141) Valtiner, M.; Banquy, X.; Kristiansen, K.; Greene, G. W.; Israelachvili, J. N. The electrochemical surface forces apparatus: The effect of surface roughness, electrostatic surface potentials, and anodic oxide growth on interaction forces, and friction between dissimilar surfaces in aqueous solutions. *Langmuir* **2012**, *28* (36), 13080–13093.
- (142) Kristiansen, K.; Valtiner, M.; Greene, G. W.; Boles, J. R.; Israelachvili, J. N. Pressure solution—The importance of the electrochemical surface potentials. *Geochim. Cosmochim. Acta* **2011**, *75* (22), 6882–6892.
- (143) Kasuya, M.; Sogawa, T.; Masuda, T.; Kamijo, T.; Uosaki, K.; Kurihara, K. Anion adsorption on gold electrodes studied by electrochemical surface forces measurement. *J. Phys. Chem. C* **2016**, *120* (29), 15986–15992.
- (144) Meyer, G.; Amer, N. M. Novel optical approach to atomic force microscopy. *Appl. Phys. Lett.* **1988**, *53* (12), 1045–1047.
- (145) Giessibl, F. J. Advances in atomic force microscopy. *Rev. Mod. Phys.* **2003**, *75* (3), 949.
- (146) Rugar, D.; Hansma, P. Atomic force microscopy. *Phys. Today* **1990**, *43* (10), 23–30.
- (147) Weisenhorn, A.; Hansma, P.; Albrecht, T.; Quate, C. Forces in atomic force microscopy in air and water. *Appl. Phys. Lett.* **1989**, *54* (26), 2651–2653.
- (148) Hutter, J. L.; Bechhoefer, J. Calibration of atomic-force microscope tips. *Rev. Sci. Instrum.* **1993**, *64* (7), 1868–1873.
- (149) Ren, S.; Masliyah, J.; Xu, Z. Studying bitumen–bubble interactions using atomic force microscopy. *Colloids Surf., A* **2014**, *444*, 165–172.
- (150) Zhou, H.; Götzinger, M.; Peukert, W. The influence of particle charge and roughness on particle–substrate adhesion. *Powder Technol.* **2003**, *135*, 82–91.
- (151) Schaefer, D.; Carpenter, M.; Gady, B.; Reifengerger, R.; Demejo, L.; Rimai, D. Surface roughness and its influence on particle adhesion using atomic force techniques. *J. Adhes. Sci. Technol.* **1995**, *9* (8), 1049–1062.
- (152) Bowen, W. R.; Doneva, T. A. Atomic force microscopy studies of membranes: Effect of surface roughness on double-layer

interactions and particle adhesion. *J. Colloid Interface Sci.* **2000**, 229 (2), 544–549.

(153) Feldman, K.; Tervoort, T.; Smith, P.; Spencer, N. D. Toward a force spectroscopy of polymer surfaces. *Langmuir* **1998**, 14 (2), 372–378.

(154) Chang, R. J.; Gent, A. Effect of interfacial bonding on the strength of adhesion of elastomers. I. Self-adhesion. *J. Polym. Sci., Polym. Phys. Ed.* **1981**, 19 (10), 1619–1633.

(155) Chang, R. J.; Gent, A. Effect of interfacial bonding on the strength of adhesion of elastomers. II. Dissimilar adherends. *J. Polym. Sci., Polym. Phys. Ed.* **1981**, 19 (10), 1635–1640.

(156) Ducrot, E.; Chen, Y.; Bulters, M.; Sijbesma, R. P.; Creton, C. Toughening elastomers with sacrificial bonds and watching them break. *Science* **2014**, 344 (6180), 186–189.

(157) Crosby, A. J.; Shull, K. R.; Lakrout, H.; Creton, C. Deformation and failure modes of adhesively bonded elastic layers. *J. Appl. Phys.* **2000**, 88 (5), 2956–2966.

(158) Gent, A.; Tobias, R. Effect of interfacial bonding on the strength of adhesion of elastomers. III. Interlinking by molecular entanglements. *J. Polym. Sci., Polym. Phys. Ed.* **1984**, 22 (8), 1483–1490.

(159) Ellul, M.; Gent, A. The role of molecular diffusion in the adhesion of elastomers. *J. Polym. Sci., Polym. Phys. Ed.* **1984**, 22 (11), 1953–1968.

(160) Ellul, M.; Gent, A. The role of molecular diffusion in the adhesion of EPDM and EPR elastomers. *J. Polym. Sci., Polym. Phys. Ed.* **1985**, 23 (9), 1823–1830.

(161) Brown, H. R. The adhesion of polymers: relations between properties of polymer chains and interface toughness. *J. Adhes.* **2006**, 82 (10), 1013–1032.

(162) Brown, H. The adhesion between polymers. *Annu. Rev. Mater. Sci.* **1991**, 21 (1), 463–489.

(163) Creton, C.; Kramer, E. J.; Brown, H. R.; Hui, C.-Y., Adhesion and fracture of interfaces between immiscible polymers: from the molecular to the continuum scale. *Molecular Simulation Fracture Gel Theory*; Springer: 2001; pp 53–136.

(164) Creton, C.; Ciccotti, M. Fracture and adhesion of soft materials: a review. *Rep. Prog. Phys.* **2016**, 79 (4), 046601.

(165) Ji, H.; De Gennes, P. Adhesion via connector molecules: the many-stitch problem. *Macromolecules* **1993**, 26 (3), 520–525.

(166) Brown, H. R.; Hui, C. Y.; Raphael, E. Interplay between intermolecular interactions and chain pullout in the adhesion of elastomer. *Macromolecules* **1994**, 27 (2), 608–609.

(167) Washiyama, J.; Creton, C.; Kramer, E. J.; Xiao, F.; Hui, C. Y. Optimum toughening of homopolymer interfaces with block copolymers. *Macromolecules* **1993**, 26 (22), 6011–6020.

(168) Schnell, R.; Stamm, M.; Creton, C. Direct correlation between interfacial width and adhesion in glassy polymers. *Macromolecules* **1998**, 31 (7), 2284–2292.

(169) Schnell, R.; Stamm, M.; Creton, C. Mechanical properties of homopolymer interfaces: Transition from simple pullout to crazing with increasing interfacial width. *Macromolecules* **1999**, 32 (10), 3420–3425.

(170) Brown, H. R.; Kramer, E. J. Craze microstructure from small-angle X-ray scattering (SAXS). *J. Macromol. Sci., Part B: Phys.* **1981**, 19 (3), 487–522.

(171) Creton, C.; Hooker, J.; Shull, K. R. Bulk and interfacial contributions to the debonding mechanisms of soft adhesives: extension to large strains. *Langmuir* **2001**, 17 (16), 4948–4954.

(172) Zeng, H.; Tirrell, M.; Israelachvili, J. Limit cycles in dynamic adhesion and friction processes: a discussion. *J. Adhes.* **2006**, 82 (9), 933–943.

(173) Wool, R. P. Polymer entanglements. *Macromolecules* **1993**, 26 (7), 1564–1569.

(174) Lake, G.; Thomas, A. The strength of highly elastic materials. *Proceedings of the Royal Society of London. Series A. Mathematical and Physical Sciences* **1967**, 300 (1460), 108–119.

(175) Sambasivam, M.; Klein, A.; Sperling, L. Energy-consuming micromechanisms in the fracture of glassy polymers. 2. Effect of

molecular weight on the fracture of polystyrene. *Macromolecules* **1995**, 28 (1), 152–159.

(176) Washiyama, J.; Kramer, E. J.; Creton, C. F.; Hui, C.-Y. Chain pullout fracture of polymer interfaces. *Macromolecules* **1994**, 27 (8), 2019–2024.

(177) Helfand, E.; Tagami, Y. Theory of the interface between immiscible polymers. *J. Polym. Sci., Part B: Polym. Lett.* **1971**, 9 (10), 741–746.

(178) Helfand, E.; Tagami, Y. Theory of the interface between immiscible polymers. II. *J. Chem. Phys.* **1972**, 56 (7), 3592–3601.

(179) Helfand, E.; Tagami, Y. Theory of the interface between immiscible polymers. *J. Chem. Phys.* **1972**, 57 (4), 1812–1813.

(180) Helfand, E.; Sapse, A. M. Theory of unsymmetric polymer–polymer interfaces. *J. Chem. Phys.* **1975**, 62 (4), 1327–1331.

(181) Cole, P. J.; Cook, R. F.; Macosko, C. W. Adhesion between immiscible polymers correlated with interfacial entanglements. *Macromolecules* **2003**, 36 (8), 2808–2815.

(182) Rocha, J.; Baydak, E.; Yarranton, H.; Sztukowski, D.; Ali-Marciano, V.; Gong, L.; Shi, C.; Zeng, H. Role of aqueous phase chemistry, interfacial film properties, and surface coverage in stabilizing water-in-bitumen emulsions. *Energy Fuels* **2016**, 30 (7), 5240–5252.

(183) Klein, J. The interdiffusion of polymers. *Science* **1990**, 250 (4981), 640–646.

(184) De Gennes, P. Glass transitions in thin polymer films. *Eur. Phys. J. E: Soft Matter Biol. Phys.* **2000**, 2 (3), 201–205.

(185) Zeng, H.; Huang, J.; Tian, Y.; Li, L.; Tirrell, M. V.; Israelachvili, J. N. Adhesion and detachment mechanisms between polymer and solid substrate surfaces: using polystyrene–mica as a model system. *Macromolecules* **2016**, 49 (14), 5223–5231.

(186) Barthel, E.; Roux, S. Velocity-dependent adherence: an analytical approach for the JKR and DMT models. *Langmuir* **2000**, 16 (21), 8134–8138.

(187) Muller, V. Viscoelastic pull-off of a sphere from flat surface. *Colloid J.* **1996**, 58 (5), 612–619.

(188) Shull, K. R.; Flanagan, C. M.; Crosby, A. J. Fingering instabilities of confined elastic layers in tension. *Phys. Rev. Lett.* **2000**, 84 (14), 3057.

(189) Zeng, H.; Zhao, B.; Israelachvili, J. N.; Tirrell, M. Liquid-to solid-like failure mechanism of thin polymer films at micro- and nanoscales. *Macromolecules* **2010**, 43 (1), 538–542.

(190) Shull, K. R.; Creton, C. Deformation behavior of thin, compliant layers under tensile loading conditions. *J. Polym. Sci., Part B: Polym. Phys.* **2004**, 42 (22), 4023–4043.

(191) Fields, R.; Ashby, M. Finger-like crack growth in solids and liquids. *Philos. Mag.* **1976**, 33 (1), 33–48.

(192) Derks, D.; Lindner, A.; Creton, C.; Bonn, D. Cohesive failure of thin layers of soft model adhesives under tension. *J. Appl. Phys.* **2003**, 93 (3), 1557–1566.

(193) Saffman, P. G.; Taylor, G. I. The penetration of a fluid into a porous medium or Hele-Shaw cell containing a more viscous liquid. *Proceedings of the Royal Society of London. Series A. Mathematical and Physical Sciences* **1958**, 245 (1242), 312–329.

(194) Homsy, G. M. Viscous fingering in porous media. *Annu. Rev. Fluid Mech.* **1987**, 19 (1), 271–311.

(195) Chuoke, R.; Van Meurs, P.; van der Poel, C., The instability of slow, immiscible, viscous liquid-liquid displacements in permeable media. *Petr. Trans, AIME* **1959**, 216, 188–194

(196) Nase, J.; Lindner, A.; Creton, C. Pattern formation during deformation of a confined viscoelastic layer: From a viscous liquid to a soft elastic solid. *Phys. Rev. Lett.* **2008**, 101 (7), 074503.

(197) Zeng, H.; Zhao, B.; Tian, Y.; Tirrell, M.; Leal, L. G.; Israelachvili, J. N. Transient surface patterns during adhesion and coalescence of thin liquid films. *Soft Matter* **2007**, 3 (1), 88–93.

(198) Greenwood, J.; Williamson, J. P. Contact of nominally flat surfaces. *Proceedings of the royal society of London. Series A. Mathematical and physical sciences* **1966**, 295 (1442), 300–319.

- (199) Fuller, K.; Tabor, D. The effect of surface roughness on the adhesion of elastic solids. *Proc. R. Soc. London, Ser. A* **1975**, *345* (1642), 327–342.
- (200) Tabor, D. *The Area of Contact between Stationary and between Moving Surfaces*; University of Cambridge, 1939.
- (201) Landman, U.; Luedtke, W.; Ringer, E. M. Molecular Dynamics Simulations of Adhesive Contact Formation and Friction. *Fundamentals of Friction: Macroscopic and Microscopic Processes*; Springer: 1992; pp 463–510.
- (202) Cheng, S.; Robbins, M. O. Defining contact at the atomic scale. *Tribol. Lett.* **2010**, *39* (3), 329–348.
- (203) Akarapu, S.; Sharp, T.; Robbins, M. O. Stiffness of contacts between rough surfaces. *Phys. Rev. Lett.* **2011**, *106* (20), 204301.
- (204) Persson, B. Elastoplastic contact between randomly rough surfaces. *Phys. Rev. Lett.* **2001**, *87* (11), 116101.
- (205) Chan, E. P.; Smith, E. J.; Hayward, R. C.; Crosby, A. J. Surface wrinkles for smart adhesion. *Adv. Mater.* **2008**, *20* (4), 711–716.
- (206) Chan, E. P.; Crosby, A. J. Fabricating microlens arrays by surface wrinkling. *Adv. Mater.* **2006**, *18* (24), 3238–3242.
- (207) Benz, M.; Rosenberg, K. J.; Kramer, E. J.; Israelachvili, J. N. The deformation and adhesion of randomly rough and patterned surfaces. *J. Phys. Chem. B* **2006**, *110* (24), 11884–11893.
- (208) Zappone, B.; Rosenberg, K. J.; Israelachvili, J. Role of nanometer roughness on the adhesion and friction of a rough polymer surface and a molecularly smooth mica surface. *Tribol. Lett.* **2007**, *26* (3), 191.
- (209) Murphy, M. P.; Kim, S.; Sitti, M. Enhanced adhesion by gecko-inspired hierarchical fibrillar adhesives. *ACS Appl. Mater. Interfaces* **2009**, *1* (4), 849–855.
- (210) Murphy, M. P.; Aksak, B.; Sitti, M. Gecko-inspired directional and controllable adhesion. *Small* **2009**, *5* (2), 170–175.
- (211) Hu, S.; Xia, Z. Rational Design and Nanofabrication of Gecko-Inspired Fibrillar Adhesives. *Small* **2012**, *8* (16), 2464–2468.
- (212) Jin, K.; Tian, Y.; Erickson, J. S.; Puthoff, J.; Autumn, K.; Pesika, N. S. Design and fabrication of gecko-inspired adhesives. *Langmuir* **2012**, *28* (13), 5737–5742.
- (213) Li, X.; Tao, D.; Lu, H.; Bai, P.; Liu, Z.; Ma, L.; Meng, Y.; Tian, Y. Recent developments in gecko-inspired dry adhesive surfaces from fabrication to application. *Surf. Topogr.: Metrol. Prop.* **2019**, *7* (2), 023001.
- (214) Guiselin, O. Irreversible adsorption of a concentrated polymer solution. *EPL (Europhysics Letters)* **1992**, *17* (3), 225.
- (215) Migler, K.; Massey, G.; Hervet, I.; Leger, L. The slip transition at the polymer-solid interface. *J. Phys.: Condens. Matter* **1994**, *6* (23A), A301.
- (216) Kienle, S.; Gallei, M.; Yu, H.; Zhang, B.; Krysiak, S.; Balzer, B. N.; Rehahn, M.; Schlüter, A. D.; Hugel, T. Effect of molecular architecture on single polymer adhesion. *Langmuir* **2014**, *30* (15), 4351–4357.
- (217) Klein, J. Dynamics of entangled linear, branched, and cyclic polymers. *Macromolecules* **1986**, *19* (1), 105–118.
- (218) Li, L.; Yan, B.; Zhang, L.; Tian, Y.; Zeng, H. Mussel-inspired antifouling coatings bearing polymer loops. *Chem. Commun.* **2015**, *51* (87), 15780–15783.
- (219) Han, L.; Xiang, L.; Zhang, J.; Chen, J.; Liu, J.; Yan, B.; Zeng, H. Biomimetic Lubrication and Surface Interactions of Dopamine-Assisted Zwitterionic Polyelectrolyte Coatings. *Langmuir* **2018**, *34* (38), 11593–11601.
- (220) Autumn, K.; Sitti, M.; Liang, Y. A.; Peattie, A. M.; Hansen, W. R.; Sponberg, S.; Kenny, T. W.; Fearing, R.; Israelachvili, J. N.; Full, R. J. Evidence for van der Waals adhesion in gecko setae. *Proc. Natl. Acad. Sci. U. S. A.* **2002**, *99* (19), 12252–12256.
- (221) Tian, Y.; Pesika, N.; Zeng, H.; Rosenberg, K.; Zhao, B.; McGuiggan, P.; Autumn, K.; Israelachvili, J. Adhesion and friction in gecko toe attachment and detachment. *Proc. Natl. Acad. Sci. U. S. A.* **2006**, *103* (51), 19320–19325.
- (222) Zhou, M.; Pesika, N.; Zeng, H.; Tian, Y.; Israelachvili, J. Recent advances in gecko adhesion and friction mechanisms and development of gecko-inspired dry adhesive surfaces. *Friction* **2013**, *1* (2), 114–129.
- (223) Zeng, H.; Pesika, N.; Tian, Y.; Zhao, B.; Chen, Y.; Tirrell, M.; Turner, K. L.; Israelachvili, J. N. Frictional adhesion of patterned surfaces and implications for gecko and biomimetic systems. *Langmuir* **2009**, *25* (13), 7486–7495.
- (224) Boesel, L. F.; Greiner, C.; Arzt, E.; Del Campo, A. Gecko-inspired surfaces: a path to strong and reversible dry adhesives. *Adv. Mater.* **2010**, *22* (19), 2125–2137.
- (225) Yu, J.; Chary, S.; Das, S.; Tamiel, J.; Pesika, N. S.; Turner, K. L.; Israelachvili, J. N. Gecko-inspired dry adhesive for robotic applications. *Adv. Funct. Mater.* **2011**, *21* (16), 3010–3018.
- (226) Kwak, M. K.; Jeong, H. E.; Suh, K. Y. Rational design and enhanced biocompatibility of a dry adhesive medical skin patch. *Adv. Mater.* **2011**, *23* (34), 3949–3953.
- (227) Li, J.; Celiz, A.; Yang, J.; Wang, Q.; Wamala, I.; Whyte, W.; Seo, B.; Vasilyev, N.; Vlassak, J.; Suo, Z. Tough adhesives for diverse wet surfaces. *Science* **2017**, *357* (6349), 378–381.
- (228) Lee, K. Y.; Mooney, D. J. Hydrogels for tissue engineering. *Chem. Rev.* **2001**, *101* (7), 1869–1880.
- (229) Feiner, R.; Dvir, T. Tissue–electronics interfaces: From implantable devices to engineered tissues. *Nature Reviews Materials* **2018**, *3* (1), 17076.
- (230) Yuk, H.; Zhang, T.; Lin, S.; Parada, G. A.; Zhao, X. Tough bonding of hydrogels to diverse non-porous surfaces. *Nat. Mater.* **2016**, *15* (2), 190.
- (231) Roy, C. K.; Guo, H. L.; Sun, T. L.; Ihsan, A. B.; Kurokawa, T.; Takahata, M.; Nonoyama, T.; Nakajima, T.; Gong, J. P. Self-Adjustable Adhesion of Polyampholyte Hydrogels. *Adv. Mater.* **2015**, *27* (45), 7344–7348.
- (232) Sun, M.; Bai, R.; Yang, X.; Song, J.; Qin, M.; Suo, Z.; He, X. Hydrogel interferometry for ultrasensitive and highly selective chemical detection. *Adv. Mater.* **2018**, *30* (46), 1804916.
- (233) Bernkop-Schnürch, A. Thiomers: a new generation of mucoadhesive polymers. *Adv. Drug Delivery Rev.* **2005**, *57* (11), 1569–1582.
- (234) Hu, X.; Vatanikhah-Varnoosfaderani, M.; Zhou, J.; Li, Q.; Sheiko, S. S. Weak hydrogen bonding enables hard, strong, tough, and elastic hydrogels. *Adv. Mater.* **2015**, *27* (43), 6899–6905.
- (235) Le Floch, P.; Yao, X.; Liu, Q.; Wang, Z.; Nian, G.; Sun, Y.; Jia, L.; Suo, Z. Wearable and washable conductors for active textiles. *ACS Appl. Mater. Interfaces* **2017**, *9* (30), 25542–25552.
- (236) Wirthl, D.; Pichler, R.; Drack, M.; Kettlhuber, G.; Moser, R.; Gerstmayr, R.; Hartmann, F.; Bradt, E.; Kaltseis, R.; Siket, C. M. Instant tough bonding of hydrogels for soft machines and electronics. *Science advances* **2017**, *3* (6), No. e1700053.
- (237) Yang, C.; Suo, Z. Hydrogel ionotronics. *Nature Reviews Materials* **2018**, *3* (6), 125.
- (238) Yang, J.; Bai, R.; Chen, B.; Suo, Z. Hydrogel adhesion: A supramolecular synergy of chemistry, topology, and mechanics. *Adv. Funct. Mater.* **2019**, 1901693.
- (239) Yang, Y.; Wang, X.; Yang, F.; Shen, H.; Wu, D. A universal soaking strategy to convert composite hydrogels into extremely tough and rapidly recoverable double-network hydrogels. *Adv. Mater.* **2016**, *28* (33), 7178–7184.
- (240) Chen, J.; Peng, Q.; Thundat, T.; Zeng, H. Stretchable, Injectible and Self-Healing Conductive Hydrogel Enabled by Multiple Hydrogen Bonding toward Wearable Electronics. *Chem. Mater.* **2019**, *31*, 4553.
- (241) Kwon, T.-w.; Choi, J. W.; Coskun, A. The emerging era of supramolecular polymeric binders in silicon anodes. *Chem. Soc. Rev.* **2018**, *47* (6), 2145–2164.
- (242) Wu, H.; Cui, Y. Designing nanostructured Si anodes for high energy lithium ion batteries. *Nano Today* **2012**, *7* (5), 414–429.
- (243) Bridel, J.-S.; Azais, T.; Morcrette, M.; Tarascon, J.-M.; Larcher, D. Key parameters governing the reversibility of Si/carbon/CMC electrodes for Li-ion batteries. *Chem. Mater.* **2010**, *22* (3), 1229–1241.

- (244) Ryou, M. H.; Kim, J.; Lee, I.; Kim, S.; Jeong, Y. K.; Hong, S.; Ryu, J. H.; Kim, T. S.; Park, J. K.; Lee, H. Mussel-inspired adhesive binders for high-performance silicon nanoparticle anodes in lithium-ion batteries. *Adv. Mater.* **2013**, *25* (11), 1571–1576.
- (245) Kwon, T. w.; Jeong, Y. K.; Lee, I.; Kim, T. S.; Choi, J. W.; Coskun, A. Systematic Molecular-Level Design of Binders Incorporating Meldrum's Acid for Silicon Anodes in Lithium Rechargeable Batteries. *Adv. Mater.* **2014**, *26* (47), 7979–7985.
- (246) Lee, H.; Scherer, N. F.; Messersmith, P. B. Single-molecule mechanics of mussel adhesion. *Proc. Natl. Acad. Sci. U. S. A.* **2006**, *103* (35), 12999–13003.
- (247) Wilker, J. J. Positive charges and underwater adhesion. *Science* **2015**, *349* (6248), 582–583.
- (248) Lee, H.; Dellatore, S. M.; Miller, W. M.; Messersmith, P. B. Mussel-inspired surface chemistry for multifunctional coatings. *Science* **2007**, *318* (5849), 426–430.
- (249) Wei, Q.; Zhang, F.; Li, J.; Li, B.; Zhao, C. Oxidant-induced dopamine polymerization for multifunctional coatings. *Polym. Chem.* **2010**, *1* (9), 1430–1433.
- (250) Zeng, H.; Hwang, D. S.; Israelachvili, J. N.; Waite, J. H. Strong reversible Fe³⁺-mediated bridging between dopa-containing protein films in water. *Proc. Natl. Acad. Sci. U. S. A.* **2010**, *107* (29), 12850–12853.
- (251) Lee, B. P.; Messersmith, P. B.; Israelachvili, J. N.; Waite, J. H. Mussel-inspired adhesives and coatings. *Annu. Rev. Mater. Res.* **2011**, *41*, 99–132.
- (252) Delparastan, P.; Malollari, K. G.; Lee, H.; Messersmith, P. B. Direct Evidence for the Polymeric Nature of Polydopamine. *Angew. Chem.* **2019**, *131* (4), 1089–1094.
- (253) Park, J.; Brust, T. F.; Lee, H. J.; Lee, S. C.; Watts, V. J.; Yeo, Y. Polydopamine-based simple and versatile surface modification of polymeric nano drug carriers. *ACS Nano* **2014**, *8* (4), 3347–3356.
- (254) Sun, G.; Zu, F.; Koch, N.; Rappich, J.; Hinrichs, K. In Situ Infrared Spectroscopic Monitoring and Characterization of the Growth of Polydopamine (PDA) Films. *Phys. Status Solidi B* **2019**, *256* (2), 1800308.
- (255) Zhang, C.; Gong, L.; Xiang, L.; Du, Y.; Hu, W.; Zeng, H.; Xu, Z.-K. Deposition and Adhesion of Polydopamine on the Surfaces of Varying Wettability. *ACS Appl. Mater. Interfaces* **2017**, *9* (36), 30943–30950.
- (256) Zhang, J.; Zhang, L.; Cui, X.; Gong, L.; Xiang, L.; Shi, C.; Hu, W.; Zeng, H. Scalable polyzwitterion–polydopamine coating for regenerable oil/water separation and underwater self-cleaning of stubborn heavy oil fouling without pre-hydration. *Chem. Commun.* **2018**, *54* (70), 9734–9737.
- (257) Han, L.; Gong, L.; Chen, J.; Zhang, J.; Xiang, L.; Zhang, L.; Wang, Q.; Yan, B.; Zeng, H. Universal Mussel-Inspired Ultrastable Surface-Anchoring Strategy via Adaptive Synergy of Catechol and Cations. *ACS Appl. Mater. Interfaces* **2018**, *10* (2), 2166–2173.

Surface Interactions between Water-in-Oil Emulsions with Asphaltenes and Electroless Nickel–Phosphorus Coating

Lu Gong, Ling Zhang, Li Xiang, Jiawen Zhang, Vahidoddin Fattahpour, Mahdi Mamoudi, Morteza Roostaei, Brent Fermaniuk, Jing-Li Luo, and Hongbo Zeng*



Cite This: *Langmuir* 2020, 36, 897–905



Read Online

ACCESS |



Metrics & More

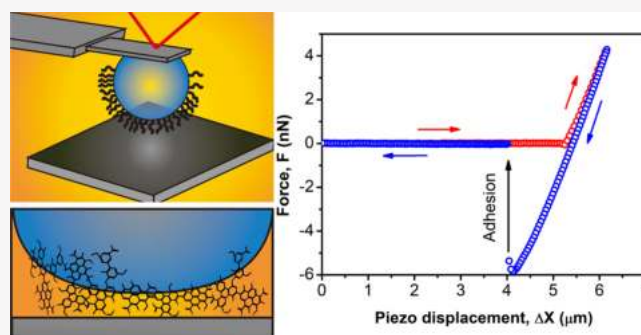


Article Recommendations



Supporting Information

ABSTRACT: Surface interactions between emulsion drops and substrate surfaces play an important role in many phenomena in industrial processes, such as fouling issues in oil production. Investigating the interaction forces between the water-in-oil emulsion drops with interfacially adsorbed asphaltenes and various substrates is of fundamental and practical importance in understanding the fouling mechanisms and developing efficient antifouling strategies. In this work, the surface interactions between water drops with asphaltenes and Fe substrates with or without an electroless nickel–phosphorus (EN) coating in organic media have been directly quantified using the atomic force microscope drop probe technique. The effects of asphaltene concentration, organic solvent type, aging time, contact time, and loading force were investigated. The results demonstrated that the adhesion between water drops and the substrates was enhanced with higher asphaltene concentration, better organic solvent to asphaltenes, longer aging time, longer contact time, and stronger loading force, which was due to the growing amount and conformational change of asphaltenes adsorbed at the water/oil interface. Meanwhile, the adhesion between the water drop and the EN substrate was much weaker than that with the Fe substrate. The bulk fouling tests also showed that EN coating had a very good antifouling performance, which was in consistency with the force measurement results. Our work sheds light on the fundamental understanding of emulsion-related fouling mechanisms in the oil industry and provides useful information for developing new coatings with antifouling performances.



INTRODUCTION

Surface interactions between emulsion drops and substrate surfaces are involved in many processes and issues in various industries, such as water or oil drop collection in chemical engineering and fouling problems in oil and gas industries. The interactions between water-in-oil emulsion drops and a substrate surface would induce the drop attachment on the substrate and potentially cause fouling problems during oil production.^{1–6} The crude oil components (e.g., bitumen or asphaltenes), mineral particles (e.g., silica and clay), and corrosive products (e.g., iron oxide) have been found to be the main compositions in the foulants.^{7–11} The undesired deposition of these foulants on the facility surfaces can further lead to the plugging and breaking-down issues in oil transportation, storage, and refinery processes,^{7,12–16} which will eventually result in damages of pipelines, malfunction of production facilities, reduction of the efficiency in oil production, and thereby, increase the oil production cost.^{10,17} Thus, it is critical and urgent to find a solution to mitigate or even solve the fouling problems.

In the past decades, much attention has been focused on the investigation of surface fouling mechanisms along oil

production. It is commonly believed that the interface-active asphaltenes, as the heaviest component in crude oil, have played an important role in the initiation and growing processes of fouling.^{18–22} Asphaltenes are defined as a solubility class, which is soluble in aromatic solvents (e.g., toluene) and insoluble in alkane solvents (e.g., heptane).^{19,23,24} Hence, toluene is commonly regarded as a good solvent for asphaltenes, and heptane is treated as a poor solvent. In the Yen–Mullins model, a typical asphaltene molecule consists of a polyaromatic core with peripheral alkyl chains and functional polar groups containing nitrogen, oxygen, and sulfur atoms.^{25,26} The strong intra- and inter-molecular interactions between the aromatic rings, alkyl chains, and functional groups, including π – π stacking, van der Waals (vdW), acid–base, and hydrogen bond interactions, could induce the instinctive aggregation behavior of asphaltenes.^{24,27–29} Therefore, it is

Received: November 9, 2019

Revised: December 23, 2019

Published: January 13, 2020



ACS Publications

© 2020 American Chemical Society

897

<https://dx.doi.org/10.1021/acs.langmuir.9b03498>
Langmuir 2020, 36, 897–905

generally inaccurate to use one specific molecular structure to describe asphaltenes and analyze their physical and/or chemical properties. Instead, the bulk properties of asphaltene solution, such as solubility and distribution of asphaltene aggregation sizes, are usually used.¹⁹ Experiments have been designed and conducted to study the adsorption behaviors of asphaltenes onto various surfaces, including both solid surfaces (e.g., silica, steel, and gold) and water/oil interfaces (e.g., water/toluene interface).^{30–35} It was found that the asphaltenes could irreversibly adsorb to the water/oil interface and form a protective layer to enhance the stability of the emulsion drops.^{29,36–39} Meanwhile, the strong intermolecular interactions between asphaltenes could induce the agglomeration and flocculation of the water–oil emulsion systems,^{40–43} which would form a complex mixture and finally lead to fouling problems. So far, the fouling mechanisms of water-in-oil emulsions with interfacially adsorbed asphaltenes on iron-based surfaces, as one of the most commonly used materials for pipelines and reactors in chemical engineering and oil industries, have not been thoroughly studied.

Electroless nickel–phosphorus (EN) coating has been used to protect the facility surfaces (e.g., iron surfaces) from abrasion in different industries because of its excellent properties of uniform hardness and great resistance to corrosion^{44–46} since the rediscovery of this coating technique by Brenner and Riddell in 1946.⁴⁷ Meanwhile, numerous studies have been conducted in order to improve the anticorrosion and antiabrasion performances of the EN coating.^{48–52} However, limited studies are available on the fouling phenomena of water-in-oil emulsions with asphaltenes on EN coating as well as the interaction mechanisms involved.

Over the past few years, the surface interactions between deformable bubbles or drops and various substrate surfaces in aqueous solutions or organic media have been quantitatively measured using the bubble/drop probe atomic force microscopy (AFM) technique.^{18,40,53–56} The obtained results described the surface deformation of the bubbles or drops, deciphered the drop attachment process on hydrophilic or hydrophobic substrates, and revealed the stability mechanisms of emulsion drops and the contributions of various interactions (e.g., vdW, electric double layer, and hydrophobic and steric interactions). It has been demonstrated that the asphaltenes at the water/oil interface could induce strong steric repulsion between water drops during surface approaching and interfacial adhesion during their separation, which is responsible for the stability and flocculation behavior of water-in-oil emulsions.¹⁸ It is expected that the interactions between asphaltenes at the water/oil interface and substrate surface could affect the stability and attachment behavior of water-in-oil emulsions on the substrates. To the best of our knowledge, the direct quantification of interaction forces between water-in-oil emulsion drops with asphaltenes and substrate surfaces has not been reported.

In this work, the surface interactions between water drops with interfacially adsorbed asphaltenes and Fe substrate with or without EN coating were directly measured in organic media (i.e., toluene, heptols, and heptane) using the drop probe AFM technique. The effects of asphaltene concentration, solvent type, aging time, contact time, and loading force were investigated. Bulk fouling tests of Fe and EN substrates in water-in-oil emulsions stabilized with asphaltenes were also conducted to evaluate their fouling and antifouling performances. Our work quantifies the interaction forces between

water-in-oil emulsion drops with interfacial asphaltenes and selected substrates (i.e., Fe and EN substrates) in organic media, which helps to elucidate the fundamental mechanisms in the fouling phenomena and facilitate the development of efficient antifouling strategies in related industrial applications.

MATERIALS AND EXPERIMENTAL METHODS

Materials. Asphaltenes were extracted from Athabasca bitumen by following the procedure reported elsewhere.⁵⁷ Asphaltene stock solution (10 000 mg/L) was prepared by dissolving asphaltenes in pure toluene (HPLC, Fisher Scientific, Canada) and sonicated for 30 min to ensure complete dissolution. Prior to the experiments, asphaltene solutions with different concentrations were prepared by diluting the stock solution with pure toluene and sonicated for 15 min. Milli-Q water with a resistivity of 18.2 M Ω ·cm (Barnstead Smart2Pure, Thermo Scientific, Canada) was used throughout the experiment. To explore the effect of organic solvent to asphaltene stability and solubility, the heptols prepared by mixing toluene and heptane (HPLC grade, Fisher Scientific, Canada) with desired volume ratios have been used as the organic media in the following experiments. Octadecyltrichlorosilane (OTS) was purchased from Sigma-Aldrich and used as received.

Preparation of Fe and EN Coating Substrates. The Fe substrate was prepared by depositing a layer of iron with the thickness of 90 nm on a pretreated silica wafer using the electron beam evaporation technique, which has been reported previously.⁵⁸ A layer of chromium with the thickness of 10 nm was deposited between iron and silica to enhance the adhesion and stability, as shown in Figure 1A. The EN-coated substrate was prepared on an Fe substrate using

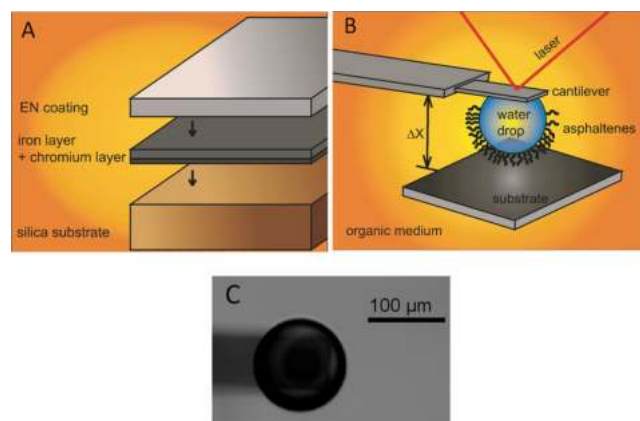


Figure 1. (A) Preparation of Fe and EN substrates. (B) Schematic of drop probe AFM technique. The ΔX shows the piezo displacement. (C) Microscopic image showing a water drop anchored on the tipless AFM cantilever in toluene for the force measurements.

the electroless bathing method as reported previously.^{52,59} The electroless bath solution was prepared following the compositions shown in Table 1 and the pH of the solution was adjusted to around 8.5. Then, the solution was heated to 85 °C with the agitation of 250 rpm. The EN coating process started when the cleaned Fe substrate was immersed in the prepared bath solution. After 30 min, the prepared substrate was washed with deionized (DI) water and ethanol and dried using pure nitrogen. The successful deposition of EN coating on the Fe substrate was confirmed using the AFM surface image, scanning electron microscopy (SEM), and energy dispersive X-ray spectroscopy (EDS).

AFM Force Measurements. The surface interaction between a water drop with asphaltenes adsorbed at the water/oil interface and Fe or EN substrate in various organic media were quantitatively measured to investigate the fouling and antifouling mechanisms using the drop probe AFM technique based on a MFP-3D-Bio AFM system

Table 1. The Compositions of the Bath Solution for EN Coating

composition	$\text{NiSO}_4 \cdot 6\text{H}_2\text{O}$	$\text{NaH}_2\text{PO}_4 \cdot \text{H}_2\text{O}$	NH_4Cl	CH_3COONa	citric acid
concentration	25 g/L	16 g/L	40 g/L	10 g/L	15 g/L

(Asylum Research, Santa Barbara, CA). The detailed experimental procedure was reported in previous studies.^{18,40,60}

For each force measurement, the AFM fluid cell was first filled with asphaltene solution, and water drops were generated in the cell using a custom-made ultrasharp glass pipette. These water drops spontaneously settled down to the glass substrate of the fluid cell because of the relatively higher density of the water. The glass substrate was slightly hydrophobized in 5 mM OTS solution to obtain a water contact angle (WCA) of $\sim 90^\circ$ prior to the experiments, which facilitates the immobilization of the water drops on the glass substrate as well as the pick-up of water drops later. The water drops were aged in the asphaltenes solution for 5 min unless specified elsewhere. Afterward, the asphaltenes solution was replaced by a large amount of organic solvent (e.g., toluene, heptane, or heptol in this work) several times to wash off all free asphaltenes in the surrounding solution and the pure solvent was used for force measurement. Thus, only the asphaltenes adsorbed at the water/oil interface were left and contributed to the measured interfacial interactions. A custom-made rectangular tipless silicon AFM cantilever ($400 \times 70 \times 2 \mu\text{m}$) was used to pick up a water drop with asphaltenes in the pure solvent to create the water drop probe, as shown in Figure 1C. Then, this drop probe was moved and placed above the Fe or EN substrate for the force measurements. A schematic illustration of the experimental setup is shown in Figure 1B. During the force measurement, the water drop anchored cantilever was driven by a piezo actuator to approach the substrate at a velocity of $1 \mu\text{m/s}$ till a certain maximum loading force was obtained. This loading force was kept at 4 nN unless specified elsewhere. Then, this probe was driven to retract. The spring constant of the AFM cantilever was calibrated using the thermal tune method in the solvent before picking up the water drop, and an optical laser beam system was used to monitor the deflection of the cantilever. Thus, the force was determined through the Hooke's law. For each experimental condition, at least 10 force measurements were conducted at different positions of each independently prepared substrate. To investigate the effect of contact time, the water drop probe was kept in contact with the substrate for a certain time after the maximum loading force of 4 nN was reached. The force profiles with respect to the piezo displacement, ΔX were obtained from the AFM software. The adhesion force data was collected and normalized by the radius of the water drop. In this work, the adhesion between the water drops with interfacial asphaltenes and Fe or EN substrate describes the difficulty for water drops and asphaltenes to be removed from the substrate surface. When the adhesion is strong, the removal process is difficult, which indicates the fouling phenomena. When the adhesion is weak, the removal process will be easy, which suggests the antifouling property. Thus, the antifouling property can be evaluated via the measured adhesion.

Bulk Fouling Tests. The experimental setup for bulk fouling tests is shown in Figure 2. The emulsion solution was prepared by mixing

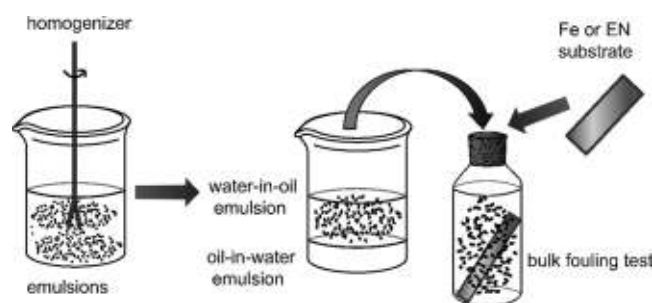


Figure 2. Schematic of bulk fouling tests for Fe and EN substrates in water-in-oil emulsions with asphaltenes.

100 mg/L asphaltene/toluene solution and DI water with the volume fraction of 7:3 using a homogenizer. The as-prepared emulsion was settled for 1 h. After the settlement, two phases were observed and the water-in-oil emulsion on the upper phase was transferred to 20 mL vials. Then, Fe and EN substrates were separately placed in the emulsions for 24 h at room temperature. The Fe and EN substrates after the bulk fouling tests were cleaned using DI water and ethanol, dried with pure nitrogen, and characterized with optical microscope, AFM surface imaging, and SEM-EDS characterization.

RESULTS AND DISCUSSION

Characterization of Fe and EN Substrates. The AFM topographic images of the silica substrate, Fe substrate, and EN substrate are shown in the Supporting Information in Figure S1A–C, respectively, which exhibit that the silica surface is featureless and flat, whereas both Fe and EN substrates are much rougher with aggregate particles. The root-mean-square (rms) roughness for the silica surface, Fe substrate, and EN substrate were 0.45, 1.33, and 4.22 nm, respectively. Moreover, Figure S1D–G shows the SEM images and EDS element mapping results, demonstrating the presence of iron element on the Fe substrate and nickel and phosphorus elements on the EN substrate. These results prove the successful deposition of EN coating on Fe substrate. The thickness of the EN coating was measured to be about $1.6 \mu\text{m}$ from the SEM image from the cross-section view (in Figure S1H).⁶¹ As shown in Figure 3, the oil (i.e., toluene) contact angles (OCAs) in DI water for

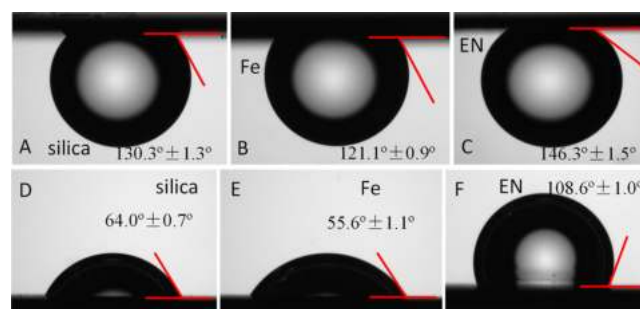


Figure 3. OCAs in water for (A) silica substrate, (B) Fe substrate, and (C) EN substrate. WCAs in oil for (D) silica substrate, (E) Fe substrate, and (F) EN substrate.

silica, Fe, and EN substrates were measured to be $130.3^\circ \pm 1.3^\circ$, $121.1^\circ \pm 0.9^\circ$, and $146.3^\circ \pm 1.5^\circ$, respectively. The WCAs in oil (i.e., toluene) for silica, Fe, and EN substrates were also measured to be $64.0^\circ \pm 0.7^\circ$, $55.6^\circ \pm 1.1^\circ$, and $108.6^\circ \pm 1.0^\circ$, respectively. The OCA and WCA for the EN substrate are bigger than those for the Fe substrate, which suggests the possible antifouling property of the EN coating.

Effect of Asphaltene Concentrations. Figure 4 shows the measured force profiles between the water drops and Fe substrate in pure toluene, after the water drops were aged in asphaltene solutions with different concentrations for 5 min. It should be noted that the piezo displacement, ΔX here, is the relative movement of the AFM cantilever, not the true surface separation between the water drop and the Fe substrate.

Figure 4A shows the measured interaction between a water drop without asphaltenes and the Fe substrate in pure toluene.

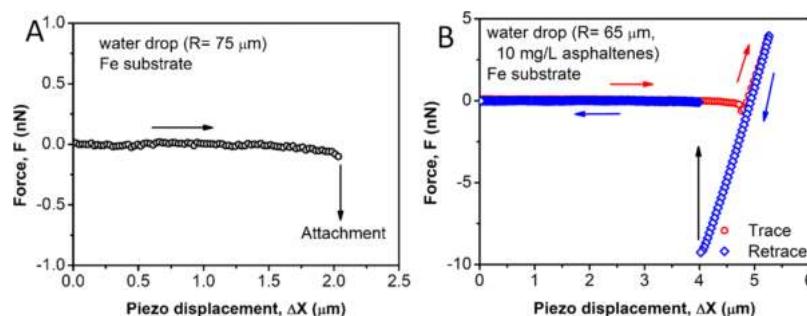


Figure 4. Measured force profiles between a water drop and Fe substrate in toluene after aging in (A) 0 and (B) 10 mg/L asphaltene solutions for 5 min. The open dots are experimental data. The arrows show the movements of water drops.

The obtained force curve was attractive as the water drop approached the substrate. When the water drop moved closer to the substrate, this attractive force became stronger till a sudden “jump-in” behavior was observed, indicating that the water drop jumped into contact with the Fe substrate. From the optical microscope, it was directly observed that the water drop detached from the AFM cantilever and attached onto the Fe substrate. This behavior was attributed to the strong vdW attraction between the water drop and Fe substrate in toluene.^{61,62}

Figures 4B and S2 show the measured force results between water drops and the Fe substrate in toluene after the water drops were aged in asphaltene solutions with different concentrations of 10, 20, 50, 100, 200, and 500 mg/L. For all cases, attraction was detected during approaching of water drop to the Fe substrate and water drop jumped into contact with the Fe substrate because of the vdW attraction, but no drop detachment from the cantilever was observed. Meanwhile, strong adhesion was measured when the water drop was retracted. A previous work showed that asphaltenes could irreversibly adsorb at a water/oil interface and form a protective layer to enhance the stability of water drops in an organic medium.^{38,63} The measured adhesion was due to the attractive interactions between the interfacially adsorbed asphaltenes and iron surface, which was in consistence with the reported results that asphaltenes could interact with various metal surfaces, such as gold and stainless steel, via hydrogen bonding, vdW force, coordinate interaction, and so on.^{64–66}

Comparing the adhesion measured at different asphaltene concentrations, it could be noted that with increasing the asphaltene concentration, the adhesion between the water drop and Fe substrate became stronger. However, the measured adhesion was almost the same at the asphaltene concentrations of 200 and 500 mg/L. The adhesion change should be caused by the different amount of asphaltenes adsorbed at the water/toluene interface. At relatively lower asphaltene concentration (<200 mg/L), increasing asphaltene concentration in the solution induced more asphaltenes adsorbed at the water/toluene interface. The increased amount of asphaltenes at the interface created more active sites to interact with the opposing Fe surface during force measurements, resulting in stronger adhesion. However, as the asphaltene concentration kept increasing (>200 mg/L), the water/toluene interface could be fully covered by asphaltenes during the aging time, forming a protective layer. Thus, active sites on the interfacial asphaltene layer did not obviously increase with further increasing the asphaltene concentration, so the adhesion showed relatively weak dependence on the concentration (>200 mg/L).

Figure S3 shows the measured force profiles between the water drops and EN substrate in toluene after being aged in asphaltene solutions with different concentrations. Figure S3A shows that the interaction force between pure water drop and the EN substrate had no obvious change when the water drop approached the substrate in toluene, till a sudden “jump-in” behavior was also observed, indicating the contact of water drop and EN substrate. From the optical microscope, the detachment of the water drop from the AFM cantilever and the following attachment on the EN substrate were also directly observed, which was similar with the force measurement between pure water drop and Fe substrate in Figure 4A. This behavior could also be contributed by the vdW attraction between the water drop and EN substrate in toluene. However, the force profile for the EN substrate did not show obvious attraction before the “jump-in” behavior occurred, suggesting that the vdW attraction between the water drop and EN substrate was relatively weaker than that between the water drop and Fe substrate.

Figure S3B–G shows the measured force profiles between the water drops with asphaltenes and the EN substrate in toluene after aging in asphaltene solutions at concentrations of 10, 20, 50, 100, 200, and 500 mg/L, respectively. For all curves, attractive interaction force during approach was observed. The tendency that the adhesion measured during retraction increased along with the increasing asphaltene concentration was also noticed. Similarly, the adhesion did not change significantly when the concentration was greater than 200 mg/L. The adhesion between the water drops with asphaltenes and Fe or EN substrates are compared as shown in Figure 5. It is obvious that the normalized adhesion between the water drop and EN substrate was much weaker than that with the Fe

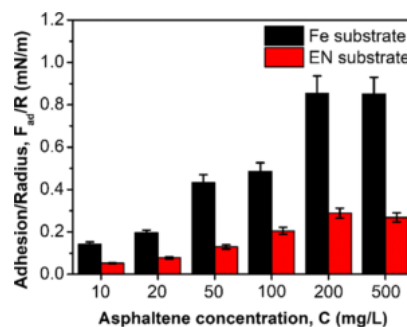


Figure 5. Normalized adhesion of a water drop on Fe substrate and EN-coated substrate in toluene after aging in asphaltene solutions with different concentrations.

surface, suggesting that asphaltenes on the EN substrate could be more easily removed than those on the Fe surface. It is noted that the EN substrate has a higher surface roughness (rms roughness 4.22 nm) than the Fe substrate (rms roughness 1.33 nm). In reported literature, the increased surface roughness could enhance the adhesion between two rough-soft surfaces because of the large contact area, which thus led to the aggravated fouling phenomena.^{67–70} However, despite the relatively higher surface roughness of EN substrates, weaker adhesion has been measured between the water drops with interfacial asphaltenes and the EN substrate than that with the Fe substrate, which further suggests better antifouling property of the EN coating.

Effect of Solvent Type. The interactions between the water drop with asphaltenes and the Fe or EN substrate were also investigated in heptols (i.e., mixtures of toluene and heptane) and heptane. Here, heptols with different volume fractions of toluene, that is, 75, 50, and 25% (denoted as 75% heptol, 50% heptol, and 25% heptol) were used. In the experiments, after aging in the 100 mg/L asphaltene-in-toluene solution for 5 min, a large amount of heptol or heptane was used to replace the asphaltene-in-toluene solution and wash off the free asphaltenes before the Fe or EN substrate was placed in the organic solvent. Because of the irreversible adsorption of asphaltenes,^{36,38,71} it was expected that the amount of asphaltenes at the water/oil interface for each water drop was almost the same, and the influences of asphaltenes dissolved in the solution or adsorbed on the substrate surface during the force measurements could be negligible.

Figure S4 shows the force results between the water drops with asphaltenes and Fe substrate in heptols (with toluene volume fraction of 75, 50, and 25%) and heptane. Similar to the force curve in pure toluene (Figure S2C), attraction was observed during approach and strong adhesion was measured during retraction. It was evident that the adhesion was weakened by decreasing the volume fraction of toluene in heptol. As heptane is a poor solvent to asphaltenes,^{36,67,68,70–73} the addition of heptane could enhance the solvophobic interaction and induce the strong aggregation between asphaltene molecules at the interface. The self-association of the active functional groups of aggregated asphaltenes could lead to less molecular mobility and lower amount of exposed active functional groups for surface adhesion. Therefore, the adhesion between the water drop with interfacial asphaltenes and substrate became weakened. In pure heptane (Figure S4D), the measured interaction force between the water drop and Fe substrate was attractive and growing stronger while approaching. Finally, the “jump-in” behavior was observed, suggesting the contact of water drop on the Fe substrate. This distinctive “jump-in” behavior could be possibly due to the significantly enhanced aggregation of asphaltenes and their reduced molecular mobility in pure heptane than in heptols, which led to disruption of the protective asphaltene layer at the oil/water interface.⁷⁴

Figure S5 shows the measured force curves between the water drops with asphaltenes and EN substrate in heptols (with toluene volume fraction of 75, 50, and 25%) and heptane. Similar force results with Fe substrates in Figure S4 were observed. In heptols, the measured adhesion also became weakened with the decreasing volume fraction of toluene, which was due to the molecular mobility of interfacial asphaltenes and their exposed active functional groups. In pure heptane, the “jump-in” behavior was also observed. The

normalized adhesion between the water drop and Fe or EN substrate is summarized in Figure 6. It was noticed that the

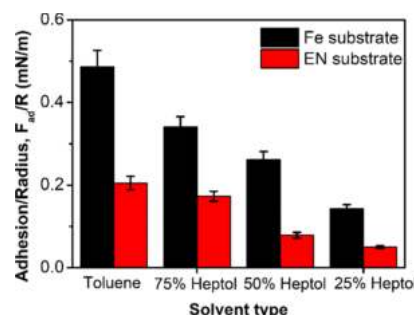


Figure 6. Normalized adhesion of a water drop on Fe substrate and EN-coated substrate in toluene and heptol.

adhesion between the water drop with interfacial asphaltenes and EN substrate was weaker than that for the Fe substrate, suggesting that the asphaltenes on the EN substrate could be more easily removed than those on the Fe substrate in different organic solvents.

Effect of Aging Time. The effect of aging time was also investigated here. Before force measurements, water drops were aged in 100 mg/L asphaltene solution for 1, 2, 5, 10, 20, and 30 min, respectively, and 50% heptol was used to replace the solution. The obtained force profiles are shown in Figure S6. All measured force profiles exhibited adhesion during retraction, which was normalized and is summarized in Figure 7A.

It was noticed that longer aging time resulted in stronger adhesion between the water drop with interfacial asphaltenes and the Fe or EN substrate, which was caused by more asphaltenes adsorbed at the water/oil interface during aging time. However, the adhesion did not obviously change when the aging time was longer than 20 min for both Fe and EN substrates, which could be the consequence of the saturated adsorption of asphaltenes at the water/oil interface. To demonstrate this statement, the adsorption behavior of asphaltenes (100 mg/L) at water/50% heptol interface was investigated by measuring the dynamic interfacial tension using the pendant drop shape method, and the result is shown in Figure 7B.⁷⁵ The obtained result showed that the interfacial tension of the water/50% heptol interface decreased sharply within 15 min, indicating the rapid adsorption of asphaltenes at the interface. Then, the decrease of the interfacial tension gradually slows down at 18–22 min, suggesting the lowered adsorption rate due to the limited interfacial area and steric hindrance of adsorbed asphaltenes.⁷⁵ After ~22 min, the interfacial tension reached a plateau, suggesting the saturated adsorption of asphaltenes at the water/50% heptol interface. Furthermore, Figure 7A also shows that the adhesion between water drops with interfacial asphaltenes and the EN substrate is much weaker than that for the Fe substrate.

Effect of Contact Time. The contact time effect was investigated by measuring the force profiles between water drops with interfacial asphaltenes and the Fe or EN substrate in 50% heptol, after aging in 100 mg/L asphaltenes solution for 5 min. The water drop probe was driven to approach the substrate till the maximum loading force of 4 nN was reached. Then, this cantilever was held for the contact time of 1, 2, 5, and 10 s, respectively, followed by retraction from the substrate. The obtained force profiles are shown in Figure

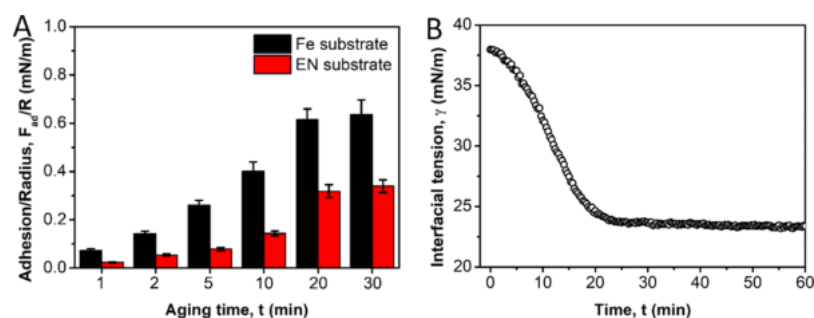


Figure 7. (A) Normalized adhesion of a water drop on Fe and EN substrate in 50% heptol after being aged in 100 mg/L asphaltene solution for 1, 2, 5, 10, 20, and 30 min, respectively. (B) Measured dynamic interfacial tension curve of water and 50% heptol with 100 mg/L asphaltene dissolved.

S7. The normalized adhesion for both the Fe substrate and EN-coated substrate is shown in Figure 8A. Obviously, much

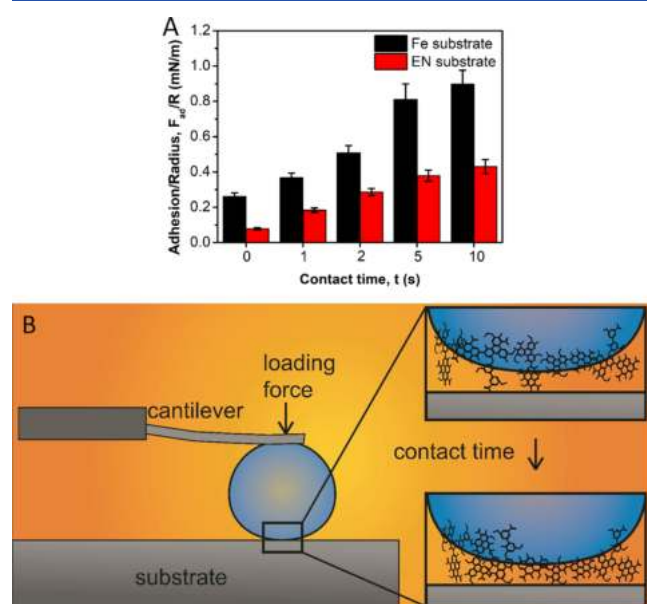


Figure 8. (A) Normalized adhesion between a water drop and Fe or EN substrate in 50% heptol after aging in 100 mg/L asphaltene solutions for 5 min with the contact time of 0, 1, 2, 5, and 10 s, respectively. (B) Schematic of conformational change of confined asphaltenes during contact with the substrate.

weaker adhesion between the water drop and EN substrate in the presence of interfacial asphaltene was detected than that for the Fe substrate under varying contact time. The results also showed that the adhesion was strengthened with longer contact time, which was most likely due to the conformational changes of confined asphaltene thus leading to stronger adhesion with the substrate, as illustrated in Figure 8B.

Effect of Loading Force. The effect of the loading force was investigated between the water drop and Fe or EN substrate in 50% heptol after aging in 100 mg/L asphaltene solutions for 5 min with the loading force of 1, 2, 4, 10, 20, and 40 nN, respectively. The measured force profiles are shown in Figure S8. Figure 9 shows the normalized adhesion between water drops and the Fe or EN substrate, which becomes stronger as the loading force increases. The strengthened adhesion is due to the enlarged contact area under the higher loading force, which facilitates stronger interactions between more confined asphaltene and substrates. Figure 9 also

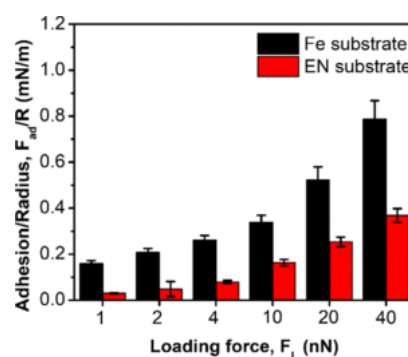


Figure 9. Normalized adhesion between the water drop and Fe or EN substrate in 50% heptol after aging in 100 mg/L asphaltene solutions for 5 min under the loading force of 1, 2, 4, 10, 20, and 40 nN, respectively.

demonstrates that the EN coating showed weaker adhesion with the water drop in the presence of asphaltene than the Fe substrate under different loading conditions.

Bulk Fouling Tests. To further evaluate the antifouling performances, the bulk fouling tests were conducted with both Fe and EN substrates. The obtained results are shown in Figure 10.

Figure 10A shows the optical images of Fe and EN substrates before and after the bulk fouling tests. Before bulk fouling tests, both Fe and EN substrates were flat and clean. After bulk fouling tests, obvious aggregates were found on the Fe substrate, indicating that Fe substrate could be easily fouled in the water-in-oil emulsion with asphaltene. However, the EN substrate remained relatively clean with only some grey remnants on the surface. The AFM surface images in Figure 10B,C further show that there are a large number of aggregates deposited on the Fe substrate, suggesting the severe fouling phenomenon in the emulsions; whereas the EN substrate showed much less deposits. The rms roughness of the Fe and EN substrates after bulk fouling tests was found to increase to 23.7 and 6.4 nm, respectively. Furthermore, the SEM-EDS characterizations have been conducted and the obtained results show that much higher weight percentage of carbon element on the Fe substrate has been detected than that on the EN substrate (as shown in Figure S9). The above bulk fouling tests demonstrate that the EN coating exhibits good antifouling performance in water-in-oil emulsions, agreeing well with the adhesion results from the force measurements.

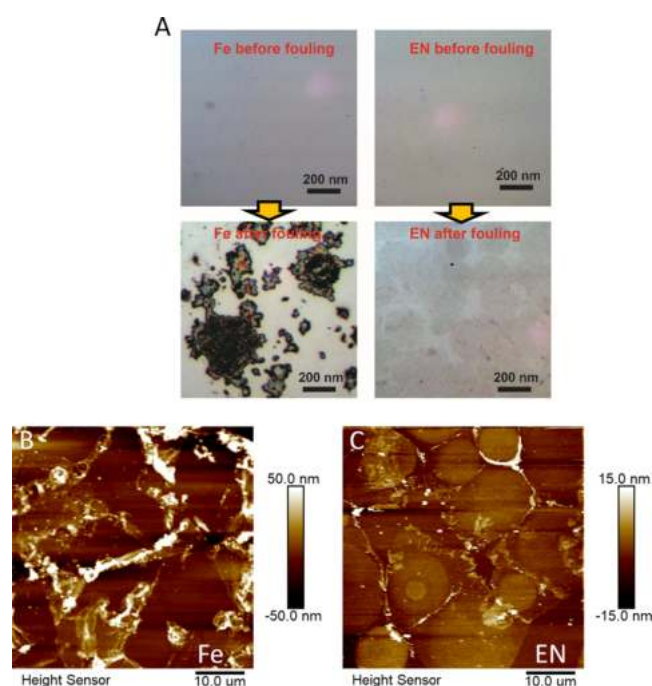


Figure 10. (A) Optical images of Fe and EN substrates before and after bulk fouling tests. AFM surface image of Fe (B) and EN (C) substrate after bulk fouling tests.

CONCLUSIONS

In this work, the drop probe AFM technique was used to directly measure the surface interaction forces between water drops with asphaltenes adsorbed at the water/oil interface and Fe or EN substrate in organic media. The effects of asphaltene concentration, solvent type, aging time, contact time, and loading force were investigated. For bare water drops, the force results revealed that the drops could easily jump into contact with the Fe or EN substrate while approaching in oil media because of the strong vdW attraction. For water drops in the presence of asphaltenes, the asphaltenes could form a protective layer at the water/oil interface. The functional groups of the interfacial asphaltenes could interact with the substrate, contributing to the measured adhesion during retraction. It was also noted that the higher asphaltene concentration and longer aging time during the aging process could result in more asphaltenes adsorbed at the water/oil interface, which then lead to stronger adhesion between the water drop and the substrate. The addition of a poor solvent (i.e., heptane) in the organic medium could cause strong aggregation of asphaltenes, thus lowering the molecular mobility of interfacial asphaltenes and preventing the interactions between the functional groups of asphaltenes and the substrate. Consequently, the weaker adhesion was measured. In pure heptane, the aggregation of interfacial asphaltenes was so strong that the protective layer of interfacial asphaltenes would be disturbed and direct water–substrate contact could occur. Hence, “jump-in” behavior of the water drop on the substrate was observed. The longer contact time during the force measurements could allow interfacial asphaltenes to change their conformation and have stronger interaction with the substrate. The stronger loading force could enlarge the contact area of the water drop on the substrate and include more interfacial asphaltenes within the contact area, which thereby strengthened the adhesion between the water

drop and substrate. Meanwhile, much weaker adhesion was measured between the water drop with interfacial asphaltenes and the EN substrate than that for the Fe substrate, suggesting that asphaltenes on the EN substrate could be more easily removed than those on the Fe substrate. Furthermore, the bulk fouling tests in water-in-oil emulsions also demonstrated that more significant fouling phenomenon was detected on the Fe substrate than that on the EN substrate, which agreed well with the force measurement results. This work improves the fundamental understanding of the surface interactions between water-in-oil emulsions with asphaltenes and iron substrate or EN coating, demonstrates the antifouling properties of the EN coating, and provides useful information on the intermolecular and surface interactions contributing to the fouling phenomena in oil production. Such information helps the design and selection of coating materials and facilitates the development of new efficient coatings with antifouling performances in related industrial applications.

ASSOCIATED CONTENT

Supporting Information

The Supporting Information is available free of charge at <https://pubs.acs.org/doi/10.1021/acs.langmuir.9b03498>.

AFM images, SEM images, and EDS element mapping images of Fe and EN substrate; measured force profiles between a water drop and Fe or EN substrate in toluene after aging in 20, 50, 100, 200, and 500 mg/L asphaltene solutions for 5 min; measured force profiles between a water drop and Fe or EN substrate in 75% heptol, 50% heptol, 25% heptol, and heptane after aging in 100 mg/L asphaltene solutions for 5 min; measured force profiles of a water drop with Fe substrate and EN-coated substrate in 50% heptol after aging in 100 mg/L asphaltenes solutions for 1, 2, 5, 10, 20 and 30 min; measured force profiles of a water drop with Fe substrate and EN-coated substrate in 50% heptol after aging in 100 mg/L asphaltenes solutions for 5 min with the contact time of 0, 1, 2, 5, and 10 s; and measured force profiles of a water drop with Fe substrate and EN-coated substrate in 50% heptol after aging in 100 mg/L asphaltenes solutions for 5 min with the loading force of 1, 2, 4, 10, 20, and 40 nN (PDF)

AUTHOR INFORMATION

Corresponding Author

Hongbo Zeng – Department of Chemical and Materials Engineering, University of Alberta, Edmonton T6G 1H9, Canada; orcid.org/0000-0002-1432-5979; Email: hongbo.zeng@ualberta.ca

Authors

Lu Gong – Department of Chemical and Materials Engineering, University of Alberta, Edmonton T6G 1H9, Canada

Ling Zhang – Department of Chemical and Materials Engineering, University of Alberta, Edmonton T6G 1H9, Canada

Li Xiang – Department of Chemical and Materials Engineering, University of Alberta, Edmonton T6G 1H9, Canada

Jiawen Zhang – Department of Chemical and Materials Engineering, University of Alberta, Edmonton T6G 1H9, Canada; orcid.org/0000-0003-3004-5536

Vahidoddin Fattahpour – RGL Reservoir Management Inc., Calgary T2P 2W1, Canada

Mahdi Mamoudi – RGL Reservoir Management Inc., Calgary T2P 2W1, Canada

Morteza Roostaei – RGL Reservoir Management Inc., Calgary T2P 2W1, Canada

Brent Fermaniuk – RGL Reservoir Management Inc., Calgary T2P 2W1, Canada

Jing-Li Luo – Department of Chemical and Materials Engineering, University of Alberta, Edmonton T6G 1H9, Canada; orcid.org/0000-0002-2465-7280

Complete contact information is available at:

<https://pubs.acs.org/10.1021/acs.langmuir.9b03498>

Author Contributions

The manuscript was written through contributions of all authors. All authors have given approval to the final version of the manuscript.

Notes

The authors declare no competing financial interest.

ACKNOWLEDGMENTS

The authors are grateful for the financial support from the Natural Sciences and Engineering Research Council of Canada (NSERC), RGL Reservoir Management Inc. (RGL), Canada Foundation for Innovation (CFI), and the Canada Research Chairs Program (H.Z.).

REFERENCES

- (1) Yang, F.; Tchoukov, P.; Dettman, H.; Teklebrhan, R. B.; Liu, L.; Dabros, T.; Czarnecki, J.; Masliyah, J.; Xu, Z. Asphaltene subfractions responsible for stabilizing water-in-crude oil emulsions. Part 2: Molecular representations and molecular dynamics simulations. *Energy Fuels* **2015**, *29*, 4783–4794.
- (2) Czarnecki, J.; Tchoukov, P.; Dabros, T.; Xu, Z. Role of asphaltenes in stabilisation of water in crude oil emulsions. *Can. J. Chem. Eng.* **2013**, *91*, 1365–1371.
- (3) Li, M.; Xu, M.; Ma, Y.; Wu, Z.; Christy, A. A. Interfacial film properties of asphaltenes and resins. *Fuel* **2002**, *81*, 1847–1853.
- (4) Long, Y.; Dabros, T.; Hamza, H. Stability and settling characteristics of solvent-diluted bitumen emulsions. *Fuel* **2002**, *81*, 1945–1952.
- (5) Lu, Q.; Huang, J.; Maan, O.; Liu, Y.; Zeng, H. Probing molecular interaction mechanisms of organic fouling on polyamide membrane using a surface forces apparatus: implication for wastewater treatment. *Sci. Total Environ.* **2018**, *622–623*, 644–654.
- (6) Xia, Y.; Adibnia, V.; Huang, R.; Murschel, F.; Faivre, J.; Xie, G.; Olszewski, M.; De Crescenzo, G.; Qi, W.; He, Z.; Su, R.; Matyjaszewski, K.; Banquy, X. Biomimetic Bottlebrush Polymer Coatings for Fabrication of Ultralow Fouling Surfaces. *Angew. Chem.* **2019**, *131*, 1322–1328.
- (7) Srinivasan, M.; Watkinson, A. P. Fouling of some Canadian crude oils. *Heat Transfer Eng.* **2005**, *26*, 7–14.
- (8) Collins, I. A new model for mineral scale adhesion. *International Symposium on Oilfield Scale*; Society of Petroleum Engineers, 2002.
- (9) Gentzis, T.; Parker, R. J.; McFarlane, R. A. Microscopy of fouling deposits in bitumen furnaces. *Fuel* **2000**, *79*, 1173–1184.
- (10) Bott, T. General fouling problems. *Fouling Science and Technology*; Springer, 1988; pp 3–14.
- (11) Kazi, S. N.; Duffy, G. G.; Chen, X. D. Mineral scale formation and mitigation on metals and a polymeric heat exchanger surface. *Appl. Therm. Eng.* **2010**, *30*, 2236–2242.
- (12) Leontaritis, K. Asphaltene deposition: A comprehensive description of problem manifestations and modeling approaches. *SPE Production Operations Symposium*; Society of Petroleum Engineers, 1989.
- (13) Wiehe, I. A.; Kennedy, R. J.; Dickkian, G. Fouling of nearly incompatible oils. *Energy Fuels* **2001**, *15*, 1057–1058.
- (14) Bennett, C. A.; Kistler, R. S.; Nangia, K.; Al-Ghawas, W.; Al-Hajji, N.; Al-Jemaz, A. Observation of an isokinetic temperature and compensation effect for high-temperature crude oil fouling. *Heat Transfer Eng.* **2009**, *30*, 794–804.
- (15) Hammami, A.; Ratulowski, J. Precipitation and deposition of asphaltenes in production systems: A flow assurance overview. *Asphaltenes, Heavy Oils, and Petroleomics*; Springer, 2007; pp 617–660.
- (16) Asomaning, S. Heat exchanger fouling by petroleum asphaltenes. Ph.D. Thesis, University of British Columbia, 1997.
- (17) Awad, M. M. Fouling of heat transfer surfaces. *Heat Transfer-Theoretical Analysis, Experimental Investigations and Industrial Systems*; InTech, 2011.
- (18) Shi, C.; Zhang, L.; Xie, L.; Lu, X.; Liu, Q.; He, J.; Mantilla, C. A.; Van den Berg, F. G. A.; Zeng, H. Surface interaction of water-in-oil emulsion droplets with interfacially active asphaltenes. *Langmuir* **2017**, *33*, 1265–1274.
- (19) Adams, J. J. Asphaltene adsorption, a literature review. *Energy Fuels* **2014**, *28*, 2831–2856.
- (20) Rana, M. S.; Sámano, V.; Ancheyta, J.; Diaz, J. A. I. A review of recent advances on process technologies for upgrading of heavy oils and residua. *Fuel* **2007**, *86*, 1216–1231.
- (21) Mendoza de la Cruz, J. L.; Argüelles-Vivas, F. J.; Matías-Pérez, V.; Durán-Valencia, C. d. I. A.; López-Ramírez, S. Asphaltene-induced precipitation and deposition during pressure depletion on a porous medium: an experimental investigation and modeling approach. *Energy Fuels* **2009**, *23*, 5611–5625.
- (22) Drummond, C.; Israelachvili, J. Fundamental studies of crude oil–surface water interactions and its relationship to reservoir wettability. *J. Pet. Sci. Eng.* **2004**, *45*, 61–81.
- (23) Natarajan, A.; Xie, J.; Wang, S.; Masliyah, J.; Zeng, H.; Xu, Z.; Xu, Z. Understanding molecular interactions of asphaltenes in organic solvents using a surface force apparatus. *J. Phys. Chem. C* **2011**, *115*, 16043–16051.
- (24) Shi, C.; Zhang, L.; Xie, L.; Lu, X.; Liu, Q.; He, J.; Mantilla, C. A.; Van den berg, F. G. A.; Zeng, H. Surface Interaction of Water-in-Oil Emulsion Droplets with Interfacially Active Asphaltenes. *Langmuir* **2017**, *33*, 1265–1274.
- (25) Mullins, O. C. The asphaltenes. *Annu. Rev. Anal. Chem.* **2011**, *4*, 393–418.
- (26) Mullins, O. C.; Sheu, E. Y. *Structures and Dynamics of Asphaltenes*; Springer Science & Business Media, 2013.
- (27) Gray, M. R.; Tykwinski, R. R.; Stryker, J. M.; Tan, X. Supramolecular assembly model for aggregation of petroleum asphaltenes. *Energy Fuels* **2011**, *25*, 3125–3134.
- (28) Langevin, D.; Argillier, J.-F. Interfacial behavior of asphaltenes. *Adv. Colloid Interface Sci.* **2016**, *233*, 83–93.
- (29) Eyssautier, J.; Levitz, P.; Espinat, D.; Jestin, J.; Gummel, J.; Grillo, I.; Barré, L. Insight into asphaltene nanoaggregate structure inferred by small angle neutron and X-ray scattering. *J. Phys. Chem. B* **2011**, *115*, 6827–6837.
- (30) Visser, J. Particle adhesion and removal: A review. *Part. Sci. Technol.* **1995**, *13*, 169–196.
- (31) Faille, C.; Jullien, C.; Fontaine, F.; Bellon-Fontaine, M.-N.; Slomianny, C.; Benezech, T. Adhesion of Bacillus spores and Escherichia coli cells to inert surfaces: role of surface hydrophobicity. *Can. J. Microbiol.* **2002**, *48*, 728–738.
- (32) Lee, S.; Elimelech, M. Relating organic fouling of reverse osmosis membranes to intermolecular adhesion forces. *Environ. Sci. Technol.* **2006**, *40*, 980–987.
- (33) Choo, K.-H.; Lee, C.-H. Understanding membrane fouling in terms of surface free energy changes. *J. Colloid Interface Sci.* **2000**, *226*, 367–370.
- (34) Bartels, L. Tailoring molecular layers at metal surfaces. *Nat. Chem.* **2010**, *2*, 87.

- (35) Ye, Q.; Zhou, F.; Liu, W. Bioinspired catecholic chemistry for surface modification. *Chem. Soc. Rev.* **2011**, *40*, 4244–4258.
- (36) Mikami, Y.; Liang, Y.; Matsuoka, T.; Boek, E. S. Molecular Dynamics Simulations of Asphaltenes at the Oil–Water Interface: From Nanoaggregation to Thin-Film Formation. *Energy Fuels* **2013**, *27*, 1838–1845.
- (37) Alvarez, G.; Jestin, J.; Argillier, J. F.; Langevin, D. Small-Angle Neutron Scattering Study of Crude Oil Emulsions: Structure of the Oil–Water Interfaces. *Langmuir* **2009**, *25*, 3985–3990.
- (38) Tchoukov, P.; Yang, F.; Xu, Z.; Dabros, T.; Czarnecki, J.; Sjöblom, J. Role of asphaltenes in stabilizing thin liquid emulsion films. *Langmuir* **2014**, *30*, 3024–3033.
- (39) Yarranton, H. W.; Hussein, H.; Masliyah, J. H. Water-in-hydrocarbon emulsions stabilized by asphaltenes at low concentrations. *J. Colloid Interface Sci.* **2000**, *228*, 52–63.
- (40) Shi, C.; Zhang, L.; Xie, L.; Lu, X.; Liu, Q.; Mantilla, C. A.; van den Berg, F. G. A.; Zeng, H. Interaction mechanism of oil-in-water emulsions with asphaltenes determined using droplet probe AFM. *Langmuir* **2016**, *32*, 2302–2310.
- (41) Rocha, J. A.; Baydak, E. N.; Yarranton, H. W.; Sztukowski, D. M.; Ali-Marciano, V.; Gong, L.; Shi, C.; Zeng, H. Role of aqueous phase chemistry, interfacial film properties, and surface coverage in stabilizing water-in-bitumen emulsions. *Energy Fuels* **2016**, *30*, 5240–5252.
- (42) Zhang, L.; Shi, C.; Lu, Q.; Liu, Q.; Zeng, H. Probing molecular interactions of asphaltenes in heptol using a surface forces apparatus: Implications on stability of water-in-oil emulsions. *Langmuir* **2016**, *32*, 4886–4895.
- (43) Zhang, L.; Xie, L.; Shi, C.; Huang, J.; Liu, Q.; Zeng, H. Mechanistic Understanding of Asphaltene Surface Interactions in Aqueous Media. *Energy Fuels* **2016**, *31*, 3348–3357.
- (44) Huang, Y. S.; Zeng, X. T.; Hu, X. F.; Liu, F. M. Corrosion resistance properties of electroless nickel composite coatings. *Electrochim. Acta* **2004**, *49*, 4313–4319.
- (45) Rabizadeh, T.; Allahkaram, S. R.; Zarebidaki, A. An investigation on effects of heat treatment on corrosion properties of Ni–P electroless nano-coatings. *Mater. Des.* **2010**, *31*, 3174–3179.
- (46) Sahoo, P.; Das, S. K. Tribology of electroless nickel coatings—A review. *Mater. Des.* **2011**, *32*, 1760–1775.
- (47) Brenner, A.; Riddell, G. Deposition of nickel and cobalt by chemical reduction. *J. Res. Natl. Bur. Stand.* **1947**, *39*, 385–395.
- (48) Grosjean, A.; Rezzazi, M.; Takadoum, J.; Berçot, P. Hardness, friction and wear characteristics of nickel–SiC electroless composite deposits. *Surf. Coat. Technol.* **2001**, *137*, 92–96.
- (49) Chen, C. K.; Feng, H. M.; Lin, H. C.; Hon, M. H. The effect of heat treatment on the microstructure of electroless Ni–P coatings containing SiC particles. *Thin Solid Films* **2002**, *416*, 31–37.
- (50) Sudagar, J.; Lian, J.; Sha, W. Electroless nickel, alloy, composite and nano coatings—A critical review. *J. Alloys Compd.* **2013**, *571*, 183–204.
- (51) Chen, X. H.; Chen, C. S.; Xiao, H. N.; Liu, H. B.; Zhou, L. P.; Li, S. L.; Zhang, G. Dry friction and wear characteristics of nickel/carbon nanotube electroless composite deposits. *Tribol. Int.* **2006**, *39*, 22–28.
- (52) Luo, H.; Leitch, M.; Behnamian, Y.; Ma, Y.; Zeng, H.; Luo, J.-L. Development of electroless Ni–P/nano-WC composite coatings and investigation on its properties. *Surf. Coat. Technol.* **2015**, *277*, 99–106.
- (53) Shi, C.; Chan, D. Y. C.; Liu, Q.; Zeng, H. Probing the hydrophobic interaction between air bubbles and partially hydrophobic surfaces using atomic force microscopy. *J. Phys. Chem. C* **2014**, *118*, 25000–25008.
- (54) Shi, C.; Cui, X.; Xie, L.; Liu, Q.; Chan, D. Y. C.; Israelachvili, J. N.; Zeng, H. Measuring forces and spatiotemporal evolution of thin water films between an air bubble and solid surfaces of different hydrophobicity. *ACS Nano* **2015**, *9*, 95–104.
- (55) Khodakarami, M.; Alagha, L.; Burnett, D. J. Probing Surface Characteristics of Rare Earth Minerals Using Contact Angle Measurements, Atomic Force Microscopy, and Inverse Gas Chromatography. *ACS Omega* **2019**, *4*, 13319–13329.
- (56) Gao, Z.; Xie, L.; Cui, X.; Hu, Y.; Sun, W.; Zeng, H. Probing anisotropic surface properties and surface forces of fluorite crystals. *Langmuir* **2018**, *34*, 2511–2521.
- (57) Zhang, L. Y.; Lawrence, S.; Xu, Z.; Masliyah, J. H. Studies of Athabasca asphaltene Langmuir films at air–water interface. *J. Colloid Interface Sci.* **2003**, *264*, 128–140.
- (58) Hayashi, T.; Ohno, T.; Yatsuya, S.; Uyeda, R. Formation of ultrafine metal particles by gas-evaporation technique. IV. Crystal habits of iron and fcc metals, Al, Co, Ni, Cu, Pd, Ag, In, Au and Pb. *Jpn. J. Appl. Phys.* **1977**, *16*, 705.
- (59) Kar, K. K.; Sathiyamoorthy, D. Influence of process parameters for coating of nickel–phosphorous on carbon fibers. *J. Mater. Process. Technol.* **2009**, *209*, 3022–3029.
- (60) Shi, C.; Yan, B.; Xie, L.; Zhang, L.; Wang, J.; Takahara, A.; Zeng, H. Long-Range Hydrophilic Attraction between Water and Polyelectrolyte Surfaces in Oil. *Angew. Chem., Int. Ed.* **2016**, *55*, 15017–15021.
- (61) Gong, L.; Qiu, X.; Zhang, L.; Huang, J.; Hu, W.; Xiang, L.; Zhu, D.; Sabbagh, R.; Mahmoudi, M.; Fattahpour, V. Probing the Interaction Mechanism between Oil-in-Water Emulsions and Electroless Nickel–Phosphorus Coating with Implications for Antifouling in Oil Production. *Energy Fuels* **2019**, *33*, 3764–3775.
- (62) Israelachvili, J. N. *Intermolecular and Surface Forces*; Academic Press, 2011.
- (63) Wu, X. Investigating the stability mechanism of water-in-diluted bitumen emulsions through isolation and characterization of the stabilizing materials at the interface. *Energy Fuels* **2003**, *17*, 179–190.
- (64) Rudrake, A.; Karan, K.; Horton, J. H. A combined QCM and XPS investigation of asphaltene adsorption on metal surfaces. *J. Colloid Interface Sci.* **2009**, *332*, 22–31.
- (65) Abdallah, W. A.; Taylor, S. D. Surface characterization of adsorbed asphaltene on a stainless steel surface. *Nucl. Instrum. Methods Phys. Res., Sect. B* **2007**, *258*, 213–217.
- (66) Wang, J.; Buckley, J. S.; Creek, J. L. Asphaltene deposition on metallic surfaces. *J. Dispersion Sci. Technol.* **2004**, *25*, 287–298.
- (67) Zhong, Z.; Li, D.; Zhang, B.; Xing, W. Membrane surface roughness characterization and its influence on ultrafine particle adhesion. *Sep. Purif. Technol.* **2012**, *90*, 140–146.
- (68) Hoek, E. M. V.; Bhattacharjee, S.; Elimelech, M. Effect of Membrane Surface Roughness on Colloid–Membrane DLVO Interactions. *Langmuir* **2003**, *19*, 4836–4847.
- (69) Richard Bowen, W.; Doneva, T. A. Atomic force microscopy studies of membranes: Effect of surface roughness on double-layer interactions and particle adhesion. *J. Colloid Interface Sci.* **2000**, *229*, 544–549.
- (70) Crittenden, B. D.; Alderman, N. J. Negative fouling resistances: the effect of surface roughness. *Chem. Eng. Sci.* **1988**, *43*, 829–838.
- (71) Eyssautier, J.; Levitz, P.; Espinat, D.; Jestin, J.; Gummel, J.; Grillo, I.; Barré, L. Insight into asphaltene nanoaggregate structure inferred by small angle neutron and X-ray scattering. *J. Phys. Chem. B* **2011**, *115*, 6827–6837.
- (72) McLean, J. D.; Kilpatrick, P. K. Effects of asphaltene solvency on stability of water-in-crude-oil emulsions. *J. Colloid Interface Sci.* **1997**, *189*, 242–253.
- (73) McLean, J. D.; Kilpatrick, P. K. Effects of Asphaltene Aggregation in Model Heptane–Toluene Mixtures on Stability of Water-in-Oil Emulsions. *J. Colloid Interface Sci.* **1997**, *196*, 23–34.
- (74) Destribats, M.; Lapeyre, V.; Wolfs, M.; Sellier, E.; Leal-Calderon, F.; Ravaine, V.; Schmitt, V. Soft microgels as Pickering emulsion stabilisers: role of particle deformability. *Soft Matter* **2011**, *7*, 7689–7698.
- (75) Zhang, S.; Zhang, L.; Lu, X.; Shi, C.; Tang, T.; Wang, X.; Huang, Q.; Zeng, H. Adsorption kinetics of asphaltenes at oil/water interface: Effects of concentration and temperature. *Fuel* **2018**, *212*, 387–394.

奖励证书

龚露

编号：2020-178

荣获二〇二〇年度国家优秀自费留学生
奖学金，特颁证嘉奖，以资鼓励。


中国国家留学基金管理委员会



扫描全能王 创建